Lifetime Models for Lithium-ion Batteries used in Virtual Power Plant Applications

Stroe, Daniel Ioan

Publication date:
2014

AALBORG UNIVERSITY
DENMARK

Lifetime Models for Lithium Ion Batteries used in Virtual Power Plants

Daniel-Ioan Stroe

Dissertation submitted to Faculty of Engineering, Science, and Medicine at
Aalborg University in partial fulfilment of the requirements
for the degree of Doctor of Philosophy in Electrical Engineering

AALBORG UNIVERSITY
Department of Energy Technology
September 2014

Aalborg University
Department of Energy Technology
Pontoppidanstræde 101
9220 Aalborg East
Denmark
Phone: +45 9940 9240
Fax: +45 9815 1411
Web: http://www.et.aau.dk

Printed in Denmark by UniPrint
ISBN: XXX-XX-XXXXX-XX-X

Abstract

The penetration of wind power into the power system has been increasing in recent years. However, despite its environmental friendliness, the wind power grid integration at a large scale faces several limitations, mainly caused by the characteristics of the wind (i.e. intermittent, variable, and not 100% predictable), which can lead to power system instability, reliability issues, and power quality issues. Consequently, a lot of concerns related to the reliable and stable operation of the power system have been recently addressed. Several solutions were identified and proposed in the literature, in order to mitigate the aforementioned issues.

An attractive solution is represented by the use of energy storage systems (ESSs) together with wind power plants (WPPs). The inherent characteristics of the ESSs will allow the new system, often referred as virtual power plant (VPP), to behave similar to today's conventional generating units seen from the TSO's perspective, by complying with future harsher grid codes and by providing a diversity of grid support services (e.g. frequency regulation, forecast error balancing).

A wide variety of energy storage technologies are available on the market; however, because of their advantages, which include fast response, high efficiency, long lifetime and environmental friendliness, Lithium-ion (Li-ion) batteries represent suitable candidates for integration within VPPs, especially when they are required to provide short- and medium-time services. The family of Li-ion batteries is broad with many different chemistries available at present on the market. Nonetheless, the Li-ion battery based on the lithium iron phosphate/graphite (further referred LFP/C) chemistry is investigated in this thesis.

The lifetime of the Li-ion battery ESS represents a key parameter in the analysis of the economic feasibility of integrating such systems in WPPs. Even though their price is decreasing due to the research carried out mainly in the portable electronics and automotive sectors, Li-ion batteries are still expensive energy storage devices. Therefore, accurate information about Li-ion batteries' lifetime is mandatory in the project planning

stage in order to assess its economic feasibility. Moreover, the performance of the Li-ion batteries is lifetime-dependent and thus accurate information about their state-of-health (SOH), in each operating point during their life, will allow the selection of the best energy management strategy; this would further result in the cost-optimal delivery of the application (service).

The main objective of this thesis was to develop accurate lifetime models for LFP/C battery cells, which are applicable for VPP applications. Several approaches to model the lifetime degradation of Li-ion batteries are presented in the literature. In this thesis an equivalent-electrical circuit performance-degradation modelling approach was followed to develop the lifetime models for the selected LFP/C battery cells. In order to develop the desired lifetime model, laboratory ageing tests are mandatory. However, ageing the Li-ion batteries in the laboratory under real operating conditions, which are characteristic to VPP applications are extremely time consuming and cost demanding. Thus, the Li-ion battery cells were aged in laboratory following an accelerated lifetime testing methodology, which considers both the cycling and the calendar lifetime dimensions. Based on the obtained ageing results, it was found out that the capacity fade and the pulse power capability decrease of the tested LFP/C battery cells are very sensitive to the operating conditions (temperature, SOC-level, cycling and idling time etc.); however, the capacity of the tested battery cells is degrading much faster than the pulse power capability and thus in most cases it will be the performance parameters, which will limit the lifetime.

The developed lifetime models, have been verified in laboratory using two different mission profiles and it was concluded that they are able to predict with good accuracy the capacity fade of the tested LFP/C battery cells for both calendar and cycling ageing conditions.

Moreover, the proposed lifetime models were used to analyse the degradation behaviour, in terms of capacity fade and power capability decrease, of LFP/C battery cells while providing primary frequency regulation on the Danish energy market. For this study case, a realistic mission profile, measured on field during one year, was considered. Based on the proposed lifetime models and considering the field measured mission profile, it was shown that the studied Li-ion battery cells will survive approximately ten years before a 20% capacity fade end-of-life criterion has been reached.

Resumé

Indtrængen af vindkraft i el-nettet er stigende i de seneste år. På trods af dens miljømæssige imødekommenhed, støder vindkraft integrering i storskala med el-net adskillig begrænsninger, hovedsagelig på grund af vindens karakteristikker (såsom intermitterende, varierende og ikke 100% forudsigelig), som kan føre elnettet til ustabilitet, pålidelighedsproblem og el kvalitetsproblem. Derfor retter sig på det seneste mange bekymring omkring pålidelig og driftssikker af elnettet. Mange løsninger er identificeret og foreslået i litteratur for at mindske fornævnte problemer.

En attraktiv løsning er fremlægget, ved at gøre brug energi lagret systemer (ESSs) sammen med vindkraftværk (WPPs). Den iboende karakteristikker af ESSs vil tillade det ny system, ofte refereret som virtuel kraftværk (VPP), til at opføre sig tilsvarende til nu om dages konventionel genereringsenhed set fra TSOs perspektiv, ved at opfylde fremtidig skarpe elnet kode og yde forskellige elnet støtte ydelse (eksempelvis frekvens regulering, forudse fejl balancering).

En bred assortiment af energi lagret teknologier er tilgængeligt på marked, men på grund af dens fordele, hvilke omfatte hurtig reaktion, høj virkningsgrad, lang levetid og miljømæssige imødekommenhed, litium-ion(Li-ion) batterier vise sig egnet til integrering inden for WPPs, især når der kræver kort og medium-tids ydelser. Li-ion-slægt er bred med mange forskellig kemi er for øjeblik tilgængelig på marked. Ikke desto mindre, Li-ion batteri baseret på litium-jern-fosfat/grafit (senere refereret som LFP/C) kemi er undersøgt i denne afhandling.

Levetid af Li-ion batteri ESS repræsenterer en nøgle parameter i analysen af den økonomiske gennemførlighed af integrering af sådan systemer in WPPs. Selv om dens pris er faldende på grund af forskning, hovedsaglig udført inden for automotiv sektor, er Li-ion batterier stadig nogle kostbar energi lagret elementer. Derfor, præcis information om Li-ion batteriers levetid er påkrævet i projektet planlægningsfase for at kunne vurdere dens økonomisk gennerførlighed. Ydermere, ydeevne af Li-ion er levetidsafhængig og således præcist information om state-of-heath i hver arbejdspunkt i løbet af dens liv vil

tillade valget af den bedst energistyringsstrategi; denne vil yderlige resultere i succesfuld levering af applikationen (ydelse).

Hovedformålet i denne afhandling var at udvikle nøjagtig levetids modeller for LFP/C batteri celler, hvilken er brugt i VPP applikationer. Adskillig fremgangsmåde til at modeller levetid af Li-ion batterier er præsenteret i litteraturen. I denne afhandling et ækvivalent elektriskkredsløb ydeevne degradering modellering fremgangsmåde blev efterfulgt til at udvikle levetids modeller for valgt LPF/C batteri celler. For at kunne udvikler tilsigtet levetid model, laboratorium aldringstest er obligatorisk. Dog, ældes Li-ion batterier i laboratorium under reel arbejdsbetingelse, hvilken er særpræget til VPP applikationer er ekstrem tidskrævende og omkostningsfuld. Dermed, Li-ion batteri celler er ældet i laboratorium efterfølgende af en accelererende levetids test metodologi, hvilken tage både hensyn til cyklus og kalender levetid dimensioner. Baseret på det opnået ældes resultatet, er det afsløret at kapacitet svinde og pulserende effekt kapabilitet aftagende for de testet LFP/C batteri celler er meget følsom for arbejdsbetingelser (temperatur, SOC-niveau, cyklus og tomgangstid etc.); dog, kapacitet af de testet batteri celler er aftagende meget hurtigere end pulserende effekt kapabilitet og derfor i de flest tilfælde være ydeevnes parameter der vil begrænse levetid.

De udviklet levetids modeller er verificeret ved anvendte to forskellig mission profiler og der konkluderet at de er i stand til at forudse med god nøjagtighed kapacitets svinde af de tested LFP/C batteri celler for både kalender og cyklus ældes betingelser.

De udviklet levetids modeller var brugt til at analysere degradering adfærd, i form af kapacitet svinde og effekt kapabilitetstab af LFP/C batteri celler mens yder primær frekvens regulering på den danske energi marked. For dette undersøgelsestilfælde, en realistisk mission profil, målet på felt i løbet af et år var påtænkt. Baseret på de foreslået levetids modeller og betænke felt målet mission profil, det er vist at de undersøgt Li-ion batteri celler vil holde sig omtrent ti år før 20% af kapacitet er svindet; end-of-life kriteriet er nået.

Acknowledgements

This research was part of the Intelligent Energy Management System for a Virtual Power Plant project financially supported by the Danish National Advanced Technology Foundation, Vestas Wind Systems A/S and Aalborg University.

First and foremost, I would like to express my sincerest thanks to my main supervisor Remus Teodorescu and to my co-supervisor Søren Juhl Andreasen for their guidance, support, and valuable inputs provided during my entire PhD study.

Furthermore, I would like to thank Philip Carne Kjaer and Rasmus Laerke from Vestas Wind Sytems A/S for giving me the opportunity to follow closely the operation of the first north-European grid-tide Li-ion battery-based energy storage system providing primary frequency regulation.

I would like to also thank my colleague and friend Maciej Swierczynski for the hundreds of discussions and for his valuable feedback during my PhD study. Moreover, special thanks are dedicated to Vaclav Knap and Tiberiu Stanciu for their help in the laboratory related work.

I wish to thank also all my fellow PhD students, who supported me in various ways during this three years; in particularly, I would like to thank Sergiu Spataru, Cristian Busca, Cristian Santamarean, and Bogdan Craciun.

Last but not least, I would like to thank to my entire family in Romania and to my wife, Irina, for their continuous support, encouragements and unlimited patience.

Daniel-Ioan Stroe
Aalborg, Denmark
August 2014

Contents

Contents xv

1 Introduction **1**

1.1 Background 1
1.2 Wind Power Plants with Energy Storage. The Virtual Power Plant . . . 3
1.2.1 The Virtual Power Plant 4
1.3 The Need for Lifetime Models 5
1.4 Objectives 6
1.5 Methodology 7
1.6 Limitations 8
1.7 Publications 8
1.8 Outline 10

2 Energy Storage Technologies for Virtual Power Plants **13**

2.1 VPP applications 13
2.2 Energy Storage Technologies 17
2.2.1 Electromagnetic Energy Storage 18
2.2.2 Mechanical Energy Storage 20
2.2.3 Electrochemical Energy Storage 20
2.3 Selection of Energy Storage Technology 26
2.3.1 Requirements imposed by VPP applications 26
2.3.2 ES technology scorecard 28
2.3.3 Discussions 29
2.4 Lithium-Ion Battery Family Overview 29
2.4.1 Rechargeable Lithium-based batteries 29
2.4.2 Lithium-ion battery chemistries 31
2.4.3 Lithium Iron Phosphate/Carbon Batteries 35

3 Performance Modelling of Li-ion Battery Cells **37**
3.1 Overview of Li-ion Battery Performance Modelling 37
3.1.1 Electrochemical Performance Models 38
3.1.2 Mathematical Performance Models 39
3.1.3 Electrical Performance Models 39
3.1.4 Comparison 42
3.2 Performance Modelling of $LiFePO_4/C$ Battery Cells 42
3.2.1 Characterization of $LiFePO_4/C$ battery cell 43
3.2.2 $LiFePO_4/C$ battery cell performance model 54
3.3 Verification of the Performance Model 63
3.3.1 Verification based on charge/discharge pulses 64
3.3.2 Verification based on PFR profile 66
3.3.3 Discussion 67
3.4 Summary 68

4 Lifetime Modelling of Li-ion Battery Cells **69**
4.1 The Ageing Mechanisms of Li-ion Batteries 69
4.1.1 Ageing during storage 70
4.1.2 Ageing during cycling 71
4.2 Overview of Li-ion Battery Lifetime Modelling 73
4.2.1 Pure-lifetime models 74
4.2.2 Performance-degradation models 77
4.2.3 Comparison of lifetime modelling approaches 79
4.3 Summary 79

5 Accelerated Ageing Testing of $LiFePO_4/C$ Battery Cell **81**
5.1 Introduction 81
5.2 Accelerated calendar lifetime tests 83
5.3 Accelerated cycling lifetime tests 85
5.4 Reference performance tests 87
5.5 Procedure for accelerated lifetime tests 91

6 Calendar Ageing Results for the $LiFePO_4/C$ Battery Cell **95**
6.1 Introduction 95
6.2 Capacity fade 96
6.2.1 Dependence on storage time 97
6.2.2 Dependence on storage temperature 98

6.2.3 Dependence on storage SOC-level . . . 100
6.3 Pulse power capability decrease . . . 101
6.3.1 Dependence on storage time . . . 104
6.3.2 Dependence on storage temperature . . . 105
6.3.3 Dependence on storage SOC-level . . . 106
6.4 Changes in EIS plots . . . 108
6.4.1 Ageing evaluation of series resistance R_s . . . 110
6.4.2 Ageing evaluation of resistance R_1 . . . 111
6.4.3 Ageing evaluation of resistance Q_1 . . . 113
6.5 Self-Discharge . . . 114
6.6 Summary . . . 118

7 Cycling Ageing Results for the $LiFePO_4$/C Battery Cell 119
7.1 Introduction . . . 119
7.2 Capacity fade . . . 120
7.2.1 Dependence on number of cycles . . . 121
7.2.2 Dependence on cycle depth . . . 122
7.2.3 Dependence on temperature . . . 123
7.2.4 Dependence on average SOC-level . . . 124
7.3 Pulse power capability decrease . . . 126
7.3.1 Dependence on number of cycles . . . 126
7.3.2 Dependence on cycle depth . . . 127
7.3.3 Dependence on temperature . . . 128
7.4 Changes in EIS plots . . . 129
7.4.1 Ageing evaluation of series resistance R_s . . . 130
7.4.2 Ageing evaluation of series resistance R_2 . . . 132
7.4.3 Ageing evaluation of generalized capacitance Q_2 . . . 134
7.5 Summary . . . 136

8 $LiFePO_4$/C Battery Cell Performance-Degradation Model 137
8.1 Performance-Degradation Model Structure . . . 137
8.2 Incremental Decrease of LFP/C Battery Cell Performance Parameters . . . 141
8.3 Verification of the Performance-Degradation Model . . . 146
8.3.1 Procedure for verification of the performance-degradation model 146
8.3.2 Laboratory ageing tests . . . 147
8.4 Summary . . . 152

9 Evaluation of the $LiFePO_4$/C Battery Cell Lifetime in VPP **155**
9.1 Primary Frequency Regulation in Denmark with Li-ion Battery ESS . . 155
9.1.1 Primary frequency regulation in Denmark 156
9.1.2 PFR with Li-ion battery ESS in DK1 156
9.2 Procedure for Lifetime Evaluation 157
9.2.1 Grid frequency 157
9.2.2 State-of-charge profile 158
9.3 Performance Degradation of LFP/C Battery Cells 159
9.3.1 Capacity fade of LFP/C battery cells 160
9.3.2 PPC decrease of LFP/C battery cells 161
9.4 Discussion 162

10 Summary, Conclusions, and Future Work **165**
10.1 Summary 165
10.2 Conclusions 167
10.3 Future Work 170

Bibliography **186**

Appendix **186**

A Parameters of the $LiFePO_4$/C battery cells under study **187**

B Laboratory Equipment **189**
B.1 Description of battery test stations 189
B.2 Description of universal ovens 190

C Characterization test of the LFP/C battery cell **193**
C.1 Preconditioning Test 193
C.2 Relaxation Test 195
C.3 Capacity Test 198
C.4 OCV vs SOC Test 199
C.5 HPPC Test 201
C.6 Pulse Power Capability calculation 202
C.7 EIS Test 203

D Verification of the LFP/C battery cell performance model **205**
D.1 Verification based on dynamic charge - discharge profile 205
D.2 Verification based on PFR current profile 207

E Results of the Accelerated Ageing Tests **209**
E.1 Results from accelerated calendar ageing tests 209
E.1.1 Measured Capacity Fade 209
E.1.2 Dependence of capacity fade on storage time 209
E.1.3 Measured Discharge Pulse Power Capability 211
E.1.4 Dependence of PPC decrease on storage time 221
E.1.5 Measured EIS spectra 223
E.1.6 Time evolution of EEC parameters and their dependence on storage temperature and SOC-level 226
E.1.7 Dependence of EEC parameters' time evolution on storage temperature and SOC-level 232
E.2 Results of the Accelerated Ageing Tests 234
E.2.1 Measured Capacity Fade 234
E.2.2 Dependence of capacity fade on the number of cycles 237
E.2.3 Measured Discharge Pulse Power Capability 239
E.2.4 Dependence of PPC decrease on the number of cycles 242
E.2.5 Measured EIS spectra 244
E.2.6 Time evolution of EEC parameters and their dependence on cycle depth, temperature, and average SOC-level 246
E.2.7 Dependence of EEC parameters' on cycle depth and cycling temperature 252

F Results of the Verification Tests **255**
F.1 Verification with symmetrical charging/discharging SOC profile 255
F.2 Verification with profile characteristic for PFR service 256

G LFP/C battery cells lifetime evaluation **257**

Chapter 1

Introduction

1.1 Background

Driven by environmental and geopolitical concerns, the energy generation paradigm is changing from fossil-fuels to renewable resources. Thus, in the chase of sustainable and more environmentally friendly energy sources, wind energy has emerged, in the last decade, as the most popular solution; this trend is illustrated in Fig.1.1, where the shares of installed power capacity, which is generated from various resources, are compared [1], [2].

Moreover, the increasing level of installed wind power capacity, presented in Fig.1.2, will increase even more since this tendency can be directly related to the European Union's ambitious goals concerning the share of the electricity generated from renewable sources (i.e. 20% of total electricity generated from renewables by 2020 [3]).

On the other hand, despite its environmental friendliness, the grid integration of the wind energy faces several challenges, especially in countries (or regions) with high wind power penetration levels as is the case of Denmark, Germany or Spain [4]. These challenges are mainly caused by the characteristics of the wind resource: variable, intermittent, and not 100% predictable [5]. Moreover, these characteristics will be translated to the produced wind power, which in consequence will be more variable and less predictable than the power produced from conventional sources.

Traditionally, the electrical energy is generated by conventional generating units (CGUs), which in contrast to the wind power plants (WPPs), are able to regulate their production in order to deliver non-fluctuating power according to a predefined schedule.

The most common solution used, at present, to mitigate the variability of the wind

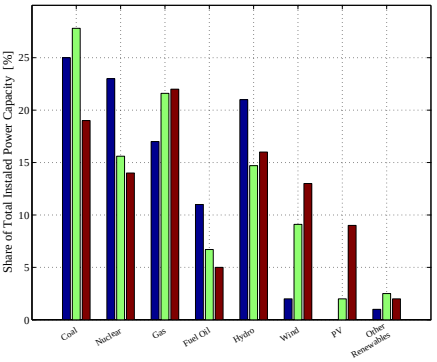

Figure 1.1: *Change in the installed power capacity paradigm between year 2000 (blue), 2009 (green), and 2013 (red) in European Union*

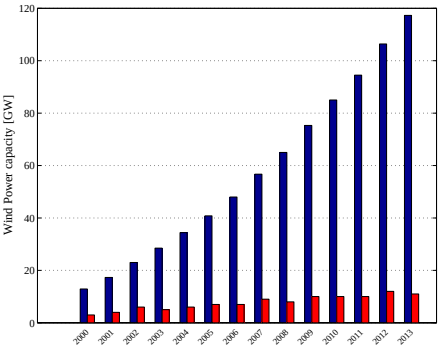

Figure 1.2: *Cumulative installed wind power capacity (blue) and annual installed wind power capacity (red) in European Union*

power is to commit spinning reserves provided by fast-responding CGUs [6]. However, with the increasing level of wind power penetration, the amount of spinning reserves that needs to be scheduled might increase as well [7]; this would result in an increase of the wind energy cost, which will further increase if the spinning reserves commitment is not efficiently realized [7], [8].

The wind power production is proportional to the cube of the wind speed; therefore, even small errors in the wind speed forecast will cause a significant error on the power production forecast. A straightforward solution to improve the predictability of wind power is to operate the wind turbines (WTs) or the WPP below the maximum power point; however, by following this approach, a high decrease in the wind power production will be caused, which would further lead to an increase of the wind power cost. A more common solution to compensate the wind power production error is the use of fast-reacting fossil fuel-based CGUs [6].

In conclusion, considering the increasing wind power penetration trends, the environmental friendliness characteristic of wind power will be alleviated, since most of currently operating CGUs will not be decommissioned but rather used to improve the availability and predictability of the wind power. Therefore, other solutions for bringing the characteristics of the wind power closer to the ones of the conventionally generated power (e.g. reliable, dispatchable etc.) are needed.

1.2 Wind Power Plants with Energy Storage. The Virtual Power Plant

The main disadvantage of wind power is its strong dependence on the not fully predictable weather conditions. Thus, wind power grid integration at a large scale raises serious concerns regarding the reliable and stable operation of the power systems [9], [10], [11]. Besides the aforementioned, traditional but environmental unfriendly solution of committing CGUs to improve the wind power reliability, several other solutions have been proposed: large scale aggregation of WPPs, improvement of the wind forecast methods, improvement of the demand side management techniques, and the use of energy storage systems as power and energy buffers.

The large scale aggregation of wind power has a positive effect on the reliable operation of the power system and on the power quality since an increased number of interconnected WPPs reduces the effect of poor forecasts and the wind power variability [9]. The aggregation of multiple WPPs can be realized by constructing transmission capacity to interconnect large wind power plants. Katzenstein *et al.* presented in [12] that by interconnection, the wind power variability can be reduced by 30% to 87% depending on the used time scale. Another important aspect is represented by the fact that reduction of the wind power variability depends on the number of interconnected WPPs, and their size and location [9], [12].

Another solution to improve the wind power reliability is represented by the improvement of the accuracy of the wind speed forecast methods [10]. Moreover, by improving the accuracy of wind forecasts, the number of fast-responding CGUs at stand-by would be reduced. At present, a lot of research is being carried out in the area of wind speed forecasting and the improvements are targeting both extreme events (e.g., gusts) and long-term wind speed forecasting [13], [14]. However, even though the improvements of the forecasting methods will lead to an increase of the wind forecast accuracies, this solution is complex and not 100% accurate [14].

Demand side management, or demand response, represents an alternative to the use of CGUs for supporting wind power grid integration [15]; however, at the moment, because of various issues which include also missing infrastructure (e.g. transmission lines etc.), the experience in using this technique is still limited, even though yearly progresses are reported in the United States [15], [16].

The use of energy storage systems (ESSs) together with WTs and/or WPPs can make the wind power more reliable by increasing its controllability and predictability and reducing its variability [5], [10]. ESSs are able to solve most of the wind power

grid integration issues [17]; however, their widespread use either as stand-alone grid-connected systems or together with WTs/WPPs was bounded until recently by several factors such as capital and operational cost and limited field experience [17], [18], [19]. Currently, because of the advances in different energy storage technologies and their price decrease, ESSs based on different storage technologies are considered in several pilot projects, where their ability for enhancing the wind power grid integration and for supporting the grid is demonstrated [20], [21].

All the aforementioned solutions have their advantages and disadvantages when used for improving the wind power reliability. However, in this thesis, the use of ESS together with WPPs is investigated.

1.2.1 The Virtual Power Plant

By integrating ESSs within WPPs, the output power of the new system, further refereed as virtual power plant (VPP), will become more dispatchable, predictable, and less variable [5]. Consequently, the VPP will behave similar to today's CGUs, seen from the transmission system operator's perspective, and will be able to meet future more stringent grid codes, which will ask for more flexibility from the WPPs side [22], [23]. Moreover, the VPP will be able to provide ancillary services such as inertia [20], primary frequency regulation [24], and will be able to reduce the wind power forecast error [25], [26]. The schematic representation of the VPP concept is illustrated in Fig. 1.3.

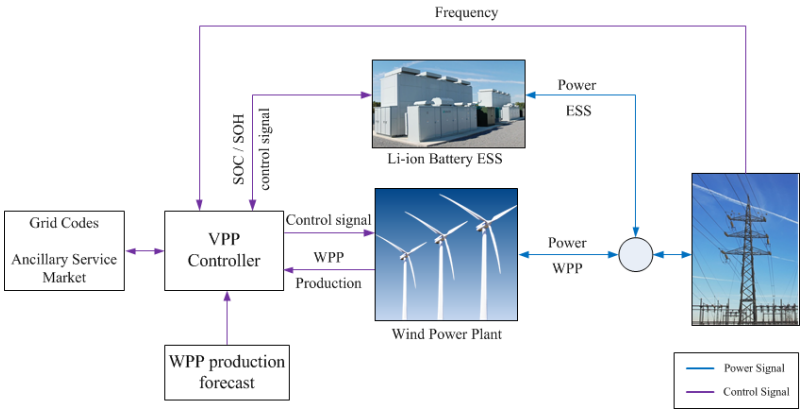

Figure 1.3: *The Virtual Power Plant*

The VPP consists of the WPP, the ESS and the VPP controller. The ESS is composed of the energy storage (ES) device (e.g. electrochemical battery, flow battery etc.), the battery management system (BMS), and the power conditioning system, which en-

sures the grid integration. The purpose of the BMS is to monitor the state-of-charge (SOC) and state-of-health (SOH) of the ES device and to deliver this information to the VPP controller. Additionally, the VPP controller receives information from the WPP regarding the instantaneous generated power; moreover, the VPP controller has information regarding the forecasted wind power and the grid codes, which have to be fulfilled. By analysing all the gathered information, the VPP controller determines at each operating point the best operating strategy, which ensures the successful delivery of the service, and sends the control signals to the WPP and ESS, accordingly.

Different ES technologies are available at this moment on the market and most of them are suitable for VPP integration [27]. Each of these ES technologies has its own technical and economical characteristics and its own maturity level. Therefore, the selection of the most suitable ES technology for integration with VPP is not a straightforward process, depends on many parameters, and in most of the cases is application-dependent [28]. However, because of their advantages, which are briefly discussed in Chapter 2, the Lithium-ion (Li-ion) battery technology will be studied as the ESS to be integrated with VPPs.

1.3 The Need for Lifetime Models

One of the bottlenecks for the widespread use of ESS (and especially of the Lithium-ion batteries) together with WPPs is their cost competitiveness [29]. The effect of the cost can be minimized by an accurate and reliable lifetime estimation of the ESS.

From the economic perspective, not knowing the lifetime or having erroneous information about the lifetime of the ESS would introduce uncertainty in the VPP project profitability; this is because the lifetime of ESS is a key factor in the profitability calculation of the investment in ESS for VPP integration, as presented in [26]. Thus, accurate lifetime models are necessary even from the initial stage of planning a project where ESS are involved.

From the technical perspective, lifetime models are required because the performance of ESS, and especially of the Li-ion batteries based ESS, are lifetime-dependent. The performance parameters (e.g. capacity, power capability, efficiency etc.) of Li-ion batteries are degrading in time and thus their degradation (lifetime) behaviour needs to be known in order to choose at every moment the best operational energy management strategy; the best operational energy management strategy will ensure both the successfully delivery of the application (e.g. primary frequency regulation) and the ESS lifetime maximization. Moreover, by having accurate information about the ESS degradation,

reliable cooling systems that allow for ESS lifetime optimization can be designed [30]. Besides the aforementioned features, an accurate lifetime model should also be able to estimate precisely the performance of the ESS at its end-of-life (EOL); by knowing this, the ESS will be optimally sized and will be able to provide the targeted application (service) throughout its life [31].

The information provided by the Li-ion battery manufacturers about the lifetime of their products is, in most of the cases, limited and can not be used when the batteries are working under complex operating conditions. Therefore, lifetime models for Li-ion battery cells need to be developed by the end-users.

However, developing a lifetime model that is able to estimate accurately the SOH of the Li-ion battery cells, which are used in VPP applications, is a challenging process because of two main reasons. Firstly, the battery mission profiles, which are characteristic for VPP applications are complex and in most of the cases difficult to predict in advance. This is in opposition with the battery mission profiles, which are characteristic for consumer electronics (e.g. laptops, mobiles etc.) and even for electrical vehicles (EVs). Secondly, the degradation mechanism of Li-ion batteries is a complex process and there are many factors (i.e. temperature, cycle depth etc.) that are influencing the lifetime of the battery [32]. Consequently, in order to build accurate lifetime models for Li-ion batteries, which are used in VPP applications, extensive laboratory tests or field measurements are required.

At present, a wide variety of Li-ion battery chemistries exists on the market [33] and generally a lifetime model developed for a certain chemistry cannot be directly transferred to another chemistry. In this thesis, a battery cell based on the lithium iron phosphate chemistry (i.e. Li-ion cells using $LiFePO_4$ cathodes and graphite anodes) will be used for lifetime investigation.

1.4 Objectives

In order to make use of the Li-ion batteries integrated into a VPP in an optimal way, information regarding their performance parameter at each operating point during their life become necessary. Thus, the objective of this thesis is to:

Develop accurate lifetime models for $LiFePO_4$-based battery cells, which can be used for lifetime estimation of the batteries when used in various VPP applications

These lifetime models must be able to predict the degradation behaviour of the battery performance parameters (i.e. capacity, power capability, and internal resistance) both for cycling and idling operation.

1.5 Methodology

This section presents the methodology, which was followed, to develop the desired lifetime models for the $LiFePO_4$ cathode-based battery cells.

A thorough **literature survey** was carried out in order to analyse and determine:

- the most appealing grid service (application), which can be provided by the VPP;
- the most suitable ES technology for integration in the VPP;
- the most appropriate lifetime modelling approach for the selected ES technology.

Experimental characterization of the selected ES device, under various operating conditions and development of the performance model.

Experimental investigation on the lifetime of the selected ES device by performing accelerated calendar and cycling lifetime tests under laboratory conditions, as illustrated in Fig. 1.4 (*see Part I*).

Development and parametrization of the lifetime models based on the results obtained from the accelerated lifetime tests, as illustrated in Fig. 1.4 (*see Part II*).

Experimental validation of the developed lifetime models by testing, in laboratory, the selected ES device with a mission profile, which is characteristic to the targeted grid service, as illustrated in Fig. 1.4 (*see Part III*).

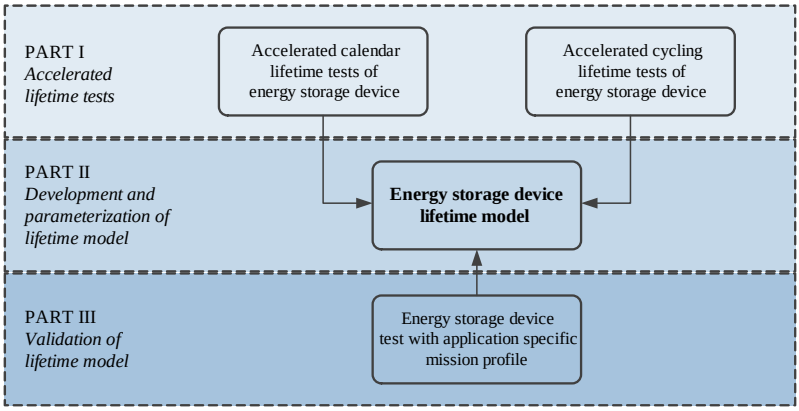

Figure 1.4: *The used methodology for developing the lifetime model*

Evaluation of the ageing behaviour of the selected ES device when it is subjected to a real mission profile; the mission profile was measured on an ES device, integrated into a VPP, while it was delivering the targeted grid service in the Danish energy market.

1.6 Limitations

Lifetime modelling of Li-ion batteries is a complex topic and several assumptions were considered in order to cope with the limited time period allocated to this project.The most important limitations, which were considered and have influenced the results presented in this PhD thesis are summarized below:

- the performance model of the tested $LiFePO_4$-based battery cell was developed and validated only for the typical operating temperature of ESS in stationary applications (i.e. 25^oC);
- not all the accelerated ageing tests have been performed until the tested battery cells have reached the EOL criterion; in this case the degradation characteristics was extrapolated;
- the Li-ion battery cells tested for validation of the developed lifetime model have reached only a reduced degradation level, at the time of writing this; thus, the verification process and the obtained error for the lifetime model might be influenced by this issue;
- the possible interactions between the stress factors, which are influencing the ageing of the tested Li-ion batteries, were not analysed;
- the age-dependence of the performance (dynamic) model of the $LiFePO_4$ was not included in the present version of the proposed lifetime model.

Moreover, it has to be stressed that the results presented in this thesis are mainly valid for the tested $LiFePO_4/C$ battery cell. The obtained results are not transferable to other Li-ion battery chemistries even though some tendencies and conclusions derived from the proposed models might be applicable. Nevertheless, the proposed and validated lifetime modelling approach can be applied, or can be used as a guideline, for lifetime modelling of all Li-ion battery chemistries, which are available at present on the market.

1.7 Publications

During the PhD period, the following papers have been published or were accepted for publication. The papers are divided into two categories, journal and conference papers, and are listed in chronological order.

[J-1] M. Swierczynski, D.I. Stroe, A.-I. Stan, R. Teodorescu, and D.U. Sauer. Selection and performance-degradation modeling of $LiMO_2/Li_4Ti_5O_{12}$ and $LiFePO_4/C$ battery cells as suitable energy storage systems for grid integration with wind power plants: An example for the primary frequency regulation service. *Sustainable Energy, IEEE Transactions on*, 5(1):90--101, Jan 2014

[J-2] D.-I. Stroe, M. Swierczynski, A.-I. Stan, R. Teodorescu, and S.J. Andreasen. Accelerated lifetime testing methodology for lifetime estimation of lithium-ion batteries used in augmented wind power plants. *Industry Applications, IEEE Transactions on*, PP(99):1--1, 2014

[J-3] M. Swierczynski, D.-I. Stroe, A.-I. Stan, and R. Teodorescu. Lifetime and economic analyses of lithium-ion batteries used for balancing the wind power forecast error: A case study for a single wind turbine. *International Journal of Energy Research, Wiley*, accepted for publication

[J-4] M. Swierczynski, D.-I. Stroe, R Laerke, A.-I. Stan, R. Teodorescu, P.C. Kjaer, and S.K. Kjaer. Field experience from li-ion bess delivering primary frequency regulation in the danish energy market. *ECS Transactions*, 2014 - under review

[C-1] D.-I. Stroe, A.-I. Stan, R. Diosi, R. Teodorescu, and S.J. Andreasen. Short term energy storage for grid support in wind power applications. In *Optimization of Electrical and Electronic Equipment (OPTIM), 2012 13th International Conference on*, pages 1012--1021, May 2012

[C-2] D.-I. Stroe, M. Swierczynski, A.-I. Stan, R. Teodorescu, and S.J. Andreasen. Performance-degradation model for $Li_4Ti_5O_{12}$-based battery cells used in wind power applications. In *7th International Renewable Energy Storage Conference and Exhibition, IRES 2012*, 2012

[C-3] M. Swierczynski, D.-I. Stroe, A.-I. Stan, and R. Teodorescu. Evaluation of different operational strategies for lithium ion battery systems connected to a wind turbine for primary frequency regulation and wind power forecast accuracy improvement. In *11th International Workshop on Large-Scale Integration of Wind Power into Power Systems*, 2012

[C-4] D.-I. Stroe, M. Swierczynski, A.-I. Stan, and R. Teodorescu. Accelerated lifetime testing methodology for lifetime estimation of lithium-ion batteries used in augmented wind power plants. In *Energy Conversion Congress and Exposition (ECCE), 2013 IEEE*, pages 690--698, Sept 2013

[C-5] D. Stroe, M. Swierczynski, A.-I. Stan, R. Teodorescu, and S.J. Andreasen. Experimental investigation on the internal resistance of lithium iron phosphate battery cells during calendar ageing. In *Industrial Electronics Society, IECON 2013 - 39th Annual Conference of the IEEE*, pages 6734--6739, Nov 2013

[C-6] M. Swierczynski, D. Stroe, A.-I. Stan, and R. Teodorescu. The lifetime of the lifepo4/c battery energy storage system when used for smoothing of the wind power plant variations. In *Industrial Electronics Society, IECON 2013 - 39th Annual Conference of the IEEE*, pages 6825--6830, Nov 2013

[C-7] M. Swierczynski, D.-I. Stroe, A.-I. Stan, R. Teodorescu, R. Laerke, and P.C. Kjaer. Field tests experience from 1.6mw/400kwh li-ion battery energy storage system providing primary frequency regulation service. In *Innovative Smart Grid Technologies Europe (ISGT EUROPE), 2013 4th IEEE/PES*, pages 1--5, Oct 2013

[C-8] M. Swierczynski, D.I. Stroe, A.I. Stan, and R. Teodorescu. Primary frequency regulation with li-ion battery energy storage system: A case study for denmark. In *ECCE Asia Downunder (ECCE Asia), 2013 IEEE*, pages 487--492, June 2013

[C-9] M. Swierczynski, D.I. Stroe, A.I. Stan, R. Teodorescu, and H. Vikelgaard. Selection and impedance based model of a lithium ion battery technology for integration with virtual power plant. In *Power Electronics and Applications (EPE), 2013 15th European Conference on*, pages 1--10, Sept 2013

[C-10] D.-I. Stroe, M. Swierczynski, A.-I. Stan, V. Knap, R. Teodorescu, and S.J. Andreasen. Diagnosis of lithium-ion batteries state-of-health based on electrochemical impedance spectroscopy technique. In *Energy Conversion Congress and Exposition (ECCE), 2014 IEEE*, 2014, in press

[C-11] V. Knap, R. Sinha, M. Swierczynski, D.-I. Stroe, and S.K. Chaudhary. Grid inertial response with lithium-ion battery energy storage. In *Industrial Electronics (ISIE), 2014 IEEE International Symposium on*, 2014

1.8 Outline

The present PhD thesis is organized as follows:

Chapter 1 presents the background and the motivation of the thesis; moreover, the objectives, the followed methodology and the limitations of the thesis are presented as well.

Chapter 2 presents the literature overview of the energy storage technologies (with special emphasis on the Li-ion batteries), which are suitable for integration in VPPs; furthermore, the most appropriate services (applications) for being provided by the Li-ion battery ESS, are discussed. The requirements imposed by the considered VPP applications are summarized and

Chapter 2 discusses the most appropriate short- and medium-term VPP services (applications) for being provided by ESSs. Moreover, the literature overview of the energy storage technologies (with special emphasis on the Li-ion batteries), which are suitable for integration in VPPs, is carried out. The requirements imposed by the considered VPP applications are juxtaposed to the characteristics of the presented ES technologies, and the suitability, for VPP integration, of the considered storage technology is derived.

Chapter 3 is dedicated to the performance modelling of the Li-ion batteries. Firstly, the state-of-the-art of the Li-ion batteries performance models is briefly presented. Secondly, the methodology proposed for characterization and performance modelling of the LFP/C-battery cells is introduced. Finally, the procedure for the verification of the developed performance model is shown.

Chapter 4 presents the literature overview regarding the ageing mechanisms of Li-ion batteries. Different approaches to model the lifetime of the Li-ion batteries are presented and compared. Based on this comparison, the approach used in this work for Li-ion batteries lifetime modelling (i.e., EEC-based performance-degradation modelling), is selected.

Chapter 5 describes the methodology based on accelerated ageing, which was followed to develop the desired lifetime models. The procedure for accelerated calendar and cycling lifetime testing are discussed separately. Furthermore, in this chapter is presented the structure of the periodical check-up tests, which are used to measure the degradation of the performance parameters of the tested LFP/C battery cells.

Chapter 6 and *Chapter 7* present and analyse the results obtained from the performed accelerated calendar and cycling ageing tests, respectively. The procedures followed for developing the lifetime models for the capacity fade and power decrease of the tested Li-ion battery cells, for the calendar and cycling dimensions are described in detail as well.

Chapter 8 presents in detail the structure of the proposed performance-degradation model for the studied LFP/C battery cells. The accuracy of the model was verified by performing additional laboratory tests, considering two different mission profiles, and the results from the verification tests are presented as well in this chapter.

In *Chapter 9*, the degradation behaviour of the performance parameters of the LFP/C

battery cells is analysed for the case when such batteries are used for providing primary frequency regulation in the Danish ancillary services market.

Chapter 10 summarizes the work carried out in this thesis, provides concluding remarks regarding the obtained results, and suggests possible topics for future work.

Chapter 2

Energy Storage Technologies for Virtual Power Plants

Several applications of storage, which can support integration of wind power and bring the characteristics of WPPs close to those of CGUs, are presented in the first section of this chapter. The second section gives an overview of the ES technologies which are suitable for integration into VPPs; their characteristics, advantages, disadvantages are presented. The most suitable ES technology candidate for integration in VPP is selected, based on various requirements, in the third section of this chapter. The last section discusses in more detail the Li-ion battery technology and focuses mainly on the $LiFePO_4/C$ chemistry, which will be further investigated in this thesis.

2.1 VPP applications

ESSs are able to provide a wide variety of services, both for facilitating the grid-integration of large WPPs and for supporting the grid operation (i.e. ancillary services) [9], [27], [47], [48]. However, in the following, only the services provided by the ESSs, which will bring the characteristics of the VPPs close to the ones of the CGUs are described. Besides describing the services, the requirements (e.g. size, lifetime etc.), which have to be fulfilled by the ESS in order to ensure the proper delivery of each service, will be mentioned, as well.

Inertia Emulation

In the case of traditional CGUs, their rotor speed is directly coupled with the grid frequency; in this manner, the rotating mass of the CGUs acts as a kinetic energy (which is

released) and provides inertia to the grid when sudden load or generation changes occur, reducing the initial rate of change of frequency. However, because of the aforementioned trend of replacing CGUs with distributed wind power generators, whose rotor speed is decoupled form the grid frequency by the power electronics system, the amount of inertia in the grid is reduced significantly.

The decrease of the system inertia (due to decommissioning of CGUs) combined with the increasing levels of variable wind generation, will have a negative effect on the reliable operation of the power system. Thus, alternative solutions for increasing the grid inertia have to be found. By applying certain control structures, the WPPs can provide to some extent inertial response, as presented in [49] and [50].

Fast-responding ESSs integrated into VPPs represent an alternative solution for emulating the grid inertia. The use of ESS-based on Li-ion batteries was illustrated in [46]. Moreover, Kjaer *et al.* have presented in [20] results from field testing of a grid-connected ESS providing inertial response.

In order to ensure a proper delivery of the discussed application, the ESS should respect the following requirements [46], [48]:

ESS size = 5% of the WPP size;

ESS discharge time = 5 - 10 seconds;

ESS lifetime = 250 - 10 000 cycles;

Grid Frequency Regulation

The purpose of the grid frequency regulation (GFR) service is to maintain the grid frequency within a predefined interval (i.e. 50Hz $\pm$ 0.02Hz) following a disturbance, which was caused by, or it results in, a significant imbalance between generation and loads. Traditionally, CGUs, which are online, are providing GFR by increasing or decreasing their production depending if under-frequencies (i.e. $f < 49.98$) or over-frequencies (i.e. $f > 50.02$) were detected, respectively [47]. To maintain the balance between load and generation, most of the TSOs are using three levels of controls and reserves, performed in successive steps [51]; however, in this work, the focus is on the first level, the primary frequency regulation (PFR).

In systems with high wind penetration levels, such imbalances are occurring more frequently (due to the characteristics of wind power) and maintaining the grid frequency, in the aforementioned interval, becomes more difficult [9], [18].

Similar to the case of the inertial response application, considering the trend of withdrawing the CGUs from operation, alternative solutions for providing the PFR service are required. WPPs can contribute themselves to the restoration of the grid frequency

by providing downward and/or upward regulation by pitching or power curtailment, respectively [52], [53]. Furthermore, there are certain grids with high levels of wind power penetration, as is the case of Denmark, where WPPs are required to provide PFR [54]. However, operating the WPPs in curtailment mode for long periods has a negative economic impact on energy production [52].

Consequently, ESS integrated in VPPs or stand-alone become an attractive alternative for providing PFR [27], [48], [55]; when required, the ESS integrated into the VPP will provide downward-regulation by charging from the grid and upward-regulation by discharging to the grid.

Especially suitable for this application are the ES technologies, which are characterized by fast response time, long cycle lifetime at partial charge/discharge, and high power capability as is the case of supercapacitors, flywheels and some electrochemical batteries (e.g. Li-ion batteries) [42], [56].

The requirements, which the ESS has to fulfill in order to provide PFR are [48], [47], [27]:

ESS size = 1 - 100 MW;

ESS discharge time = 15 minutes;

ESS lifetime = 250 - 10 000 cycles;

Wind Power Forecast Accuracy Improvement

In order to bid into the markets, WPP operators need to predict their power production in advance. The bids should be placed ahead of the hour of delivery at different intervals (e.g. 2.5 hours or 36 hours), depending on the TSO requirements [57], [58]. However, the wind power production is not 100% predictable, even though the wind speed forecast methods have improved recently [14].

Therefore, whenever their is an unbalance between the actual power production and the forecasted (bided) power, the WPP operators are faced with significant expenses since they have to buy balancing power in order to cover the forecast error. In order to minimize the aforementioned expenses, improved forecasting techniques and bidding strategies are used, as presented in [18].

An alternative countermeasure for minimizing the penalties and to improve the wind power forecast accuracy is the use of ESS together with WPPs [18], [58], [59]. In this application, the ESS will work similar to a CGU, which is providing balancing power, by delivering power when the actual production is lower than the forecast and will absorb power when the actual power production is higher than the forecasted production.

Different ES technologies are suitable for providing the forecast accuracy improvement, such as sodium-sulphur and Li-ion batteries [18], [48].

In order to be able to improve the wind power forecast accuracy, the ESS has to fulfil the following requirements [5], [26]:

ESS size = 20 - 25% of the WPP size;

ESS discharge time = minutes to hours;

ESS lifetime = -;

Power Gradient Reduction

One of the challenges encountered by the wind power grid integration at a large scale is related to the wind variability; the wind variability is further transferred into variability of the wind power production, which could have a negative impact on the stable operation of the grid, particularly in areas with high wind penetration levels or if WPPs are connected to weaker parts of the transmission network [9], [60]. At present, these wind power fluctuations are suppressed by fast-reacting CGUs.

The use of ESSs integrated into VPPs was identified as a viable and environmental-friendly alternative for smoothing the wind power fluctuations [5], [9], [61]. In this application, the ESS will work similar to a low-pass filter and will keep the power gradient $(\frac{dP}{dt})$ within the desired limits [43]. Thus, the issues regarding the stable operation of the grid are mitigated and the costs for the spinning reserves are decreased.

The most suitable ES technologies for this application are the ones which are characterized by fast response and a relative high power capability [5], [9]. There are several demonstration projects where ESSs are used to provide power gradient reduction; an example is the 1.5 MW ESS-based on advanced lead-acid batteries located in Maui, Hawaii, which is used to provide power gradient reduction (1MW/min) for a 30 MW WPP [62].

The requirements imposed to ESS in order to successfully deliver this service are [18], [43], [62]:

ESS size = 1 - 15 MW, depending on the gradient reduction level;

ESS discharge time = 15 minutes - 1 hour;

ESS lifetime = > 100 000;

Black Start

A power source which has the capability to go from shut-down to the operating condition without the assistance from the grid is referred to have the black start ability [63]. Moreover, after going to the operating condition, the power source is energizing the grid and is helping other units to start-up after the failure has occurred.

ESSs have the black start capability and an example is the use of Nickel Cadmium batteries to energize the transmission lines in Fairbanks, Alaska whenever an outage occurs [64].

The requirements for the ESS, in order to provide this service, are the following [47]:
ESS size = 5 - 50 MW;
ESS discharge time = 15 minutes - 1 hour;
ESS lifetime = 10 - 20 cycles;

By providing the aforementioned services, ESSs integrated into VPPs could bring the characteristics of WPPs close to those of CGUs. Besides these services, ESSs integrated into VPPs could be used for: energy arbitrage, load following, transmission upgrade deferral [27], [47], [48].

2.2 Energy Storage Technologies

The purpose of this section is to present an overview of the ES technologies that are suitable for integration into VPPs.

A wide variety of energy storage technologies are currently available on the market [47]. As it will be shown in this section, each of these technologies has its own electrical characteristics, lifetime characteristics, and maturity level. The advantages and drawbacks of each ES technology will be presented, example from already existing applications will be summarized, and finally their suitability for VPP integration will be briefly discussed.

A classification of the most common energy storage technology, grouped according to the form of stored energy is presented in Fig. 2.2.

Theoretically, all the ES technologies presented in Fig. 2.2 are able to provide the services discussed in Chapter 2.1. However, the installation of pumped-hydro ESSs and compressed-air ESSs is dependent on specific geological formations [65], which sometimes are in contradiction with the requirements of WPPs. Moreover, they require high capital investments, which often is much higher the investment in WPP; thus, their future integration in VPPs is rather questionable. Consequently, these two ES technologies are not presented in the upcoming sections.

Moreover, thermal energy storage technologies (e.g. phase change materials, molten salt energy storage, cryogenic energy storage) were not considered, since these technologies are usually characterized by low efficiencies and lack of maturity and thus their suitability for VPP integration, at this moment, is arguable [48].

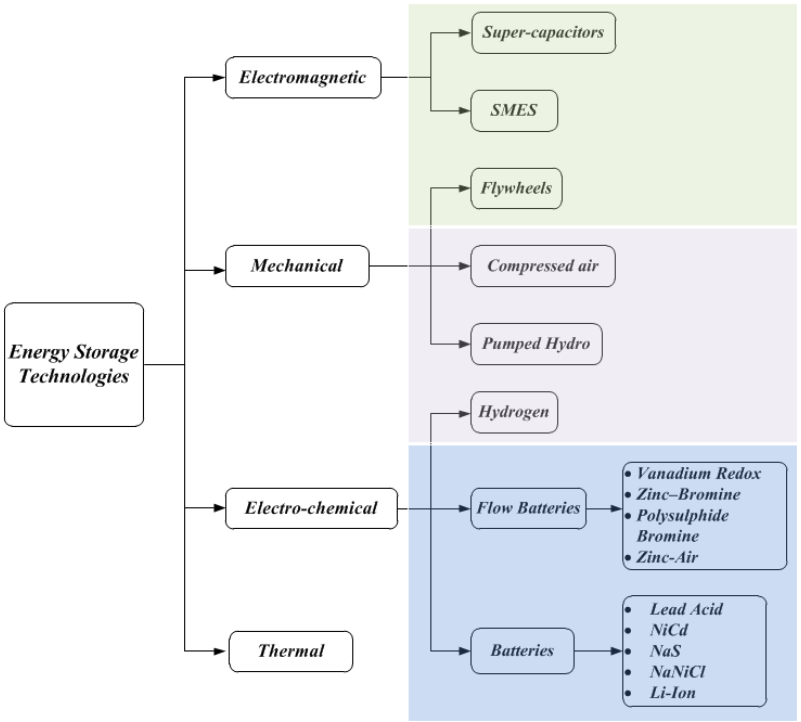

Figure 2.1: *Classification of energy storage technologies; green denotes short-term ES, magenta denotes medium-term ES, and blue denotes long-term ES*

2.2.1 Electromagnetic Energy Storage

Supercapacitors

Supercapacitors, also known as electrochemical double-layer capacitors or ultra-capacitors, use an electrochemical double-layer of charge to store the electrostatic energy in the electric field. To increase their storage capacity, the supercapacitors use large surface-area electrodes made of special materials (e.g. carbon nanotubes) [66].

Supercapacitors are characterized by a fast response time (i.e. 10 - 20 ms) and high-power capability [66], [67], [68]. Moreover, supercapacitors have a long cycle lifetime (around 100 000 cycles) and are highly efficient (90%-98%) ES devices [68], [69]. On the other hand, the main drawbacks of supercapacitors is their high self-discharge rate (i.e. 20-40%/day) and their low energy density, which makes this ES technology very expensive per unit of energy capacity [67], [68]. Other drawbacks of this ES technology are related with the reliability of the pack design and voltage monitoring issues, as presented in [66].

Because of the aforementioned characteristics, ESSs based on supercapacitors are suitable for short-time applications which require charging and discharging at high rates. Thus, if integrated into VPPs, supercapacitors would be able to reduce the wind power fluctuations, at small-time scale (from seconds - up to few minutes) as mentioned in [18] and to provide inertial response to the grid.

At present, there are very few demonstration projects of grid-connected ESSs based on supercapacitors; an example is the 500 kW system located in Hawaii, which was used to damp the wind power fluctuations [18]. A second example is a 28 kW/ 5 minutes system, located in San Diego, US, which is at the moment under construction; the ultracapacitor system should be used in connection with a concentrated photovoltaic system for providing power smoothing [70].

Superconducting Magnets

The superconducting magnetic energy storage (SMES) devices store the electricity into a magnetic field, which is produced by flowing current through a superconducting coil [67]; the energy losses are close to zero because the coil, which is made from a superconducting material, offers almost no resistance to electron flow [67], [69].

SMES devices are characterized by a very high efficiency (i.e. 90-98%), fast reponse times (i.e. < 100 ms), high power capability, and long cycle lifetime (i.e. 100 000 cycles) [66], [67], [68]. Similar to the case of supercapacitors, SMES devices are having low energy densities, which implies a high cost per unit of energy and relative high self-discharge rates (i.e. 10-15%) [67], [68]. Moreover, SMES devices have an increased complexity since they require a refrigeration system, which ensures that the superconducting coil is maintained at very low temperatures (in order to maintain the superconducting state) [66], [69].

Based on the aforementioned characteristics, SMES devices are suitable for very short-term charge/discharge applications (i.e. 1-5 seconds) and micro-SMES are utilized in several industrial applications [63], [67]. However, mainly because of the high complexity of the refrigeration system and the high cost of superconducting materials, large SMES devices are at an early demonstration stage [67]. Consequently, at the present level of development, their integration into VPPs is rather unlikely.

2.2.2 Mechanical Energy Storage

Flywheels

Flywheels are storing the energy as kinetic energy in rotating discs, which are supported by magnetic bearings and are operated in vacuum in order to eliminate the friction losses [69]. One can distinguish between low-speed flywheels (designed for high-power applications) and high-speed flywheels (designed for high-energy applications) [63], [66].

Flywheels are very fast responding ES devices (i.e. 10 - 20 ms) and are able to achieve high efficiencies (i.e. 80 - 95%) for short durations of storage time [66], [67]; the efficiency is fast decreasing with increasing the storage time [65]. Moreover, flywheels are characterized by long cycle lifetime (i.e. 20 000 full cycles) [67], [68]. An important advantage of flywheels over other ES technologies is that their power and energy are decoupled [63]. On the other hand, similar to the aforementioned ES devices, flywheels are characterized by low energy densities (even though high-energy flywheels are on the design stage) and high self-discharge rates (even 100% per day) [66], [67], [68]. Moreover, besides the high initial investment cost, extra expenses are caused by the regular replacement of the bearings [66], [67].

Thus, based on the presented characteristics, flywheels are suitable for integration in VPPs and providing short- and medium-term applications (up to 15 minutes), such as inertia emulation, frequency regulation, and small time-scale wind power fluctuations reduction [9], [18].

There are already existing flywheel-based ESSs connected to the grid, providing various services; an example is the 20 MW/ 5MWh flywheel ESS plant (4 seconds response time and 85% efficiency), located in Stephentown, New York, which provides frequency regulation since 2012 [67]; a second example is the 23 MW flywheel ESS located in Okinawa, Japan, providing frequency regulation since 1996 [71]. Moreover, there are additional demonstration projects under construction worldwide [27].

2.2.3 Electrochemical Energy Storage

This subsection aims to give a brief overview of the most common flow batteries (e.g. Vanadium Redox, Zinc-Bromine, etc.) and secondary batteries (e.g. Lead Acid, Nickel Cadmium, Lithium-ion etc.), which are present on the market and might be suitable for VPP integration.

The main difference between flow batteries and the other secondary batteries, comes from the design point of view. In flow batteries, the electrolytes are stored in two separate electrolyte tanks and circulated, by a complex pump system, through the electrode

compartment, which is a collection of multiple cells (referred as cell stack) [66]. However, this complex system has a big advantage over conventional secondary batteries: the power and energy density are decoupled [66], [67], [69]; the energy density is dependent on the size of the tanks and/or on the amount of electrolyte and its concentration, while the power density is dependent on the rates of the electrode reactions occurring at anode and cathode [69].

The three main flow battery technologies are briefly introduced in the upcoming paragraphs.

Vanadium Redox Flow Batteries

The vanadium redox battery (VRB) is the most mature type of flow batteries [27]. This flow battery concept is unique in the sense that all the chemical reactions are based on the transfer of electrons between different vanadium ions (V^{2+} and V^{3+} at anode and V^{4+} and V^{5+} at cathode) [63].

Besides the advantage of having the power and energy densities decoupled, which allows a system design for many applications, VRB batteries are characterized as well by long calendar and cycle lifetime (i.e. 10 years and > 12 000 cycles, respectively) and fast response time (if the stacks are primed with reactants) [47], [68]. The main drawbacks of this flow battery technology are related to the complexity of the system (e.g. pumps, pipes, valves etc.), which require regular maintenance and to the relatively lower efficiency (65% - 80%) [66], [67].

Because of their long lifetime and power and energy decoupling characteristics, VRB batteries represent suitable candidates for providing most of the VPP applications discussed in Chapter 2.1; the only concern might come from their reduced maturity level in comparison to other technologies (e.g. flywheels and some conventional batteries) [67].

Several VRB systems used in various stationary applications have been deployed worldwide [72]; the most common example is the 4 MW/ 6 MWh unit installed at Tomamae, Japan, which provides wind power smoothing for a 32 MW wind farm [67].

Polysulphide Bromine Flow Battery

The polysulphide bromine (PSB) battery is another type of flow battery, in which the positive electrode uses sodium bromide and the negative electrode uses sodium polysulfide [66]. Similar to the case of VRBs, the power and energy capacity are decoupled, thus allowing the PSB systems to be highly scalable.

PSB batteries are characterized by long calendar lifetime (i.e. 10 - 15 years), and low self-discharge rate [68]. Moreover, PSB batteries are tolerant to over-charging and

over-discharging without a high impact on their lifetime [66]. On the other hand this type of flow batteries have a lower efficiency (i.e. 60% - 75%) and a shorter cycling lifetime (i.e. 2000 cycles) than VRBs [66]. Furthermore, due to the dangerous nature of the electrolytes, environmental concerns arise [66], [63].

Considering the aforementioned characteristics, PSB batteries are suitable for medium- and long-term applications (e.g. black start, load levelling etc.); however, at their present maturity level they are unlikely to be integrated into VPPs.

According to [68], two demonstration projects were supposed to be build by Regenesys Technologies; however, these PSB storage systems have never been completed.

Zinc Bromine Flow Battery

Zinc Bromine batteries have the same structure as VRBs and PSB batteries, however their operating principle is closer to the one of conventional batteries [63]. Similar to the already presented flow battery chemistries, the power and energy capacity of zinc bromine batteries are decoupled [66]. Besides the regular maintenance issues related with flow batteries (e.g. pumps, pipes etc.), zinc bromine batteries have to be totally discharged each 5-10 cycles in order to ensure that the system works with the highest efficiency [63].

The efficiency of zinc bromine is slightly higher (i.e. 65% - 75%) than the one of PSB batteries, but lower than the efficiency of VRBs [63], [68]. These ESSs are able to withstand more than 2000 full cycles and their calendar lifetime varies between five and ten years [66], [68]. Another drawbacks of zinc bromine flow batteries is related with their operation: electrolyte has to be almost continuously circulated in order to avoid zinc dendrites growing [63].

Even though zinc bromine batteries could be used for some VPP applications (e.g. black start), their integration together with WPPs is rather doubtful because of lack of maturity and limited field experience [47].

At present, several zinc bromine flow batteries pilot projects are operational providing various services; however the installed sizes are below 1 MW and none of them are directly related with wind applications [27], [73].

For more details about the operating principles (charging, discharging, materials etc.) of flow batteries, the reader is referred to [63] and [47].

Lead Acid Battery

Lead acid batteries are the most mature electrochemical energy storage technology available on the market. The operating principle of lead acid batteries is based on the redox

reaction in electrochemical cells; the positive electrode is based on lead dioxide, the negative electrode is based on metallic lead, while the electrolyte is a sulphuric acid solution [47]. From the design perspective, there is a large variety of lead-acid batteries [63]; however, this is out of the scope of this overview.

Apart from their commercial maturity, lead acid batteries are characterized by relative high efficiencies (i.e. 70% - 80%), low cost, and relative long calendar lifetime (i.e. 5 - 15 years) for batteries designed for stationary applications [68], [66]. On the other hand, the main drawbacks of this ES technology is its low energy density, poor performance at low temperatures and reduced cycling lifetime, which is very sensitive to the cycle depth [68]. Even though, lead acid batteries contain extremely toxic materials, this issue was mitigated by extensive recycling programs [66].

The traditional stationary applications for lead acid batteries are represented by UPSs [47]. Because of their reduced cycling lifetime and power capability, lead acid batteries are not suitable for many VPP applications (e.g. frequency regulation, power gradient reduction etc.). A possible VPP applications for which lead acid battery could be appealing is the black start, since for this application only a reduced number of cycles are required.

In order to overcome some of their traditional drawbacks, advanced lead acid batteries are under development or under early demonstration stage [27]. This is the case of the advanced lead acid battery developed by Hitachi; a 10.4 MWh ESS based on Hitachi advanced lead acid batteries is used since 2010 to stabilize a 15 MW WPP located in Goshogawara, Japan [74]. Another example is the advanced lead acid battery developed by Xtreme Power [75]; a 1.5 MW/ 375 kWh ESS based on Xtreme Power lead acid batteries is operating since 2009 to provide wind power smoothing and power gradient reduction ($\pm 1 MW/min$) for a 30 MW WPP in Maui, Hawaii [76].

Nickel Cadmium Battery

Nickel Cadmium (NiCd) batteries are the second most mature battery technology after lead acid batteries. They operate based on the redox reaction in electrochemical cells; the positive electrode is based on nickel hydroxide, the negative electrode is based on cadmium hydroxide, while the electrolyte potasium hydroxide [63].

In comparison to the lead acid batteries, NiCd batteries have a higher energy density and are more tolerable to extreme operating conditions (e.g. deep discharges, low temperatures etc.) [66], [68]. Moreover, NiCd batteries are characterized by long calendar lifetime (i.e. 10 - 20 years) and a cycle lifetime of 2500 - 3500 cycles at 80% cycle depth [66], [68]. The drawbacks of NiCd batteries are related with their relative low efficiencies (i.e. 60% - 70%), the memory effect, increased cost [63], [66]. Furthermore,

concerns about using this battery technology arise due to the use of cadmium, which is an environmental unfriendly material [68].

Based on their features, NiCd batteries might be suitable for integration in VPP and provide certain services; in [63], NiCd batteries were suggested as possible candidates for providing frequency regulation and power oscillation damping in the grid. However, the environmental issues might be a barrier for the widespread use of this battery technology at a large scale.

Since NiCd batteries reached maturity, they are used in several projects; the most known is the NiCd-based ESS located in Fairbanks, Alaska rated at 27 MW/ 6.75 MWh and used since 2003 for providing standby power during power shortfalls [63], [77]. Another operational NiCd-based ESS (3 MW/ 0.25MWh) is located in the Netherlands Antilles and is used as well for providing standby power [78].

Sodium Sulphur Battery

Sodium Sulphur (NaS) batteries are operating, similar as lead acid battery, based on a redox reaction; however, what makes them different from conventional batteries is their electrodes which are molten (molten sodium for the negative and molten sulphur for the positive electrode) and the operating temperature which is in the range of 300 - 350^{o}C [47].

The main advantages of NaS batteries is their long calendar and cycling lifetime (i.e. 15 years and 2500 - 4500 cycles, respectively), high efficiency (i.e. 75% - 90%), and their high specific energy [67], [47]. Moreover, NaS batteries are able to provide short bursts of power, six times their continuos power rating [68].

The major drawback of NaS batteries is their need to be maintained at elevated temperature, fact which implies a decrease of batteries' performance (increased self-discharged) [68].

Because of their characteristics, which are superior to most of the available ES technologies, NaS batteries are suitable for providing most of the VPP applications mentioned in Chapter 2.1.

Even though NaS batteries did not reach the maturity levels of lead acid and NiCd batteries, this ES technology is already commercial and many systems are under operation world-wide. The biggest NaS-based ESS (34 MW/ 238 MWh) is operating since 2008 in Japan, in conjuction with a 51 MW WPP; the ESS system is mainly used for power gradient reduction [21], [67]. Another system (1 MW/ 7.2 MWh) is located in Lucerne, U.S., and is providing, since 2008, energy production time shifting and wind power smoothing [79].

Sodium Nickel Chloride Battery

Sodium Nickel Chloride batteries are high temperature batteries, operating at 270^{o}C - 350^{o}C, very similar to the NaS systems [47]; the negative electrode is based on liquid sodium amd the positive electrode is based on solid nickel chloride, while the electrolyte is solid beta alumina [66]. In comparison to the more established NaS batteries, this technology is less tolerant to deep discharges and overcharges, but more safe [68].

Sodium Nickel Chloride batteries are characterized by relative long calendar and cycling lifetime (i.e. 10 years and 2500 cycles, respectively) and high efficiencies (i.e. 85%). On the other hand, this ES technology has a high self-discharged rate (i.e. 10% per day) if the system is not cycling [66].

Due to their present characteristics and limited field demonstration projects, it is rather unlikely that ESS based on this technology will be integrated into VPPs. Moreover, at present, there are no operational sodium nickel chloride-based ESS in the MW range.

Zinc-Air Battery

Zinc-air batteries, a newer ES technology, are metal air batteries using zinc in electrochemical couple with oxygen from the air to generate electricity [47].

Zinc-air batteries lack maturity and the field experience operating ESS based on this technology is minimal. However, because of their attractive characteristics this energy storage technology has been considered in the present overview.

The main advantages of the zinc-air batteries in comparison to the conventional batteries available on the market are their potential high energy densities and their reduced cost (zinc is an abundant and cheap metal) [47]. At present, zinc-air batteries have low efficiencies (i.e. 50%) and are very sensitive to changes in the ambient air conditions [47].

Currently, only one manufacturer exists on the market, whose product is targeting a calendar lifetime of 30 years and a cycling lifetime of 10 000 cycles [80]. The first pilot project based on zinc-air batteries (1 MW/ 6 MWh) is expected to begin in 2014.

Lithium-ion Battery

Lithium-ion batteries have become in the last years one of the most popular energy storage technology for stationary applications. Their operating principle is based on the redox reactions in electrochemical cells; in most of the cases, the negative electrode is based on graphite carbon, while the positive electrode is based on litiathed metal oxide [68].

Li-ion batteries are characterized by the highest efficiencies (i.e. up to 98%) among the electrochemical energy storage technologies. Moreover, certain Li-ion battery

chemistries have a long calendar (i.e. 5-20 years, depending on chemistry) and cycling (i.e. > 5 000 full cycles) lifetime and a low self-discharge rate (i.e. 0.1-0.3% per day) [68], [81]. The main drawbacks of Li-ion batteries is their high cost and safety (but only of some chemistries) [66], [82]; moreover, Li-ion battery packs and modules need special circuits for balancing the individual cells' voltage.

Due to their aforementioned characteristics, Li-ion batteries are suitable candidates for most of the VPP applications (especially for the short- and medium-term ones).

Because of their fast development, which led to manufacturing Li-ion batteries with superior characteristics, many MW-scale demonstration project based on Li-ion battery ESSs are running worldwide [20], [47], [81].

More details about different Li-ion battery chemistries, their advantages and drawbacks and ongoing demonstration projects are presented in Chapter 2.4.

2.3 Selection of Energy Storage Technology

2.3.1 Requirements imposed by VPP applications

The services, which have to be provided by the ESS in order to bring the characteristics of the VPP close to the ones of present CGUs and to allow even higher wind power penetration levels were presented in Chapter 2.1. Each of this services has its own requirements seen from the ESS perspective (e.g. some of them require very long cycle lifetime time, while for others this parameter is not so important). Therefore, it is rather difficult to find an ES technology which is able to fulfil the requirements imposed by all VPP applications and to be economical viable in the same time; the selection of the ESS has to be done in close relation with the main service, which needs to be delivered [28].

The purpose of this section is to define the requirements that the ESS has to fulfil in order to successfully deliver the five applications described in Chapter 2.1. The most important requirements imposed by each application, were mentioned while the applications were described and are summarized in Table 2.1.

Based on Table 2.1, and not considering the size requirement (because it varies in a wide range, depending on the application), the following requirements have been defined:

- *Response time* : the ESS should have a fast response time, in terms of milliseconds, in order to be able to provide inertial response and primary frequency regulation and to remove fast wind power fluctuations;

Table 2.1: *Main requirements imposed by the considered VPP applications*

ESS Requirement	Inertia Emulation	Primary Frequency Regulation	Forecast Accuracy Improv.	Power Gradient Reduction	Black Start
Size	5% from VPP size	1 - 100 MW	20 - 25% from VPP size	1 - 15 MW	5 - 50 MW
Discharge time	5 - 10 seconds	15 minutes	minutes - hours	15 minutes - 1 hour	15 minutes - 1 hour
Cycle lifetime	250 - 10 000 cycles	250 - 10 000 cycles	-	> 100 000 cycles	10 - 20 cycles

- *Discharge time* : based on the requirements summarized in Table 2.1, the ESS should be able to deliver the requested power for up to one hour;
- *Cycling lifetime* : for the considered applications (except black start), the ESSs are usually subjected to very demanding cycling conditions (both in terms of cycle numbers and cycle depths). Thus, the ESS should have a very long cycling lifetime, in order to withstand a high number of cycles, including deep cycles;
- *Calendar lifetime* : the ESS has to be characterized by a very long calendar lifetime (e.g. up to 20 years, which represents the projected lifetime of most WPPs);
- *Self-discahrge* : the ESS should have a low self-discharge rate because there can be frequent periods when the storage system will be in idling mode, as is the case of the black start application;
- *Efficiency* : the efficiency of the ESS should be very high, in order to limit the losses;
- *Envrionment* : if possible, the ESS should be environmentally benign, in order to maximize the environmental friendliness characteristic of the wind power;
- *Maturity* : the ES technology should be relatively mature;
- *Demonstartion* : already existing demonstration projects in MW-range represents an advantage for the ESS since field experience was already gained. Thus, the ESS could be better designed based on available information from other ongoing projects;
- *Cost/cycle* : since for the considered applications, the ESS is subjected to demanding cycling conditions, a reduced cost/cycle is demanded;

While the first three requirements from the presented list are more related to the considered VPP applications, the other requirements could be interpreted as general requirements for stationary ESSs.

2.3.2 ES technology scorecard

.

Based on the ES overview presented in Chapter 2.2 and considering the aforementioned requirements, the suitability for VPP integration of each ES technology was analysed. The results are presented in the scorecard given in Table 2.2.

Table 2.2: *Evaluation of the ES technologies based on VPP requirements; "++" denotes good characteristics, "+" denotes acceptable characteristics, and "-" denotes poor characteristics.*

Requirements	Energy storage technologies											
	VRB	PSB	ZnBr	ZnAir	Supercap	SMES	Flywheel	Lead	NiCd	NaS	NaNiCl	Li-ion
Response time	+	+	+		++	++	++	++	++	++	+	++
Discharge time	++	++	++	++	-	-	+	++	++	++	++	++
Cycle lifetime	++	-	+	++	++	++	++	-	+	+	+	++
Calendar	+	+	-	+	++	++	++	+	++	++	+	++
Self discharge	++	++	++	++	-	-	-	++	++	+	+	++
Efficiency	+	-	+	-	++	++	++	+	-	++	+	++
Environment	++	-	+	+	++	+	++	+	-	++	++	++
Maturity	+	-	+	-	+	-	+	++	++	+	+	+
Demonstration in MW	+	-	+	-	-	+	+	+	-	++	-	++
Cost/cycle	+				-		+	-	-	+		+

No consistent information about the cost per cycle of different ES technology were available in the literature. Thus, the cost per cycle evaluation presented in the Table

2.2 is based on the results for the primary frequency regulation service (one of the five considered VPP applications), obtained in [28] by Swierczynski et al.

2.3.3 Discussions

According to the results obtained from the scorecard, the most suitable ES technologies for VPP integration are the Li-ion, NaS and VRB batteries. Even though none of this technologies is as mature as the lead-acid batteries, their characteristics makes them very suitable for stationary applications. Moreover, mainly for the Li-ion battery chemistry there exist a relative high number of ongoing demonstration projects worldwide. Consequently, based on these results, the Li-ion battery chemistry was considered the most suitable ES technology for integration into VPP. In the next section, the Li-ion battery family will be presented in more detail.

2.4 Lithium-Ion Battery Family Overview

2.4.1 Rechargeable Lithium-based batteries

The rechargeable Lithium batteries represent a broad family of energy storage devices. According to the structure of their negative electrode, Lithium batteries can be classified into two main categories: lithium metal batteries (based on metallic lithium) and lithium-ion batteries (based on intercalation compounds) as illustrated in Fig. 2.2 [83].

Lithium-metal batteries, with either liquid or polymer electrolyte, are having a high energy density and specific energy and a low self-discharge rate; on the other hand most of lithium-metal batteries have a low cycle life, poor high-rate performance, and they present safety issues [83]. Their commercialization has been limited during the 1980s to few applications like low-power portable applications and consumer electronics [83]. Thus, lithium-metal batteries are out of the scope of this investigation.

Lithium-ion batteries, utilize lithiated carbon or different other intercalation materials for the negative electrode instead of metallic lithium. Thus, the safety issues are mitigated. Li-ion batteries have been firstly commercialized by Sony in 1990s and because of their high specific energy and energy density they have rapidly become the standard power source for consumer electronics applications. Because their performances have continuously improved (driven especially by the portable electronics and automotive industry), Li-ion batteries have recently entered the market for short- and medium-term stationary energy storage applications.

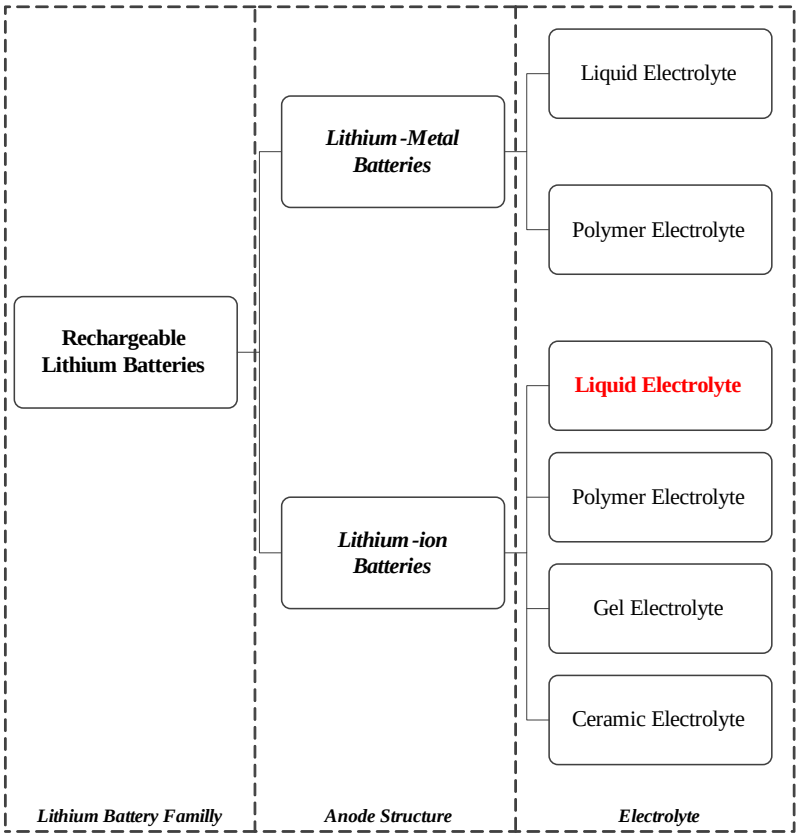

Figure 2.2: *Classification of the rechargeable lithium battery family based on anode structure and electrolyte type*

As it is shwon in Fig. 2.2 different electrolytes could be used for developing Lithium-ion battery systems. However, liquid electrolyte-based Li-ion batteries are considered in this thesis since Li-ion batteries based on gel and ceramic electrolytes are not so mature and Li-ion batteries based on polymer electrolytes have a reduced power capability (even though their safety is improved) [83].

In their most conventional structure, Li-ion batteries are composed of an anode, based on graphite carbon (with layered structure), a cathode, based on lithium metal oxide (with a layered structure too), and an electrolyte based on lithium salts (e.g. lithium hexafluorophosphate) disolved in a mixed organic solvent embedded in a separator foil [82], [83]. The current collectors are made of aluminium foil and copper for the cathode and anode, respectively [83].

Figure 2.3 shows the typical configuration of a Li-ion battery. During the battery charging, lithium atoms are de-intercalated from the layered cathode, become ions and

migrate through the electrolyte to the carbon anode; at the anode, they combine with external electrons and are intercalated as lithium atoms in-between the carbon layers [68]. During the battery discharging, this process is reversed.

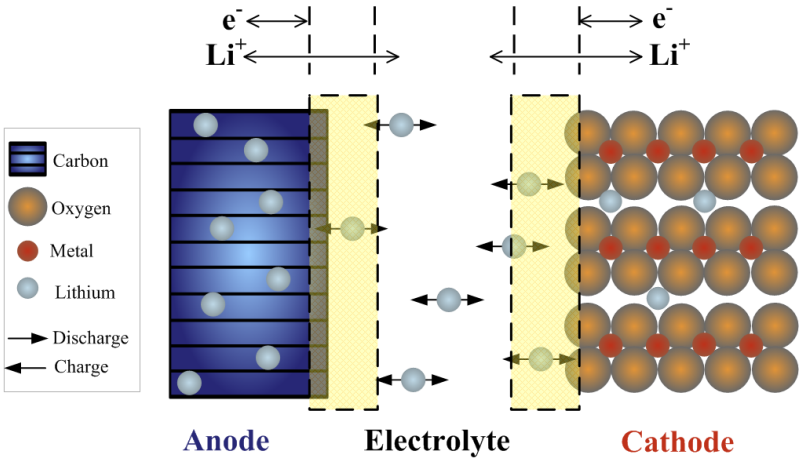

Figure 2.3: *Schematic representation of a common Li-ion battery cell.*

Because of continuous development, which were targeting both the cathode and anode (e.g. new raw materials, moving from bulk materials to nanosize particles etc.), as well as the electrolyte, the present Li-ion batteries are characterized by unique features: high specific energy and energy density, long cycle and calendar lifetime, low self-discharge rate, high power capability (during both charging and discharging), high coulombic and energy efficiency; on the other hand their drawback are related with relative high cost and extra circuitry for cell balancing [82], [83], [84].

2.4.2 Lithium-ion battery chemistries

The aforementioned advances have lead to the gradual replacement of initial Li-ion batteries based on graphite and lithium cobalt oxide with Li-ion batteries based on new cathode (e.g. lithium iron phosphate) and anode (e.g. lithium titanate oxide) materials [84]. Thus, many Li-ion battery chemistries are available at present on the market, each of them with its unique particularities [33]. In the followings the advantages and disadvantages of the most common Li-ion batteries are presented. Moreover, examples of existing demonstration projects for ESS-based on different chemistries are summarized.

Lithium Cobalt Oxide Batteries

Lithium cobalt oxide ($LiCoO_2$)-based batteries are the most mature Li-ion battery chemistry; their anode is based on graphite, while the cathode is based on lithium cobalt oxide. Lithium cobalt oxide is easy to be prepared and batteries based on this cathode material are used mainly for consumers electronics because of their good electrical performance and high energy density [83], [85]. The drawbacks of this chemistry are related to safety issues, since the cathode material is highly reactive and has poorer thermal stability than other cathode materials [85].

Lithium Manganese Spinel Batteries

Lithium manganese spinel ($LiMn_2O_4$)-based batteries have a lower cost and higher performance in comparison to the lithium cobalt oxide-based batteries. On the other hand they have a lower specific capacity than the lithium cobalt oxide batteries (20% - 30% lower) [83], [33]. Furthermore, they have an increased safety than previous developed Li-ion batteries (based on Cobalt and Nickel) and a cycle lifetime of 1000 cycles [83], [86]. Even though they have an increased safety, lithium manganese spinel batteries are susceptible to thermal runaway if overcharged or discharged with too high current rates [87].

Lithium Nickel Cobalt Aluminium Oxide Batteries

Lithium nickel cobalt aluminium oxide ($LiNiCoAlO_2$) -based batteries, also referred as NCA batteries, are characterized by relative high specific power and energy densities and reasonable long cycle lifetime (e.g. 2000 - 3000 cycles) [86], [87]. The main disadvantages of this chemistry are related with their high cost and reduced safety [33].

Lithium Nickel Manganese Cobalt Oxide Batteries

Lithium nickel manganese cobalt oxide ($LiNi_xMn_xCo_xO_2$)-based batteries, also referred as NMC batteries, provide a compromise between the high capacity and high current [88]. Furthermore, Li-ion batteries based on NMC cathode are having similar lifetime characteristics as NCA-based batteries; however, they are showing better safety than all the aforementioned battery chemistries [86].

Lithium Iron Phosphate Batteries

Lithium iron phosphate ($LiFePO_4$) -based batteries (with anode based on graphite carbon and cathode based on lithium iron phosphate) have become extremely attractive for various applications because of their inherent safety and relatively low cost [84].

Moreover, lithium iron phosphate-based batteries can have long cycling lifetime (e.g. more than 7000 full cycles) and high charge and discharge current rates (e.g. up to 35C) [81], [88]. The main disadvantage of lithium iron phosphate is their reduced energy density in comparison to other Li-ion chemistries such as NMC and NCA [82].

More details about the lithium iron phosphate chemistry are presented in Chapter 2.4.3.

Lithium Titanate Oxide Batteries

The lithium titanate oxide ($Li_4Ti_5O_{12}$) material represent an appealing and competitive candidate for new types of anodes in Li-ion battery [89]. Thus, Li-ion batteries based on this anode material have emerged into the market. Batteries based on lithium titanate oxide anodes and lithium manganese spinel cathodes are characterized by very long calendar and cycle lifetime (e.g. more than 15 years and 10 000 cycles, respectively) and are considered the most safe Li-ion batteries that are currently on the market [82], [86], [90]. The main disadvantages of lithium titanate oxide-based batteries are their high cost and reduced energy density [82], [87].

Li-ion-based ESSs demonstration projects

Table 2.3 summarizes various demonstration projects where Li-ion battery based ESSs are used in different applications (both for wind power grid integration and for grid support).

Selection of Li-ion battery Chemistry

Throughout Chapter 2.4, the most mature Li-ion battery chemistries that are currently present on the market where briefly introduced. As it was shown, each chemistry has its own advantages and disadvantages in terms of energy density, safety, lifetime etc., which makes them suitable for different applications.

Table 2.4 presents a comparison along six dimensions of the discussed Li-ion battery chemistries. The evaluation does not consider the characteristics of the discussed Li-ion battery chemistries in respect to other energy storage technologies(e.g. lead acid batteries, NaS batteries etc.)

Table 2.3: *ESSs based on Li-ion batteries in operational demonstration projects for wind integration and grid support*

Project Name	Commission. Year	Li-ion chemistry	Size	Application	Ref.
Mount Laurel, US	2011	LFP	32 MW/ 8 MWh	frequency regulation, ramping	[91]
Los Andes, Chile	2009	LFP	12 MW/ 4 MWh	frequency regulation	[81]
Lemkaer, Denmark	2013	LFP and LTO	1.6 MW/ 0.4 MWh	frequency regulation	[42]
Kensas City Power, US	2012	$LiMn_2O_4$	1 MW/ 1 MWh	-	[27]
Zhangbei Storage Demo, China	2011	LFP	6 MW/ 6 MWh	time shift, power gradient reduction	[92]
Tehachapi Wind Energy Storage	2012	LFP	8 MW/ 32 MWh	13 applications	[93]
CFN Saskatchewan, Canada	2013	NMC or NCA	0.4 MW/ 1 MWh	wind integration	[94]

Table 2.4: *Comparison of Li-ion battery chemistries from various perspectives (legend: "++" denotes very good performance, "+" denotes good performance, "-" denotes acceptable performance, "--" denotes low performance) [33], [87].*

Chemistry	Specific Energy	Specific Power	Safety	Performance	Lifetime	Cost
$LiCoO_2$	++	-	-	-	--	+
$LiMn_2O_4$	+	+	+	-	-	+
NCA	++	++	-	+	+	-
NMC	++	+	+	+	+	+
$LiFePO_4$	-	+	++	+	++	+
$Li_4Ti_5O_{12}$	-	+	++	++	++	--

As Table 2.4 shows, none of the Li-ion battery chemistries is superior to the other chemistries on all the six considered dimensions. In most of the cases, optimizing a Li-ion battery chemistry for one dimensions means compromising other dimension (or dimensions); for example Li-ion batteries based on NCA chemistry have very good specific energy and specific power characteristics but present safety issues, while on contrary Li-ion batteries based on $Li_4Ti_5O_{12}$ are having lower specific energy and power characteristics but they are very safe and characterized by long lifetime. Thus, the selection of

the most suitable Li-ion battery chemistry for integration in VPP has to be performed considering the requirements of the applications.

Based on the characteristics summarized in Table 2.4 and considering that VPP applications are less demanding in terms of weight and volume (i.e. specific energy and energy density), but more demanding on terms of lifetime (long cycle and calendar lifetime), Li-ion batteries based on $LiFePO_4$ chemistry and Li-ion batteries based on $Li_4Ti_5O_{12}$ represent suitable candidates for providing the VPP applications discussed in Chapter 2.1 [48].

$LiFePO_4$-based battery cells have two main advantages over the Li-ion batteries based on $Li_4Ti_5O_{12}$. Firstly, their capital cost is lower and thus the initial investment cost on the ESS will be lower if $LiFePO_4$-based batteries are used. Secondly, at present, ESS based on $LiFePO_4$ are evaluated in several MW-scale stationary energy storage demonstration projects [84], some of them being summarized in Table 2.3. Thus, Lithium ion batteries based on $LiFePO_4$ cathodes and graphite anodes, further referred as LFP/C, are the subject of this thesis for lifetime modelling.

2.4.3 Lithium Iron Phosphate/Carbon Batteries

Lithium iron phosphate was firstly proposed as a cathode material for rechargeable batteries by Padhi *et al.* in 1997 [95]. This material is extremely attractive because of several characteristics which include: reasonable high capacity (170 mAh g^{-1}), high intrinsic safety (the operating voltage of the cathode material is compatible with the thermodynamic stability of the electrolyte), low cost (use of abundant and low cost constituents), environmental friendliness (use of benign elements), and flat voltage profile [82], [84], [95].

The major drawback of the lithium iron phosphate cathode material is represented by their poor electronic conductivity (high intrinsic resistance) [82], [96]. Thus, special electrode preparations is necessary in order to have access to its full capacity; different methods for improvement of the electronic conductivity of the lithium iron phosphate, such as carbon coating or reducing the active material particle size (in the scale of nanometers) are summarized in [97].

By preparing the lithium iron phosphate material in the form of carbon-coated nanoparticles by various chemical and physical process, their electronic conductivity is increased and the their full capacity is accessible even after prolonged cycling [82], [96].

Thus, present nanoparticle-based LFP/C battery cells are characterized by long cycling and calendar lifetime, low self-discharge rate, high charge and discharge power capability, flat discharge voltage curve and intrinsic safety [39], [81]. On the other hand,

because of low operational voltage (i.e. 3.3V) and low tap density, LFP/C battery cells suffer from low volumetric energy density [33], [82]; however, as already mentioned, low volumetric density does not represent an issue for the use of this battery chemistry in stationary ES applications.

The main characteristics of the LFP/C-based battery cell used in this thesis are summarized in Appendix A.

Chapter 3

Performance Modelling of Li-ion Battery Cells

This chapter is entirely dedicated to the performance modelling of Li-ion batteries. The first section is dedicated to a brief overview of performance modelling approaches for Li-ion batteries; a special emphasis is put on the electrical modelling approach based on the electrochemical impedance spectroscopy technique, which will be used in this thesis. The second section deals with the performance modelling of the LFP/C-based battery cells. In order to develop the desired model, extensive characterization tests of a LFP/C-based battery cell were performed in laboratory at various operating conditions (e.g. temperatures, currents etc.) and the results are introduced in this section. Than, the proposed structure of the performance model is presented and the model is parametrized based on the results obtained from the characterization tests. The developed model is verified, in the last section of this chapter, using different load profiles including a real mission profile, which was measured on the field.

3.1 Overview of Li-ion Battery Performance Modelling

Li-ion batteries are increasingly considered in different stationary applications (both in connection with WPPs or as stand-alone systems) as it was presented in Table 2.3. In order to assess their technical and economical feasibility for various applications, precise knowledge about their performance and ageing behaviour becomes mandatory.

This chapter focuses mainly on the performance modelling of the selected LFP/C-based battery cell, while the ageing behaviour of the same battery cells is presented and discussed in Chapter 6 (calendar ageing) and Chapter 7 (cycling ageing).

Li-ion battery performance models should be able to predict with high accuracy the

electrical performance (mainly the voltage) of the battery cell at different operating conditions; by operating conditions it is meant the sum of the conditions given by the load current, temperature, and SOC. A precise Li-ion battery cell performance model allows to run simulations in order to: improve the battery cell design, verify different operational strategies for the Li-ion ESS, optimize the size of the Li-ion ESS [98], [99]. Thus, by relying on models, which are able to estimate accurately the behaviour of the Li-ion battery cells, time and cost demanding laboratory experimental tests are minimized or even avoided.

Performance modelling of Li-ion batteries could by realized by following different approaches, depending on the final purpose of the model. These approaches, characterized by different degrees of complexity, can be devided in three main categories as proposed in [98]. Each of this modelling approaches is briefly discussed in the upcoming sections.

3.1.1 Electrochemical Performance Models

Electrochemical models are generally used to optimize the design of the Li-ion battery cells and to determine which are the processes that are limiting the performance of the Li-ion battery cells [100]; for example, Randall *et al.* in [101], have built a model that is able to estimate the growth of solid electrolyte interface in Li-ion batteries while Newman *et al.* in [102] have modelled, considering various aspects, the mass transport in the electrolyte, which has a significant effect on the battery performance. Most of the developed electrochemical models for Li-ion batteries are based on the model proposed in [103].

A main advantage of the electrochemical models over the other models is their ability to predict both macroscopic battery quantities (e.g. voltage, current etc.) and microscopic battery quantities (e.g. concentration gradients, battery potentials, temperature inside the battery etc.) [100], [104]; moreover correlations between the microscopic and macroscopic parameters can be found [98]. On the other hand, electrochemical models for complete battery cells are described by a system of coupled time-variant partial different equations, which are difficult to parametrize without expensive and specialized equipment and require huge computational efforts for being solved [98], [100]. Nevertheless, Li-ion battery performance models developed by following the electrochemical modelling approach are able to estimate with very high accuracy the behaviour of the modelled battery cell. Moreover, small changes in the battery cell structure and/or materials does not require additional laboratory tests.

3.1.2 Mathematical Performance Models

Mathematical models are in most of the cases developed based on empirical equations and are able to predict only macroscopic quantities such as voltage, efficiency, and SOC [98], [105]. The majority of the developed mathematical models are based on the Shepherd relation [106]:

$$V_{bat} = E_0 - K(\frac{Q}{Q - it})i - R_i \tag{3.1}$$

where, V_{bat} represents the voltage of the battery cell, E_0 represents the open-circuit voltage of the battery cell when it is fully charged, K represents the polarization resistance, Q represents the instantaneous current and, R represents the internal resistance, and $it = \int i \cdot dt$.

The regular mathematical battery models, which are based on Shepherd's relation, could be improved by adding or modifying various terms of the battery model, in order to overcome the assumptions considered in (3.2); for example, consider the influence of temperature, or consider different capacity values during charging and discharging etc. [105], [107].

However, even if improvements to the Shepherd's relation are considered, the Li-ion battery mathematical models are limited in accuracy (i.e. 5-20%) [98].

3.1.3 Electrical Performance Models

Electrical models are using an equivalent electrical circuit (ECC) to describe the performance behaviour of Li-ion batteries. The EECs are composed of combinations of voltage sources, capacitors, resistances and inductances, which are describing with relatively high accuracy (1 - 5%) the electrical performances (e.g. voltage, current etc.) of the battery cells [98]. However, in comparison with the electrochemical models, the Li-ion battery cell electrical models cannot be extrapolated to other Li-ion battery designs or chemistries [48], [108].

Two methods are used to parametrize the EEC of a Li-ion battery model. The first method relays on applying a DC pulse to the Li-ion battery and measuring the voltage response of the cell, while the second method involves performing electrochemical impedance spectroscopy (EIS) measurements.

The DC pulse-based electrical models are using a series resistance and a RC parallel network to predict the Li-ion battery cell response to transient load events [98]. The accuracy of these models depends on the number of RC networks used to estimate the battery cell voltage, as shown in [109], [110]; a higher number of RC networks will

increase the accuracy of the performance model but in the same time will increase the computation time.

Since this modelling approach is not used in the thesis, for more details the reader is referred to [98], [109], [110].

The second electrical approach, which can be used, to model the performance behaviour of Li-ion battery cells is based on the EIS technique.

EIS technique represents a non-destructive and reliable method in material research, which can be applied as well for characterizing and modelling the dynamic behaviour of Li-ion batteries [111], [112]. This measurement technique allows developing dynamic battery cell models whose elements can be often correlated to the physic-chemical processes that occur inside the battery cell (e.g. charge transfer, diffusion etc.) [112], [113], [114].

The measurement approach consists in applying to the battery a sinusoidal current or voltage of a certain amplitude and frequency and measuring the phase shift and amplitude of the output voltage (galvanostaic mode) or current (potentiostatic mode), respectively [111]. This procedure is usually repeated for a number of frequencies and thus the impedance spectrum of the investigated battery is derived:

$$Z_{cell} = \frac{U\sin(\omega t)}{I\sin(\omega t - \varphi)} \tag{3.2}$$

where Z_{cell} represents the impedance of the Li-ion battery cell, U represents the amplitude of the measured voltage, I represents the amplitude of the excitation current, ω represents the angular frequency, and φ represents the phase shift.

Most frequently, the results of the EIS measurement are presented in the Nyquist plane, where the inverse of the imaginary part of the impedance is plotted against its real part. The typical shape of Li-ion batteries' Nyquist diagram (also referred in literature as impedance characteristic or impedance spectrum) is presented in Fig. 3.1.

The impedance spectrum presented in Fig. 3.1 is composed of five distinct sections, which in literature are related to different processes [114]:

- *Section 1* - at very high frequencies, the impedance spectrum shows an inductive behaviour;
- *Section 2* - the value of the ohmic resistance R_s of the battery is found at the intersection of the impedance spectra with the real axis ($Im(Z) = 0$);
- *Section 3* - is represented by a small semi-circle, which is related with the presence of the solid electrolyte interface (SEI) layer;

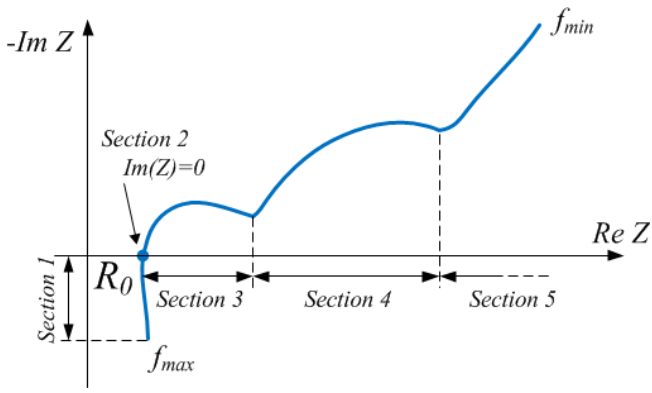

Figure 3.1: *Typical Nyquist curve of a Li-ion battery cell*

- *Section 4* - is represented by a larger semi-circle, which is associated with the charge transfer process and the double layer capacitance;
- *Section 5* - located at small frequencies, corresponds to the diffusion process.

However, measured impedance spectra can show variations from the theoretical curve, illustrated in Fig. 3.1; the number of semi-circles is just one or the inductive behavior of the impedance spectrum is a loop instead of a line due to the skin effect of the material [114], [115].

In order to parametrize the performance model of the Li-ion battery, the measured impedance spectra are fitted using a complex non-linear least square (CNLS) algorithm and considering an EEC. A typical EEC used for curve fitting the typical impedance spectrum of Li-ion battery cells (see Fig. 3.1) is illustrated in Fig. 3.2.

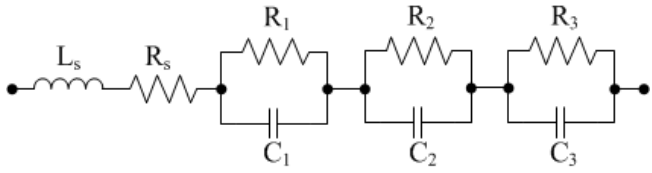

Figure 3.2: *Typical EEC used for curve fitting the impedance spectrum of Li-ion battery cells*

Li-ion batteries cells are highly non-linear systems and their performance behaviour depends on many parameters such as SOC, temperature, current, and age. Therefore, in order to develop an accurate performance model, multiple EIS measurements, carried out at various conditions, have to be considered.

3.1.4 Comparison

Table 3.1 summarizes the features of the three presented approaches, which are traditionally used for performance modelling of Li-ion battery cells.

Table 3.1: *Comparison of the characteristics of different approaches used to model the performance behaviour of Li-ion batteries.*

Modelling Approach / Criteria	**Electrochemical**	**Mathematical**	**Electric**
Accuracy	High	Reduced	Relatively High
Computation complexity	Very High	Reduced	Medium
Parametrization	Based on extensive laboratory measurements. *a priori* knowledge is required	Based on battery data-sheet	Based on laboratory measurements
Physic-chemical meaning	Very good	Poor	Relatively good

Even though electrochemical models are having a very high accuracy, they are difficult to parametrize because the needed parameters are not provided by the manufacturers in data-sheets and are difficult to determine in the laboratory without specialized equipment. In the same time, mathematical models are characterized by reduced accuracy and lack of physic-chemical meaning.

Generally, the electrical models are regarded as a trade-off solutions between the electrochemical and mathematical models since they offer a relatively high accuracy and moderate modelling and parametrization complexity [48]. Therefore, an electrical modelling approach based on the EIS technique is followed in this work, in order to develop the performance model for the studied LFP/C battery cell.

3.2 Performance Modelling of LiFePO$_4$/C Battery Cells

In order to build an accurate performance model for Li-ion batteries, extensive laboratory tests are mandatory. This is because most of the performance parameters (e.g. capacity, open-circuit voltage etc.) of the Li-ion battery cells are changing with the operating conditions (e.g. temperature, load current etc.). As it will be shown throughout this chapter this is also the case of the tested LFP/C-based battery cell.

In the first part of this chapter the results obtained from the characterization tests will be introduced and discussed, while in the second part of this chapter the performance model developed for the LFP/C battery cell will be presented.

3.2.1 Characterization of $LiFePO_4$/C battery cell

The main purpose of the characterization tests was to determine the characteristics of the LFP/C battery cell at the beginning-of-life (BOL). Based on the results obtained from the characterization tests, the performance model of the LFP/C battery cell was parametrized.

The characterization procedure was composed of several tests, which were performed following the sequence illustrated in Fig. 3.3.

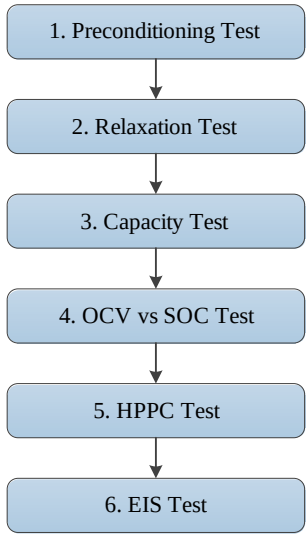

Figure 3.3: *Test sequence for characterization of the LFP/C battery cells at BOL.*

The procedures followed for all the tests mentioned in Fig. 3.3 as well as the obtained results are presented in the following paragraphs.

Preconditioning Test

The purpose of the preconditioning test was to remove any possible passivation to which the tested LFP/C battery cell might have been subjected in the interval between cell manufacturing and the first test. Moreover, this test was used to verify that the LFP/C battery cell is showing stable capacity [116].

The preconditioning test was performed at 25 ^{o}C and was composed of five successive full charge-discharge cycles according to the procedure presented in Table C.1 (see Appendix C.1).

The results of the preconditioning test are presented in Fig. 3.4 and Fig. 3.5, respectively. The measured discharging capacity of the LFP/C battery cell is stable with a tendency of slight increase. The change in capacity, illustrated in 3.5, is related to the discharging capacity measured during the first cycle.

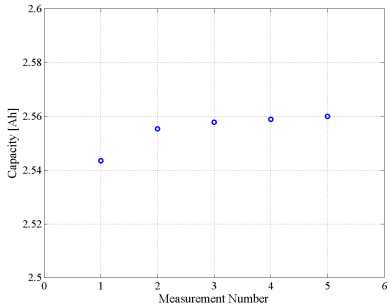

Figure 3.4: *Capacity of the LFP/C battery cell measured during the preconditioning test*

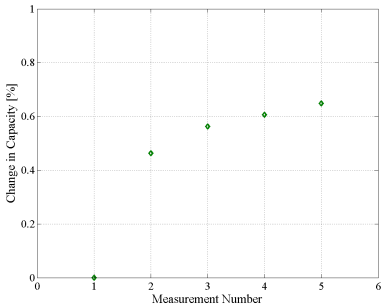

Figure 3.5: *Change in the LFP/C battery cell capacity, during five consecutive charge/discharge cycles*

The LFP/C battery cell was considered preconditioned since the discharged capacity during two consecutive discharges did not change with a value greater than 3% of the initial measured capacity [116].

The charging and discharging capacity values measured during the five preconditioning cycles are summarized in Appendix C.1 together with the measured voltage profiles.

Moreover, it has to be stressed that the preconditioning test was applied to all the LFP/C battery cells, which were subjected to accelerated ageing tests and verification tests. However, except for the LFP/C battery cell, which was subjected to the full characterization procedure, the results for the other cells were not included in the thesis.

Relaxation Test

In order to accurately measure the parameters (e.g. capacity, open-circuit voltage etc.) of the battery cell, it has to be ensured that the cell has reached thermodynamic stability before starting the desired measurement. The battery behaviour is altered by the concentration gradients of the ionic charge carriers immediately after the current is switched off [117]. Thus, a relaxation period has to be applied to the battery between the switch off of the load current (from previous test) and the desired measurement.

The objective of the relaxation test was to investigate the behaviour of the open circuit voltage (OCV) of the tested LFP/C battery cells after the load current is interrupted and to determine the optimal relaxation period before performing the desired measurement.

Since the stabilization of the Li-ion battery cells' OCV is influenced by the allowed relaxation time, the relaxation test was performed following the procedure presented in Table C.3 (see Appendix C.2).

The same procedure was applied for the charging case, considering the same SOC levels. However, because of its long duration, the relaxation test was not repeated for other temperatures of the battery cell.

A relaxation time of 24 hours was considered long enough for the cell to stabilize (reach thermodynamic stabilization) and the voltage value after 24 hours was considered the OCV.

The voltage profile of the LFP/C battery cell, which was measured at 50% SOC after a charging and discharging pulse is presented in Fig. 3.6 and Fig. 3.7, respectively. In order to evaluate the effect of the relaxation time on the OCV, the voltage values measured with one second resolution during the 24 hours relaxation period were related to the OCV value measured after 24 hours. Thus, the OCV error was computed according to 3.3, and the results are presented in Fig. 3.8 and Fig. 3.9.

$$\epsilon_{OCV} = \frac{|V_i - OCV|}{OCV} \cdot 100 \tag{3.3}$$

where, ε_{OCV} represents the OCV error, and V_i represents the voltage measured at every second during the 24 hours relaxation.

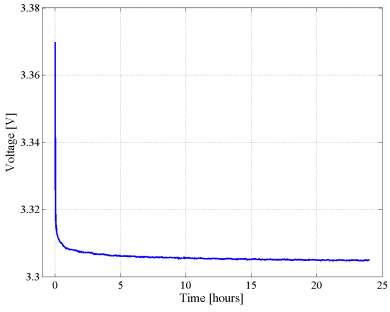

Figure 3.6: *Voltage recovery during 24 hours relaxation, after charging (SOC=50%)*

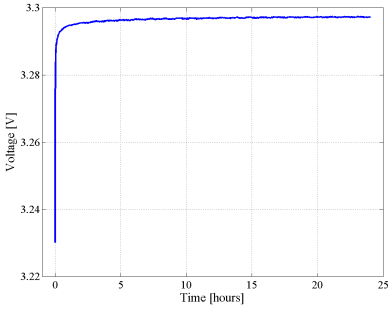

Figure 3.7: *Voltage recovery during 24 hours relaxation, after discharging (SOC=50%)*

The OCV error varies in both cases between 0% and 2%, depending on the con-

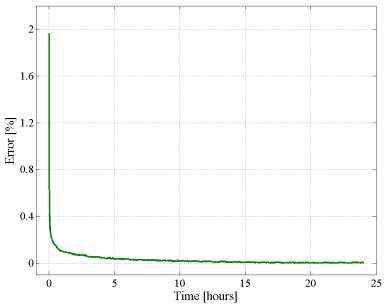

Figure 3.8: *Open-circuit voltage error depending on the relaxation time (charging case, SOC=50%)*

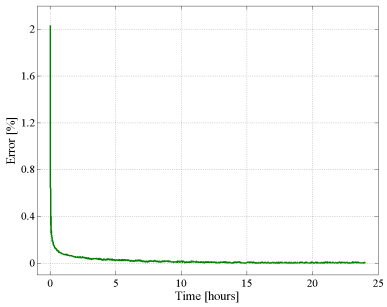

Figure 3.9: *Open-circuit voltage error depending on the relaxation time (discharging case, SOC=50%)*

sidered relaxation time. In Table 3.2 there are summarized the values of the OCV after various relaxation time periods together with their corresponding error.

Table 3.2: *Voltage of the LFP/C battery cell measured at 50% SOC after various relaxation time periods*

Relaxation time	**Charging**		**Discharging**	
	Voltage [V]	OCV error [%]	Voltage [V]	OCV error [%]
1 second	3.370	1.96	3.230	2.03
15 minutes	3.311	0.19	3.292	0.15
1 hour	3.308	0.10	3.295	0.07
2 hours	3.307	0.07	3.295	0.05
24 hours	3.305	0	3.297	0

Based on the results summarized in Table 3.2, it was concluded that OCV value, measured at 50% SOC, is only slightly influenced by a relaxation time, which varies between 15 minutes and 24 hours. Similar results were obtained for the other two SOC levels at which the relaxation tests were performed, as presented in Appendix C.2 (see Table C.4 and Table C.5 for 20% and 80% SOC, respectively). Therefore, a relaxation period of one hour was considered enough for the LFP/C battery cell to stabilize and consequently to allow for accurate measurements of the desired parameters. This relaxation period was used for the measurement of the battery cell's capacity and OCV vs SOC.

Capacity Test

The capacity of Li-ion battery is varying depending on the operating conditions (i.e. temperature and load current) [118].

Thus, the goal of the capacity test was to investigate how the capacity of the tested LFP/C battery cells is varying with the load current (C-rate) and temperature. The capacity of the LFP/C was measured both during charging and discharging based on the procedure summarized in Table C.6 (see Appendix C.3).

The voltage profiles measured on the LFP/C battery cell during the capacity check test, performed at 25^{o}C with the aforementioned currents, are presented in Fig. 3.10 and Fig. 3.11, for the charging and discharging cases, respectively.

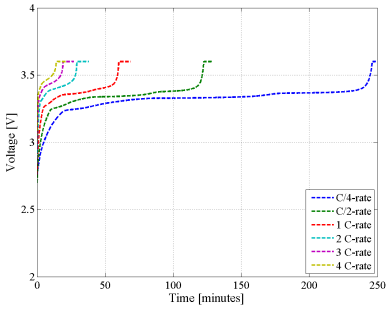

Figure 3.10: *Voltage profiles measured during the capacity test of the LFP/C battery cell (charging, T = 25^{o}C)*

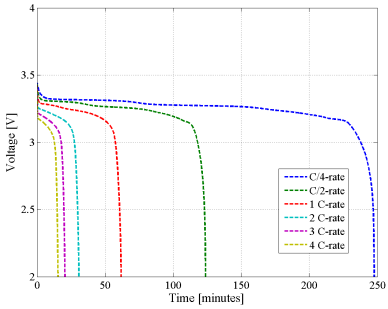

Figure 3.11: *Voltage profiles measured during the capacity test of the LFP/C battery cell (discharging, T = 25^{o}C)*

The voltage profiles measured during the capacity test at the other considered temperatures, are presented in Appendix C.3 (see Fig. C.11).

The capacity values measured during both charging and discharging at 25^{o}C and various C-rates are summarized in Table 3.3. The measured discharged capacity of the LFP/C battery cell is decreasing as the applied discharging C-rate is increasing; however, the variation of the discharged capacity for the considered C-rate interval is less than 1% (Peukert number very close to 1).

Moreover, the Coulombic efficiency of the LFP/C battery cell was calculated based on (3.4), for all the considered C-rates, and the obtained values are summarized in Table 3.3. The computed Coulombic efficiency is very close to 100%, which is characteristic for the majority of the Li-ion battery chemistries [83].

Table 3.3: *LFP/C battery cell measured capacity at 25^{o}C and various C-rates*

Condition	C-rate / Current					
	C/4 (0.625 A)	C/2 (1.25 A)	1C (2.5 A)	2C (5 A)	3C (7.5 A)	4C (10 A)
Charged Ah	2.573	2.582	2.577	2.574	2.562	2.557
Discharged Ah	2.579	2.578	2.572	2.560	2.556	2.555
Coulombic Efficiency [%]	100.23	99.85	99.81	99.50	99.73	99.91

$$\eta_{Ah} = \frac{Ah_{discharged}}{Ah_{charged}} \cdot 100[\%] \tag{3.4}$$

where, η_{Ah} represents the Coulombic efficiency, and $Ah_{discharged}$ and $Ah_{charged}$ represent the discharged and charged capacity of the battery cell, respectively.

OCV vs SOC Test

Similar to other battery parameters, the OCV is dependent on the operating conditions (i.e. SOC, temperature). Moreover, as it was shown during the relaxation test, the OCV of the tested LFP/C depends as well on the allowed relaxation time.

The goal of this test was to determine the OCV - SOC characteristic of the battery cell at various temperatures. This characteristic of the LFP/C battery cell will also be used for the performance modelling (see Chapter 3.2.2).

The OCV for each SOC, for both charging and discharging conditions, was determined with a 5% SOC resolution according to the procedure summarized in Table C.7 (see Appendix C.4).

The OCV vs SOC characteristics measured at 25 ^{o}C for both charging and discharging conditions are shown in Fig. 3.12.

By analyzing the OCV vs SOC characteristic presented in Fig. 3.12, a hysteresis effect is visible especially at low SOCs (e.g. below 10% - 40% SOC). A similar behaviour of the OCV vs SOC characteristics was observed for the other considered temperatures, as presented in Fig. C.12 - Fig. C.14 (see Appendix C.4).

HPPC Test

The internal resistance of the tested LFP/C battery cell was measured following a modified version of the hybrid pulse power characterization (HPPC) test presented in [116]. The charge and discharge internal resistances of the battery cell were measured for the

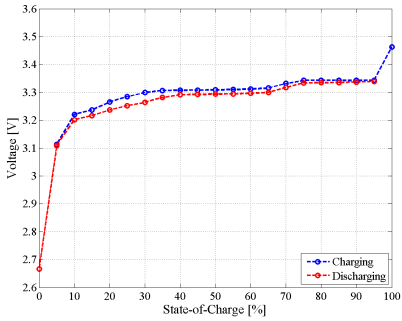

Figure 3.12: *The OCV vs SOC characteristic of the LFP/C battery cell measured at 25 °C.*

entire SOC interval (i.e., 5% - 95% SOC), with different C-rates. Moreover, based on the modified HPPC test, the charging and discharging pulse power capability (PPC) of the LFP/C battery cell was determined.

The test profile applied to the LFP/C battery cell consists of consecutive charge and discharge current pulses of different C-rates (i.e. 0.1C, 0.5C, 1C, 2C, 3C, and 4C) as presented in Fig. 3.13; the pulse duration was 18 seconds for both charging and discharging conditions and the relaxation time between two consecutive pulses was set at 15 minutes.

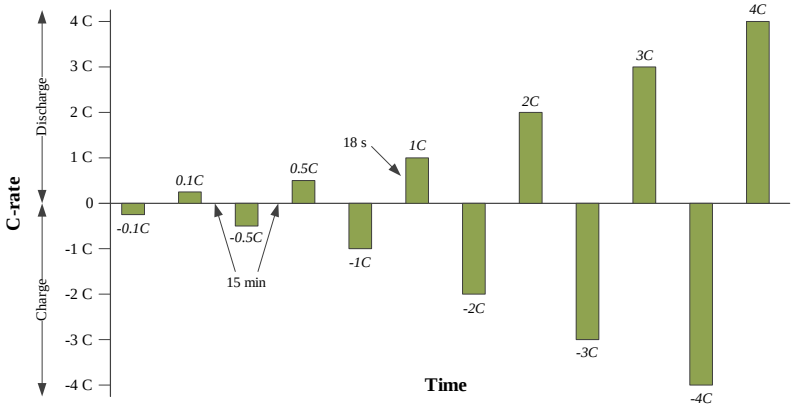

Figure 3.13: *Pulse profile applied to the LFP/C battery cell for measuring the internal resistance.*

The procedure applied to measure the internal resistance of the LFP/C battery cell is presented in Table C.8 (see Appendix C.5).

The typical voltage response of a Li-ion battery cell to a discharging current pulse is presented in Fig. 3.14. As presented in the ISO 1405-1:2011 standard, the charging and

discharging internal resistance of the Li-ion battery could be calculated for various pulse lengths (i.e. 0.1 *s*, 2 *s*, 18 *s*) [116]; however, in this thesis, only the 18 seconds internal resistance is of interest and will be calculated.

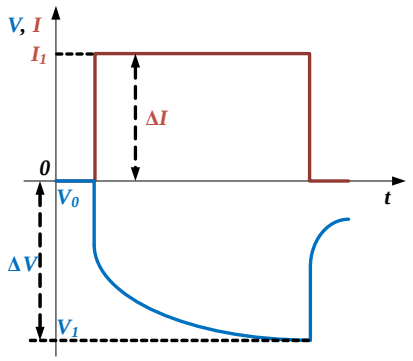

Figure 3.14: *Li-ion battery cell's theoretical voltage response due to a discharging current pulse.*

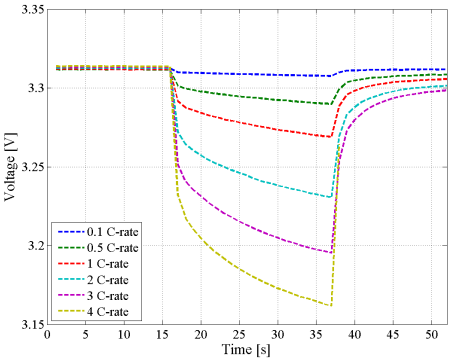

Figure 3.15: *Voltage response of the LFP/C battery cell at current pulses of different amplitudes, during the HPPC test (SOC = 25%, T = 25°C), various C-rates.*

The internal resistance of the LFP/C battery cell was computed based on the Ohm's Law, as:

$$R_i = \frac{\Delta V}{\Delta I} = \frac{|V_1 - V_0|}{I_1} \tag{3.5}$$

where, R_i represents the internal resistance of the battery, ΔV represents the change in the voltage due to the applied current pulse, ΔI represents the change in the current, V_1 represents the voltage measured after 18 seconds, V_0 represents the voltage measured just before applying the current pulse (i.e. OCV), and I_1 represents the amplitude of the applied current pulse.

The voltage response of the LFP/C battery cell to current pulses of various amplitudes, which was measured during the HPPC test, is presented for SOC = 50% in Fig. 3.15; similar voltage behaviour was obtained at the other considered SOC levels. Based on the battery cell's voltage response and considering (3.5), the charging and discharging internal resistance was computed for all the considered testing conditions.

The internal resistance of the LFP/C battery cell, measured at 25°C and different SOC levels, is presented for the charging case in Fig. 3.16 and for the discharging case in Fig. 3.17.

Both charging and discharging internal resistances are showing a nearly parabolic dependence on the SOC. The characteristic of the discharging internal resistance as function of SOC is relatively flat in the interval 20-90% SOC, with a slight increase in the

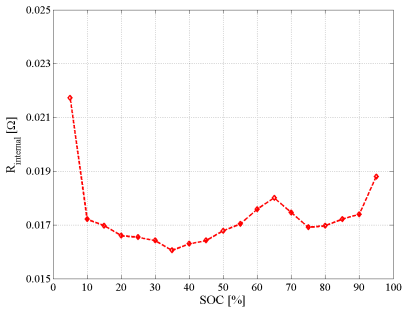

Figure 3.16: *Internal resistance during pulse charging of the LFP/C battery cell at different SOC values (T = 25°C, 1C-rate).*

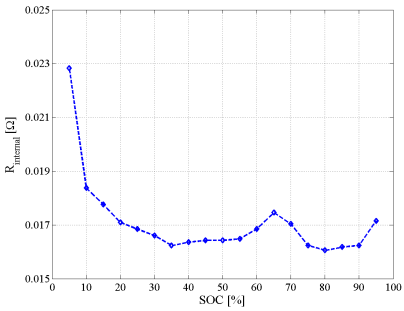

Figure 3.17: *Internal resistance during pulse discharging of the LFP/C battery cell at different SOC values (T = 25°C, 1C-rate).*

region 60-70% SOC (visible also for charging internal resistance). Furthermore, the internal resistance measured both during charging and discharging shows a quite significant increase for SOCs lower than 15% and higher than 95%. Thus, it can be concluded that the LFP/C battery cell operates at BOL with high efficiency over a wide SOC interval (i.e. 20-90% SOC).

The dependence of the internal resistance (discharging case) on the operating temperature is illustrated in Fig. 3.18. Independent on the operating temperature, the characteristic of the discharged internal resistance as function of SOC remains almost unchanged (however, values slightly changing). Moreover, it was found out that, for the considered temperature interval (i.e. 15-45°C), the discharged internal resistance has nearly exponential dependence on the temperature. Similar dependences were obtained for the charging internal resistance as presented in Appendix C.5 (see Fig. C.15)

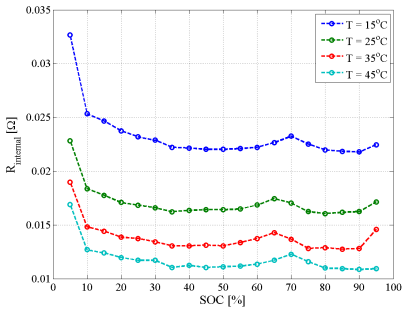

Figure 3.18: *Dependence of the discharging internal resistance on the operating temperature (measured for 1C).*

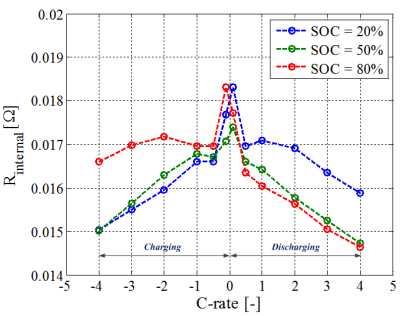

Figure 3.19: *Dependence of the internal resistance on the C-rate (measured at T = 25°C).*

Fig. 3.19 shows the current (C-rate) dependency of the LFP/C battery cell internal resistance, measured at 25^{o}C at various SOC levels. As it is illustrated, the dependence of the internal resistance on the C-rate is slightly changing depending on the SOC.

Pulse Power Capability Calculation

Based on the HPPC test, the PPC of the LFP/C battery cell was determined. The charging and discharging PPC were calculated at each available SOC increment from the OCV and the internal resistance for that SOC, using (3.6) and (3.7) [119].

$$PPC_{charge} = V_{max}\frac{V_{max} - OCV_{ch}}{R_{i,ch}} \tag{3.6}$$

$$PPC_{discharge} = V_{min}\frac{OCV_{dch} - V_{min}}{R_{i,dch}} \tag{3.7}$$

where, V_{max} represents the cell's voltage at the end of the charging current pulse, OCV_{ch} represents the cell's OCV measured before applying the charging current pulse, $R_{i,ch}$ represents the internal resistance measured during charging, V_{min} represents the cell's voltage at the end of the discharging current pulse, OCV_{dch} represents the cell's OCV measured before applying the discharging current pulse, and $R_{i,dch}$ represents the internal resistance measured during discharging.

The PPC characteristic of the LFP/C battery cell, measured during both charging and discharging, at different temperatures are illustrated in Fig. 3.20 and Fig. 3.21. The PPC values were calculated for a battery current value equivalent to 1C-rate (i.e. 2.5A).

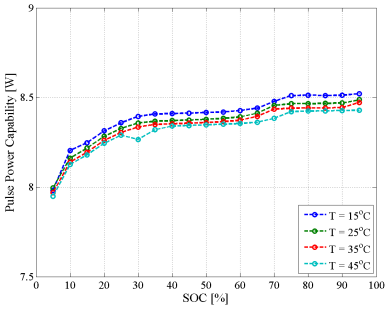

Figure 3.20: *Charging PPC of the LFP/C battery cell measured for the entire SOC range at various temperatures (measurements performed with nominal current, 2.5 A).*

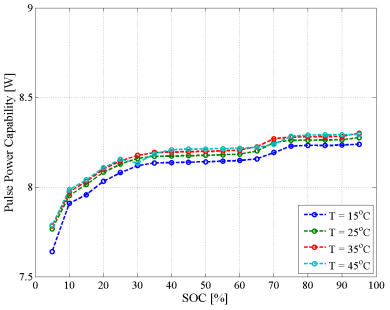

Figure 3.21: *Discharging PPC of the LFP/C battery cell measured for the entire SOC range at various temperatures (measurements performed with nominal current, 2.5 A).*

As a consequence of the flat charge and discharge voltage curves [84], [95], the mea-

sured PPC characteristics of the LFP/C battery cell, presented in Fig. 3.20 and Fig. 3.21, are flat as well, for almost the entire SOC interval. Moreover, the PPC of the studied battery cell varies with the operating temperature in a narrow interval.

The maximum PPC characteristics of the LFP/C battery cell, measured at different temperatures considering the maximum current of the cell (i.e. 10 A) are presented in Fig. C.16 and Fig. C.17 (see Appendix C.6).

EIS Test

The small signal AC impedance of the tested LFP/C battery cell was measured using the EIS technique. The EIS test was performed in galvanostatic mode, considering the following measurement parameters:

- *Frequency Range* : 10 kHz - 10 mHz;
- *Points per decade* : 8;
- *Measurement Time* : 4 seconds;
- *Measurement Periods* : 2.

Moreover, all the EIS measurements were performed without superimposed DC current.

Similar to the case of the other parameters, the small signal AC impedance of the LFP/C battery cell is dependent on the operating conditions (SOC, temperature). Thus, the procedure summarized in Table C.9 (see Appendix C.7) was applied to measure the the impedance spectra the LFP/C battery cell over the entire SOC interval at various temperatures:

The impedance spectrum of the tested LFP/C battery cell measured at 25^{o}C and 50% SOC is illustrated in Fig. 3.22. The Nyquist curve of the LFP/C differs from the theoretical Li-ion batteries' Nyquist curve (see Fig. 3.1); however, this is quite common since the shape of the impedance spectrum of Li-ion batteries varies from chemistry to chemistry.

The dependence of the impedance spectrum of the LFP/C battery cell's on the SOC is presented in Fig. 3.23. The shape of the Nyquist curve has remained almost unchanged at the variation of the SOC: a decrease of the first semicircle of the impedance spectrum was observed (especially on the zoom view) once the SOC-level has increased. This trend is better visible on Fig. C.18 (see Appendix C.7), where the impedance spectra measured over the whole SOC interval are presented. Thus, one can conclude that, for the tested LFP/C battery cell, the charge transfer and diffusion processes are less dependent on the SOC.

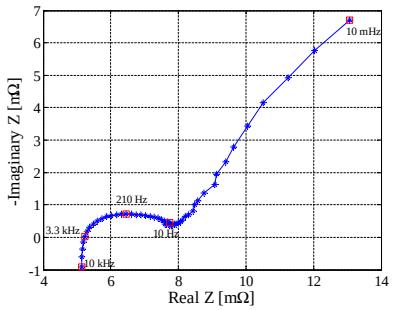

Figure 3.22: *Impedance spectrum of the tested LFP/C battery cell, measured at BOL, 25°C, and 50% SOC.*

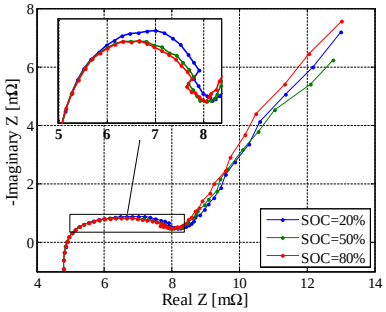

Figure 3.23: *Dependence of the impedance spectra on the SOC (measured at T = 25°C).*

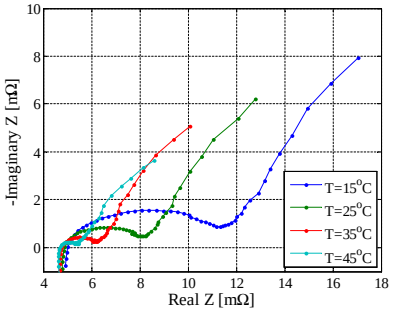

Figure 3.24: *Dependence of the impedance spectra on the temperature (measured at SOC = 50%).*

The dependence of the impedance spectrum of the tested LFP/C battery cells on the operating temperature is illustrated in Fig. 3.24 for 50% SOC. The ohmic resistance, and both the charge transfer and the diffusion processes are very sensitive to changes of the operating temperature. This trend was observed over the entire SOC interval as shown in Fig. C.19 and Fig. C.20 from Appendix C.7.

3.2.2 LiFePO$_4$/C battery cell performance model

Definition of the battery cell voltage

The performance model of the LFP/C battery cell was developed using an EIS-based electrical modelling approach. The basic configuration of the EIS-based electrical model of the LFP/C battery cell is presented in Fig. 3.25.

According to the schematic presented in Fig. 3.25, the voltage of the LFP/C battery cell is calculated as given in (3.8).

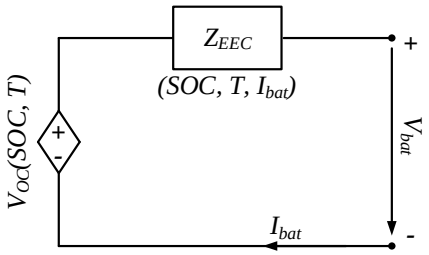

Figure 3.25: *The basic configuration of the EIS-based electrical battery cell model .*

$$V_{bat} = V_{OC} \pm V_{EEC} \tag{3.8}$$

where, V_{bat} represents the voltage of the battery cell, V_{OC} represents the OCV of the battery cell, and V_{EEC} represents the voltage drop over the EEC used to model the dynamics of the battery cell.

The voltage drop over the EEC is obtained as the sum of various over-voltages, which are caused by different processes occurring inside the battery cell during charging and discharging [120]:

$$V_{EEC} = V_{ohmic} + V_{ch.tr} + V_{diffusion} \tag{3.9}$$

Thus, the voltage of the LFP/C battery cell could be re-written as:

$$V_{bat} = V_{OC} \pm V_{ohmic} \pm V_{ch.tr} \pm V_{diffusion} \tag{3.10}$$

where:

- V_{OC} - represents the OCV, which is dependent on electrolyte concentration, composition of the active materials, temperature, and SOC [120];
- V_{ohmic} - represents an over-voltage caused by the resistance of the poles, current collectors and electrolyte; it is direct proportional to the load current [120];
- $V_{ch.tr}$ - represents an over-voltage caused by the electrochemical and chemical reaction at inner surfaces; it shows a non-linear dependence on the load current [120];
- $V_{diffusion}$ - represents an over-voltage caused by a deficit or surplus of reactants (concentration gradients of charge carriers) at the location of the reaction.

Selection of the EEC configuration

In order to obtain the contribution of the V_{EEC} to the battery cell voltage, the EEC has to be parametrized. The parametrization is realized by curve fitting the impedance spectra measured for the LFP/C battery cell at different conditions.

However, curve fitting of the impedance spectra is not a straightforward process. The most challenging step is to identify a configuration of the EEC, which represents optimally the shape of the measured impedance spectrum on one hand and is composed from a reduced number of parameters on the other hand [48], [117]. Based on the proposed configuration of the EEC, the curve fitting process is started and the parameters of the EEC are obtained by minimizing the deviation between the measured and estimated impedance spectra [48]. The minimization process is performed for both the real and imaginary part of the impedance in the same time by applying a CNLS algorithm. At the end of the fitting process, the fitting error is evaluated; if the fitting error is higher than a predefined threshold value, either the fitting process is resumed with a new set of initial guess values or a new EEC configuration is proposed.

In this work, the accuracy of the fitting was evaluated by computing the normalized root mean square error (NRMSE) given by (3.11). The NRMSE was computed separately for the real and the imaginary parts of the impedance and the final impedance spectra fitting error is given by the mean value of the two separately computed errors.

$$NRMSE = \frac{\sqrt{\frac{\sum_{i=1}^{n}(Z_{meas,i} - Z_{fit,i})^2}{n}}}{Z_{meas,max} - Z_{meas,min}} \tag{3.11}$$

Different configurations of the EEC might be used for fitting the impedance spectra of Li-ion batteries, depending on shape of the measured Nyquist curve [99], [112], [121]. However, in this work, based on *a priori* knowledge and visual inspection of the measured Nyqusit curves, two EEC configurations have been initially selected for curve fitting. The first configuration, presented in Fig. 3.26, is based on series and parallel connections of resistances and capacitors [**?**], while the second configuration, presented in Fig. 3.27, is based on ZARC elements [112].

The EEC configurations presented in Fig. 3.26 and Fig. 3.27 were evaluated in order to determine, which configuration is more suitable for fitting the measured impedance spectra of the tested LFP/C battery cell. Thus, the Nyquist curve measured at SOC = 50% and 25^{o}C were curve fitted using both configurations; the fitting results are presented in Fig. 3.28 and Fig. 3.29.

The accuracy of the curve fitting process (NRMSE) when the two EEC configura-

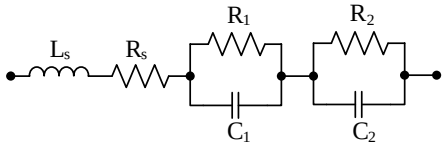

Figure 3.26: *EEC based on RC parallel networks.*

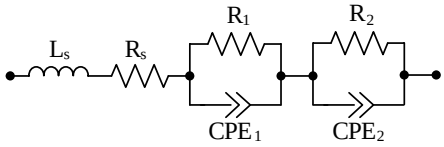

Figure 3.27: *EEC based on ZARC elements.*

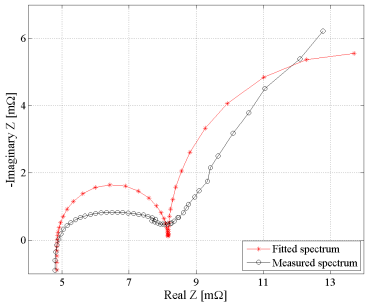

Figure 3.28: *Measured and fitted impedance spectrum using the EEC configuration based on RC parallel networks (see Fig. 3.26).*

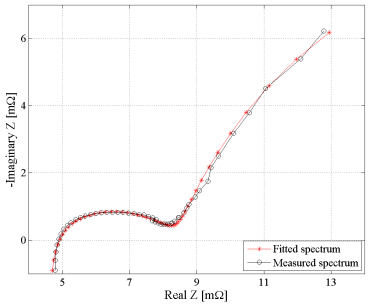

Figure 3.29: *Measured and fitted impedance spectrum using the EEC configuration based on ZARC elements (see Fig. 3.27).*

tions were used are presented in Table 3.4.

Table 3.4: *Comparison between the curve fitting results obtained for the two considered EEC configurations*

EEC Configuration / Criteria	**EEC-based on RC networks**	**EEC-based on ZARC elements**
Fitting Accuracy [%]	5.56	0.80
No. of parameters	6	8

As shown in Table 3.4, the EEC based on ZARC elements is able to fit better (lower NRMSE) the impedance spectra of the tested LFP/C than the EEC configuration based on RC networks. The better fitting accuracy is mainly due to the use of ZARC elements, which are able to fit better the depressed semi-circles, which are characteristics for Nyquist curves measured on Li-ion batteries [99], [112]. Consequently, the EEC configuration based on ZARC elements was used to fit all the measured impedance spectra (at different conditions) and to model the performance behaviour of the tested LFP/C battery cell.

Structure and implementation of the performance model

The impedance of the selected EEC configuration (see Fig. 3.27) is given by:

$$Z_{EEC-ZARC} = j\omega L_s + R_s + \frac{R_1}{1 + (j\omega)^{n_1} Q_1 R_1} + \frac{R_2}{1 + (j\omega)^{n_2} Q_2 R_2} \tag{3.12}$$

where, L_s and R_s represent the series inductance and resistance of the battery, respectively, R_1 and R_2 represent the other resistances from the circuit, Q_1 and Q_2 represent the generalized capacitances, n_1 and n_2 represent the depression factors, and ω represents the angular frequency.

The first term in (3.12) is used to describe to inductive behaviour at high frequencies, the second term is used to calculate the over-voltage caused by the ohmic resistance, while the last two terms are used to determine the contributions of the charge transfer and diffusion processes to the overall voltage of the battery cell.

Thus, considering (3.12), the voltage equation (3.10) of the LFP/C battery cell was re-written as:

$$V_{bat} = V_{OC} + I_{bat} \cdot (j\omega L_s + R_s + \frac{R_1}{1 + (j\omega)^{n_1} Q_1 R_1} + \frac{R_2}{1 + (j\omega)^{n_2} Q_2 R_2}) \tag{3.13}$$

As illustrated in Fig. 3.25, besides being dependent on SOC and temperature, the parameters of the EEC (mainly the charge transfer resistance [122]) are dependent as well on the load current. However, since during the characterization tests all the EIS measurements were performed without superimposed DC current, the effect of the load current on the parameters of the EEC was not considered.

The non-linear dependence of the charge-transfer resistance, and subsequently of the corresponding over-voltage, on the battery current, measured on the tested LFP/C battery cell is presented in Fig. 3.30.

Usually, the exponential relationship between the battery cell current and the potential is described using the Butler-Volmer equation given in (3.14) [122], [123].

$$i = i_0 \cdot (e^{\frac{\alpha n F}{RT} \cdot \eta} - e^{-\frac{(1-\alpha) n F}{RT} \cdot \eta}) \tag{3.14}$$

where, i is the electrode current density, i_0 is the exchange current density, α is the symmetry factor, n is the number of electrons, R is the universal gas constant (8.3144 $J\ K^{-1}\ mol^{-1}$), F is the Faraday constant (96 485.339 $C\ mol^{-1}$), η is the overpotential (i.e. the difference between the electrode potential and equilibrium potential).

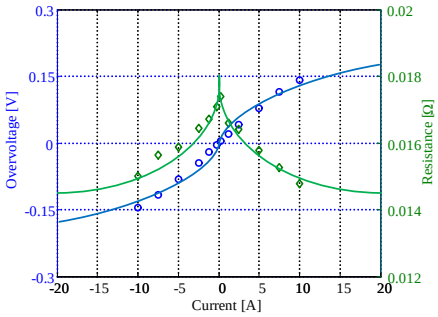

Figure 3.30: *Non-linear variation of the charge transfer resistance and of the corresponding over-voltage as function of the current of the LFP/C battery cell.*

Because information about various parameters given in (3.14) were not available, in order to consider the effect of the current on the LFP/C battery cell voltage the following procedure was used. A comparison was performed between the voltage response measured for 18 seconds in laboratory (during the internal resistance tests - see Chapter 3.2.1) and the simulated voltage response; the obtained difference between the two curves were considered to describe the impact of the current on the voltage of the LFP/C battery cell. The procedure was repeated for all the considered temperatures, SOCs, and C-rates and the results were stored in 3D look-up tables.

Based on (3.13) and considering the effect of the current on the battery cell's voltage, the performance model of the LFP/C battery cell was implemented according to the schematic presented in Fig. 3.31.

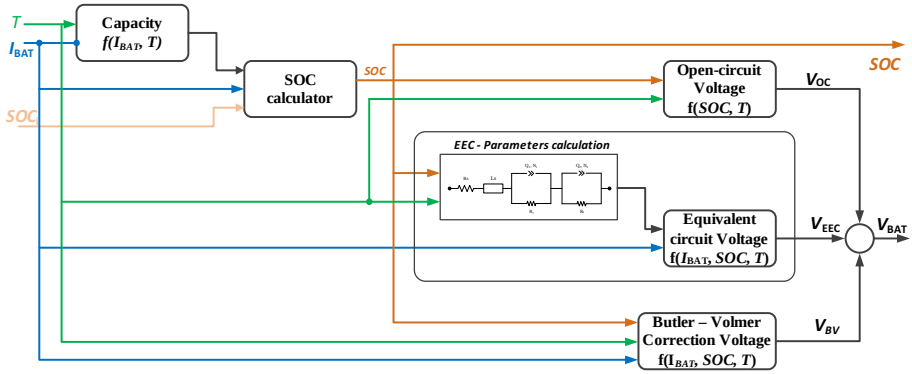

Figure 3.31: *Block diagram implementation of the performance model of the LFP/C battery cell.*

The inputs of the proposed LFP/C battery cell performance model are the applied load current, the initial SOC, and the temperature, while the outputs are the battery cell

voltage and the present SOC value; nevertheless, since no thermal model was developed, the temperature of the battery cell is considered constant during the simulation.

The parametrization of the proposed performance model was realized based on the results obtained from the characterization tests, which were previously carried out on the LFP/C battery cell (see Chapter 3.2.1). The battery cell parameters were implemented as 2D- or 3D-look-up tables in order to consider their dependence on the operating conditions (i.e., SOC, temperature, and current).

1. Capacity

   The capacity of the LFP/C battery cell, which has been measured at various temperature and current rates, was implemented as a 2D-look-up table. The measured charging and discharging capacity of the battery cell have been implemented separately in two distinct look-up tables as presented in Fig. 3.32 and Fig. 3.33.

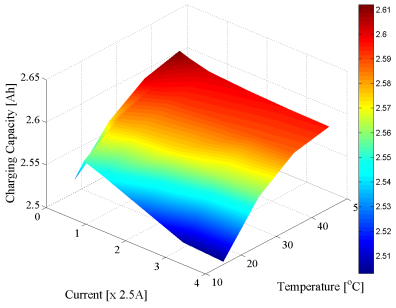

Figure 3.32: *Look-up table implementation of the charging capacity of the LFP/C battery cell.*

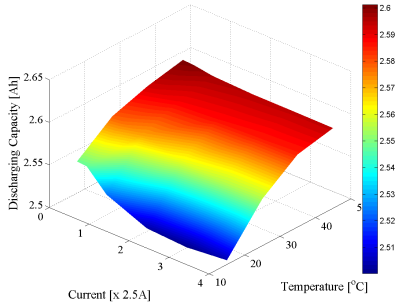

Figure 3.33: *Look-up table implementation of the discharging capacity of the LFP/C battery cell.*

2. SOC Calculator

   The present SOC of the LFP/C battery cell is calculated, based on the initial SOC (SOC_i), by integrating the cell current I_{bat} and is always related to the measured capacity (C_{meas}) at the considered conditions.

$$SOC = SOC_i - \frac{1}{C_{meas}} \int I_{bat} dt \tag{3.15}$$

3. Open-circuit Voltage

   The OCV of the LFP/C battery cell, which has been measured at various temperatures with a 5% SOC resolution was implemented as 2D-look-up table. Similar to the case of the battery cell's capacity, two different look-up tables were considered;

one for the charging case (see Fig. 3.34) and one for the discharging case (see Fig. 3.35).

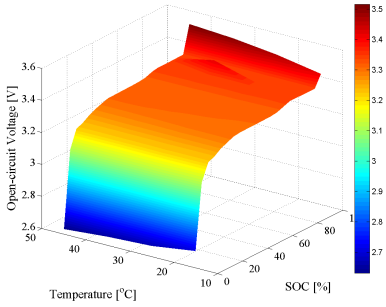

Figure 3.34: *Look-up table implementation of the OCV of the LFP/C battery cell (charging case).*

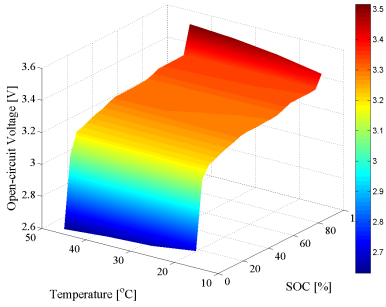

Figure 3.35: *Look-up table implementation of the OCV of the LFP/C battery cell (discharging case).*

4. Equivalent Circuit Voltage

The impedance spectra measured on the LFP/C battery cell at various temperatures and SOCs were curve fitted using the EEC presented in Fig. 3.29. During the fitting processes it has been observed that the parameters L_s, n_1 and n_2 are only slightly dependent on the operating conditions. Therefore, they were assumed constant for all the considered operating conditions and their values are summarized in Table 3.5.

Table 3.5: *Values of EEC parameters kept constant for all operating conditions.*

Parameter	Value
Series inductance, L_s	$1.8 \cdot 10^{-8}$ H
Depression factor, n_1	0.50
Depression factor, n_2	0.80

The other parameters of the EEC, the series resistance R_s, the resistances R_1 and R_2, and the generalized capacitances Q_1 and Q_2 were implemented as 2D-look-up tables as shown in Fig. 3.36 - Fig. 3.40, respectively.

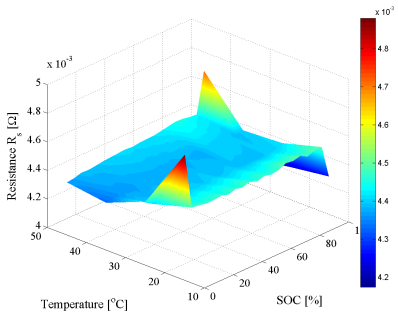

Figure 3.36: *Look-up table implementation of the series resistance R_s of the EEC.*

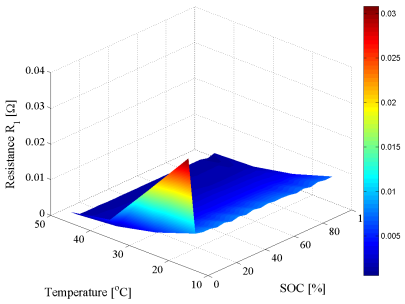

Figure 3.37: *Look-up table implementation of the resistance R_1 of the EEC.*

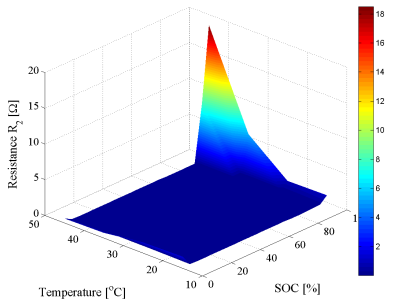

Figure 3.38: *Look-up table implementation of the resistance R_2 of the EEC.*

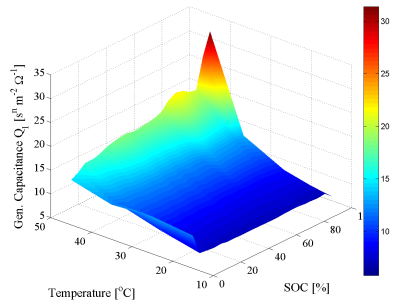

Figure 3.39: *Look-up table implementation of the generalized capacitance Q_1 of the EEC.*

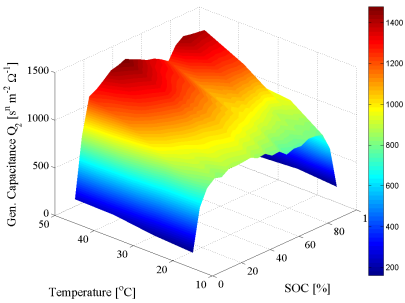

Figure 3.40: *Look-up table implementation of the generalized capacitance Q_2 of the EEC.*

Based on the implemented 2D-look-up tables and considering the battery current I_{bat}, the contribution of the EEC to the battery voltage was found for all the

considered operating conditions.

5. Butler-Volmer Correction Voltage

   The voltage correction factors, assigned to the non-linear effect of the battery current on the charge transfer resistance, which have been previously computed were implemented as 3D-look-up tables; the correction factors depend on the SOC, battery current, and temperature. Fig. 3.41 presents the look-up table implementation of the voltage correction factors for the 25^{o}C dimension.

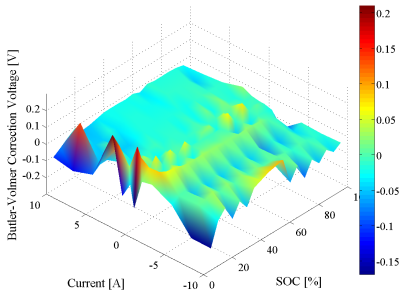

Figure 3.41: *Look-up table implementation of the voltage correction factors for the T=25$_o$C dimension.*

3.3 Verification of the Performance Model

In order to validate the developed performance model of the LFP/C battery cell, different current profiles were applied. Since Li-ion batteries used in VPP applications are operating under complex partial charging-discharging conditions, similar current profiles were used to validated the developed model.

The accuracy of the LFP/C battery cell performance model was evaluated by computing the coefficient of determination R^2 obtained by comparing the measured and estimated voltage profiles, according to (3.16).

$$R^2 = 1 - \frac{\sum_{i=1}^{n}(V_{model}(i) - V_{meas}(i))^2}{\sum_{i=1}^{n}(V_{model}(i) - \overline{V_{meas}})^2} \tag{3.16}$$

where, V_{model} represents the estimated voltage, V_{meas} represents the measured voltage, and n represents the number of observations.

Furthermore, the mean and maximum deviation between the measured and estimated voltage profiles were computed for all the considered verification profiles, according to (3.17) and 3.18, respectively.

$$|\overline{\epsilon}| = \overline{|V_{meas}(i) - V_{model}(i)|} \tag{3.17}$$

$$\epsilon_{max} = max(100 \cdot \frac{|V_{meas}(i) - V_{model}(i)|}{V_{meas}(i)}) \tag{3.18}$$

3.3.1 Verification based on charge/discharge pulses

Pulse charge and discharge

The first validation of the performance model was performed using charging and discharging pulse profiles, which are typically used for verification studies. The LFP/C battery cell was fully charged with 1C-rate (2.5 A) in steps of 10% SOC; between two consecutive charging current pulses, a relaxation period of 15 minutes was considered. The measured and estimated results of the LFP/C battery cell pulse charging are presented in Fig. 3.42.

As it can be observed from Fig. 3.42, the developed model is able to predict with high accuracy the LFP/C battery cell voltage. For the considered pulse charging profile, the model is able to predict the voltage behaviour with a maximum error ϵ_{max} of 4.01% and a mean error $|\overline{\epsilon}|$ of 7.1 mV; by comparing the measured and estimated voltage profiles, a coefficient of determination $R^2 = 0.9637$ was obtained. The distribution of the voltage deviations (expressed as the relative error) is presented in Fig. 3.43, showing that the developed model has a slight tendency of under-estimating the behaviour of the voltage of the LFP/C battery cell.

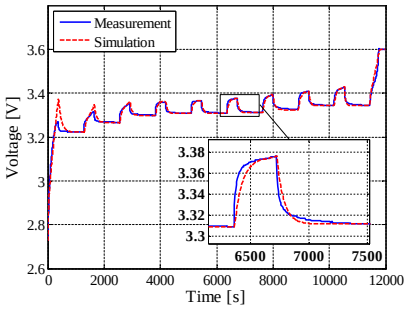

Figure 3.42: *Measured and estimated voltage profiles during pulse current charging (I_{bat}=2.5 A, T=25°C).*

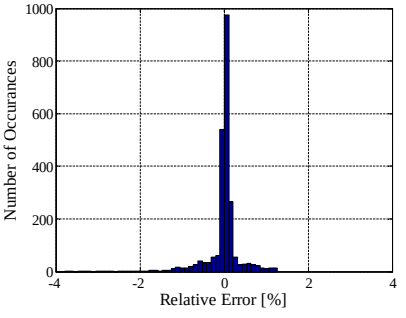

Figure 3.43: *Distribution of the relative error obtained during the pulse current charging verification.*

The measured and estimated voltages, which were obtained during the performance model verification using a discharging current pulse profile are presented in Fig. 3.44. The discharging of the LFP/C battery cell was performed with 1C-rate in steps of 10% SOC. The developed performance model is able to estimate very accurately the voltage of the tested battery cell, with a maximum error of 3.66% and a mean error of 6.8 *mV*. Contrary to the previous case, the distribution of the relative voltage deviations (see Fig. 3.45), is showing that the model has a slight tendency of over-estimating the voltage behaviour of the LFP/C battery cell. The main contribution to this tendency is represented by the voltage estimation error after the current pulse is cut-off.

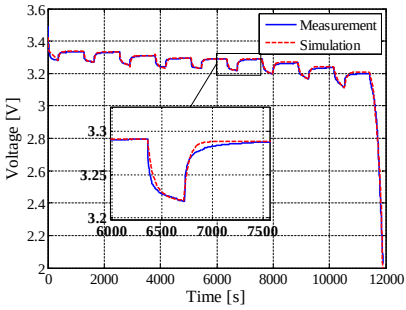

Figure 3.44: *Measured and estimated voltage profiles during pulse current discharging (I_{bat}=2.5 A, T=25°C).*

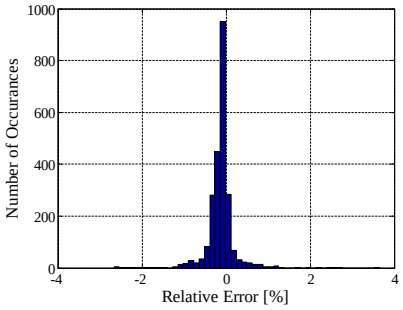

Figure 3.45: *Distribution of the relative error obtained during the pulse current discharging verification.*

Dynamic charge and discharge

Due to the characteristics of the VPP applications, Li-ion batteries used in such application are subjected to complex charging - discharging profiles. Therefore, the second validation of the proposed LFP/C performance model is based on a current profile composed of charging and discharging pulses of various C-rates applied over the whole SOC interval. The procedure for this verification process is summarized in Appendix D.1. In order to allow for a non-biased verification, the C-rates used for the dynamic profile are different from the ones utilized, in previous section, to compute the Butler-Volmer correction voltage (see also Chapter 3.2.1 - HPPC test).

The measured and estimated voltage profiles obtained by applying the dynamic charging-discharging current profile are illustrated in Fig. 3.46. The model is able to predict the battery cell's voltage with a mean error of 6.4 *mV* and a maximum error of 4.89%. Moreover, by comparing the measured voltage profile with the estimated voltage profile for the present verification case a coefficient of determination R^2 = 0.9255 was obtained.

For the dynamic charging - discharging current profile, the distribution of the relative

voltage error, which is presented in Fig. 3.47, shows a slight under-estimation of the battery cell voltage. This under-estimation of the cell voltage is mainly caused by the inability of the model to react to sudden and large variation of the C-rate (i.e. 3.5C to 1C), as it is shown in the zoomed view from Fig. 3.46.

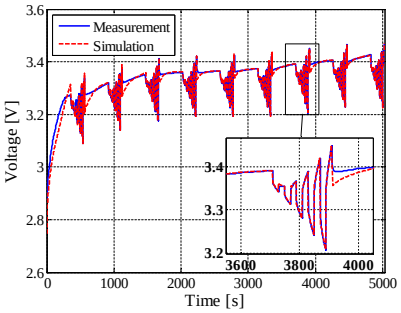

Figure 3.46: *Measured and estimated voltage profiles obtained by applying a dynamic current pulses profile (T=25° C).*

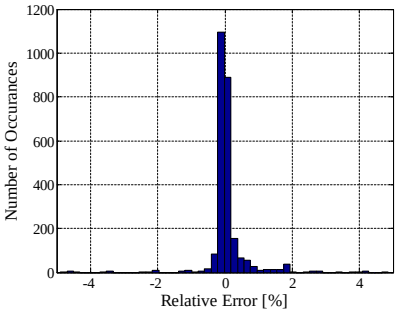

Figure 3.47: *Distribution of the relative error obtained during the model verification with a dynamic current pulses profile.*

3.3.2 Verification based on PFR profile

The last verification of the developed performance model was performed using a realistic current profile, which is characteristic for Li-ion batteries providing PFR service. The applied PFR profile was measured on field on a 400 kW/ 100 kWh battery ESS; more details about the PFR current profile are presented in Appendix D.2.

The comparison between the measured and estimated LFP/C battery cell voltage when the PFR current profile was applied is presented in Fig. 3.48. The proposed performance model estimates generally with good accuracy the voltage of the tested battery cell; however, the model has the tendency to overestimate the voltage response of the battery cell when sudden and large variation of the applied current are occurring (i.e. sudden changes in the applied current from below 1C to 4C).

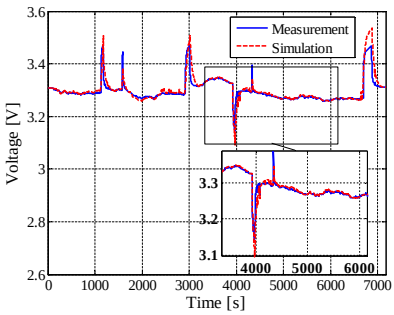

Figure 3.48: *Measured and estimated voltage profiles obtained by applying a realistic PFR current profile (T=25°C).*

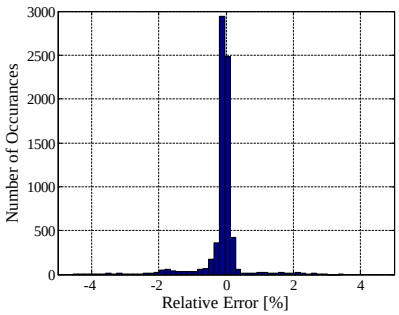

Figure 3.49: *Distribution of the relative error obtained during the model verification with a realistic PFR current profile.*

The slight tendency of the performance model to over-estimate the battery voltage when the PFR current profile was used is visible also on Fig. 3.49, which presents the distribution of the relative voltage errors. Nevertheless, the developed performance model is able to predict accurately the voltage of the LFP/C battery cell, with a mean error of 8.4 *mV*, a maximum error of 4.54%, and a coefficient of determination of $R^2 = 0.7724$.

3.3.3 Discussion

The developed performance model was verified using various current profiles. As it was shown throughout Chapter 3.3, the model is able to estimate with high accuracy the voltage behaviour of the tested LFP/C battery cell, independent on the applied current profile. The accuracy of the developed performance model obtained for all the considered verification profiles is summarized in Table 3.6.

Table 3.6: *Performance model accuracy for different current profiles.*

Profile	Mean error, $\|\bar{\epsilon}\|$	Max. error, ϵ_{max}	R^2
Pulse charging	7.1 mV	4.01%	0.9637
Pulse discharging	6.8 mV	3.66%	0.9917
Dynamic profile	6.4 mV	4.89%	0.9255
PFR profile	8.4 mV	4.54%	0.7724

For all the considered profiles, the performance model shows a maximum error lower than 5% and a mean error below 8.5 *mV*. The model validation process was car-

ried out only for a temperature of 25^oC, since this is the typical operating temperature of Li-ion batteries which are used in stationary applications [42]. Furthermore, it can be concluded that the proposed characterization methodology for the LFP/C battery cell has offered accurate parameters for developing and parametrizing the performance model.

3.4 Summary

This chapter was dedicated to the performance modelling of the LFP/C battery cell. During the first part of the chapter, the most common approaches for performance modelling of Li-ion batteries were described and compared. Because of its characteristics (which include high accuracy, relatively easily parametrization etc.), an EIS-based electrical approach was selected for performance modelling of the LFP/C battery cell.

The second part of the chapter has focused on the full characterization of the LFP/C battery cell by performing various tests including capacity, HPPC and EIS tests. The results obtained from the characterization tests have been further used to parametrize the performance model of the tested Li-ion battery cell. The developed performance model considers the effect of all the factors (i.e., SOC, current, and temperature) on the behaviour of the LFP/C battery voltage.

In the last part of the chapter, the developed performance model was verified using four different current profiles. The model is able to estimate with high accuracy (i.e. $\epsilon_{max} < 5\%$) the voltage of the LFP/C battery cell independent on the applied current profile.

Chapter 4

Lifetime Modelling of Li-ion Battery Cells

The present chapter gives an overview of the most common approaches, which may be used to build lifetime models for Li-ion batteries. The first part of this chapter presents briefly the ageing mechanisms that are causing the degradation of Li-ion batteries; both ageing during storage and during cycling are discussed. The second part of the chapter presents four of the most used Li-ion battery lifetime modelling approaches, together with their advantages and drawbacks.

4.1 The Ageing Mechanisms of Li-ion Batteries

Li-ion batteries are failing because of different causes, as presented in [48]. One of the failure sources of Li-ion battery cells is the gradual decrease of their performance parameters (i.e., capacity and power capability), known as ageing.

Besides the cost, another root cause for the relatively slow penetration of Li-ion batteries into the stationary ES market is their limited lifetime. In order to use the Li-ion batteries with high efficiency throughout their entire lifetime, good understanding of their ageing mechanisms and ageing behaviour is required. Moreover, a good understanding of the ageing mechanisms will allow for an optimal sizing of the Li-ion battery ESS and for defining the best EMS for the ESS, which will further allow for lifetime maximization of the Li-ion batteries.

However, independent on the chemistry, the ageing processes of Li-ion batteries are complicated and dependent on the operating conditions [124], [125], [126]. Most of the times, the capacity fade and the power capability decrease do not originate from one

single ageing mechanism, but from a number of different processes and their interaction [124], [126]. Moreover, degradation of battery capacity and of the power capability are observed together during while the ageing process evolves [125].

Generally, each Li-ion chemistry has its own properties and its ageing mechanisms are influenced by the nature of its components (e.g. electrolyte composition, active material and electrode design etc.) [124]. Thus, it is beyond the scope of this thesis to offer a comprehensive overview of all possible ageing mechanisms encountered in Li-ion batteries. Since a Li-ion battery based on the LFP/C chemistry is studied in this thesis, this overview will focus mainly on the ageing mechanisms encountered on Li-ion batteries with graphite-based anodes.

Li-ion batteries are ageing both during use and during storage; ageing during storage is affecting the calendar lifetime of the battery and ageing during use is affecting the cycling lifetime of the battery. Generally, these two ageing dimensions are considered additive by most researchers, but interactions between them might definitely occur [125]. Furthermore, either during storage or during cycling, the ageing of Li-ion batteries causes changes:

- at the electrode-electrolyte interface and in the electrolyte;
- of the active materials;
- of the composite electrode (active materials, current collector etc.) [124].

However, changes at the electrode-electrolyte interface, which are caused by the side reactions of the electrodes (especially the lithiated carbon electrode) with the electrolyte, are considered to be the major source for ageing of the Li-ion batteries based on graphite anodes [125], [124], [127].

4.1.1 Ageing during storage

Li-ion batteries' ageing during storage is caused by side reactions, which are resulting from the thermodynamic instability of the materials [125]. The thermodynamic stability of the negative electrode is the most critical since the graphite is not electrochemically stable when used together with most types of electrolytes [125], [126].

While, the Li-ion battery cell is charged for the first time, lithium reacts directly with the graphite and forms a thin solid surface, known as solid electrolyte interface (SEI) [124], [125], [128]. This initial process causes an irreversible capacity loss [126]. The SEI has the unique property of being permeable for lithium ions, but in the same time impermeable for electrons and other electrolyte components, which are susceptible

of reduction [125]. Moreover, according to Vetter *et al.*, the SEI protects the electrolyte compounds from further reduction and the charged electrodes from corrosion [124]. However, the SEI is usually not 100% hermetic and thus a reaction of the electrolyte with the graphite anode leading to corrosion is observed [48], [125]. Further SEI formation leads to increase of the battery cell impedance and loss of capacity [126], [124].

During storage, ageing of the Li-ion batteries at the positive electrode is observed as well. The main ageing factor is the oxidation of the positive electrode against the electrolyte, which is mainly enhanced by high temperature and high SOC levels [48], [125]. Furthermore, storage at high temperature and high SOC-levels may cause gas evolution in the Li-ion batteries [124].

The calendar ageing of Li-ion batteries is mainly enhanced by high temperature and high SOC-levels, which are causing both capacity fade and power capability decrease as presented in [32], [125], [129].

4.1.2 Ageing during cycling

Ageing during cycling of the Li-ion batteries is assigned to the kinetic induced effects, such as volume variations and/or concentration gradients [125]. Similar to ageing during storage case, ageing of the Li-ion batteries during cycling is observed at both electrodes, which are expanding and shrinking during charging-discharging [48].

At the positive electrode, ageing during cycling is described as the result of the degradation of active materials reversibility, which is caused by the phase transformation during lithium insertion [125]. Moreover, the insertion and extraction of lithium ions lead to changes in the volume of the materials, which will induce mechanical stress to the electrode [124]. Mechanical stresses are also the result of phase transitions, which can occur at the positive electrode, leading to partcile cracking and gas formations [124], [126].

At the negative electrode, lithium plating is one of the main ageing mechanism observed during the cycling process of Li-ion batteries [125]. This ageing mechanism can be explained by the progressive clogging of the micropores of the anode by the passivation layer growth. This will cause the capacity fade of the Li-ion battery, which is accelerated by low temperature and high current rates (C-rates) [125], [124]. Consequently, the electrode porosity is considered as one of the parameters that are controlling the capacity fade of the cell during cycling [125].

Moreover, at the anode side, volume changes of the carbon material while cycling will lead to the partial degradation of the SEI layer, which will be immediately restored; however, during the restoration process, available lithium will be consumed [125].

The cycling ageing of Li-ion batteries is mainly influenced by the temperature, the

Table 4.1: *Ageing mechanisms of graphite based Li-ion batteries [124], [125].*

Ageing Mechanism	Effect	Enhanced by
Electrolyte decomposition → SEI formation and growth	Capacity Fade Power Decrease	high temperature high SOC
Conductor corrosion	Power Decrease	low SOC, over-discharging
Lithium plating	Capacity Fade Power Decrease	low temperature, high C-rate
Decrease of active surface area	Power Decrease	high temperature, high SOC
Changes in electrode porosity due to volume change	Power Decrease	high C-rate, high SOC
Solvent co-intercalation, gassing → graphite cracking	Capacity Fade	over-charge
Volume changes during cycling → contact loss of active materials particles	Capacity Fade	high C-rate, high cycle depth
Binder decomposition	Capacity Fade	high SOC , high temperature

SOC level, the cycle depth and the charging/discharging C-rate and high SOC-levels, which are causing both capacity fade and power capability decrease as presented in [125], [130], [131].

Both during cycling and storage, the rate of the capacity fade of the Li-ion batteries decreases while the ageing process evolves. This phenomenon is caused by the consolidation of the SEI layer, which produces a more stable interface and thus reduces the corrosion rate [125]. Furthermore, the decrease of the power capability is directly related with the Li-ion battery cells' impedance growth [124], [125], [126].

Table 4.1 summarizes the most common ageing mechanisms encountered in Li-ion battery cells based on graphite anodes; the stress factors enhancing the ageing mechanisms and their effects on the performance of the Li-ion battery cells are presented as well. Since, ageing mechanisms encountered at the cathode side of Li-ion batteries depend greatly on the cathode chemistry [124], they are not summarized in this table.

The ageing of Li-ion battery originates from various complex mechanisms, which are caused both by cycling and/or storage conditions. The battery ageing results mainly in capacity fade, impedance increase and subsequently power capability decrease, and changes of te AC impedance spectrum [32], [124]. Even though the SEI formation and

growth is the most important ageing mechanism of Li-ion batteries based on graphite anodes, the overall ageing behaviour of the cell is determined by the chemistry of the cathode and its reactivity [125].

The ageing of the selected LFP/C battery cell during cycling and storage will be investigated in Chapter 5 and its effect on the capacity, power capability and AC impedance spectrum will be discussed in detail. However, due to limited resources, the correlation between the LFP/C battery cell parameters' degradation and the corresponding ageing mechanisms was not determined.

4.2 Overview of Li-ion Battery Lifetime Modelling

Accurate lifetime prediction of Li-ion batteries is of high importance from both economical and technical point of views. Li-ion batteries' lifetime models are required from the early planning step of the project because this parameters is of great importance for the economic calculations. Moreover, having accurate knowledge about the lifetime of various Li-ion batteries, allows for the selection of the most suitable battery for the targeted application [132].

As described in Chapter 4.1, the performance parameters (e.g. capacity and power capability) of the Li-ion batteries are degrading as the batteries are ageing. Therefore, accurate lifetime models that are able to predict the capacity fade and power capability decrease of the Li-ion batteries are necessary in order to allow for selection of the optimal EMS at every point during batteries' life. Furthermore, a precise lifetime prediction will allow for a reliable and optimal sizing of the Li-ion battery ESS [31]; this will further ensure project cost reduction. Last but not least, an accurate estimation of the Li-ion battery impedance increase during ageing allows for designing reliable cooling systems which will guarantee ESS lifetime optimization.

However, accurate estimation of the Li-ion batteries lifetime is not a straightforward process. As it was presented in Chapter 4.1, the degradation of Li-ion batteries performance parameters is a complex process, influenced by many ageing mechanisms, which are enhanced by different operating conditions (stress factors). Thus, lifetime estimation of the Li-ion battery has to consider the operating conditions imposed by the application, which most of the time lead to a combination of stress factors that usually do not induce one dominant ageing process [132]. This is also the case of Li-ion batteries used in VPP applications, which are working under complex cycling conditions, as presented in Fig. 4.1. Thus, in order to develop accurate lifetime models, Li-ion battery cells have to be tested in such a manner that the effect of possible interactions between different

stress factors on the ageing is minimized or eliminated. Nevertheless, according to Sauer *et al.* this fact is very difficult and often not possible [108].

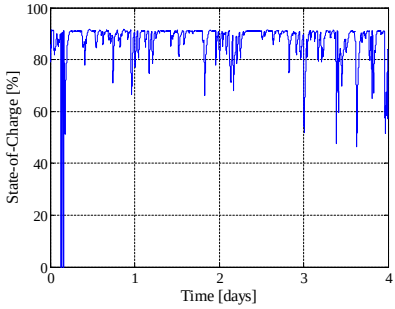

Figure 4.1: *SOC mission profile measured on a ESS-based on Li-ion batteries that is providing PFR service on the Danish energy market*

Lifetime estimation of Li-ion batteries can be realized by following different modelling approaches. The most common approaches presented in the literature are illustrated in Fig. 4.2 [39]; this modelling approaches are divided in two main categories, which will be briefly discussed in the following sections.

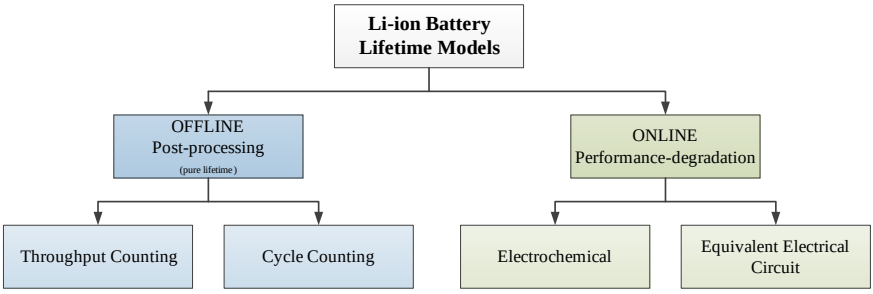

Figure 4.2: *Lifetime modelling approaches of Li-ion batteries*

4.2.1 Pure-lifetime models

The pure-lifetime models, also referred as post-processing models, are models, which provide information only about the remaining useful lifetime (RUL) of the batteries but no information about the degradation of the performance parameters [133]. These models are based on the concept of incremental loss of lifetime that is caused by the operating conditions. Depending on the considered stress factor, the pure-lifetime models can be divided in two sub-groups: cycle counting models and throughput counting models [39].

Cycle counting models

In this modelling approach, the considered stress factor is the cycle depth. The cycle counting models are based on the assumption that the magnitude of the cycle determines the fraction of the consumed battery cell life [133]. Thus, the higher the amplitude of the cycle depth, the more battery life is consumed and fewer cycles the battery can withstand until the EOL [39], [133]. The relation between the number of cycles that a Li-ion battery can withstand until it reaches the EOL criterion and the corresponding depth-of-discharge (DOD) is usually given as a lifetime curve as illustrated in Fig. 4.3.

In its basic format, the cycle counting lifetime modelling approach considers several simplifying assumptions [133]; however, the method can be improved, for example, by considering the effect of other stress factors such as temperature, C-rate etc. This becomes possible by assigning weighting factor, which will allow to take into consideration the effect on the lifetime curve of more demanding battery operating conditions (e.g. operation at high temperature or with a high C-rate) [39].

Nevertheless, despite considering several simplifying assumptions, cycle counting models are suitable for being used in planning tools (see [134]), where the simulation speed is preferred instead of detailed information about the degradation of various Li-ion battery parameters such as capacity or power capability.

One example of a cycle counting modelling approach, which is applicable to lifetime modelling of Li-ion battery cells is the rainflow cycle counting method [135].

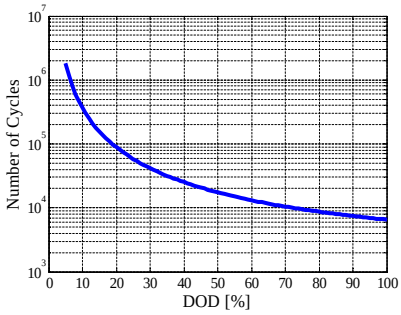

Figure 4.3: *Number of cycles vs. DOD lifetime curve (values only exemplary).*

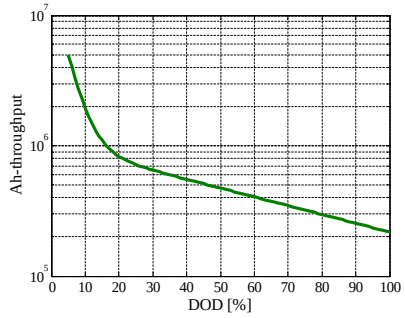

Figure 4.4: *Ah-Throughput vs. DOD lifetime curve (values only exemplary).*

Throughput counting models

The stress factor which is considered in this lifetime modelling approach is either the Ah-throughput or the Wh-throughput. These models are simply counting the amount of charge (Ah-throughput), or energy (Wh-throughput) passed through the battery and

are comparing these values to a predefined Ah(Wh)-throughput value that the battery cell can withstand until the EOL criterion is reached [108], [132]. The Li-ion battery is considered to have reached the EOL once the measured throughput exceeds the total allowable throughput of the battery. Based on the throughput counting modelling approach, the RUL of the Li-ion battery is computed according to the (4.1).

$$RUL_{Ah}[years] = \frac{Ah_{EOL}}{Ah_{year}} \tag{4.1}$$

where, RUL_{Ah} represents the RUL of the Li-ion battery cell computed based on the Ah-throughput counting method, Ah_{EOL} represents the EOL that the battery cell can withstand until the EOL, and Ah_{year} represents the Ah passed through the battery cell during one year of operation. Equation (4.1) assumes that each year causes the same degradation.

Similar to the cycle counting models, the throughput counting models are considering several simplifying assumptions [133]. First of all, the basic throughput counting models are assuming that during the use of the battery cell, the lifetime is reduced proportionally to the total Ah-throughput [132]. Moreover, the effect of the operating conditions (i.e. temperature, SOC-level, and C-rate) are not considered in simple throughput counting lifetime models [133].

If more accurate lifetime models are desired, weighting factors, which are considering the effect of other stress factors (e.g. operating temperature) on the lifetime, besides the influence of the Ah/Wh-throughput, might be applied [39], [133].

The EOL, in terms of Ah-throughput, for certain Li-ion battery DOD can be determined from the number of cycles vs. DOD lifetime curve (see Fig. 4.3) according to the formula:

$$Ah_{throughput}(DOD) = \int_{DOD=0}^{DOD=100} (Cycles(DOD) \cdot 2 \cdot DOD \cdot Cap) \tag{4.2}$$

where *Cycles(DOD)* represent the number of cycles which the battery can with stand at the corresponding DOD, and *Cap* represents the capacity of the battery cell.

Based on the number of cycles vs. DOD lifetime curve and considering (4.1), the lifetime curve showing the Ah-throughput that a Li-ion battery can withstand for a certain DOD until EOL, illustrated in Fig. 4.4, was obtained.

The main advantage of the pure-lifetime models is their very high computational speed, which makes them suitable for system design tools where a large number of systems have to be analysed in the same time [108], [133]. However, these models are

incapable to relate the degradation of the Li-ion battery cell with the corresponding ageing mechanisms [108].

4.2.2 Performance-degradation models

The performance-degradation lifetime models combine a performance model (see Chapter 3) with a lifetime model, where the performance values (e.g., capacity, power capability, voltage etc.) of the Li-ion battery cell are updated while the ageing processes evolve [132], [133]. These models are usually very accurate and are suitable for determining the technical and economical viability of a business case [132].

Depending on the approach, which is followed to develop the performance-degradation lifetime models, these models are divided in two sub-categories: electrochemical and EEC-based lifetime models.

Electrochemical models

The electrochemical lifetime models are basically describing the physical and electrochemical changes of the electrode and electrolyte during ageing [108], [132], [133].

Based on the electrochemical approach, the lifetime modelling of the Li-ion battery is performed by following a two steps procedure; during the first step, a battery performance model is built based on the fundamental equations of the electrochemical reactions, Ohm's law and diffusion processes of the reactants in the battery [108]. This model is able to estimate the state variable of the Li-ion batteries (e.g. local potential, local current density, temperature etc.) at every operating point as, already discussed in Chapter 3.1.1. In the second step, information about the ageing processes and their impact on the performance of the battery are added to the model [108], [132]. The electrochemical lifetime models are based on a set of differential equations, which describe the relationship between the operating conditions and the decrease of Li-ion battery cell performance during ageing [132].

Compared, to the pure-lifetime models, the electrochemical lifetime models are very accurate but at the same time more complex [108], [132]. As already discussed in Chapter 3.1.1, the parametrization of electrochemical lifetime models is rather difficult since many data about the physical and chemical properties of the Li-ion battery cell are required. Moreover, the design of experiment for performing the ageing tests is complex since it has to be assured that interactions between parallel ageing effects is minimized [108].

Besides the high accuracy, the electrochemical models have that advantage to provide a very detailed understanding of the ageing processes in the Li-ion battery and to study

in depth the interaction between the operating strategies and the ageing of the Li-ion battery [108]. However, this is at the expense of a reduced computation speed of the simulations.

Equivalent electrical circuit models

The second group of performance-degradation models are the EEC-based lifetime models. The characteristics, structure, and parametrization approach of an EEC-based model were presented throughout Chapter 3. The EEC-based lifetime models are obtained by adding the "ageing-dimension" to the EEC-based performance models; thus, in order to represent the ageing behaviour of the Li-ion battery cell, the values of the parameters of the EEC are updated while the ageing process evolves [39], [133]. In Fig. 4.5, a possible configuration of an EEC, which considers the dependence on the parameters on ageing is presented.

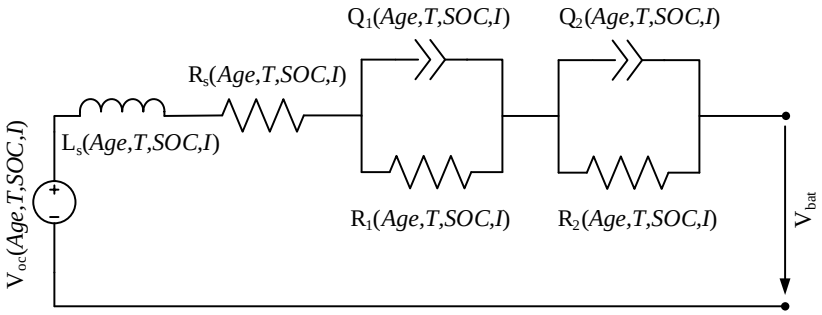

Figure 4.5: *Schematic representation of EEC configuration for lifetime modelling of Li-ion battery cells considering the dependence of EEC parameters on the operating conditions.*

Apart from being able to estimate the variation of the EEC parameters during ageing and consequently to predict the voltage behaviour of the battery cell at every operating point during its life, the EEC-based lifetime models offer information about the capacity fade and power capability decrease of the Li-ion battery as well.

The EEC-based lifetime models, are generally able to provide accurate results about the degradation of the Li-ion battery cell performance parameters (i.e. capacity, power capability, and voltage). The parametrization of such models is based on extended laboratory ageing tests; however, in contrast with the electrochemical lifetime models, they do not require detailed information about the physical and chemical properties of the battery cell [48].

4.2.3 Comparison of lifetime modelling approaches

The presented lifetime modelling approaches differ in complexity, input requirements and output parameters. Thus, in order to compare them, Table 4.2 summarizes the most important characteristics of the discussed lifetime modelling approaches.

Table 4.2: *Comparison of different lifetime modelling approaches for Li-ion battery cells*

Condition	**Lifetime Modelling Approach**			
	Cycle Counting	*Ah/Wh-throughput*	*Electrochemical*	*EEC*
Complexity	Reduced	Reduced	High	Medium
Computation Time	Reduced	Reduced	High	Medium
Accuracy	Medium	Reduced	Very High	High
Parametrization	Data-sheet	Data-sheet	Complex lab. measurements	Laboratory measurements
Output	RUL	RUL	RUL, SOH, voltage	RUL, SOH, voltage
Transfer to other chemistry	No	No	Yes	No

By analysing the properties of the lifetime modelling approaches, which are presented in Table 4.2 one can conclude that the EEC-based lifetime models are a trade-off solution between the electrochemical and pure-lifetime models. Even though their accuracy is slightly lower than the one of the electrochemical models, the EEC-based lifetime models are easier to parametrize and are able to estimate the lifetime of the Li-ion batteries in terms of capacity fade and power capability decrease. The pure-lifetime models are not of interest for this research since their accuracy is reduced and they offer limited information (only RUL) about the ageing behaviour of the tested battery.

Consequently, in this thesis an EEC-based lifetime modelling approach was selected for developing the lifetime model of the tested LFP/C battery cell.

4.3 Summary

This chapter has presented a brief overview of the ageing mechanisms and lifetime modelling approaches of Li-ion battery cells.

The most common ageing mechanisms for graphite-based were presented. Since Li-ion batteries are ageing both during cycling and storage, the ageing mechanisms for the two dimensions were discussed separately.

Four different approaches for lifetime modelling of Li-ion battery cells were presented and their characteristics were discussed. Because of its characteristics which includes predicting the capacity fade, power capability decrease, and voltage behaviour of Li-ion battery cells with high accuracy, the EEC-based lifetime modelling approach was selected for developing the lifetime models for the tested LFP/C battery cell.

Next chapter presents the results obtained from laboratory performed accelerated ageing tests, which are used to parametrize the EEC-based lifetime model of the LFP/C battery cell.

Chapter 5

Accelerated Ageing Testing of $LiFePO_4$/C Battery Cell

This chapter presents the methodology, which was followed for testing the LFP/C battery cells in accelerated manner. At the beginning of the chapter, the procedures and conditions used for performing the accelerated calendar and cycling lifetime tests are introduced. In the second part of the chapter, the procedure (RPT) that was used periodically for measuring the decrease of battery cell performance parameters is introduced. The last section of the chapter discusses other practical aspects regarding the performed lifetime tests.

5.1 Introduction

In order to develop and parametrize an accurate EEC-based lifetime model for the LFP/C battery cells, laboratory ageing tests are necessary. However, ageing the LFP/C battery cells at real operating conditions (mainly temperatures close to 25^oC for stationary applications [42]) are extremely time and cost demanding since the lifetime of present Li-ion batteries is in the range of years [34]. Thus, in this thesis, accelerated ageing tests were performed and the obtained data were used to develop accurate models, which are able to estimate the lifetime of the tested LFP/C battery cells at the normal operating conditions.

The main stress factor used to accelerate the ageing of the tested LFP/C battery cells was the temperature. As shown by Swierczynski *et al.* in [42], the normal operating temperature of LFP/C-based ESSs operating in VPP applications is in the range of 25^oC. Thus, in order to accelerate the ageing of the battery cells, during the laboratory tests,

temperatures higher than $25^{o}C$ have been used, as shown in Chapter 5.2 and in Chapter 5.3; testing the LFP/C battery cells at temperatures values below the normal operating temperature (of the considered application) was of no interest.

Because, Li-ion batteries operating in VPP applications are subjected to complex charge/discharge cycling conditions, the LFP/C battery cells had to be tested considering a wide variety of stress factors (e.g. temperature, cycle depth, SOC-level). This will further allow to develop accurate models that are able to predict the lifetime of the LFP/C battery cells independent on the considered operating conditions.

Usually, independent on the stress factor, the stress levels have a non-linear effect on the degradation of the Li-ion battery cells. Consequently, in order to be able to interpolate between the considered stress levels and to extrapolate to the normal operating stress level, at least three stress levels have to be considered for each stress factor, as illustrated in Fig. 5.1.

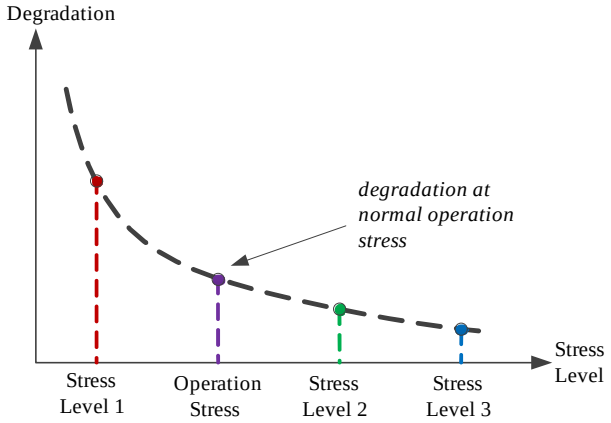

Figure 5.1: *Hypothetical dependence of Li-ion battery cell degradation on the applied stress levels and extrapolation to the normal operating conditions.*

Nevertheless, the stress level values for each stress factors should be selected after analysing the stress levels, which are encountered during the normal operation of the tested battery cell, in order to avoid irrelevant degradation mechanisms [48]. Furthermore, from the same considerations, the selected values for the stress levels should be kept below the maximum values allowed by the manufacturers; as a rule of thumb, a 5% window should be considered between the selected stress level values for performing the accelerated ageing tests and the maximum stress levels, which are given in the data-sheet of the battery cell.

Since the operation of batteries in VPP applications involves both periods when the

Li-ion batteries are idling and periods when they are cycled, both ageing dimensions should be considered when performing the laboratory tests. Thus, LFP/C battery cells were tested in accelerated manner considering both calendar ageing conditions and cycling ageing conditions. To quantify the incremental degradation of the LFP/C battery cells, which was caused by the different considered ageing conditions, the performance parameters (e.g. capacity, power capability etc.) of the cells were periodically checked during all the accelerated lifetime tests; the procedure used to measure the performance parameters is presented in detail in Chapter 5.4.

The conditions for the accelerated calendar ageing tests and for the accelerated cycling ageing tests are discussed in Chapter 5.2 and Chapter 5.3, respectively. All the results obtained from the accelerated ageing tests are presented in detail throughout Chapter 6 for the calendar ageing dimension and throughout Chapter 7 for the cycling ageing dimension.

5.2 Accelerated calendar lifetime tests

Accelerated calendar lifetime tests were used to determine the ageing behaviour of the LFP/C battery cells during idling (stand-by) conditions. As it was presented in Chapter 4.1.1, the calendar lifetime of the Li-ion batteries is influenced by the storage temperature and by the SOC-level. In order to determine the effect of these stress factors, and their possible interactions, on the performance degradation of the LFP/C battery cells a minimum of nine test cases (TCs) should be performed, as presented in Fig. 5.2. In the proposed testing matrix, three stress levels were considered for each stress factor in order to take into account the non-linear effect of the stress factors on the lifetime of the tested battery; thus a total of nine possible combinations between stress factors can be considered.

However, because of different limitations in terms of available battery cells and testing resources, the possible interaction between the two stress factors were disregarded. Thus, only the main contribution from each stress factor on the degradation of the LFP/C battery cell will be considered when developing different lifetime models. Consequently, the complex test matrix illustrated in Fig. 5.2 was reduced to a five TCs matrix, which is presented in Fig. 5.3.

The details of the accelerated lifetime testing conditions for each of the five TCs, which were illustrated in Fig. 5.3, are summarized in Table 5.1.

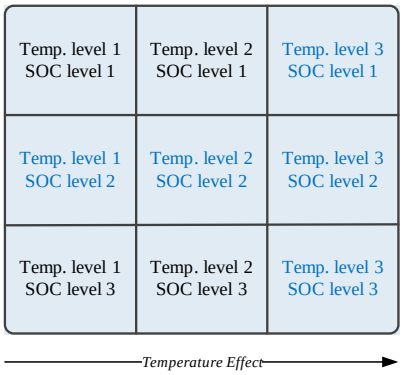

Figure 5.2: *Complex test matrix for determining the calendar lifetime of the LFP/C battery cells (temperature and SOC-level ageing stress factors).*

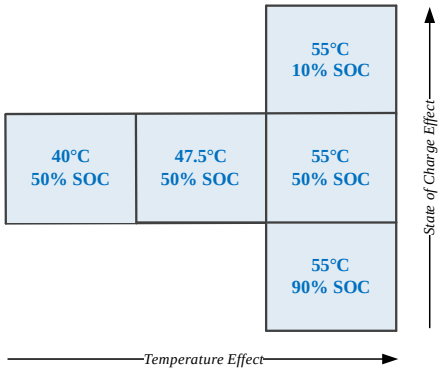

Figure 5.3: *Reduced test matrix for determining the calendar lifetime of the LFP/C battery cells (possible interaction between stress factors is not considered).*

Table 5.1: *Accelerated calendar lifetime tests - testing conditions.*

Test case	LFP/C cells	Stress factors/levels		Performance check
		Temperature	SOC	
Calendar 1	C.1, C.2, C.3	55^oC	50%	1 month
Calendar 2	C.4, C.5, C.6	47.55^oC	50%	
Calendar 3	C.7, C.8, C.9	40^oC	50%	
Calendar 4	C.10, C.11, C.12	55^oC	10%	
Calendar 5	C.13, C.14, C.15	55^oC	90%	

During all the accelerated calendar ageing TCs, the LFP/C battery cells were stored at open-circuit conditions, as illustrated in Fig. 5.4, in various industrial ovens; a description of the testing equipment used for the accelerated calendar lifetime tests is given in Appendix B. Since the battery cells were stored at open circuit conditions (no equalizing charge to maintain the SOC was applied), it has been possible to determine their self-discharge and the dependence of the self-discharge on the storage conditions (see Chapter 6).

In order to quantify the degradation of the tested LFP/C battery cells caused by the various ageing conditions, check-ups of the performance parameters were performed at the cells' BOL and periodically thereafter at intervals of one month (30 days). The results obtained from all the accelerated calendar lifetime tests are discussed in Chapter 6.

Figure 5.4: *LFP/C battery cells stored in oven during one of the accelerated calendar lifetime tests.*

5.3 Accelerated cycling lifetime tests

Accelerated cycling lifetime tests were performed in order to determine the lifetime of the LFP/C battery cells for cycling at different conditions. As shown in Chapter 4.1.2, the stress factors, which are influencing the cycling lifetime of the Li-ion batteries are: the temperature, the cycle depth, the SOC-level, and the charging/discharging C-rate. However, all the accelerated cycling TC were performed considering a C-rate equal to 4C ($10A$), which can be treated as a worst case scenario for these battery cells (4C-rate is the maximum continuous charging current, which the battery can withstand - see Appendix A).

If three stress factors are considered for each of the three remaining stress levels (i.e. temperature, cycle depth, and SOC-level) and if the possible interactions between stress factors are considered, a complex test matrix composed of 27 TCs could be developed, as shown in 5.5. However, because of the same considerations, which were exposed in 5.2 when the calendar ageing test matrix was developed, the possible interactions between the three stress factors affecting the cycling lifetime of the LFP/C battery cells were disregarded. Consequently, by taking into account only the main contribution of each of the three stress factors on the lifetime of the tested battery cells, the initial test matrix was reduced to a matrix composed of only seven TCs as illustrated in 5.6.

The detailed testing conditions to which the LFP/C battery cells were subjected in order to determine their cycling lifetime are summarized in Table 5.2.

During each of the considered accelerated cycling lifetime tests, the LFP/C battery cells were placed in temperature controlled chambers in order to allow stable temper-

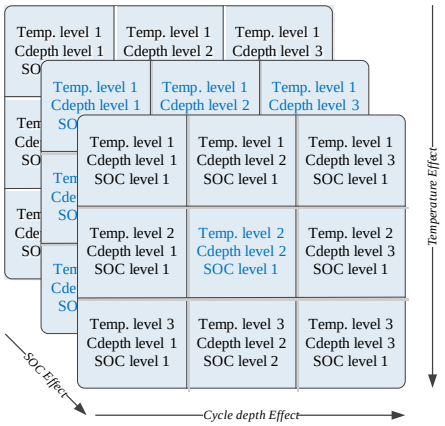

Figure 5.5: *Complex test matrix for determining the cycle lifetime of the LFP/C battery cells (temperature, cycle depth, and SOC-level ageing stress factors).*

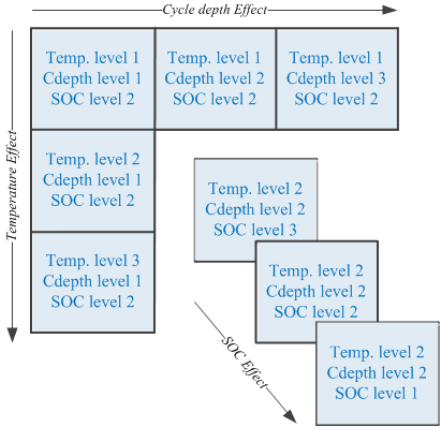

Figure 5.6: *Reduced test matrix for determining the cycle lifetime of the LFP/C battery cells (possible interaction between stress factors is not considered).*

ature during the tests. Moreover, the temperature values summarized in Table 5.2 refer to the average temperature measured on the battery cell during cycling and not to the ambient temperature inside the various temperature chambers. The SOC parameter mentioned in Table 5.2 refers to the average SOC of the LFP/C battery cell during charging-discharging cycles; for exemplification, Fig. 5.7 illustrates the cycling process with different cycle depths considering the average SOC-value equal to 50%.

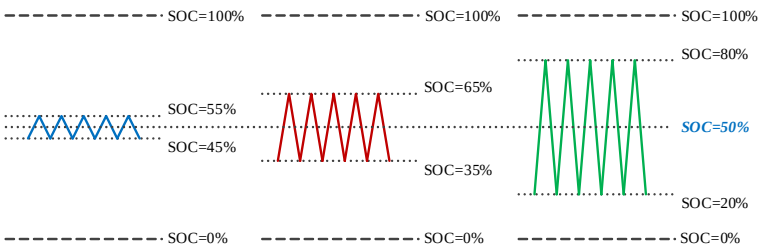

Figure 5.7: *Charging/discharging cycles of three different cycle depths, considering an 50% average SOC.*

Fig. 5.8 presents three LFP/C battery cells connected in series while subjected to one of the considered accelerated cycling lifetime tests. The voltage and temperature of each cell were monitored separately, as shown in Fig. 5.8. A description of the battery test stations, which were used for carrying out the accelerated cycling lifetime tests is given in Appendix B.

Similar to the case of the accelerated calendar lifetime tests, in order to quantify the degradation of the tested LFP/C battery cells caused by the various cycling ageing

Table 5.2: *Accelerated cycling lifetime tests - testing conditions (for all considerd TCs, the charging/discharging C-rate is 4C).*

Test case	LFP/C cells	Stress factors/levels			Performance check
		Temp.	Cycle depth	SOC	
TC 1	3.7, 3.8, 3.9	50^oC	10%	50%	each 3250 cycles
TC 2	3.4, 3.5, 3.6	50^oC	35%	50%	each 950 cycles
TC 3	3.1, 3.2, 3.3	50^oC	60%	50%	each 550 cycles
TC 5	3.22, 3.23, 3.24	42.5^oC	35%	50%	each 950 cycles
TC 6	3.10, 3.11, 3.12	42.5^oC	60%	50%	each 550 cycles
TC 9	3.13, 3.14, 3.15	35^oC	60%	50%	each 550 cycles
TC 10	3.32, 3.35, 3.36	42.5^oC	35%	27.5%	each 950 cycles
TC 11	3.37, 3.38, 3.39	42.5^oC	35%	72.5%	each 950 cycles

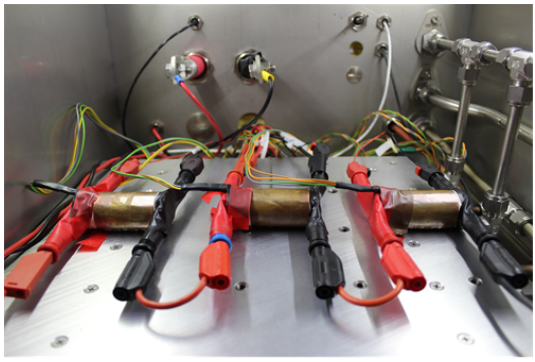

Figure 5.8: *LFP/C battery cells placed in a temperature chamber during one of the accelerated cycling lifetime tests.*

conditions, check-ups of the performance parameters were performed at the cells' BOL and periodically thereafter at various intervals, as mentioned in Table 5.2. The results obtained from all the accelerated cycling lifetime tests are discussed in Chapter 7.

5.4 Reference performance tests

In order to measure and quantify the incremental degradation of the performance parameters of the LFP/C battery cells, which were subjected to different accelerated ageing tests (see Fig. 5.3 and Fig. 5.6), periodical check-ups of the batteries were performed. All the periodical check-ups, further referred as reference performance tests (RPTs), have been performed at 25^oC and at predefined time intervals (certain number of cycles for

cycling TCs - see Table 5.2 and one month for calendar TCs) during the lifetime tests. Moreover, before starting each TCs from the proposed matrixes, moment which corresponds to the cells' BOL, an initial RPT was carried out for each individual LFP/C battery cell.

The RPT procedure, designed to measure the specific battery cell parameters, which are changing with the age, was composed of the following tests: capacity measurements, internal resistance measurements, and EIS measurements.

The capacity measurements were used to determine the capacity of the LFP/C battery cells during charging and discharging with 1C- and 4C-rate.

The internal resistance measurements were used for determining the charge and discharge DC internal resistance of the LFP/C battery cell at three SOC-levels (i.e. 20%, 50%, 80%) for current pulses of various amplitudes. The current pulse profile applied to the battery cells, at each considered SOC, is presented in Fig. 5.9; the length of each current pulse (independent on the amplitude) was 18 seconds and the relaxation interval between two consecutive pulses was 15 minutes. Furthermore, based on the obtained internal resistance values for current pulses of 4C (i.e., $10A$), the pulse power capability of the LFP/C battery cells was computed according to (3.6) and (3.7).

The EIS measurements were used to determine the small-signal AC impedance characteristic of the LFP/C battery cells at the same SOC-levels as the ones used to measure the cells' internal resistance. All the EIS measurements have been performed for the following test conditions:

- *Frequency Range* : 10 kHz - 10 mHz;
- *Points per decade* : 8 points/decade;
- *Measurement Time* : 4 seconds;
- *Measurement Periods* : 2.

Figure 5.10 shows and example of current and voltage profiles measured on one LFP/C battery cell during the RPT.
This profile is characteristic to all the battery cells, which are subjected to accelerated cycling lifetime tests. The profiles are divided in 25 sections which are described in the followings:

1. Initial full discharge of the battery cell, with 1C-rate current, until the end of discharge voltage (i.e. 2 V) is reached;
2. Relaxation of the battery cell for 15 minutes;

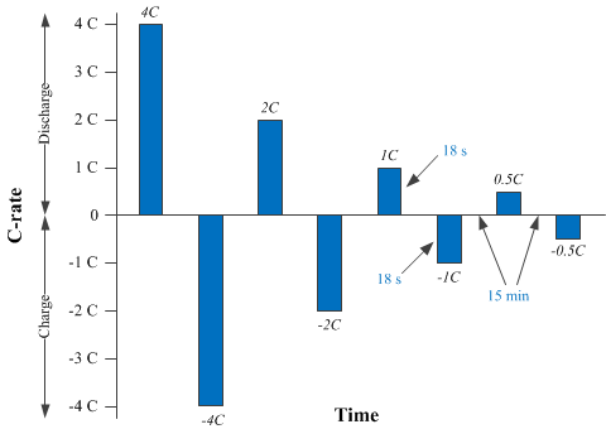

Figure 5.9: *Current pulse profile applied to measure the internal resistance of the LFP/C battery cell at each performed RPT.*

3. Full charging of the LFP/C battery cell following a constant current - constant voltage pattern by applying a 1C-rate current and maximum cell voltage (i.e, 3.6V); the charging process is considered finished when a cut-off current equal to 4% of the nominal battery cell capacity is reached;

4. Relaxation of the battery cell for 15 minutes;

5. Full discharging of the LFP/C battery cell by applying 1C-rate current; the discharging process is considered finished when a cut-off voltage equal to 2V is reached;

6. Relaxation of the battery cell for 15 minutes;

7. Full charging of the LFP/C battery cell following a constant current - constant voltage pattern by applying a 4C-rate current and maximum cell voltage (i.e, 3.6V); the charging process is considered finished when a cut-off current equal to 4% of the nominal battery cell capacity is reached;

8. Relaxation of the battery cell for 15 minutes;

9. Full discharging of the LFP/C battery cell by applying 4C-rate current; the discharging process is considered finished when a cut-off voltage equal to 2V is reached;

10. Relaxation of the battery cell for 15 minutes;

11. Charging of the LFP/C battery cell with 1C-rate current to SOC=20%;

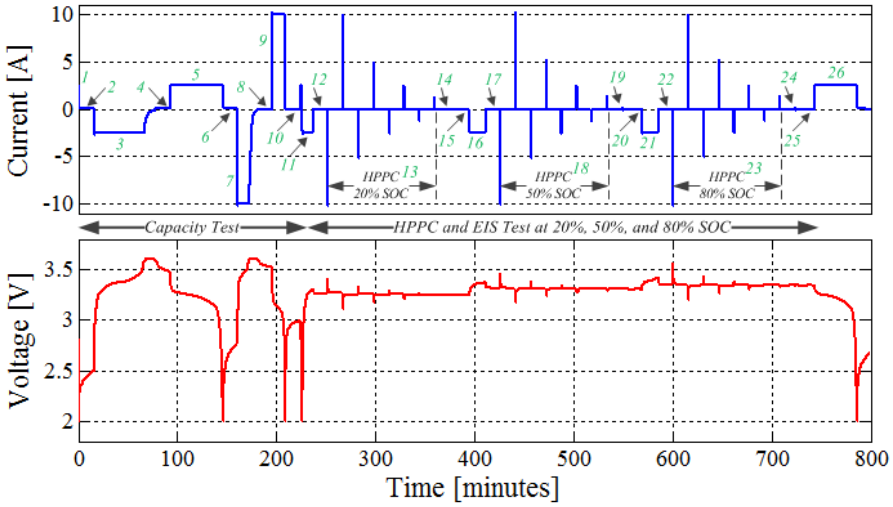

Figure 5.10: *Current (top) and voltage (bottom) profiles measured on the LFP/C battery cells during the RPT.*

12. Relaxation of the battery cell for 15 minutes;
13. Measurement of the internal resistance of the LFP/C battery cell at 20% SOC by applying the profile illustrated in Fig. 5.9;
14. Relaxation of the battery cell for 15 minutes;
15. Measurement of the impedance spectrum (Nyquist curve) of the LFP/C battery cell at 20% SOC;
16. Charging of the LFP/C battery cell with 1C-rate current to SOC=50%;
17. Relaxation of the battery cell for 15 minutes;
18. Measurement of the internal resistance of the LFP/C battery cell at 50% SOC by applying the profile illustrated in Fig. 5.9;
19. Relaxation of the battery cell for 15 minutes;
20. Measurement of the impedance spectrum (Nyquist curve) of the LFP/C battery cell at 50% SOC;
21. Charging of the LFP/C battery cell with 1C-rate current to SOC=80%;
22. Relaxation of the battery cell for 15 minutes;

23. Measurement of the internal resistance of the LFP/C battery cell at 80% SOC by applying the profile illustrated in Fig. 5.9;

24. Relaxation of the battery cell for 15 minutes;

25. Measurement of the impedance spectrum (Nyquist curve) of the LFP/C battery cell at 80% SOC;

26. Full discharging of the LFP/C battery cell by applying 1C-rate current - in order to for the prepare the cell for a new sequence of accelerated cycling ageing.

It has to be stressed that in order to allow for thermodynamic stabilization of the LFP/C battery cells, after being removed from the accelerated ageing test (carried out at high temperatures) and before starting the RPT procedure, the cells are tempered at 25^{o}C for a period of at least four hours. Furthermore, the 15 minutes pause period, considered between different steps of the RPT procedure, was determined during the characterization test (see Chapter 3.2.1) to be enough for the LFP/C battery cells to achieve stability.

To ensure that reliable and comparable results are measured during the periodical check-ups, the same RPT procedure was applied to all the tested battery cells, without any exception.

5.5 Procedure for accelerated lifetime tests

Most of the times, the manufacturing process of Li-ion battery cells is not perfect and thus the produced cells show a certain tolerance. Consequently, certain variations of the performance parameters of the Li-ion battery cells will be observed. This is also the case of the tested LFP/C battery cells, which were showing variations of their capacity and internal resistance values at the BOL. The variation of the discharge capacity values and internal resistance values measured for a population of 42 LFP/C cells at the cells' BOL is presented in Fig. 5.11 and Fig. 5.12, respectively.

These differences in various parameters of the Li-ion batteries, which are visible since their BOL, will result in slightly different moments when the battery cells will reach the EOL. Therefore, it is recommended to describe the degradation of the performance parameters not as a singular point, but using a probability density function [48]. However, because developing lifetime models based on probability density functions is a complex process, which requires a high number of battery cells and testing equipment, in this work a simplified approach was followed. Three LFP/C battery cells were tested for each of

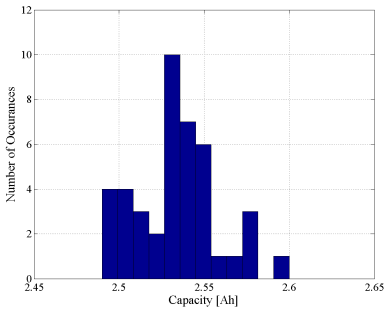

Figure 5.11: *Distribution of the discharge capacity values measured at the BOL of the LFP/C battery cells (T=25°C, I=2.5A).*

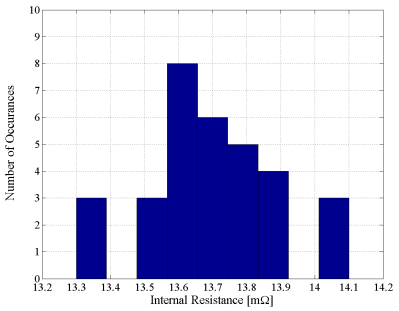

Figure 5.12: *Distribution of the internal resistance values measured at the BOL of the LFP/C battery cells (T=25°C, I=10A, SOC=50%).*

the considered calendar and cycling ageing TCs and the average value of the performance parameters of interest were used for developing the desired lifetime models. Moreover, considering three cells per TCs has allowed to eliminate altered results obtained from testing possible outliers.

All the accelerated calendar and cycling lifetime tests have been performed until the subjected LFP/C battery cells reached their EOL. The EOL was related to the decrease of the discharge capacity of the tested LFP/C cells, measured with 1C-rate at 25°C. Thus, each considered lifetime test was stopped when the capacity values of the three battery cells from that TC went below 80% of their initial measured capacity at BOL (independently on the observed changes in the other parameters). The 20% capacity fade EOL-criterion was selected arbitrary and was not constraint by the battery cell manufacturer or by the VPP requirements.

Due to the limitations imposed by the testing equipments, for most of the carried out accelerated cycling lifetime TCs, the cells were connected in series during the ageing test. Therefore, this limitation has allowed to apply the same Ah-throughput to all the LFP/C cells.

Generally, at macroscopic scale, the ageing of Li-ion batteries causes degradation of their performance parameters: capacity, internal resistance (and subsequently, power capability), and AC impedance [32], [129], [130], [131].

The upcoming chapters will presents the ageing results obtained for the tested LFP/C battery cells, which were caused by performing the accelerated calendar and cycle lifetime tests described in Chapter 5.2 and Chapter 5.3, respectively. The ageing results will be investigated in terms of capacity fade, pulse power capability decrease, and changes in the AC impedance characteristic of the LFP/C battery cells.

For both the calendar and cycling ageing dimensions, the influence of the considered stress factors (i.e. temperature, SOC-level, and cycle depth) on the performance parameters is investigated individually in the first phase. In the second phase, the individual effects of the stress factors on each of the studied performance parameters are merged into one figure of merit, referred as lifetime model.

Summary

This chapter has focused on the description of the accelerated ageing conditions to which the studied LFP/C battery cells were subjected.

During the first part, the procedure, which was followed for testing the LFP/C battery cells in accelerated manner was described in detail. Since the performance of the Li-ion batteries are degrading both during cycling and idling, the LFP/C battery cells were subjected to both accelerated calendar and cycling lifetime tests. The stress factors considered to influence the calendar lifetime of the tested battery cells were the storage temperature and storage SOC-level, while the stress factors considered to influence the cycling lifetime were the cycle depth, the temperature and the average SOC-level. Moreover, since all these stress factors have a non-linear effect on the degradation rate of the LFP/C battery cells, three stress levels were taken into consideration for each stress factor; thus, a reliable extrapolation and interpolation between the testing conditions was possible. Based on the aforementioned things, two test matrices have been built for determining separately the calendar and cycle lifetime of the tested LFP/C battery cells. Because of different limitations, the initial matrices were reduced and possible effects on the cells' lifetime caused by interactions between stress factors were neglected.

The structure of the RPT procedure, which was used for measuring the incremental degradation of the performance parameters of the tested LFP/C battery cells during calendar and cycling ageing, was presented in detail.

Chapter 6

Calendar Ageing Results for the $LiFePO_4$/C Battery Cell

This chapter presents the results obtained from the accelerated calendar lifetime tests, which were performed at different conditions, as discussed in the previous chapter. The effect of different stress factors on the degradation of the LFP/C battery cells' performance parameters is quantified. Based on the obtained ageing results, lifetime models, which are able to estimate the capacity fade, power capability decrease, and changes of the EEC parameters were developed and are introduced in this section.. Moreover, since all the calendar ageing tests were carried out with the battery-cells at open-circuit condition, information about the self-discharge of the LFP/C battery cells were gathered and the dependence of this parameter on ageing conditions is analysed, as well.

6.1 Introduction

The accelerated calendar ageing tests have been performed according to the conditions illustrated in Fig. 5.3 with the final goal of determining the lifetime of the LFP/C battery cells at various storage conditions. The incremental degradation of the investigated performance parameters was quantified by following the procedure presented in Fig. 6.1

All the accelerated calender lifetime tests were intended to be run until the cells would have reached the predefined EOL criterion (i.e., 20% capacity fade). However, due to the slow ageing process during storage, only one of the considered TCs (i.e. *Calendar 1*) has reached EOL; for the other calendar TCs, the capacity fade characteristic has been extrapolated until the EOL criterion was reached.

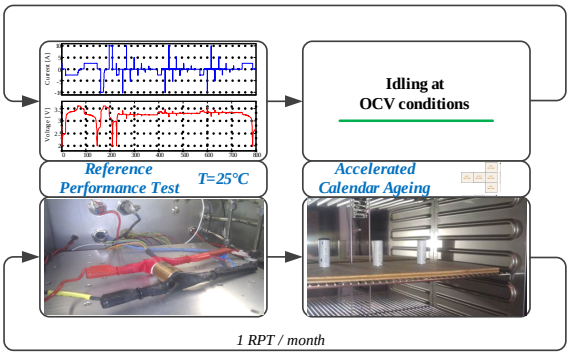

Figure 6.1: *Procedure for determining the degradation of the LFP/C battery cell's performance parameters during storage at various conditions.*

6.2 Capacity fade

The capacity of the LFP/C battery cells were measured during the RPTs for both charging and discharging conditions with 1C-rate and 4C-rate; nevertheless, in this work, for analysing the degradation behaviour of this parameter, only the measurements carried out during discharging with 1C-rate current (2.5 A) will be considered. The measured capacity fade as function of the battery cell voltage is presented in Fig. 6.2 for one of the performed accelerated calendar lifetime tests. As illustrated, the shape of the discharging voltage curve did not change, while the calendar ageing process of the LFP/C battery cells has evolved.

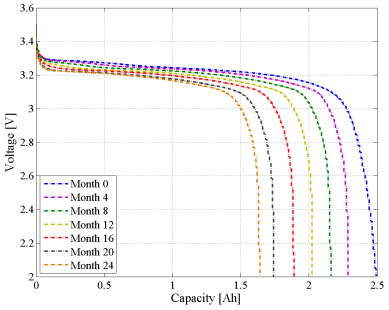

Figure 6.2: *Exemplification of the effect of the accelerated calendar ageing on the discharging voltage profile of the studied LFP/C battery cells (calendar ageing: T=55°C, SOC=50%; RPT: T=25°C, I=2.5A).*

The capacity values of the LFP/C battery cells, measured during consecutive RPTs throughout the accelerated calendar lifetime tests are presented in Appendix E for all the five TCs (see Fig. E.1, Fig. E.3, Fig. E.5, Fig. E.7 and Fig. E.9). The decrease of

capacity for each individual cell and the obtained average capacity decrease were plotted in the same graph.

The capacity fade of the LFP/C battery cells was computed according to (6.1) and the results are presented in Appendix E for all the five calendar TCs (see Fig. E.2, Fig. E.4, Fig. E.6, Fig. E.8, and Fig. E.10).

$$C_{fade}[\%] = \frac{C_{BOL} - C_{present}}{C_{BOL}} \cdot 100 \tag{6.1}$$

where, C_{fade} represents the capacity fade of the battery cell (expressed in per cent), C_{BOL} represents the capacity of the battery cell measured at the BOL (expressed in *Ah*), and $C_{present}$ represents the capacity of the battery measured after each RPT (expressed in *Ah*).

In order to analyze the capacity fade behaviour of the tested LFP/C battery cells, a two steps fitting process was followed. In the first step, the dependence of the capacity fade on the storage time for each considered TC was fitted, while in the second step, the dependence of the capacity fade on the storage temperature and SOC-level was obtained.

All the fitting processes presented in this chapter were performed using the *Curve Fitting Toolbox* from MATLAB considering a nonlinear least squares method [136]. The quality of the fitting was evaluated using the coefficient of determination R^2, which is calculated as given in (6.2); a R^2 value closer to 1 indicates a better fit.

$$R^2 = 1 - \frac{SS_{res}}{SS_{tot}} = \frac{\sum_{i=1}^{n}(y_i - f_i)^2}{\sum_{i=1}^{n}(y_i - \bar{y})^2} \tag{6.2}$$

where, SS_{res} - sum of squares of residuals, describes the deviation between the measured points and fitted curve and SS_{tot} - total sum of squares, describes the deviation between the measured points and their average value.

6.2.1 Dependence on storage time

The fitting of the capacity fade as function of the storage time was realized for the average capacity fade values, which were obtained separately for each TC; by average capacity fade values it is meant the capacity fade obtained for the average value of the capacity between the three cells from the same TC. Five different functions have been initially evaluated for fitting the capacity fade measured on the LFP/C battery cells during calendar ageing; the fitting results are presented in Fig. E.11 (see Appendix E.1.2). Based on

Table 6.1: *Dependence of the capacity fade on the storage time. Fitting functions and accuracy*

Test Case	Fitting Function	R^2
Calendar 1	$C_{fade-Cal1}(t) = 2.6110 \cdot t^{0.8}$	0.9978
Calendar 2	$C_{fade-Cal2}(t) = 1.4150 \cdot t^{0.8}$	0.9959
Calendar 3	$C_{fade-Cal3}(t) = 0.7449 \cdot t^{0.8}$	0.9862
Calendar 4	$C_{fade-Cal4}(t) = 1.6000 \cdot t^{0.8}$	0.9903
Calendar 5	$C_{fade-Cal5}(t) = 3.0820 \cdot t^{0.8}$	0.8904

the performed comparison, the power law defined in (6.3) was selected for fitting the measured capacity fade characteristics obtained for the LFP/C battery cells.

$$C_{fade}(t) = a_t \cdot t^{0.8} \tag{6.3}$$

where, a_t represents the coefficient of the power law and t represents the storage time, expressed in months.

The capacity fade characteristics obtained for the five performed calendar TCs have been fitted using the fitting function (6.3). The results of the fitting processes are presented individually for each TC in Fig. E.12 - E.16 (see Appendix E.1.2). The obtained fitting function for each TC and the corresponding fitting accuracy values are summarized in Table 6.1.

Based on the R^2 values presented in Table 6.1, it has been concluded that the proposed fitting functions (given in 6.3) are able to describe with high accuracy the dependence of the calendar capacity fade on the storage time.

The second step of the two-step fitting procedure, which has been considered for modelling the calendar lifetime (in terms of capacity fade) of the LFP/C battery cells, was to determine the dependence of the capacity fade on the storage temperature and SOC-level.

6.2.2 Dependence on storage temperature

The measured and fitted capacity fade characteristics for the LFP/C battery cells stored at 50% SOC and three different temperatures (i.e. *Calendar 1*, *Calendar 2*, and *Calendar 3*) are presented in Fig. 6.3.

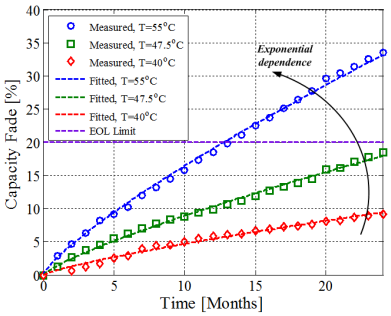

Figure 6.3: *Dependence on the storage temperature of the capacity fade measured on the LFP/C cells subjected to accelerated calendar lifetime tests.*

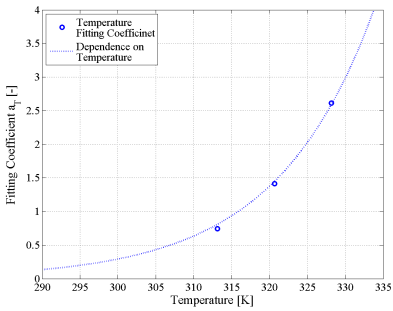

Figure 6.4: *Exponential relationship between the obtained curve fitting coefficients and the considered storage temperatures.*

In order to determine the influence of the storage temperature on the capacity fade of the LFP/C battery cells, the a_t fitting coefficients (corresponding to the TCs *Calendar 1*, *Calendar 2*, and *Calendar 3*) were used during the second step of the two-step fitting procedure. The exponential function given in (6.4) was found to fit the dependence of the aforementioned coefficients on the considered storage temperature values. The results of the second round of curve fitting are illustrated in Fig. 6.4.

$$a_t(T) = 2.327 \cdot 10^{-11} \cdot e^{0.07511 \cdot T} \tag{6.4}$$

The obtained exponential fitting function is able to accurately predict ($R^2 = 0.9903$) the dependence of the capacity fade on the temperature; thus, being in good agreement with Arrhenius' law, which postulates a doubling of the reaction rate (e.g., capacity fade) for a 10^oC increase in temperature [32].

By combining the power law (6.3), which describes the dependence of the capacity fade on the storage time with the exponential function (6.4), which describes the dependence of the capacity fade on the storage temperature, a general model that is able to predict the capacity fade during storage at SOC=50% and different temperatures (mainly, higher than 25^oC), was obtained:

$$C_{fade}(t, T) = 2.327 \cdot 10^{-11} \cdot e^{0.07511 \cdot T} \cdot t^{0.8} \tag{6.5}$$

where, t represents the storage time, expressed in months and T represents the storage temperature, expressed in degrees Kelvin.

6.2.3 Dependence on storage SOC-level

During the second step of the fitting procedure, the dependence of the capacity fade on SOC-level, at which the battery cells are stored, was investigated as well. The measured and fitted capacity fade characteristics for the LFP/C battery cells stored at 55^{o}C and three different SOC levels (i.e., 10%, 50%, and 90% SOC, respectively) are presented in Fig. 6.5.

If for most Li-ion battery cell chemistries, the dependence of capacity fade on temperature is exponential, the SOC-level dependency differs from chemistry to chemistry and is strongly influenced by the used electrode material and its corresponding phase transitions, during intercalation [32].

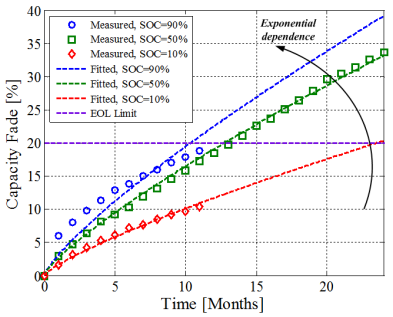

Figure 6.5: *Dependence on the storage SOC-level of the capacity fade measured on the LFP/C cells subjected to accelerated calendar lifetime tests.*

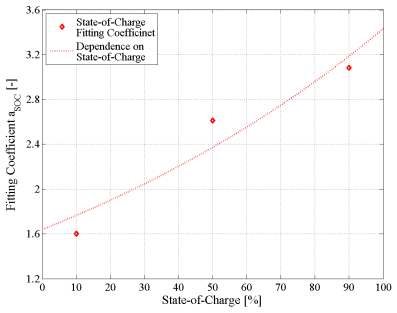

Figure 6.6: *Exponential relationship between the curve fitting coefficient and the corresponding storage SOC-levels.*

Similar to the case of the capacity fade dependence on the temperature, in order to determine the influence of the storage SOC-level on the capacity fade of the LFP/C battery cells, the a_t fitting coefficients (corresponding to the TCs *Calendar 4*, *Calendar 1*, and *Calendar 5*) were used during the second step of the two-step fitting procedure. An exponential function (see 6.6) was found to express with good accuracy (R^2 = 0.9169) the relationship between the fitting coefficients and the storage SOC-level as shown in Fig. 6.6.

$$a_t(SOC) = 1.639 \cdot e^{0.007388 \cdot SOC} \tag{6.6}$$

Based on power law (6.3) and the exponential function (6.6), a general model that is able to predict the capacity fade during storage at 55^{o}C and different SOC-levels was obtained:

$$C_{fade}(t, SOC) = 1.639 \cdot e^{0.007388 \cdot SOC} \cdot t^{0.8} \tag{6.7}$$

As described until this point, the dependences of the capacity fade on the storage temperature and on the storage SOC-level were fitted separately. In order to obtain a function which connects both contributions into a single figure of merit, a scaling of the two functions was used. Because possible interactions between the two stress factors were neglected, the scaling process was considered accurate enough. Consequently, the developed model which is able to predict the calendar lifetime in terms of capacity fade is given in (6.8).

$$C_{fade}(t, T, SOC) = 1.9775 \cdot 10^{-11} \cdot e^{0.07511 \cdot T} \cdot 1.639 \cdot e^{0.007388 \cdot SOC} \cdot t^{0.8} \tag{6.8}$$

Based on the obtained capacity fade lifetime model (6.8), the calendar lifetime of the studied LFP/C battery cells was extrapolated to lower temperature values, including the normal operating temperature (i.e., 25^{o}C), as presented in Fig. 6.7.

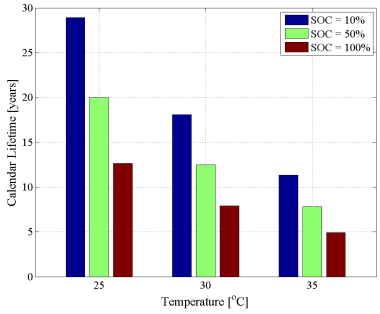

Figure 6.7: *Estimation of capacity fade for LFP/C battery cells stored at different temperature and SOC values (the EOL criterion was set at 20% capacity fade).*

According to the developed capacity fade lifetime model, the tested LFP/C battery cells are able to withstand approximately 20 years, if stored at 50% SOC and 25^{o}C, until they will reach the EOL criterion; however, the lifetime will decrease dramatically, to 12.5 years, if the cells are stored at 100% SOC.

6.3 Pulse power capability decrease

The PPC of the LFP/C battery cells, at various conditions (e.g. age and SOC), was calculated based on the internal resistance values obtained from performing the HPPC

tests during various RPTs (see Chapter 5.4). The PPC values of the LFP/C cells were determined during the accelerated calendar ageing tests only for the maximum C-rate (i.e, 4C-rate corresponding to 10A) which was applied during the RPTs. Furthermore, for analysing the PPC decrease of the studied cells that was caused by the accelerated calendar ageing, only the PPC values obtained for the discharging conditions have been used.

The effect of calendar ageing on the voltage drop of the LFP/C cells that was observed during the internal resistance measurements at different moments during the ageing process is presented in Fig. 6.8. Based on these measurements, the internal resistance of the battery cells was computed by applying Ohm's Law (3.5) and is presented, for different ages, in Fig. 6.9.

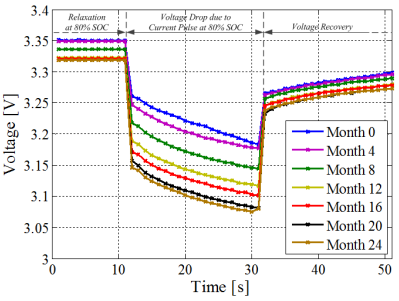

Figure 6.8: *Voltage profile during the periodical internal resistance measurements, performed throughout the accelerated calendar lifetime tests (calendar ageing: T=55°C, SOC=50%; RPT: T=25°C, I=10A).*

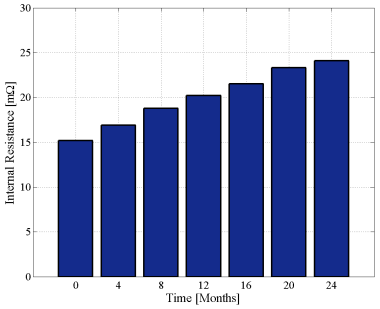

Figure 6.9: *Internal resistance of the LFP/C battery cells, derived based on Ohm's Law from the voltage profiles illustrated in Fig.6.8 (calendar ageing: T=55°C, SOC=50%; RPT: T=25°C, I=10A).*

Based on the measured internal resistance values, the discharge PPC of the tested LFP/C battery cells was computed using (3.7) for all SOC levels considered in the RPT procedure taking into account the maximum charge/discharge current specified by the manufacturer. Fig. 6.10 exemplifies the measured PPC at the three considered SOC levels (i.e., 20%, 50%, 80%) at different moments during the accelerated calendar ageing procedure.

The presented procedure was used to determine the discharging PPC and its ageing behaviour of the LFP/C battery cells, which were subjected to the accelerated ageing conditions summarized in Table 5.1.

The discharge PPC values measured for the LFP/C battery cells during consecutive RPTs throughout the accelerated calendar lifetime tests are presented in Appendix E for all the three considered SOCs and for each TC separately. Similar to the case of the

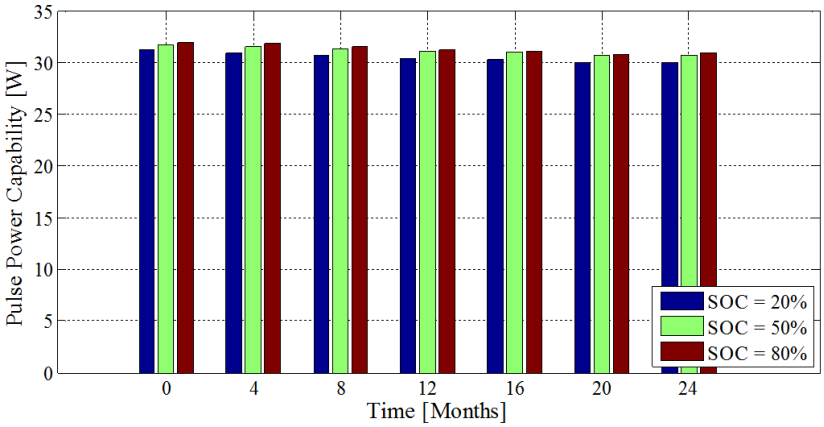

Figure 6.10: *Pulse power capability measured for an 18 seconds discharging current pulse during accelerated calendar ageing tests (calendar ageing: T=55°C, SOC=50%; RPT: T=25°C, I=10A, various SOC-levels).*

capacity fade, the average values of the PPC were obtained for each calendar TC. These average values have been further used to analyse the ageing behaviour of the PPC, which was induced by the considered calendar ageing conditions.

The discharge PPC decrease of the LFP/C cells, caused by the accelerated calendar ageing, was computed according to (6.9) for the average PPC values. The discharge PPC decrease characteristics for all performed TCs are summarized in Appendix E.

$$PPC_{decrease}[\%] = \frac{PPC_{BOL} - PPC_{present}}{PPC_{BOL}} \cdot 100 \tag{6.9}$$

where, $PPC_{decrease}$ represents the PPC decrease of the battery cell (expressed in per cent), PPC_{BOL} represents the PPC of the battery cell measured at the BOL (expressed in W), and $PPC_{present}$ represents the PPC of the cell measured after each RPT (expressed in W).

The PPC decrease measured at 20%, 50%, and 80% SOC, for one of the carried out accelerated calendar lifetime tests, are presented in Fig. 6.11.

As it can be observed from the above presented plots, the decrease of the PPC of the LFP/C battery cells is very small (approximately 4%) independent on the SOC-level at which the measurements were performed. It has to be stressed that for the same ageing conditions (T=55^oC, SOC=50%) during the same storage time, the LFP/C battery cells have reached more than 35% capacity fade. Moreover, the PPC decrease characteristics, obtained for the three different SOC levels, are following very similar trends. Consequently, the dependence of the discharge PPC decrease on the storage time, temperature and SOC-level, will be further analysed only for the values measured during the

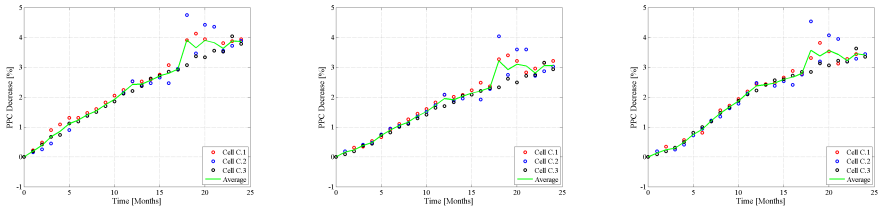

(a) SOC=20% (b) SOC=50% (c) SOC=80%

Figure 6.11: *Discharging PPC decrease of LFP/C battery cells aged under Calendar 1 conditions (RPT: T=25°C, I=10A, various SOCs)*

RPT at 80% SOC.

The two-steps fitting procedure was used as well for analysing the ageing behaviour of the LFP/C cells in terms of PPC decrease. Thus, in the first stage, the dependence of the PPC decrease on the storage time was analysed, while in the second stage the dependence on the storage temperature and SOC-level was investigated.

6.3.1 Dependence on storage time

A first order polynomial function, defined in 6.10, was found to fit with high accuracy the measured decrease of the PPC over the storage time.

$$PPC_{decrease}(t) = b_t \cdot t \tag{6.10}$$

where b_t represents the coefficient of the first order polynomial function, and t represents the storage time, expressed in months.

The results of fitting the measured PPC decrease characteristics with the linear function (6.10) are presented in Appendix E.1.4 (see Fig. E.47 - see Fig. E.51) for the five different performed calendar lifetime tests. Table 6.2 summarizes the obtained fitting functions which are describing the PPC decrease for the considered TCs and the corresponding values for the accuracy of the fit (computed based on (6.2)).

Based on the obtained fitting functions and their corresponding coefficients, the second step of the two-step fitting procedure was carried out, in order to determine the effect of temperature and SOC-level stress factors on the PPC decrease.

6.3.2 Dependence on storage temperature

The measured and fitted PPC decrease characteristics for the LFP/C battery cells which were aged at 50% SOC and three different elevated temperatures (i.e., 55^{o}C, 47.5^{o}C, and 40^{o}C) are presented in Fig. 6.12.

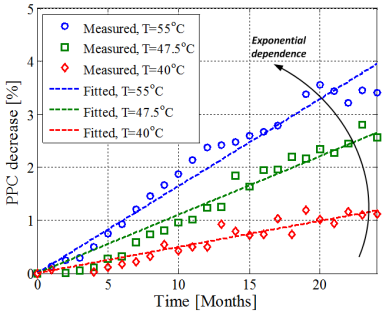

Figure 6.12: *Dependence on the storage temperature of the PPC decrease measured on the LFP/C cells subjected to accelerated calendar lifetime tests.*

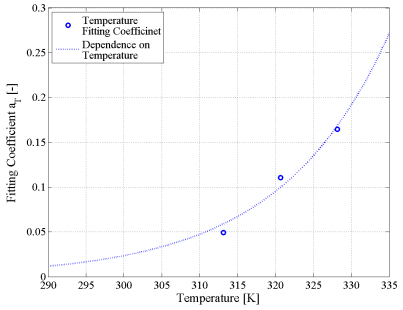

Figure 6.13: *Exponential relationship between the curve fitting coefficients (see Table 6.2) and the storage temperature.*

To determine the dependence of the PPC decrease on the temperature, the b_t coefficients corresponding to the *Calendar 1*, *Calendar 2*, and *Calendar 3* TCs, were subjected to a second fitting process. The results of this fitting process are shown in Fig. 6.13. Similar to the case of the capacity fade, it was found that an exponential function (see 6.11) is able to accurately correlate ($R^2 = 0.9661$) the fitting coefficients obtained during the first-stage and the storage temperature. Consequently, it can be concluded that the PPC of the LFP/C battery cells degrades during storage following Arrhenius' law.

$$b_t(T) = 1.808 \cdot 10^{-11} \cdot e^{0.06995 \cdot T} \tag{6.11}$$

By combining the dependence of the fitting coefficient b_t on the temperature ex-

Table 6.2: *Dependence of the PPC decrease on the storage time. Fitting functions and accuracy*

Test Case	Fitting Function	R^2
Calendar 1	$PPC_{decrease-Cal1}(t) = 0.1647 \cdot t$	0.9616
Calendar 2	$PPC_{decrease-Cal2}(t) = 0.1106 \cdot t$	0.9567
Calendar 3	$PPC_{decrease-Cal3}(t) = 0.04937 \cdot t$	0.8895
Calendar 4	$PPC_{decrease-Cal4}(t) = 0.07085 \cdot t$	0.9596
Calendar 5	$PPC_{decrease-Cal5}(t) = 0.1989 \cdot t$	0.9858

pressed in (6.11) with the linear function (6.10), which describes the decrease of the PPC caused by storage time, a model able to estimate the PPC decrease during storage at 50% SOC and various temperature levels (not lower than 25^{o}C) was obtained:

$$PPC_{decrease}(t,T) = 1.808 \cdot 10^{-11} \cdot e^{0.06995 \cdot T} \cdot t \tag{6.12}$$

6.3.3 Dependence on storage SOC-level

The measured and fitted PPC decrease characteristics of the LFP/C battery cells, which were subjected to calendar ageing at 55^{o}C and three different SOC-levels (i.e., 10%, 50%, and 90% SOC) are illustrated in Fig. 6.14.

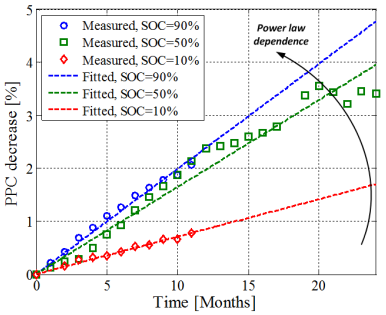

Figure 6.14: *Dependence on the storage SOC-level of the PPC decrease measured on the LFP/C cells subjected to accelerated calendar lifetime tests.*

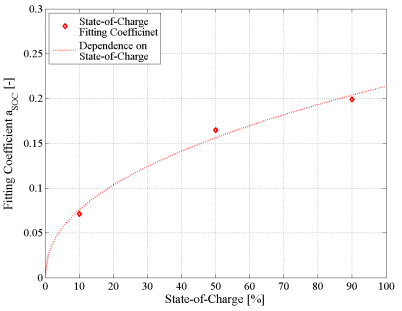

Figure 6.15: *Power-law relationship between the curve fitting coefficients (see Table 6.2) and the storage SOC-level.*

In order to determine the influence of the SOC-level on the PPC decrease of the calendar aged LFP/C cells, different functions have been evaluated, as presented in Table 6.3.

Table 6.3: *Evaluation of various functions for fitting the dependence of PPC decrease on SOC-level*

Name	Fitting Function	R^2
Exponential	$b_t = 0.08229 \cdot e^{0.0103 \cdot SOC}$	0.8607
Linear	$b_t = 0.001601 \cdot SOC + 0.06479$	0.9325
Power Law	$b_t = 0.02672 \cdot SOC^{0.4513}$	0.9867

Based on the obtained results, the power law given in (6.13) was selected for expressing the dependence of the PPC decrease on the SOC level (see Fig. 6.15). Thus, one can conclude that the SOC-level influences in a different manner the calendar (stoarge) degradation of the LFP/C cells' PPC (power law dependence) than their capacity (exponential dependence).

$$b_t(SOC) = 0.02672 \cdot SOC^{0.4513} \tag{6.13}$$

Thus, knowing the dependence of the b_t fiiting coefficient on the storage SOC-level (6.13) and considering the power law (6.10), a model, which is able to estimate the PPC decrease of LFP/C cells stored at 55^{o}C and any SOC-level, was obtained:

$$PPC_{decrease}(t, SOC) = 0.02672 \cdot SOC^{0.4513} \cdot t \tag{6.14}$$

Similar as for the capacity fade, the dependences of the PPC decrease on the storage temperature and on the storage SOC-level were modelled separately. Since any possible interactions between the two stress factors were neglected (see Fig. 5.3) , a scaling of the two functions had to be applied. Consequently, based on this assumption, the model which is able estimate the PPC decrease during calendar ageing conditions is given in (6.15).

$$PPC_{decrease}(t, T, SOC) = (1.075 \cdot 10^{-10} \cdot e^{0.06995 \cdot T}) \cdot (0.02672 \cdot SOC^{0.4513}) \cdot t \tag{6.15}$$

Based on the developed lifetime model (6.15), the PPC decrease of the LFP/C battery cells can be extrapolated to storage temperatures close to ones encountered during normal operation, as shown in Fig. 6.16.

By comparing the structure of models developed for predicting the calendar lifetime of the LFP/C battery cells in terms of capacity (see 6.8) and PPC (see 6.15), it might be concluded that the degradation, during storage, of these two performance parameters is not caused by the same ageing mechanisms.

Moreover, it has to be stressed that the use of the aforementioned lifetime models for determining the ageing behaviour at temperatures below 25^{o}C might return erroneous results; this is because lifetime tests performed at lower temperatures (e.g. 10^{o}C, 15^{o}C etc.) were not considered when developing the test matrices, being out of the scope of this thesis.

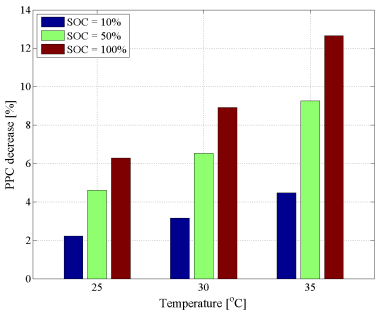

Figure 6.16: *Estimation of pulse power capability decrease caused by calendar ageing at various conditions (the predictions are made for a battery lifetime of 20 years at the considered conditions).*

6.4 Changes in EIS plots

Similar to capacity fade and PPC decrease, the changes in the impedance spectra (measured by EIS technique) of the LFP/C battery cells during calendar ageing at various conditions (see Table 5.1) were evaluated. All the EIS measurements have been performed following the conditions presented in Chapter 3.2.1 (see EIS Test).

The evolution of the EIS spectra during ageing for the LFP/C cells tested under *Calendar 1* conditions are presented in Fig. 6.17 - Fig. 6.19, for 20%, 50%, and 80%, respectively. No major differences were observed on the impedance spectra (nor on the curve fitting results) measured at different SOC-levels; therefore, similar to the case of the PPC, only the results obtained at 80% SOC will be investigated and lifetime models will be build based on these results.

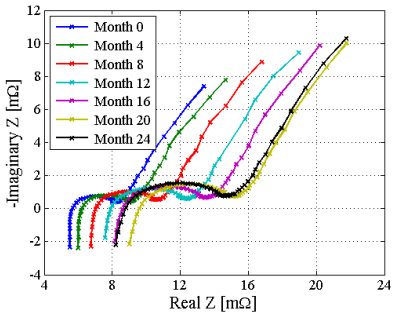

Figure 6.17: *Dependence of LFP/C battery cells' EIS spectra on the storage time (ageing conditions: T=55°C, SOC=50%, RPT conditions: T=25°C, SOC=20%).*

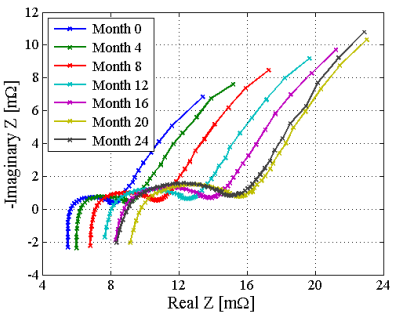

Figure 6.18: *Dependence of LFP/C battery cells' EIS spectra on the storage time (ageing conditions: T=55°C, SOC=50%, RPT conditions: T=25°C, SOC=50%).*

By analysing the Nyquist curves plotted in Fig. 6.19, it can be observed that mainly

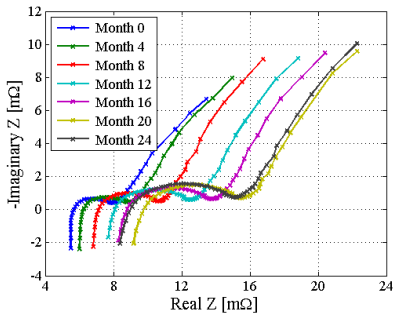

Figure 6.19: *Dependence of LFP/C battery cells' EIS spectra on the storage time (ageing conditions: T=55°C, SOC=50%, RPT conditions: T=25°C, SOC=80%).*

the intercept with the real axis is moving towards the right side of the Nyquist plane. This phenomenon is usually related with the increase of the ohmic resistance while the ageing process evolves [45], [122]. Moreover, it was observed that the first semi-circle of the Nyquist curves, measured at mid-frequencies, had gradually increased with ageing. The same ageing behaviour of the impedance spectra was observed independent on the considered ageing conditions; the Nyquist curves measured on the LFP/C cells, aged under *Calendar 2* - *Calendar 5* conditions, are summarized in Appendix E.1.5 (see Fig. E.52 - E.63).

In order to evaluate in detail the aforementioned tendencies, the impedance spectra measured throughout the considered ageing TCs, were curve fitted using the EEC presented in Fig. 3.27 and the corresponding parameters of the circuit were extracted. During all the curve fitting processes the series inductance L_s and the two depression factors n_1 and n_2 have been kept constant. Moreover, the values of the resistance R_2 and the generalized capacitance Q_2, of the second ZARC-element, have shown a large scattering over time, independent on the ageing conditions. Thus, the dependence on storage time of these parameters was not further investigated.

Therefore, only the ageing dependence on storage time, temperature , and SOC-level of the series resistance R_s, resistance R_1, and generalized capacitance Q_1 has been investigated. The evolution over time of these three parameters under different accelerated calendar ageing conditions are presented in Appendix E.1.6 (see Fig. E.64 - Fig. E.78).

The investigation of the aforementioned EEC parametrs' dependence on the ageing conditions was performed using the same two-steps fitting procedure as in the case of capacity fade and PPC decrease. Thus, since the procedure was already explained, only the major findings will be presented for R_s, R_1, and Q_1.

6.4.1 Ageing evaluation of series resistance R_s

Similar to the case of the PPC decrease, the series resistance R_s shows a linear dependence on the storage time. Thus, by fitting the increase of R_s over time (see Fig. E.64 - Fig. E.68), for each calendar TC separately, with a first order polynomial function, the results summarized in Table 6.4 have been obtained. The obtained values for R^2 show that a linear function is able to accurately represent the increase of the series resistance during calendar ageing at different conditions.

Table 6.4: *Dependence of the series resistance R_s increase on the storage time. Fitting functions and accuracy*

Test Case	Fitting Function	R^2
Calendar 1	$Rs_{increase-Cal1}(t) = 2.650 \cdot t$	0.8762
Calendar 2	$Rs_{increase-Cal2}(t) = 1.665 \cdot t$	0.8504
Calendar 3	$Rs_{increase-Cal3}(t) = 0.743 \cdot t$	0.8302
Calendar 4	$Rs_{increase-Cal4}(t) = 1.338 \cdot t$	0.9940
Calendar 5	$Rs_{increase-Cal5}(t) = 3.409 \cdot t$	0.9886

The effect of the storage temperature on the increase rate of the series resistance is illustrated in Fig. 6.20. As shown in Fig. E.79 (see Appendix E.1.7), an exponential function was found to fit with very high accuracy ($R^2 = 0.9802$) the dependence of R_s increase on the storage temperature.

The influence of the storage SOC-level on the increase of the series resistance over the time is shown in Fig. 6.21. A power function was found, as shown in Fig. E.80, to express the effect of the SOC-level on R_s increase.

The functions describing the dependence of the series resistance R_s increase on the storage temperature and on the storage SOC-level were obtained separately and are presented in (6.16) and (6.17), respectively.

$$Rs_{increase}(t, T) = 4.535 \cdot 10^{-11} \cdot e^{0.07559 \cdot T} \cdot t \tag{6.16}$$

$$Rs_{increase}(t, SOC) = 0.5012 \cdot SOC^{0.4259} \cdot t \tag{6.17}$$

Based on the assumption that there are no interactions between the effects caused by the temperature and SOC-level, a lifetime model able to estimate the increase of the series resistance R_s over time at various storage conditions was obtained:

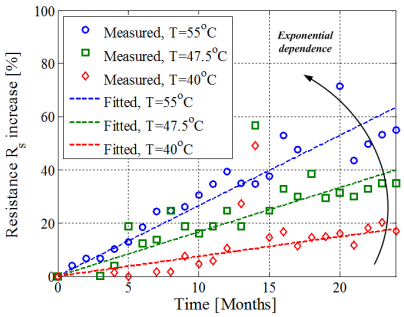

Figure 6.20: *Dependence on the storage temperature of the R_s increase measured on the LFP/C cells subjected to accelerated calendar lifetime tests.*

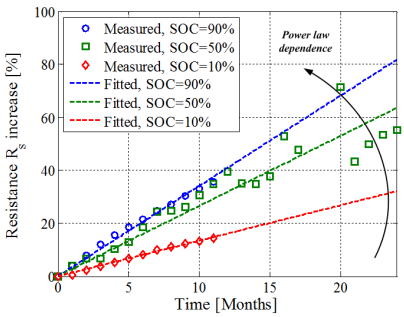

Figure 6.21: *Dependence on the storage SOC-level of the R_s increase measured on the LFP/C cells subjected to accelerated calendar lifetime tests.*

$$Rs_{increase}(t, T, SOC) = (1.6487 \cdot 10^{-11} \cdot e^{0.07559 \cdot T}) \cdot (0.5012 \cdot SOC^{0.4259}) \cdot t \qquad (6.18)$$

The calendar lifetime models developed for estimating the PPC decrease (6.15) and R_s increase (6.18) are showing similar dependences on both storage temperature and storage SOC-level; moreover, their ageing coefficients for temperature and SOC-level are very similar. Consequently, this could indicate that the PPC decrease and series resistance increase are caused by the same ageing mechanism/mechanisms.

6.4.2 Ageing evaluation of resistance R_1

The increase of resistance R_1 caused by the considered accelerated calendar lifetime tests are presented in Fig. E.69 - Fig. E.73. Similar to the case of the series resistance R_s, independent on the storage conditions, the resistance R_1 was found to increase linearly over storage time, as presented in Table. 6.5.

The influence of the storage temperature on the increase of the resistance R_1, for LFP/C battery cells stored at 50% SOC, is presented in fig. 6.22. As illustrated in Fig. E.81 (see Appendix E.1.7), the dependence of the resistance R_1 increase on the storage temperature can be expressed very accurately ($R^2 = 0.996$) using an exponential function.

Fig. 6.23 shows the dependence of the resistance R_1 increase over time on the storage SOC-level. Similar to the case of resistance R_s, it was found out that the increase rate of

Table 6.5: *Dependence of the resistance* R_1 *increase on the storage time. Fitting functions and accuracy*

Test Case	Fitting Function	R^2
Calendar 1	$R1_{increase-Cal1}(t) = 5.782 \cdot t$	0.9771
Calendar 2	$R1_{increase-Cal2}(t) = 3.178 \cdot t$	0.9709
Calendar 3	$R1_{increase-Cal3}(t) = 1.655 \cdot t$	0.9501
Calendar 4	$R1_{increase-Cal4}(t) = 2.171 \cdot t$	0.8106
Calendar 5	$R1_{increase-Cal5}(t) = 6.007 \cdot t$	0.9715

resistance R_1 depends following a power law on the storage SOC-level (see Fig. E.82).

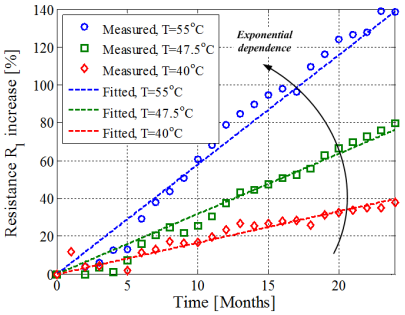

Figure 6.22: *Dependence on the storage temperature of the* R_1 *increase measured on the LFP/C cells subjected to accelerated calendar lifetime tests.*

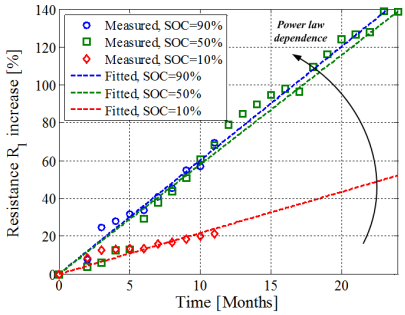

Figure 6.23: *Dependence on the storage SOC-level of the* R_1 *increase measured on the LFP/C cells subjected to accelerated calendar lifetime tests.*

The functions, which are describing the dependence of the resistance R_1 increase on the storage temperature and storage SOC-level, are given by (6.19) and (6.20), respectively.

$$R1_{increase}(t,T) = 1.224 \cdot 10^{-11} \cdot e^{0.08192 \cdot T} \cdot t \tag{6.19}$$

$$R1_{increase}(t,SOC) = 0.9778 \cdot SOC^{0.4118} \cdot t \tag{6.20}$$

In order to obtain a lifetime model, which is able to predict the increase of resistance R_1 during storage at various conditions, the functions (6.19) and (6.20) have been connected by applying a scaling factor and the result is given in (6.21).

$$R1_{increase}(t,T,SOC) = (2.1165 \cdot 10^{-12} \cdot e^{0.08192 \cdot T}) \cdot (0.9778 \cdot SOC^{0.4118}) \cdot t \tag{6.21}$$

Moreover, by comparing the results presenting the increase over time of series resistance R_s (see Fig. 6.20 and Fig. 6.21) and of resistance R_1 (see Fig. 6.22 and Fig. 6.23), one can conclude that independent on the calendar ageing conditions, R_1 increases much faster than R_s. Consequently, this ageing behaviour might suggest that the ageing mechanism responsible for the increase of resistance R_1 is the dominant ageing mechanism in the tested LFP/C battery cells.

6.4.3 Ageing evaluation of resistance Q_1

The evolution of the generalized capacitance Q_1 during the considered accelerated calendar lifetime tests is presented in Fig. E.74 - Fig. E.78 (see Appendix E.1.6). In contrast with the resistances R_s and R_1, which are increasing over time, the capacitance Q_1 is decreasing, independent on the considered ageing conditions. However, similar to the case of the previously analysed resistances, the evolution over time of the generalized capacitance Q_1 was fitted using a first degree polynomial function, as well; the results obtained from the five fitting processes are summarized in 6.6. In comparison to the previous cases, lower fitting accuracy values have been obtained, since the decrease over time of Q_1 is relatively scattered.

Table 6.6: *Dependence of the generalized capacitance Q_1 increase on the storage time. Fitting functions and accuracy*

Test Case	Fitting Function	R^2
Calendar 1	$Q1_{decrease-Cal1}(t) = 2.661 \cdot t$	0.9060
Calendar 2	$Q1_{decrease-Cal2}(t) = 1.687 \cdot t$	0.7971
Calendar 3	$Q1_{decrease-Cal3}(t) = 1.668 \cdot t$	0.6744
Calendar 4	$Q1_{decrease-Cal4}(t) = 2.144 \cdot t$	0.8660
Calendar 5	$Q1_{decrease-Cal5}(t) = 2.724 \cdot t$	0.9453

The dependence of the generalized capacitance Q_1 on the storage temperature (for 50% SOC) and on the SOC-level (for T=55ºC) are illustrated in Fig. 6.24 and Fig. 6.25, respectively. Similar to the cases of the other two EEC parameters, which have been previously analysed, the decrease of the capacitance Q_1 over time depends exponentially on the storage time, as illustrated in Fig. E.83. Furthermore, it was found out that a power law function estimates with relative-high accuracy ($R^2 = 0.9647$) the dependence of Q_1 on the storage SOC-level (see Fig. E.84).

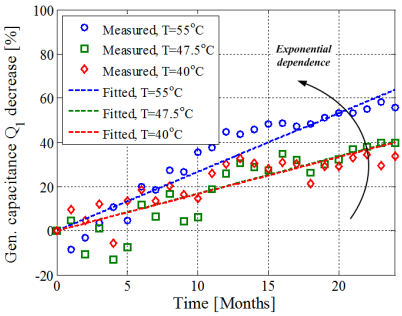

Figure 6.24: *Dependence on the storage temperature of the generalized capacitance Q_1 increase measured on the LFP/C cells subjected to accelerated calendar lifetime tests.*

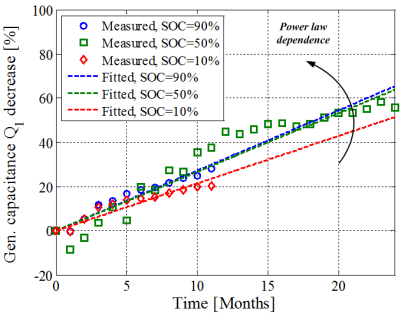

Figure 6.25: *Dependence on the storage SOC-level of the generalized capacitance Q_1 increase measured on the LFP/C cells subjected to accelerated calendar lifetime tests.*

The function, which describes the dependence of the generalized capacitance Q_1 decrease on the storage temperature and storage time is given in (6.22), while the function, which describes the dependence of the generalized capacitance Q_1 decrease on the storage SOC-level and storage time is given in (6.23).

$$Q1_{decrease}(t,T) = 1.954 \cdot 10^{-5} \cdot e^{0.03592 \cdot T} \cdot t \tag{6.22}$$

$$R1_{decrease}(t,SOC) = 1.673 \cdot SOC^{0.1121} \cdot t \tag{6.23}$$

The lifetime model, which estimates the decrease of the generalized capacitance Q_1 during calendar ageing at different conditions (mainly temperatures equal or higher than 25°C) is given in (6.24); the model was obtained by connecting the previously developed functions (6.22) and (6.23):

$$Q1_{decrease}(t,T,SOC) = (7.6043 \cdot 10^{-6} \cdot e^{0.03592 \cdot T}) \cdot (1.673 \cdot SOC^{0.1121}) \cdot t \tag{6.24}$$

6.5 Self-Discharge

All batteries are subjected to self-discharge when stored at different temperature and SOCs for a period of time, process which leads to the loss of the available capacity [137]. The self-discharge rate varies depending on the battery technology as illustrated in [66], [68]; however, the self-discharge rate of Li-ion batteries is less pronounced than

for other technologies, such as lead-acid and sodium-sulphur batteries. Besides being dependent on the chemistry, the self-discharge mechanisms is influenced by the electrode composition and design and by the electrolyte formulation and impurities [137].

Different factors (mechanisms) are contributing to the development of the self-discharge process as mentioned in [137], [138]. Nevertheless, the major contribution to the self-discharge of Li-ion batteries is the corrosion of the anode [139]. Once the corrosion process evolves, reaction products, which are dependent on the composition of electrode and electrolytes, are generated at the electrode/electrolyte interface [138], [139]. A part of these products are soluble and the reaction can be reversed during the following re-charging of the battery; this process is known as reversible capacity loss or self-discharge. The second part of these products are insoluble and are leading to irreversible capacity fade of the Li-ion battery [139].

Generally, the self-discharge of Li-ion batteries is dependent on the storage temperature and storage SOC-level. Moreover, the self-discharge rate of Li-ion batteries is changing while the ageing processes evolve.

During the performed accelerated calendar lifetime tests the ageing behaviour of the self-discharge parameters of the LFP/C battery cells was measured as well. The measurement of the self-discharge of the LFP/C battery cells was possible because during the accelerated calendar lifetime tests, the cells were kept at OCV conditions (without applying float charging). The procedure which was applied for measuring the self-discharge was the following: before storing in ovens the LFP/C battery cells at the desired conditions (see Table 5.1), they were charged with 1C-rate to the predefined SOC value. Then, after they were stored for 1 month (30 days) in ovens at the defined conditions, the battery cells, before going through the RPT procedure, were discharged with 1C-rate until the cut-off voltage was reached. Thus, the difference between the charged Ah before the one month storage period and the discharged Ah after this period was defined as the self-discharge of the LFP/C battery cells. The self-discharge was expressed in per cent according to (6.25).

$$Self-discharge[\%] = \frac{ChargedAh_{before} - DischargedAh_{after}}{ChargedAh_{before}} \cdot 100 \qquad (6.25)$$

where, *Self-discahrge* represents the measured self-discharged per month of the battery cells, expressed in per cent, *Charged-Ah$_{before}$* represents the Ah, which were charged to the battery before the one month of storage, and *Discharged-Ah$_{after}$* represents the Ah, which were discharged from the battery after the one month of storage.

The evolution of the self-discharge process during the performed accelerated calen-

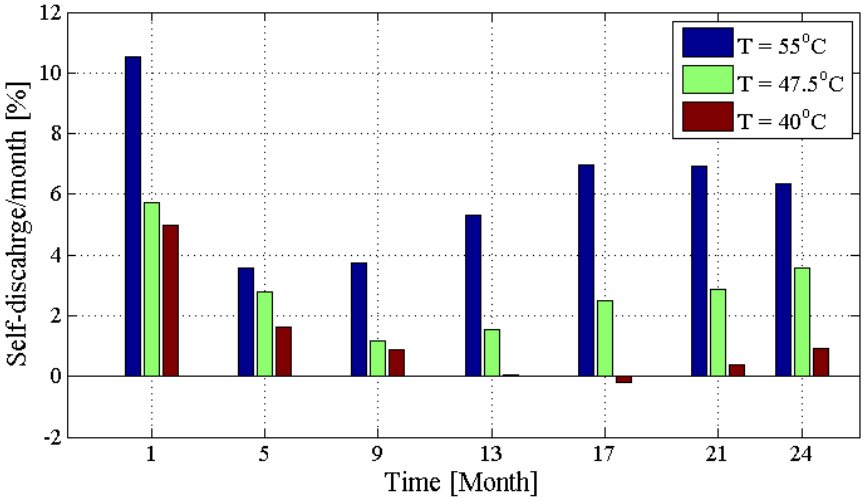

Figure 6.26: *Measured self-discharge of LFP/C battery during calendar ageing at 50% SOC and three different temperatures.*

dar ageing tests, and its dependence on storage temperature and storage SOC-level are presented in Fig. 6.26 and Fig. 6.27, respectively.

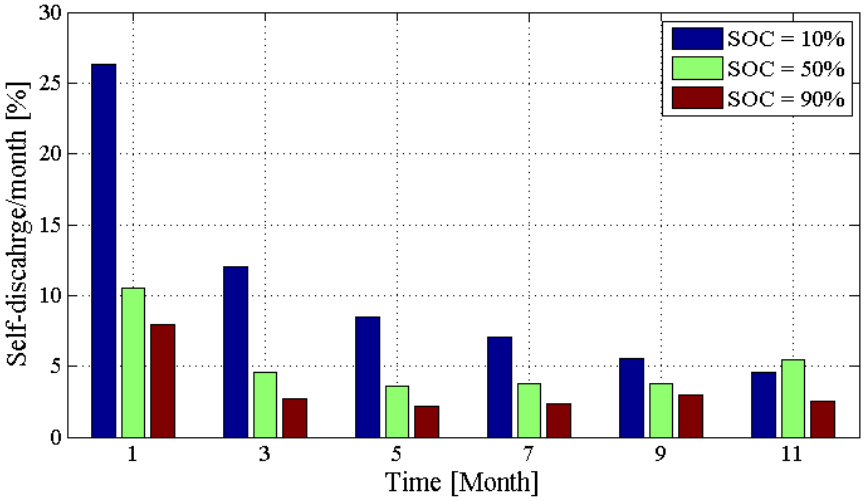

Figure 6.27: *Measured self-discharge of LFP/C battery during calendar ageing at 55°C and three different SOC-levels.*

Similar to the case of the other studied parameters of the LFP/C battery cells, the

self-discharge results presented in Fig. 6.26 and Fig. 6.27 are the average values obtained over a group of three cells.

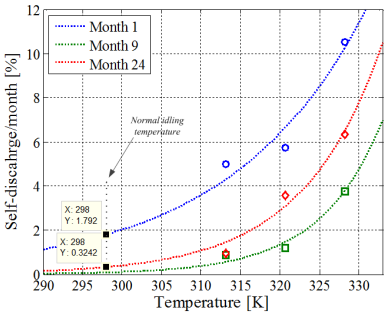

Figure 6.28: *Exponential relationship between storage temperature and self-discharge rate at different ages of the LFP/C battery cells.*

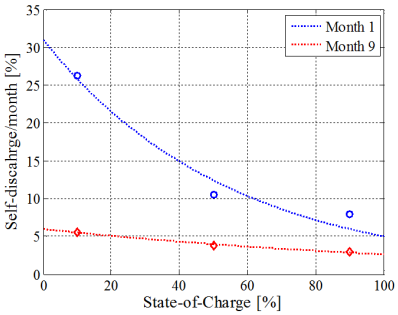

Figure 6.29: *Exponential relationship between storage SOC-level and self-discharge rate at different ages of the LFP/C battery cells.*

As presented in Fig. 6.26 and Fig. 6.27, the self-discharge of the tested LFP/C battery is highly influenced by the storage conditions. The increase of storage temperature has led to an exponentially increase in the self-discharge rate, as shown in Fig. 6.28. Moreover, this exponential relationship was visible at all SOH levels of the tested LFP/C battery cells, with some examples of fitting results given in Table 6.7.

Table 6.7: *Fitting results for estimating the self-discharge dependence on temperature with an exponential function.*

Condition	Fitting Function	R^2
Month 1	$\text{SelfDischarge}_{M1} = 5.911 \cdot 10^{-8} \cdot e^{0.05781 \cdot T}$	0.9230
Month 9	$\text{SelfDischarge}_{M9} = 2.944 \cdot 10^{-18} \cdot e^{0.127 \cdot T}$	0.9643
Month 24	$\text{SelfDischarge}_{M24} = 4.438 \cdot 10^{-14} \cdot e^{0.00993 \cdot T}$	0.9629

Moreover, the effect of the SOC on the self-discharge rate of the battery cells was expressed using an exponential function as well; this dependence was found valid at all SOH levels of the LFP/C battery cells, with examples summarized in Table 6.8.

Except the dependence of the self-discharge on the SOC-level and temperature, a strong dependence was also observed on the SOH of the LFP/C battery cells. Mainly, independent on the considered calendar ageing conditions, the self-discharge rate of the

Table 6.8: *Fitting results for estimating the self-discharge dependence on SOC with an exponential function.*

Condition	Fitting Function	R^2
Month 1	$\text{SelfDischarge}_{M1} = 31.02 \cdot e^{-0.01831 \cdot SOC}$	0.9615
Month 9	$\text{SelfDischarge}_{M9} = 5.965 \cdot e^{0.008193 \cdot SOC}$	0.9803

battery cells has decreased while the ageing process has evolved (see Fig. 6.26 and Fig. 6.27). As mentioned in [48], this behaviour might be related to the decrease rate of anode corrosion which slows down as cells are ageing. Nevertheless, for the LFP/C battery cells aged at 50% SOC and different temperatures an inflection point was observed (approximately after 10 months of tests) after which the self-discharge rate has started to increase again (see Fig. 6.26).

In Fig. 6.28, the extrapolation of the self-discharge rate to the normal operating conditions (i.e., idling at 25^oC) is presented for three different SOH-levels of the battery cells. Based on the fitting functions summarized in Table 6.7, it was found that the cells exhibit a self-discharge of 1.79%/month at BOL and 0.32%/month after 24 months of calendar ageing if they are stored at 50% SOC and 25^oC.

6.6 Summary

In this chapter, the results obtained from accelerated calendar lifetime tests were analysed and lifetime models for the battery cell's performance parameters were developed.

The capacity fade of the LFP/C during storage was found to depend exponentially on the temperature; moreover the capacity fade is accelerated following a power law by increasing the storage SOC-level. Furthermore, based on the developed capacity fade lifetime model, for a 20% capacity fade EOL criterion, the LFP/C battery cells will be able to withstand 20 years if stored at 25^oC and 50% SOC.

The PPC decrease during idling at different conditions was found to be less pronounced than the capacity fade; for example, for a 20 years storage period at 25^oC and 50% SOC, the capacity fade will reach 20%, while in the same time the PPC will decrease only by 6%. The evolution of the parameters of the EEC during calendar ageing was evaluated as well; only the series resistance R_s, resistance R_1, and generalized capacitance Q_1 were found to depend on the ageing conditions and lifetime models have been developed for each of these parameters.

Chapter 7

Cycling Ageing Results for the LiFePO$_4$/C Battery Cell

This chapter presents the results obtained from the accelerated cycling lifetime tests, which were performed at different conditions, as discussed in the Chapter 5. The effect of the different considered stress factors on the degradation of the LFP/C battery cells' performance parameters is quantified. The degradation of the LFP/C battery cells in terms of capacity fade, PPC decrease, and changes of the parameters of the EEC is analysed and lifetime models for each of aforementioned performance parameters are developed.

7.1 Introduction

The accelerated cycling ageing tests have been performed at the conditions summarized in Table 5.2. The goal of these ageing tests was to determine the cycling lifetime of the LFP/C battery cells in terms of capacity fade and PPC decrease. Moreover, a secondary objective was to analyse the effect of the considered stress factors (i.e., temperature, cycle depth, and average SOC - see Fig. 5.6) on the degradation of the cells' performance parameters. The incremental degradation of the considered battery cells' performance parameters (i.e. capacity, PPC, and AC-impedance) was quantified following the procedure presented in Fig. 7.1.

All the accelerated cycling ageing tests were intended to be performed until the tested LFP/C battery cells would have reached 20% capacity fade. However, because of various limitations, the cells subjected to *TC5*, *TC10*, and *TC11* ageing conditions (see Table 5.2) have not reached the EOL criterion and thus their corresponding capacity fade characteristics were extrapolated.

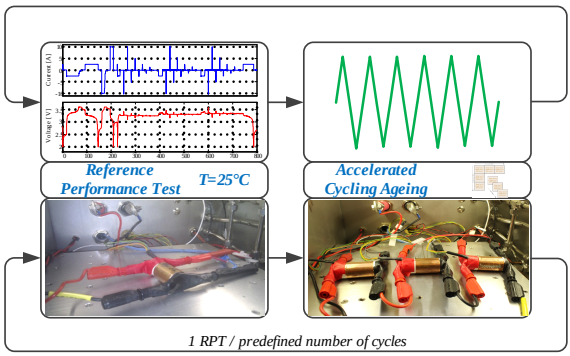

Figure 7.1: *Procedure for determining the degradation of the LFP/C battery cell's performance parameters during cycling at various conditions.*

The results, obtained from the accelerated lifetime tests, for the capacity, PPC, and evolution of the EIS plots (EEC parameters) were analysed similar to the case of the results obtained from accelerated calendar lifetime tests. Based on the considered two-steps fitting procedure, individual lifetime models have been developed for the capacity fade, PPC decrease, and parameters of the EEC, which were found to consistently follow the ageing conditions.

7.2 Capacity fade

The capacity values of the LFP/C battery cells, which have been measured during consecutive RPTs, throughout the performed accelerated cycling lifetime tests are presented for each cycling TC individually in Appendix E.2 (see Fig. E.85, Fig. E.87, Fig. E.89, Fig. E.91, Fig. E.93, Fig. E.95, Fig. E.97, Fig. E.99). The obtained average capacity values (illustrated in the aforementioned plots) were used to determine using (6.1) the capacity fade characteristics of the LFP/C battery cells for each performed accelerated cycling ageing test.

The capacity fade characteristics of the battery cells that were obtained for the eight cycling TCs, are presented in Appendix E.2 (see Fig. E.86, Fig. E.88, Fig. E.90, Fig. E.92, Fig. E.94, Fig. E.96, Fig. E.98, Fig. E.100). These capacity fade characteristics have been further used to determine and analyse the dependence of the capacity of the LFP/C battery cells on the performed number of cycles and their cycle depths, the cycling temperature, and the average cycling SOC-level.

7.2.1 Dependence on number of cycles

During the first stage of the two-stage fitting procedure, the dependence of the capacity fade on the performed number of cycles was determined for each cycling ageing conditions. In order to assess which fitting functions estimates better the decrease of the battery cells' capacity as function of the number of cycles, five different functions were considered. These fitting functions are given in (E.6) - (E.10) and the results of the five fitting processes are shown in Fig. E.101 (see Appendix E.2.2).

Based on the obtained results, the square-root of "time" (number of cycles) function, given in (7.1) was selected to relate the degradation of the capacity fade to the number of performed cycles.

$$C_{fade}(t) = b_{nc} \cdot nc^{0.5} \tag{7.1}$$

where, b_{nc} represents the coefficient of the square-root function and nc represents the number of cycles.

The square-root of time dependence is associated in the literature with the formation of the Li-ion batteries' SEI layer, which evolves following a square-root of time function [32], [131], [140] . Thus, one can conclude that the SEI growth is the main ageing mechanisms, which induces the irreversible capacity loss of the LFP/C battery cells during cycling.

All the capacity fade characteristics corresponding to each of the carried out cycling TCs, were fitted using the square-root of time function given in (7.1) and the obtained results are summarized in Table 7.1. As the R^2 values are showing, the proposed function was able to fit with relatively-high accuracy the measured capacity independent on the imposed ageing conditions.

Table 7.1: *Dependence of the capacity fade on the number of cycles. Fitting functions and accuracy*

Test Case	Fitting Function	R^2
Cycling 1	$C_{fade-TC1}(t) = 0.07895 \cdot t^{0.5}$	0.9372
Cycling 2	$C_{fade-TC2}(t) = 0.1633 \cdot t^{0.5}$	0.9467
Cycling 3	$C_{fade-TC3}(t) = 0.1934 \cdot t^{0.5}$	0.9311
Cycling 5	$C_{fade-TC5}(t) = 0.1080 \cdot t^{0.5}$	0.8572
Cycling 6	$C_{fade-TC6}(t) = 0.1618 \cdot t^{0.5}$	0.9455
Cycling 9	$C_{fade-TC9}(t) = 0.1354 \cdot t^{0.5}$	0.9574
Cycling 10	$C_{fade-TC10}(t) = 0.1736 \cdot t^{0.5}$	0.9351
Cycling 11	$C_{fade-TC11}(t) = 0.07461 \cdot t^{0.5}$	0.8097

During the second stage of the two-stage fitting procedure, the effect of the cycling temperature, cycle depth, and average SOC-level on the capacity fade of the LFP/C battery cells was analysed.

7.2.2 Dependence on cycle depth

The influence of the cycle depth on the capacity fade of the tested cells was investigated during *TC1*, *TC2*, and *TC3*; for these TCs the temperature was set at 50^{o}C and the average SOC-level at 50% SOC. The measured and fitted capacity fade characteristics for the LFP/C cells tested based on the aforementioned conditions are illustrated in Fig. 7.2. The results are showing that the capacity fade of the tested Li-ion cells is accelerated by increasing the cycle depth.

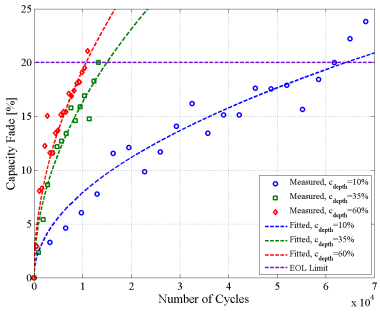

Figure 7.2: *Dependence on the cycle depth of the capacity fade measured on the LFP/C cells subjected to accelerated cycling lifetime tests.*

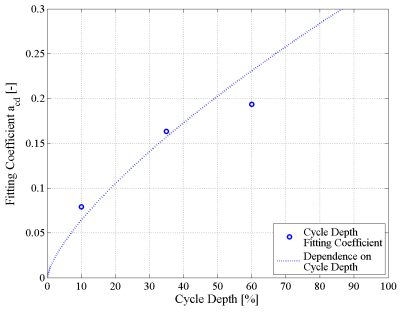

Figure 7.3: *Power-law relationship between the curve fitting coefficients (see TC1, TC2, and TC3 - Table 7.1) and the considered cycle depths.*

Furthermore, the power-law function given in (7.2) was found to express the relationship between the capacity fade and the different considered cycle depths. In Fig. 7.3, the results of the second round of fitting using the function (7.2) are presented.

$$b_{nc}(cd) = 0.0123 \cdot cd^{0.7162} \tag{7.2}$$

In order to obtain a general function, which estimates the capacity fade of the studied LFP/C battery cells at T = 50^{o}C, an average SOC-level = 50% SOC, and various cycle depths, the square-root of time function (7.1) and the power law function (7.2) were combined, yielding:

$$C_{fade}(nc, cd) = 0.0123 \cdot cd^{0.7162} \cdot nc^{0.5} \tag{7.3}$$

7.2.3 Dependence on temperature

The measured and fitted capacity fade characteristics for the LFP/C battery cells used to investigate the influence of the cycling temperature on the capacity fade are presented in Fig. 7.4. As expected, the capacity fade of the tested battery cells is strongly influenced by the cycling temperature, decreasing quickly when the temperature was increased.

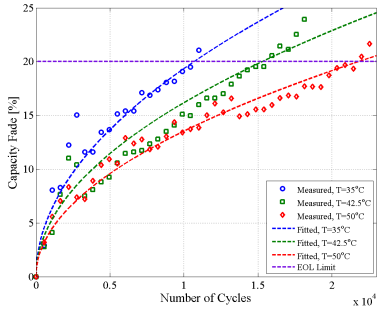

Figure 7.4: *Dependence on the temperature of the capacity fade measured on the LFP/C cells subjected to accelerated cycling lifetime tests.*

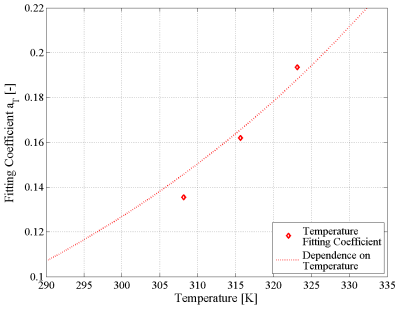

Figure 7.5: *Exponential relationship between the curve fitting coefficients (see TC3, TC6, and TC9 - Table 7.1) and the cycling temperature.*

In order to determine the relationship between the cycling temperature and the capacity fade of the LFP/C battery cells, the b_{ns} coefficients corresponding to *TC3*, *TC6*, and *TC9* (see Table 7.1) were subjected top the second step of the two-steps fitting procedure. The exponential function given in (7.4) was found to estimate with good accuracy (R^2=0.9095) the dependence of the capacity fade on the cycling temperature; the results of this second round of fitting are shown in Fig. 7.5.

$$b_{nc}(T) = 7.617 \cdot 10^{-4} \cdot e^{0.01705 \cdot T} \tag{7.4}$$

By combining the power law (7.1) that describes the dependence of the capacity fade on the number of cycles with the exponential function (7.4) that describes the temperature dependence, a more general model (see 7.5) was obtained; this model is able to predict the capacity fade of the LFP/C battery cells, which are subjected to 20%-80%-20% cyles and various temperature values.

$$C_{fade}(nc, T) = 7.617 \cdot 10^{-4} \cdot e^{0.01705 \cdot T} \cdot nc^{0.5} \tag{7.5}$$

Nevertheless, the capacity fade model given in (7.5) should be treated with caution for temperature values below 25°C since it might return erroneous results.

7.2.4 Dependence on average SOC-level

The LFP/C battery cells used to investigate the effect of the average SOC-level on the capacity fade, did not reach the EOL criterion at the moment of writing this, as shown in Fig. 7.6. Therefore, the measured capacity fade characteristics had to be extrapolated until the 20% capacity fade EOL criterion was achieved.

The measured and fitted capacity fade characteristics of the Li-ion battery cells used to investigate the effect of average SOC-level on the capacity degradation are shown in Fig. 7.6. The obtained characteristics are showing that the decrease of the capacity of the LFP/C battery cells is strongly dependent on the average SOC-level and the capacity loss is accelerated by decreasing average SOC-level. These results are in opposition with the capacity fade results obtained for calendar ageing conditions (see Chapter 6.2), which were showing a decrease of the capacity fade rate when the storage SOC-level was decreased.

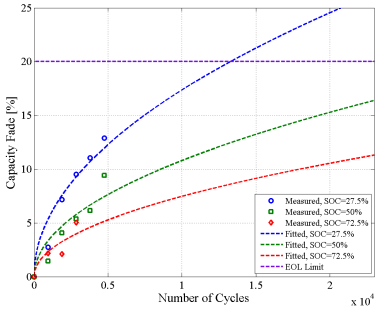

Figure 7.6: *Dependence on the average SOC-level of the capacity fade measured on the LFP/C cells subjected to accelerated cycling lifetime tests.*

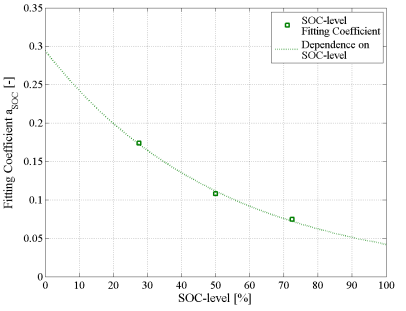

Figure 7.7: *Exponential relationship between the curve fitting coefficients (see TC5, TC10, and TC11 - Table 7.1) and the cycling average SOC-level.*

To describe mathematically the dependence of the capacity fade on the average cycling SOC-level, the fitting coefficients obtained for *TC5*, *TC10*, and *TC11* and presented in Table 7.1 went for a second round of fitting as illustrated in Fig. 7.7. Thus, it was

found that the capacity fade of the tested LFP/C battery cells depends exponentially on the average SOC-level of the cycle; this dependency is given in (7.6).

$$b_{nc}(SOC) = 0.2943 \cdot e^{-0.01943 \cdot SOC} \tag{7.6}$$

In order to obtain a model which expresses the capacity fade in function of the average SOC-level for the LFP/C cells cycled at 42.5^{o}C with a 35% cycle depth, the functions given in (7.1) and (7.6) were combined, yielding:

$$C_{fade}(nc, SOC) = 0.2943 \cdot e^{-0.01943 \cdot SOC} \cdot nc^{0.5} \tag{7.7}$$

Until this moment, the dependence of the capacity fade on the cycling cycle depth (see (7.3)), cycling temperature (see 7.5), and average SOC-level (see (7.7)) have been obtained separately. Similar to the case of the calendar ageing, a scaling of the three functions was performed in order to combine, into one single figure of merit, the main effects of the three considered stress factors on the capacity fade. Thus, the general lifetime model, which is able to predict the capacity fade of the LFP/C battery cells during cycling at all operating conditions, was obtained and is presented in 7.8.

$$C_{fade}(nc, cd, T, SOC) = 2.6418 \cdot e^{-0.01943 \cdot SOC} \cdot (0.004 \cdot e^{0.01705 \cdot T}) \cdot (0.0123 \cdot cd^{0.7162}) \cdot nc^{0.5} \tag{7.8}$$

In order to exemplify the developed capacity fade lifetime model (7.8), the cycling lifetime - expressed in number of cycles, of the tested LFP/C battery cells was estimated for different operating conditions as presented in Fig. 7.8.

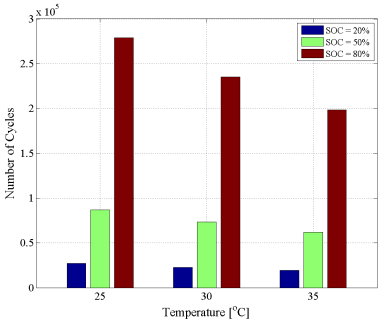

Figure 7.8: *Estimation of the cycle lifetime of LFP/C battery cells cycled at different temperature and average SOC-levels considering a 20% cycle depth (the EOL criterion was set at 20% capacity fade).*

Furthermore, according to the developed capacity fade lifetime model, the tested

LFP/C battery cells are able to withstand approximately 8500 full cycles, at 25^{o}C and considering a 50% average SOC-level, until they will reach a 20% capacity fade EOL criterion.

7.3 Pulse power capability decrease

The PPC decrease of the LFP/C battery cells, which were aged following the cycling conditions summarized in Table 5.2, was calculated similar to the case of calendar ageing using formula 6.9. In order to be consistent with the procedure and the results presented for calendar aged cells, the results obtained for the PPC decrease during cycling ageing that will be presented in this section correspond to the following conditions: discharging from 80% SOC considering the maximum current (i.e., 10A).

The discharge PPC values measured (at the aforementioned conditions) for the LFP/C battery cells during consecutive RPTs throughout the accelerated cycling lifetime tests are presented in Appendix E.2 (see Fig. E.85 - Fig. E.100) for all the carried out TCs. As one can observe, the decrease of the LFP/C cells' PPC caused by the cycling ageing conditions did not exceed 1% even though for the majority of the considered TCs, the cells have reached the predefined EOL criterion. Furthermore, since for the TCs, which were investigating the influence of the average SOC-level on the PPC decrease, the degradation of the PPC was extremely small (between 0% - 0.4%) and the number of obtained data points were reduced, the influence of this stress factor on the PPC decrease will not be investigated.

Similar to all the presented ageing results, the decrease of the PPC caused by cycling ageing was analyzed following the two-steps fitting procedure.

7.3.1 Dependence on number of cycles

The decrease of the PPC during cycling was fitted using a first order polynomial function, which is given in (7.9).

$$PPC_{decrease}(nc) = c_{nc} \cdot nc \tag{7.9}$$

where, c_{nc} represents the coefficient of the fitting function, and nc represents the number of cycles.

The results of fitting the PPC decrease evolution, corresponding to each of the performed TCs, with the proposed fitting function (7.9) are summarized in Table 7.2, while the comparison between the measured and fitted PPC decrease characteristics are shown

in Appendix E.2.4 (see Fig. E.118 - Fig. E.125). The obtained R^2 values are showing that the proposed function was able to fit with relatively-high accuracy the measured PPC decrease.

Table 7.2: *Dependence of the PPC degradation on the number of cycles. Fitting functions and accuracy*

Test Case	Fitting Function	R^2
Calendar 1	$C_{fade-TC1}(nc) = 1.710 \cdot 10^{-5} \cdot nc$	0.8958
Calendar 2	$C_{fade-TC2}(nc) = 7.173 \cdot 10^{-5} \cdot nc$	0.8161
Calendar 3	$C_{fade-TC3}(nc) = 9.277 \cdot 10^{-5} \cdot nc$	0.9415
Calendar 6	$C_{fade-TC6}(nc) = 4.720 \cdot 10^{-5} \cdot nc$	0.9434
Calendar 9	$C_{fade-TC9}(nc) = 3.823 \cdot 10^{-5} \cdot nc$	0.7944

Furthermore, it has to be stressed that the measured PPC degradation during both cycling and calendar ageing depends linearly on time. Consequently, it can be concluded that most probably the PPC decrease during cycling and storage is induced by the same ageing mechanism or by a combination of the same ageing mechanisms.

7.3.2 Dependence on cycle depth

The effect of the cycle depth on the PPC decrease of the LFP/C battery cells was investigated during *TC1*, *TC2*, and *TC3*. The obtained PPC decrease characteristics and their linear fitting as function of number of cycles are presented in Fig. 7.9.

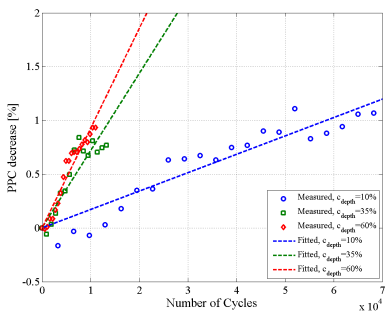

Figure 7.9: *Dependence on the cycle depth of the PPC decrease measured on the LFP/C cells subjected to accelerated cycling lifetime tests.*

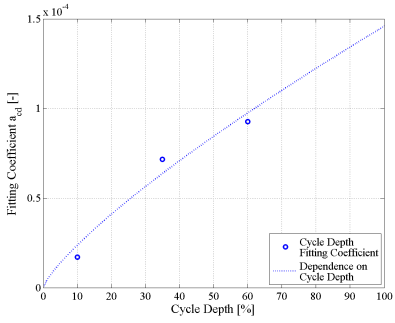

Figure 7.10: *Power-law relationship between the curve fitting coefficients (see TC1, TC2, and TC3 - Table 7.1) and the considered cycle depths.*

The power law function given in (7.10) was found to estimate with high accuracy (R^2=0.9574) the dependence of the linear fitting coefficients (correspoding to *TC1*, *TC2*, and *TC3*) on the cycle depth, as shown in Fig. 7.12.

$$c_{nc}(cd) = 3.853 \cdot 10^{-6} \cdot cd^{0.7891} \tag{7.10}$$

The general function, which expresses the decrease of the PPC as function of the number of cycles and their corresponding cycle depths for a temperature of 55^{o}C was obtained as:

$$PPC_{decrease}(nc, cd) = 3.853 \cdot 10^{-6} \cdot cd^{0.7891} \cdot nc \tag{7.11}$$

7.3.3 Dependence on temperature

The measured and fitted capacity fade characteristics obtained for the LFP/C battery cells, which were subjected to accelerated cycling lifetime tests investigating the effect of temperature, are illustrated in Fig. 7.12. The measured PPC of the tested Li-ion battery cells was found to decrease exponentially with increasing the temperature (see Fig. 7.12).

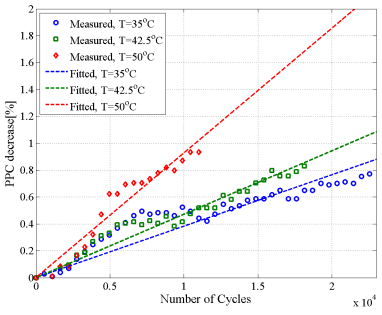

Figure 7.11: *Dependence on the temperature of the PPC decrease measured on the LFP/C cells subjected to accelerated cycling lifetime tests.*

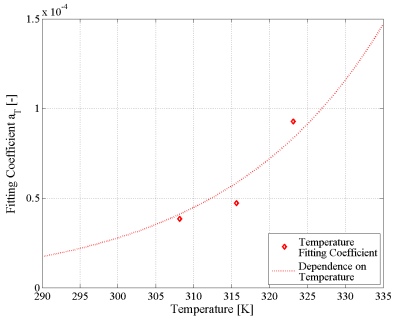

Figure 7.12: *Exponential relationship between the curve fitting coefficients (see TC3, TC6, and TC9 - Table 7.1) and the cycling temperature.*

The function, which estimates the decrease of the LFP/C battery cells' PPC as function of the cycling temperature for cycle depths of 60% is given in (7.12).

$$PPC_{decrease}(nc, T) = 1.751 \cdot 10^{-11} \cdot e^{0.04759 \cdot T} \cdot nc \tag{7.12}$$

The dependence of PPC decrease on the amplitude of the cycle depth and on the cycling temperature have been determined separately as shown in, 7.11 and 7.12 respectively. As already mentioned, the effect of the average SOC-level on the PPC decrease

was not considered since the obtained laboratory results were showing only limited degradation (due to reduced time period allowed for testing). Because any possible interactions between the considered stress factors have been neglected (see Fig. 5.6), a scaling of the obtained lifetime functions 7.11 and 7.12 was considered accurate enough to combine the degradation of the PPC during cycling caused by cycle depth and temperature. Consequently, the developed lifetime model, which is able to estimate the degradation of the PPC during cycling at various conditions is given in (7.13).

$$PPC_{decrease}(nc, cd, T) = ((2.0947) \cdot 10^{-7} \cdot e^{0.04759 \cdot T}) \cdot (3.853 \cdot 10^{-6} \cdot cd^{0.7891}) \cdot nc \quad (7.13)$$

7.4 Changes in EIS plots

The evolution of the battery cells' EIS spectra measured during accelerated cycling ageing at different conditions was investigated as well. For exemplification, the Nyquist plots measured at 20%, 50%, and 80% SOC for the LFP/C battery cells, which were subjected to *TC1* accelerated ageing conditions, are presented in Fig. 7.13 , Fig. 7.14, and Fig. 7.15.

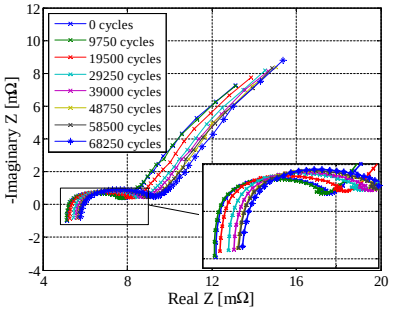

Figure 7.13: *Dependence of LFP/C battery cells' EIS spectra on the number of cycles (ageing conditions: T=50°C, cycle depth=10%, average SOC=50%, RPT conditions: T=25°C, SOC=20%).*

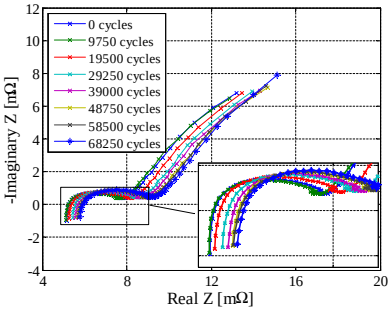

Figure 7.14: *Dependence of LFP/C battery cells' EIS spectra on the number of cycles (ageing conditions: T=50°C, cycle depth=10%, average SOC=50%, RPT conditions: T=25°C, SOC=50%).*

In order to be consistent with the results presented until this point, the ageing analysis of the impedance spectra and of the corresponding EEC parameters, was performed only for the measurements carried out at 80% SOC during the RPT. Nevertheless, by analysing the above presented Nyquist curves, which were measured at 20%, 50%, and 80% SOC, no major differences were observed in-between their ageing behaviours.

The effect of cycling ageing on the measured impedance spectra of the LFP/C bat-

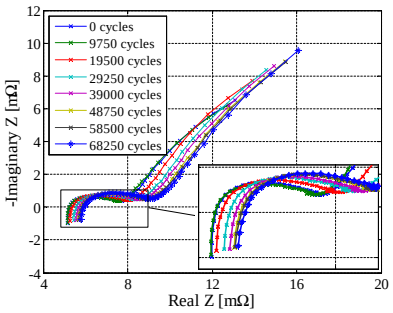

Figure 7.15: *Dependence of LFP/C battery cells' EIS spectra on the number of cycles (ageing conditions: T=50°C, cycle depth=10%, average SOC=50%, RPT conditions: T=25°C, SOC=80%).*

tery cells is mainly visible on the series resistance increase, which causes the continuous shift of the Nyquist curves to the right side of the Nyquist plane, as illustrated in Fig. 7.15; this trend is visible also in the evolution of the values of the series resistance, which were extracted by curve fitting the impedance spectra (see Fig. E.134 - Fig. E.141). Moreover, the same ageing behaviour of the impedance spectra was observed for all the battery cells tested under cycling ageing conditions (see Appendix E.2.5, Fig. E.126 - Fig. E.133).

The impedance spectra of the tested battery cells that where measured during all the accelerated cycling lifetime tests have been curved fitted using the EEC shown in Fig. 3.27 and the circuit parameters have been extracted. Similar to the fitting procedure used for calendar aged cells, the series inductance L_s and the two depression factors n_1 and n_2 have been kept constant. Moreover, the evolution of the extracted values for the resistance R_1 and the generalized capacitance Q_1 were not consistent from one cycling TC to the other. Thus, the ageing evolution of these two parameters will not be analyzed.

Consequently, in the following, only the ageing evolution and its dependence on the cycling conditions for the series resistance R_s, resistance R_2 and generalized capacitance Q_2 is analysed. The evolution during ageing of these three parameters is presented in Appendix E.2.5 (see Fig. E.134 - Fig. E.157) for all the performed TCs. Moreover, due to the same reason as mentioned before, the effect of the average SOC-level on the evolution of the three parameters was not investigated.

7.4.1 Ageing evaluation of series resistance R_s

The increase of the series resistance during the performed accelerated cycling lifetime tests (5.2), ar presented in Fig. E.134 - Fig. E.141. The series resistance R_s was found to

increase linearly with the number of cycles during cycling ageing. The results obtained for fitting the series resistance increase, for all the considered TCs, with the first degree polynomial function given in (7.14) are summarized in Table 7.3. The R^2 values obtained for fitting the series resistance increase characteristics show that the proposed linear functions were a good choice.

$$Rs_{increase}(nc) = d_{nc} \cdot nc \tag{7.14}$$

where d_{nc} represents the coefficient of the function used to fit the increase of the series resistance.

Table 7.3: *Dependence of the series resistance R_s increase on the performed number of cycles. Fitting functions and accuracy*

Test Case	Fitting Function	R^2
TC 1	$Rs_{increase-TC1}(t) = 0.000599 \cdot nc$	0.8922
TC 2	$Rs_{increase-TC2}(t) = 0.000196 \cdot nc$	0.8117
TC 3	$Rs_{increase-TC3}(t) = 0.001145 \cdot nc$	0.9394
TC 6	$Rs_{increase-TC6}(t) = 0.000501 \cdot nc$	0.9468
TC 9	$Rs_{increase-TC9}(t) = 0.000304 \cdot nc$	0.8081

The dependence of the R_s increase rate on the cycle depth is presented in Fig. 7.16. As shown in Fig. E.158, a power law function describes accurately (R^2=0.9864) the dependence of the series resistance increase on the amplitude of the cycle depth.

The influence of the temperature on the increase of the series resistance during cycling is presented in Fig. 7.17. Similar to the case of all investigated parameters, the temperature accelerates in an exponential manner the degradation of the series resistance, as shown in Fig. E.159.

The two functions, which are describing separately the increase during cycling of the series resistance R_s caused by the amplitude of the cycle depth and by the temperature, are given in (7.15) and (7.16), respectively.

$$Rs_{increase}(nc, cd) = 2.356 \cdot 10^{-5} \cdot cd^{0.9395} \cdot nc \tag{7.15}$$

$$Rs_{increase}(nc, T) = 8.733 \cdot 10^{-17} \cdot e^{0.0934 \cdot T} \cdot nc \tag{7.16}$$

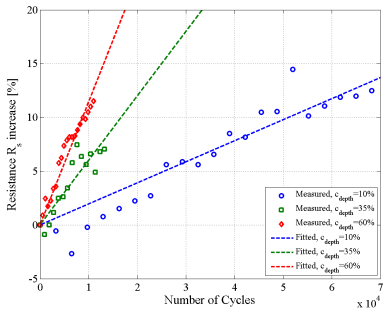

Figure 7.16: *Dependence on the cycle depth of the R_s increase, measured on the LFP/C cells subjected to accelerated cycling lifetime tests.*

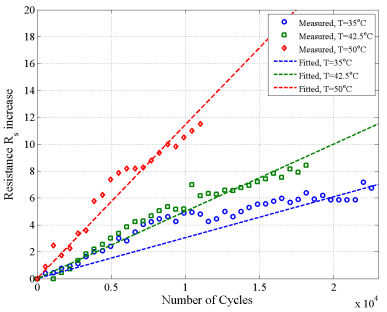

Figure 7.17: *Dependence on the cycling temperature of the R_s increase measured on the LFP/C cells subjected to accelerated cycling lifetime tests.*

The lifetime model (7.17), which is able to describe the increase of R_s at various cycling conditions was obtained by unifying the contributions of the two considered stress factors.

$$Rs_{increase}(nc, cd, T) = (7.799 \cdot 10^{-14} \cdot e^{0.0934 \cdot T}) \cdot (2.356 \cdot 10^{-5} \cdot cd^{0.9395}) \cdot nc \quad (7.17)$$

The cycling lifetime models developed for predicting the PPC decrease (7.13) and the series resistance R_s (7.17) have similar dependences on both the cycle depth amplitude (power-law dependence) and temperature (exponential dependence). Therefore, it can be concluded that the degradation of the two parameters during cycling are caused by the same ageing mechanisms. Moreover, it has to be reminded that the same relationship was found between the LFP/C battery cells which have been aged following storage (calendar) conditions.

7.4.2 Ageing evaluation of series resistance R_2

The increase of the resistance R_2 during the performed accelerated cycling lifetime tests are presented in Fig. E.142 - Fig. E.149 (see Appendix E.2.5).

By comparing the obtained results, which are showing the increase of the series resistance R_s (i.e., 6-15%) and of the resistance R_2 (i.e., 150-500%) during cycling, one can conclude that independent on the considered accelerated ageing conditions, the resistance R_2 is degrading much faster. This ageing behaviour might suggest that the ageing mechanisms responsible for the increase of resistance R_2 is one of the dominant ageing

mechanisms on the LFP/C battery cells during cycling.

Independent on the considered cycling conditions, the increase of the resistance R_2 has shown a linear dependence on the number of cycles. By fitting the increase of resistance R_2 with a first degree polynomial function, for all performed TCs, the results presented in Table 7.4 were obtained.

Table 7.4: *Dependence of the resistance R_2 increase on the performed number of cycles. Fitting functions and accuracy*

Test Case	Fitting Function	R^2
TC 1	$R2_{increase-TC1}(t) = 0.00210 \cdot nc$	0.7672
TC 2	$R2_{increase-TC2}(t) = 0.01773 \cdot nc$	0.6820
TC 3	$R2_{increase-TC3}(t) = 0.03199 \cdot nc$	0.8817
TC 6	$R2_{increase-TC6}(t) = 0.02015 \cdot nc$	0.9452
TC 9	$R2_{increase-TC9}(t) = 0.00844 \cdot nc$	0.8577

The lower accuracy values, obtained for fitting the increase of resistance R_2 with the proposed linear function, were mainly caused by the scattering of the data points, which were acquired from the fitting processes.

The effect of the cycle depth amplitude on the increase of resistance R_2 during cycling is presented in Fig. 7.18. As illustrated in Fig. E.160, the dependence of resistance R_2 increase rate on the cycle depth can be expressed with high accuracy (R^2=0.9744) using a first degree polynomial function. Thus, the model which estimates the increase of resistance R_2 during cycling at 55^{o}C with different cycle depths amplitude is given by:

$$R2_{increase}(nc, cd) = 5.342 \cdot 10^{-4} \cdot cd \cdot nc \tag{7.18}$$

The influence of temperature on the resistance R_2 increase during cycling is shown in Fig. 7.19. An exponential relationship was found between the increase of the temperature and degradation of resistance R_2 (see Fig. E.161). Thus, considering the linear increase of this resistance with the number of cycles and the exponential dependence on the temperature, the model given in (7.19) was derived.

$$R2_{increase}(nc, T) = 4.43 \cdot 10^{-11} \cdot e^{0.07742 \cdot T} \cdot nc \tag{7.19}$$

By unifying the derived effects of the cycle depth amplitude (7.18) and of the temperature (7.19) on the increase of resistance R_2, the lifetime model given in (7.20) was developed.

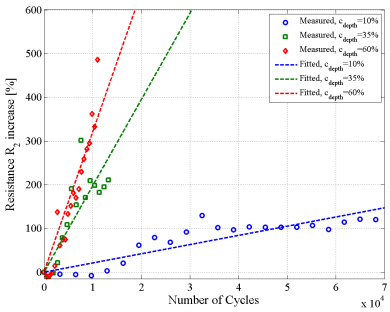

Figure 7.18: *Dependence on the cycle depth of the* R_2 *increase, measured on the LFP/C cells subjected to accelerated cycling lifetime tests.*

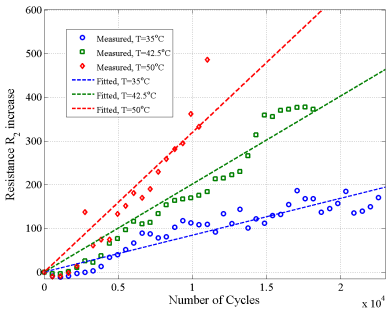

Figure 7.19: *Dependence on the cycling temperature of the* R_2 *increase measured on the LFP/C cells subjected to accelerated cycling lifetime tests.*

$$R2_{increase}(nc, cd, T) = (1.3636 \cdot 10^{-11} \cdot e^{0.07742 \cdot T}) \cdot 5.342 \cdot 10^{-4} \cdot cd \cdot nc \qquad (7.20)$$

7.4.3 Ageing evaluation of generalized capacitance Q_2

In contrast with the resistance R_2, the generalized capacitance Q_2 is decreasing during cycling ageing, independent on the applied conditions. The degradation of the generalized capacitance Q_2 during cycling for all the considered conditions is presented in Appendix E.2.6 (see Fig. E.150 - Fig. E.149). Even though Q_2 is decreasing during cycling, the same first degree polynomial function, as in the case of resistance R_2, was used to fit the degradation pace as function of the number of cycles. The results of the fitting process are summarized in Table 7.5.

Table 7.5: *Dependence of the generalized capacitance* Q_2 *increase on the performed number of cycles. Fitting functions and accuracy*

Test Case	Fitting Function	R^2
TC 1	$Q2_{increase-TC1}(t) = 0.000373 \cdot nc$	0.8536
TC 2	$Q2_{increase-TC2}(t) = 0.001745 \cdot nc$	0.6316
TC 3	$Q2_{increase-TC3}(t) = 0.001851 \cdot nc$	0.8569
TC 6	$Q2_{increase-TC6}(t) = 0.001306 \cdot nc$	0.9110
TC 9	$Q2_{increase-TC9}(t) = 0.001104 \cdot nc$	0.8054

The dependence of the generalized capacitance Q_2 on the cycle depth (for 50^{o}C) and on the temperature (for 60% cycle depth) are shown in Fig. 7.20 and Fig. 7.21, respectively. As in the case of the resistance R_2, the decrease of Q_2 during cycling depends linearly on the amplitude of the cycle depth, as presented in Fig. E.162. So, the function, which expresses the influence of the number of cycles and their cycle depths on the capacitance decrease, is given in (7.21).

$$Q2_{decrease}(nc, cd) = 3.571 \cdot 10^{-5} \cdot cd \cdot nc \tag{7.21}$$

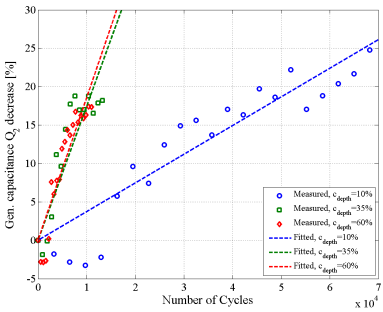

Figure 7.20: *Dependence on the cycle depth of the Q_2 decrease, measured on the LFP/C cells subjected to accelerated cycling lifetime tests.*

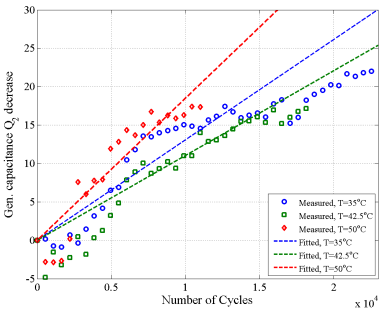

Figure 7.21: *Dependence on the cycling temperature of the Q_2 decrease measured on the LFP/C cells subjected to accelerated cycling lifetime tests.*

Moreover, it was found that the decrease of the generalized capacitance Q_2 depends exponentially on the cycling temperature; this dependence is shown in Fig. E.163. Thus, considering the linear dependence on the number of performed cycles and the exponentially dependence on the cycling temperature, the decrease of the generalized capacitance during cycling with a 60% cycle depth amplitude was expressed as:

$$Q2_{decrease}(nc, T) = 1.715 \cdot 10^{-8} \cdot e^{0.0358 \cdot T} \cdot nc \tag{7.22}$$

The general lifetime model that is able to estimate the decrease of the generalized capacitance Q_2 during cycling at different temperatures and cycle depth amplitudes was obtained by applying a scaling factor between the two sub-models (7.22) and (7.21), yielding:

$$Q2_{decrease}(nc, cd, T) = (9.457 \cdot 10^{-6} \cdot e^{0.0358 \cdot T}) \cdot 3.571 \cdot 10^{-5} \cdot cd \cdot nc \tag{7.23}$$

By comparing the structure of the lifetime models developed for the resistance R_2 (7.20) and for the generalized capacitance Q_2 (7.23), one can observe that the same dependences on the applied stress factors were found for both parameters: linear dependence on the number of performed cycles and on the cycle depth amplitudes, and exponential dependence on the cycling temperature.

7.5 Summary

This chapter was dedicated to the analysis of the results obtained from accelerated cycling ageing tests. Moreover, lifetime models, which are able to estimate the capacity fade, PPC decrease, and the variation of certain EEC parameters at various cycling conditions, were developed.

The capacity fade of the LFP/C battery cells was found to depend following a square-root function on the number of performed cycles. Moreover, the capacity loss depends exponentially on the cycling temperature and on the average SOC-level; the dependence of the capacity fade on the cycle depth follows a power function. Similar to the case of calendar ageing, the PPC of the tested Li-ion batteries is degrading much more slower than the capacity; the maximum obtained PPC decrease during cycling ageing was approximately 1%, time in which the capacity fade had already reached 20%. By analysing the ageing results obtained for the parameters of the EEC, which was used to curve fit the measured EIS spectra, it was observed that during cycling only the series resistance R_s, resistance R_2, and generalized capacitance Q_2 were showing clear degradation trends.

Chapter 8

LiFePO$_4$/C Battery Cell Performance-Degradation Model

This chapter is dedicated to the performance-degradation model for the studied LiFePO$_4$/C battery cell. The model is mainly parametrized based on the results obtained from the accelerated lifetime tests, which were analysed during Chapter 6 and 7. Starting from the general representation of the performance-degradation model, the structure of the developed LFP/C battery cell lifetime model is illustrated and the algorithm behind the proposed model is explained. The last section of this chapter is dedicated to the validation of the developed model; the validation was carried out by comparing the results obtained in laboratory from additional ageing tests with the results returned by the performance-degradation model.

8.1 Performance-Degradation Model Structure

An EEC-based performance-degradation modelling approach was selected in Chapter 4 for modelling the lifetime of the studied LFP/C battery cells. The advantages of the performance-degradation models over the throughput-counting and cycle-counting lifetime models is their capability of predicting besides the SOH and RUL, the ageing behaviour of the battery cell capacity, PPC, and voltage, as well.

The basic structure of the proposed performance-degradation model is presented in Fig. 8.1.

The performance-degradation model is composed of two sub-models: the performance model, which is mainly used to estimate the voltage of the LFP/C battery cell

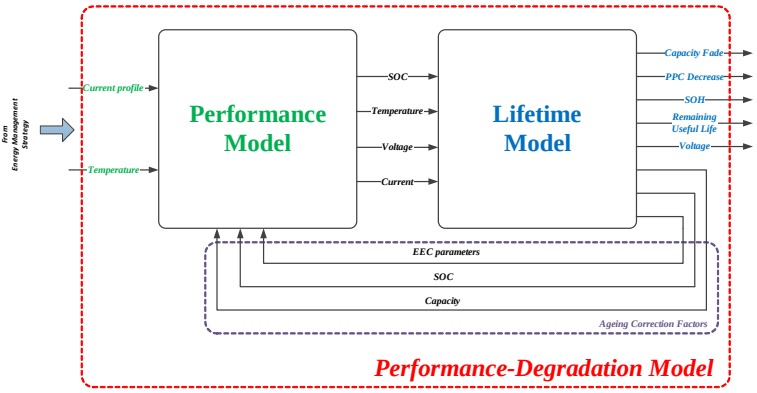

Figure 8.1: *Structure of the performance-degradation model for the LFP/C battery cell.*

and the lifetime model, which predicts the capacity fade and the PPC decrease, and calculates the SOH and the RUL of the battery cell for a given profile.

The inputs of the proposed performance-degradation model are the current and temperature profiles, which are obtained from the energy management strategy. Depending on the chosen energy management strategy and on the load, the current profile may vary significantly. The operating temperature of Li-ion batteries used in VPP applications is maintained constant, close to the value specified by the manufacturers, using a forced air-ventilation system. A temperature profile measured on LFP/C battery cells, which are used to provide primary frequency regulation on the Danish energy market [35], [42], is illustrated in Fig. 8.2.

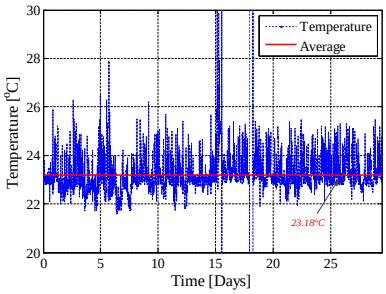

Figure 8.2: *One month temperature profile measured on LFP/C battery cells, used to provide primary frequency regulation service.*

During operation of the ESS, the temperature of the LFP/C battery cells varies in a narrow interval between 22^{o}C and 26^{o}C, with a month average value of approximately 23.2^{o}C, as shown in Fig. 8.2. Consequently, a constant temperature, equal to 25^{o}C is

considered in this thesis as the normal operating temperature for the LFP/C battery cells used in VPP applications; this temperature value was used for all the lifetime estimation investigations presented in Chapter 8 and Chapter 9.

The structure of the performance model block, which is illustrated in Fig. 8.1, is the one proposed in Fig. 3.31 for implementation of the performance model of LFP/C battery cells. Thus, for further details concerning the implementation of the performance model, the reader is referred to Chapter 3.2.2.

The proposed structure of the lifetime model for determining the ageing behaviour of the LFP/C battery cells for a certain profile is presented in Fig. 8.3. The lifetime model receives information from the performance model about the mission profile (SOC and temperature) to which the LFP/C battery cell is subjected; additionally, information about the voltage and current of the battery cell might be fed to the lifetime model, as well. The lifetime model returns at its output information about the SOH and RUL of the LFP/C battery, which are calculated from the obtained capacity fade and PPC decrease, based on a predefined EOL criterion.

The mission profiles of Li-ion battery cells operating in VPP applications are usually complex since they are composed of various combinations of cycling (cycles with different cycle depths) and idling conditions, which theoretically affect also the temperature of the batteries; however, as already mentioned, these temperatures deviations are small and thus the effect of temperature (during both cycling and idling conditions) is not considered in the upcoming analyses. An example of a SOC mission profile that is characteristic for Li-ion batteries used in VPP applications is presented in Fig. 4.1.

In order to be applied to the developed lifetime models (in the *Ageing Calculator* block - see Fig. 8.3), the SOC mission profile needs to be further processed. The cycles composing the SOC profile are extracted and sorted according to their cycle depths using a cycle counting method; in this thesis, the rainflow cycle counting algorithm was used. Besides counting and sorting the cycles according to their cycle depths, this cycle counting algorithm also extracts the periods when the battery cell is idling (calendar ageing).

The rainflow cycle counting algorithm was firstly used in mechanical engineering for counting the fatigue cycles to which materials were subjected and thus to estimate possible failure [135], [141]. Due to similarities between the fatigue of materials and the degradation of batteries, the rainflow cycle counting algorithm is suitable and was applied for determining the lifetime of batteries, as well [36], [142], [143]. The rainflow counting method is based on the Palmgren-Miner rule; this rule considers several assumptions that are also translated when the rainflow method is applied to Li-ion batteries cycle counting.

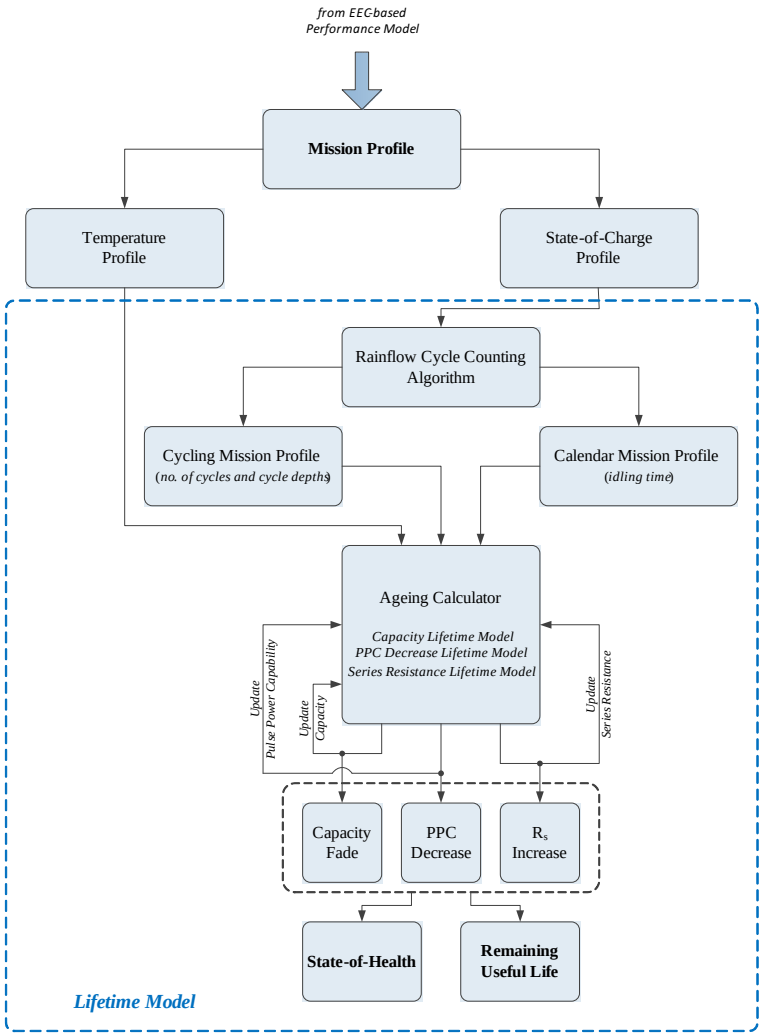

Figure 8.3: *Schematic representation of the proposed lifetime model.*

The most important assumption, which is considered by the Palmgren-Miner rule, is that the sequence of cycles does not have an influence on the lifetime of the battery; for example, a high cycle-depth cycle followed by a low cycle-depth cycle has the same influence on the lifetime of the battery as a low cycle-depth cycle followed by a high cycle-depth cycle. As already mentioned, in its basic form, the rainflow-cycle counting method extracts the cycles and counts them according to their cycle depths. In this thesis, the basic rainflow cycle counting algorithm was improved in order to consider also the average SOC-level at which the cycle was performed. An example of the functionality of the

improved rainflow cycle counting algorithm is presented in Fig. 8.4 and Fig. 8.5, where the translation from the SOC mission profile to a 3D-histogram showing the number of cycles and their corresponding cycle depths and average SOC-level is illustrated.

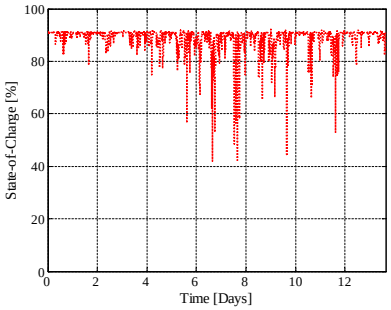

Figure 8.4: *Field-measured SOC mission profile for the LFP/C battery cell, characteristic to the PFR service.*

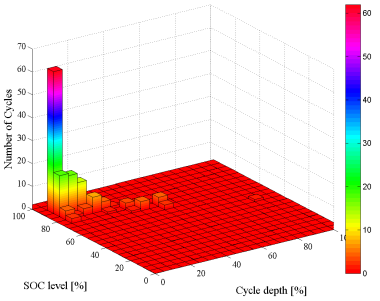

Figure 8.5: *3D-histogram extracted from the SOC-profile presented in Fig. 8.4*

The procedure behind the rainflow cycle counting algorithm is composed of several steps, which are presented in detail in [36], [135].

The stress factors and their corresponding stress levels, which have been extracted from the SOC mission profile using the rainflow cycle counting algorithm, together with the temperature profile (in this case constant at T=25^{o}C) represent the inputs for the *Ageing Calculator* block of the proposed lifetime model.

8.2 Incremental Decrease of LFP/C Battery Cell Performance Parameters

The developed lifetime model is based on the concept of the incremental decrease of the LFP/C battery cells performance parameters (e.g. capacity and PPC), which is caused by ageing. The stress factors and their corresponding levels obtained from running the rainflow cycle counting algorithm and from the temperature profile are accumulated and sent to the *Ageing Calculator* block (see Fig. 8.3). By applying the extracted sequence of stresses to the lifetime models, which were developed and presented in Chapter 6 and Chapter 7, the degradation of the LFP/C battery cell is obtained in terms of capacity fade, PPC decrease, and increase of the series resistance R_s. Furthermore, tacking into account the obtained degradation and considering the EOL criterion, the SOH of the battery cell and its RUL for the specific application are computed.

Based on the developed lifetime models, which are presented in Chapter 6 and Chapter 7, it was observed that the performance parameters of the LFP/C battery cells are degrading in time following various non-linear characteristics (e.g., see (6.8) and (7.8), for capacity fade during idling and cycling, respectively). This has suggested that the same sequence of stress factors and their corresponding levels does not cause the same degradation to the performance parameters of the LFP/C battery cell if it is applied at the cell's BOL or for an already aged cell. Consequently, in order to obtain reliable lifetime predictions, the performance parameters have to be updated after each iteration of the incremental lifetime calculations; the aforementioned sequence are graphically illustrated both in Fig. 8.1 and on Fig. 8.3.

Moreover, it has to be mentioned that the proposed performance-degradation model does not considered the degradation in time of the voltage of the tested LFP/C battery cells. This limitation was mainly caused by the results obtained from the ageing behaviour of the parameters of the EEC, which was used to fit the measured impedance spectra. As shown in Chapter 6 and Chapter 7, only for the degradation of the series resistance R_s a lifetime model was possible to be built for both calendar and cycling ageing conditions.

The *Ageing calculator* block is composed of the lifetime models developed throughout Chapter Chapter 6 and Chapter 7 for both cycling and calendar dimensions of the capacity fade, PPC decrease, and series resistance, R_s, increase. All these functions were considered in the structure of the lifetime model in order to ensure that accurate estimation of the ageing behaviour of the LFP/C battery cell and its lifetime for a certain VPP applications will be obtained.

1. Capacity fade

   The capacity fade during calendar ageing is described by the lifetime model (6.8). As the model shows, the calendar capacity fade it depends non-linearly on the storage time, storage SOC-level, and temperature. These dependences are illustrated in Fig. 8.6, where the calendar lifetime in terms of capacity fade is expressed in function of the storage temperature and storage SOC, considering an EOL criterion of 20% capacity fade. As marked on the plot, the LFP/C batery cells are able to withstand approximately 20 years, before the EOL criterion is reached, if they are stored at 25^{o}C and 50% SOC. Even though the operating temperature of the LFP/C battery cell used in VPP applications is maintained constant close to 25^{o}C, the effect of this stress factor on the capacity fade was plotted for a relative narrow interval (25^{o}C - 45^{o}C). This was done in order to show that even small deviations from the temperature set-point will have a huge impact on the capacity degradation of the battery cell during storage.

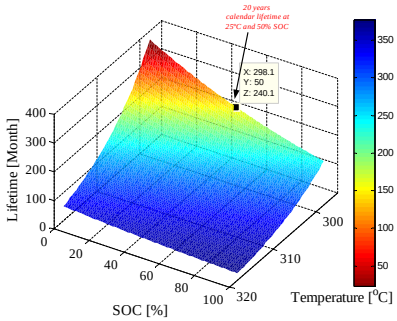

Figure 8.6: *Lifetime estimation for the LFP/C battery cell stored at different temperatures and SOC-levels, before the EOL criterion (i.e., 20% capacity fade) is reached.*

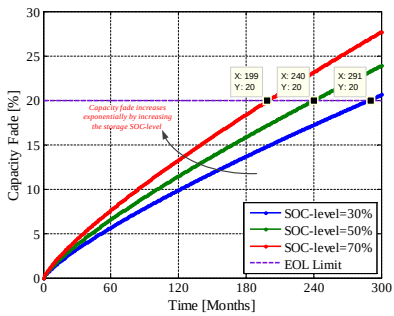

Figure 8.7: *Influence of the storage SOC-level on the capacity fade characteristic of the LFP/C battery cells stored at 25^{o}C.*

Fig. 8.7 exemplifies the capacity fade behaviour of the LFP/C battery cell, which was stored at 25^{o}C and three different SOC-levels; as illustrated, the capacity fade rate has increased exponentially when the storage SOC-level was increased. Therefore, this stress factors has to be carefully considered, when the energy management strategy of the battery ESS is developed.

The capacity fade of the LFP/C battery cells during cycling operation is described by the model (7.8) and was found to depend non-linearly on the number of cycles and their cycle depth, on the average SOC-level and on the temperature. Since the LFP/C battery cells operating in VPP applications are subjected to very complex cycling conditions (see Fig. 8.4), all the aforementioned dependences were considered in the structure of the developed lifetime model. Fig. 8.8 illustrates the variation of the number of cycles that the tested LFP/C cells can withstand depending on the cycle depth and on the operating temperature; according to the developed model the tested battery cells are able to withstand approximately 8500 full cycles for an operating temperature of 25^{o}C.

The lifetime characteristic, which presents the number of cycle that the LFP/C battery cell can perform for every cycle depth, until the EOL will be reached, is presented in Fig. 8.9.

2. Pulse power capability decrease

   The proposed lifetime model returns also information about the PPC decrease of the LFP/C battery cells that is caused by the operating (cycling and calendar) conditions. The functions describing the PPC decrease during calendar and cycling ageing at various conditions are given in (6.15) and (7.13), respectively. The depen-

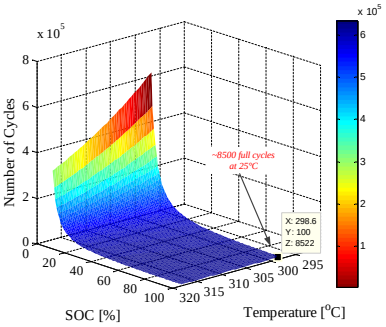

Figure 8.8: *Lifetime estimation for the LFP/C battery cell cycled at different temperatures and different cycle depths, before the EOL criterion (i.e., 20% capacity fade) is reached.*

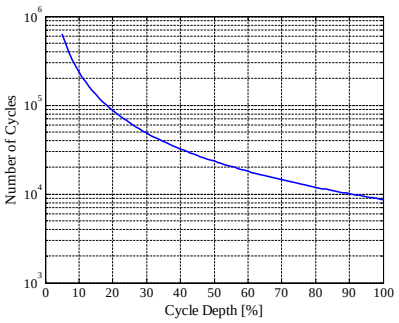

Figure 8.9: *Number of cycles that the LFP/C battery cell can withstand at different cycle depths until EOL criterion (i.e., capacity fade) is reached; T=25°C, average SOC=50%.*

dence of this performance parameter on the operating conditions are illustrated in Fig. 8.10 and Fig. 8.11 for the calendar and cycling dimensions, respectively.

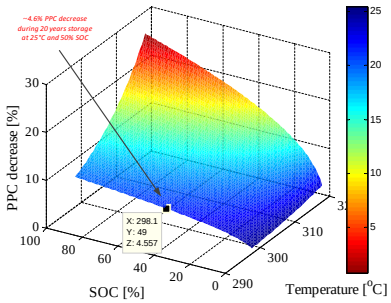

Figure 8.10: *Estimation of PPC decrease during storage at various SOC-levels and temperatures; a 20 years calendar lifetime was considered.*

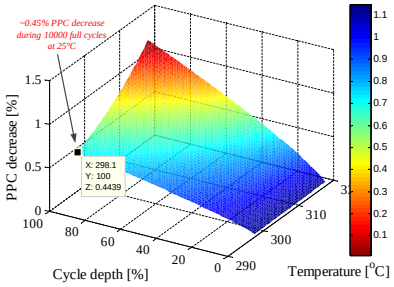

Figure 8.11: *Estimation of PPC decrease during cycling with different cycle depths and at different temperatures; a 10 000 full cycles cycling lifetime was considered.*

By analysing the results presented on Fig. 8.10 and Fig. 8.11, it was observed that for normal operating conditions (i.e., storage at 25°C and 50% SOC and cycling at 25°C, with 100% cycle depth) the obtained PPC decrease is very low (i.e., 4.5% for calendar and 0.5% for cycling) even though for the same ageing conditions the LFP/C battery reached more than 20% capacity fade. Furthermore, another important aspect is that the calendar ageing conditions are causing much higher (i.e., by one order of magnitude) degradation of the PPC than the "similar" cycling ageing conditions.

3. Series resistance (R_s) increase

The third parameter about which the proposed lifetime model returns information during ageing of the LFP/C battery cells is the series resistance (a parameter of the EEC illustrated in Fig. 3.27 used to curve fitted all the measured battery cell impedance spectra). The increase of the series resistance during calendar and cycling ageing is described by the functions (6.18) and (7.17), respectively. Based on these functions, the dependence of the series resistance on the specific stress factors is illustrated in Fig. 8.12 and in Fig. 8.13.

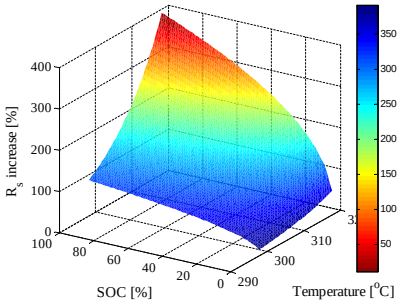

Figure 8.12: *Estimation of R_s increase during storage at various SOC-levels and temperatures for; a 20 years calendar lifetime was considered.*

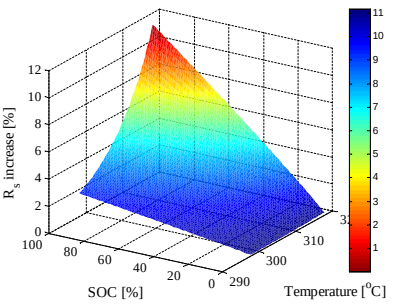

Figure 8.13: *Estimation of R_s increase during cycling with different cycle depths and at different temperatures; a 10 000 full cycles cycling lifetime was considered.*

Similar to the case of the PPC decrease, a much higher increase of the series resistance R_s is cuased by the calendar ageing conditions than by the cycling ageing conditions.

The capacity fade and the pulse power capability decrease are following different ageing patterns in case of calendar ageing, as it is presented in Fig. 8.14. Based on the developed calendar ageing models for (6.8), for capacity fade, and (6.15), for PPC decrease, one can observe that the capacity of the tested LFP/C battery cells is decreasing much faster than the PPC of the same cells, when similar ageing conditions were considered (i.e., 25^{o}C and SOC=50%). Moreover, the same behaviour is observed from Fig. 8.15 where the capacity fade and the pulse power capability decrease characteristics of the tested LFP/C cells obtained for similar cycling ageing conditions (i.e., 25^{o}C and 100% cycle depth cycles) are plotted.

Consequently, since a much faster degradation is obtained for the capacity than for the PPC of the LFP/C battery cells, independent on the ageing conditions, it is better to relate the SOH and RUL parameters to the tested battery cell capacity fade.

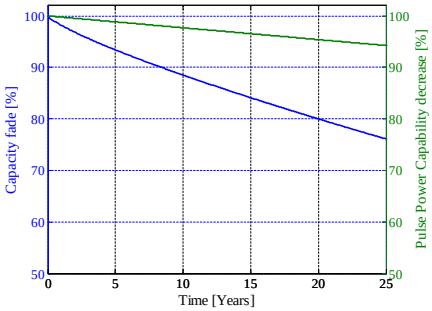

Figure 8.14: *Comparison between capacity fade and PPC decrease of calendar aged LFP/C battery cells at 25°C and SOC=50%.*

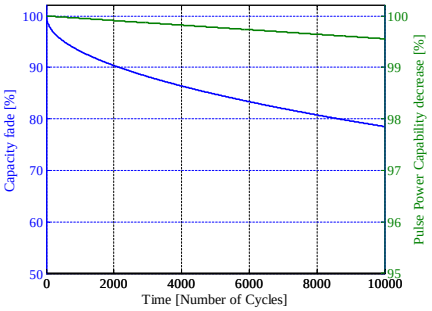

Figure 8.15: *Comparison between capacity fade and PPC decrease of cycling aged LFP/C battery cells at 25°C and 100% cycle depth.*

Moreover, the SOH and RUL of the LFP/C battery cell, for a certain application, are calculated at every operating using equations (8.1) and (8.2), based on the incremental degradation of the capacity fade, which follows the dependences presented in Fig. 8.6 and Fig. 8.8.

$$SOH = \frac{C_{fadeactual}}{C_{fadeEOL}} \tag{8.1}$$

$$RUL = \frac{C_{fadeEOL}}{C_{fadeyear}} \tag{8.2}$$

where, $C_{fadeactual}$ represents the present capacity fade, $C_{fadeEOL}$ represents the capacity fade for the EOL criterion, and $C_{fadeyear}$ represents the capacity fade during one year.

8.3 Verification of the Performance-Degradation Model

8.3.1 Procedure for verification of the performance-degradation model

In order to verify the accuracy of the developed performance-degradation model, fresh LFP/C battery cells have been tested in the laboratory considering two additional test cases. Similar to the performed accelerated ageing tests (both calendar and cycling), three LFP/C battery cells were considered for each verification test case and the obtained average degradation was further used for different analyses.

The procedure which was followed for the verification of the developed lifetime model is summarized in the flowchart presented in Fig. 8.16. The verification process

focuses on the degradation of the capacity of the LFP/C battery cells because, as it was shown in Fig. 8.14 and Fig. 8.15, this performance parameter is degrading much faster than the PPC.

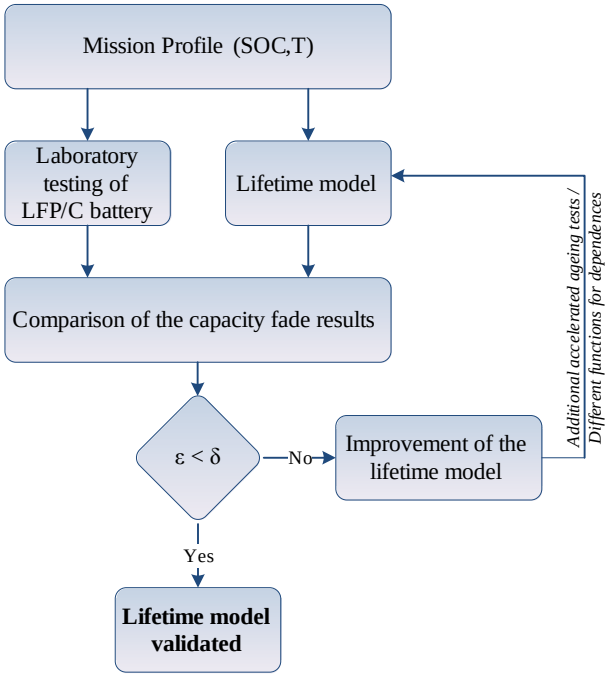

Figure 8.16: *Procedure for verification of the developed LFP/C battery cell performance-degradation model.*

The verification of the proposed performance-degradation model was realized by comparing the capacity fade resulting from laboratory tests with the capacity fade estimated by the model, when the same mission profile is applied for both cases. The developed model is considered validated if its accuracy (expressed by the estimation error ϵ_r) is lower than a predefined threshold value (i.e., $\delta < 15\%$). Nevertheless, if the estimation error is higher than the predefined threshold value, improvement of the lifetime model is necessary; the improvement of the model can be performed following different steps.

8.3.2 Laboratory ageing tests

As already mentioned, two different mission profiles were used to verify the developed performance-degradation model. The results obtained from the laboratory measurements and from the model will be discussed separately for each of the mission pro-

files.

Symmetrical charging/discharging mission profile

The first approach used to verify the performance-degradation model was based on a symmetrical charging/discharging SOC mission profile, presented in Fig. 8.17. Thus, the same approach as it was used for the cycling TCs, which were performed for developing the lifetime models for the performance parameters (e.g., capacity, PPC etc.). However, in order to ensure for a non-biased verification, the conditions used for this verification TC were different than the ones used for the accelerated ageing tests; the conditions of the verification TC using asymmetrical charging/discharging SOC mission profile are summarized in Table 8.1.

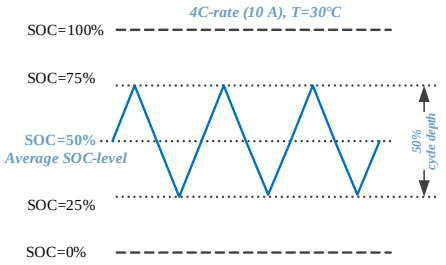

Figure 8.17: *Mission profile used to verify the performance-degradation model of the LFP/C battery cell.*

Table 8.1: *Considered test conditions for the symmetrical charging-discharging mission profile.*

Test Case	LFP/C cells	Temp.	Cycle depth	Average SOC	Performance check
Verification 1	V.1, V.2, V.3	30^{o}C	50%	50%	each 670 cycles

Following the same procedure as in the case of the accelerated cycling ageing tests (see Table 5.2), the incremental degradation of the performance parameters of the tested LFP/C battery cells was quantified by performing RPTs at regular time intervals (after each 670 cycles for this verification case). The capacity of the cells considered for this verification TC and their corresponding capacity fade, which was measured during the ageing process are presented in Fig. F.1 and Fig. F.2 (see Appendix F.1), respectively. Due to time constraints and considering that the capacity degradation at the considered temperature (i.e., 30^{o}C) is relatively slow, the LFP/C battery cells subjected to the this

verification TC did not reached the EOL criterion (see Fig. F.2); however, during the tested period, the battery cells reached a capacity fade of approximately 12%, which was considered representative for analysing the accuracy of the developed performance-degradation model.

The comparison between the capacity fade measured for the LFP/C battery cells that have been tested using the conditions summarized in Table 8.1 and the capacity fade estimated by the model, for the same ageing conditions and for the same time period, are presented in Fig. 8.18.

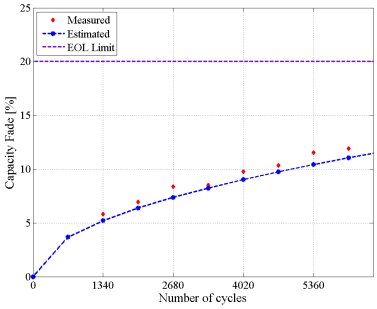

Figure 8.18: *Comparison between measured and estimated capacity fade of the LFP/C battery cells, obtained for the ageing conditions presented in Fig. 8.17.*

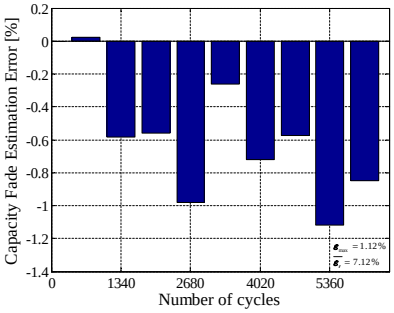

Figure 8.19: *Capacity fade estimation error (absolute error), between model and measurements for LFP/C cells tested under the conditions presented in Fig. 8.17.*

The accuracy of the developed LFP/C battery cell performance-degradation model (evaluated for the capacity fade) obtained for the considered mission profile is presented in Fig. 8.19. The accuracy is expressed in terms of absolute estimation error, which was computed by comparing the capacity fade values obtained from the measurements and model after each RPT and estimation, respectively. As shown in Fig. 8.19, the developed model has the general tendency to underestimate the capacity fade; however, over the considered testing period, the maximum absolute error, computed based on (8.3), did not exceed 1.12% of capacity fade. Furthermore, the average relative estimation error for the considered period, computed based on (8.4), was 7.12%.

$$\epsilon_{max} = max(|C_{fademeas}(i) - C_{fademodel}(i)|) \tag{8.3}$$

$$|\overline{\varepsilon_r}| = 100 \cdot \left| \frac{\overline{Cfade_{meas} - Cfade_{estim}}}{Cfade_{meas}} \right| \tag{8.4}$$

where, ϵ_{max} represents the maximum absolute error, ϵ_r represents the relative error, $C_{fademeas}$ represents the measured capacity fade, $C_{fademodel}$ represents the estimated capacity fade, and i represents the number of measurements/estimations.

Mission profile characteristic to the PFR service

The second approach used to verify the accuracy of the developed performance-degradation model was based on a more realistic mission profile, which considers both the cycling and idling operation of the LFP/C battery cells. Thus, for this verification case, a mission profile measured on field for a battery ESS based on LFP/C battery cells, which is providing PFR service, was used. For more details about the operation or the used energy management strategy of the aforementioned battery ESS, the reader is referred to [20], [35], [42].

In order to perform the evaluation of the developed model, a representative period of the mission profile, with a length of one week, was selected. This one week mission profile, illustrated in Fig. 8.20, was applied to the LFP/C battery cells for seven weeks, and RPT measurements were carried out after each week. In order to be applied to the developed model, the SOC mission profile, shown in Fig. 8.20, was decomposed using the rainflow cycle counting algorithm, following the procedure presented in Fig. 8.3. The cycling mission profile expressed in number of cycles of different cycle depths, performed at various average SOC-levels is presented in Fig. 8.21; additionally, the idling time was extracted, totalling approximately 80% of the operation time.

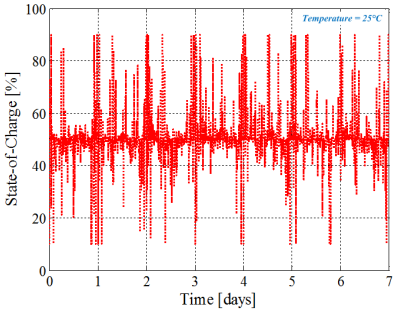

Figure 8.20: *One week mission profile used for verification of the developed LFP/C battery cell performance-degradation model.*

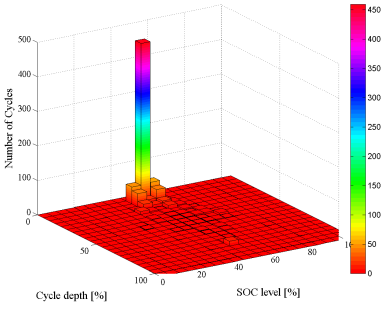

Figure 8.21: *SOC-mission profile obtained from running the rainflow algorithm on the profile presented in Fig. 8.20.*

The conditions of the second verification TC using the PFR-characteristic profile are summarized in Table 8.2.

Table 8.2: *Considered test conditions for the mission profile characteristic to the PFR service.*

Test Case	LFP/C cells	Temp.	Cycle depth	Average SOC	Performance check
Verification 2 PFR-profile	V.4, V.5	25^{o}C	Variable	50%	after each week

As presented in Table 8.2, for this verification TC, only two LFP/C battery cells were used. Consequently, in this case, the average degradation is computed only from the results obtained for two cells. The capacity of the LFP/C battery cells considered for this second verification TC and their corresponding capacity fade, which was measured during seven weeks of ageing process, are presented in Fig. F.3 and Fig. F.4 (see Appendix F.2), respectively. Because the verification profile has been composed of periods when the battery cells were cycled and periods when they were idling, both at 25^{o}C, the measured capacity fade was relatively reduced (i.e., approx. 4.5%).

The comparison between the capacity fade measured on the LFP/C battery cells, which were tested using the PFR mission profile, and the capacity fade estimated by the developed performance model, for the same ageing conditions and for seven weeks of operation, are presented in Fig. 8.22.

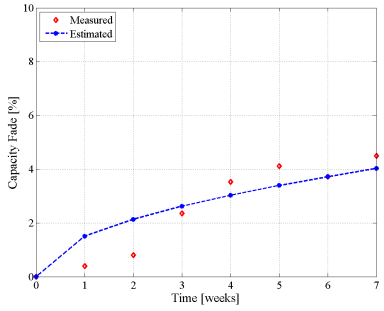

Figure 8.22: *Comparison between measured and estimated capacity fade of the LFP/C battery cells, obtained for the ageing conditions presented in Fig. 8.17.*

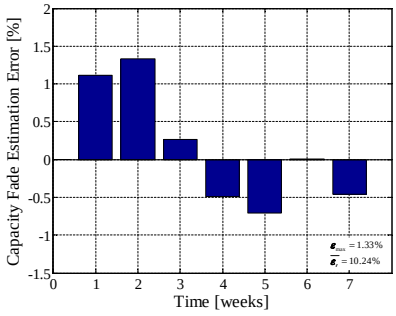

Figure 8.23: *Capacity fade estimation error (absolute error), between model and measurements for LFP/C cells tested under the conditions presented in Fig. 8.17.*

The capacity fade estimation error obtained when the mission profile characteristic to the PFR service was applied both to the LFP/C battery cells and to the developed performance-degradation model is presented in Fig. 8.23. Similar to the case of the first performed verification, the accuracy of the model was expressed in terms of absolute

error. As illustrated in Fig. 8.23, the short observation period (i.e., seven weeks) does not allow to conclude if a clear trend of underestimation or overestimation the capacity fade is present. Nevertheless, the proposed performance-degradation model is able to predict with good accuracy the capacity fade of LFP/C battery cells, which are "providing PFR service" with a maximum error, for the consider period, of 1.33% capacity fade, and an average relative estimation error of 10.24%.

Comparison of the results

By analysing the results obtained during the verification procedure, it can be concluded that the developed performance-degradation model is able to estimate with good accuracy the capacity fade of LFP/C battery cells. The results obtained from the two verification TCs are summarized in Table 8.3.

Table 8.3: *Accuracy of the LFP/C battery cell performance-degradation model for two different mission profiles.*

Test Case	Max. Error	Relative Error
Verification 1 Symmetrical ch/dch	1.12%	7.12%
Verification 2 PFR-profile	1.33%	10.24%

The higher errors, obtained when estimating the capacity fade of the tested LFP/C battery cells for the PFR profile, have been most probably caused by the structure of the second profile, which considers both periods when the cells were cycled and periods when they were idling.

Nevertheless, the obtained estimation errors are relatively-low. Consequently, the developed performance-degradation model was successfully verified and the proposed methodology for lifetime estimation of LFP/C battery cells, based on accelerated ageing tests, was validated.

8.4 Summary

In this chapter, the developed performance-degradation model for the LFP/C battery cells was presented. The proposed model is based on the concept of incremental ageing calculation and was parametrized based on the results obtained from the accelerated calendar and cycling ageing tests. The degradation characteristics of the capacity and power

capability obtained for the same operating conditions has highlighted that the capacity of the LFP/C battery cells is degrading in time much faster than its PPC. Moreover, this finding is valid for both cycling and idling operation. Consequently, for the tested battery cells the SOH information should be rather related with the fade of the capacity and not with decrease of PPC.

The last part of this chapter was dedicated to the verification of the developed performance-degradation model for the LFP/C battery cells. The verification was realized by comparing the measured and estimated capacity fade obtained from verification ageing tests performed in laboratory and by simulation, when two different mission profiles have been considered. The average relative estimation error of the capacity fade was found to vary between 7.1% and 10.2% depending on the applied mission profile. Based on the obtained results, the proposed performance-degradation model for the LFP/C battery cells was considered accurate enough.

The model will be used in the next chapter to evaluate the performance degradation of the LFP/C battery cells, which are used in a VPP applications for providing primary frequency regulation.

Chapter 9

Evaluation of the LiFePO$_4$/C Battery Cell Lifetime in VPP

The objective of this Chapter is to investigate the performance-degradation behaviour of LFP/C battery cells when they are subjected to a realistic mission profile, which was measured on field for a battery energy storage system providing PFR on the Danish energy market. The lifetime investigation is based on the performance-degradation model developed and verified in the previous chapter. The first part of this chapter gives some brief insights on the primary frequency regulation service in Denmark. Moreover, the basic features of the Li-ion battery energy storage system integrated into a VPP, which provides primary frequency regulation, are presented. The second part of the chapter, discusses the method behind the Li-ion battery lifetime evaluation and introduces the mission profile used for this evaluation. In the last part of the chapter, the results obtained from the performance-degradation analysis of the LFP/C battery cells are presented and discussed.

9.1 Primary Frequency Regulation in Denmark with Li-ion Battery ESS

In case of frequency deviations, the PFR service restores the balance between energy production and consumption, and thus stabilizes the grid frequency, close to the desired value, within a threshold interval. The general characteristics of this service, which is suitable for being provided by ESSs, were discussed in detail in Chapter 2.1; the upcoming paragraphs are mostly related to the Danish energy market.

9.1.1 Primary frequency regulation in Denmark

The Danish electricity market is divided into two regions, Western Denmark (or DK1) and Eastern Denmark (or DK2). The following description is performed for the western region, even though most of the characteristics and requirements are valid for the eastern region, as well.

Primary frequency regulation is supplied if the grid frequency deviates up to ± 200 mHz from the reference frequency of 50 Hz; however, a dead band of ± 20 mHz around the reference frequency is allowed. The primary frequency regulation market differentiates between the upward regulation and downward regulation, which are sold separately at daily auctions, for the next day [144].

The PFR service has to be delivered linearly at frequency deviations of between ± 20 and ± 200 Hz, as illustrated in Fig. 9.1. Moreover, the first half of the reserve must be supplied within 15 seconds after the deviation occurs and it has to be fully activated within 30 seconds for a frequency deviation of ± 200 Hz [144]. Maximum power has to be supplied for maximum 15 minutes after which the reserve has to be re-established within the next 15 minutes.

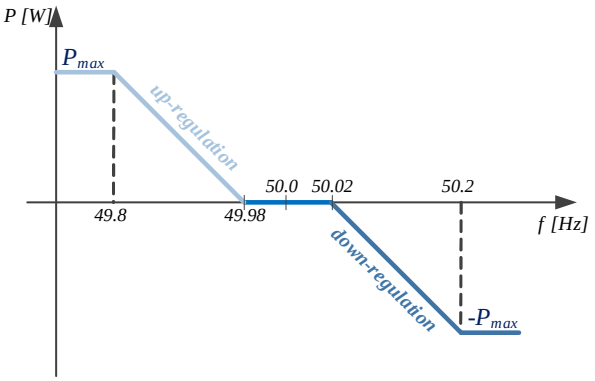

Figure 9.1: *Characteristics of primary frequency regulation in Western Denmark.*

9.1.2 PFR with Li-ion battery ESS in DK1

A 1.6 MW/ 0.4 MWh Li-ion battery ESS was installed, in conjunction with a 13 MW WPP, in Western Denmark and since February 2013 participates in Western Denmark primary frequency regulation market [145]. The ESS is composed from two sub-systems (i.e., 1.2MW/ 0.3MWh and 0.4MW/ 0.1MWh) provided from two different suppliers

[42], [145]; the smaller system is based on similar LFP/C battery cells as the ones investigated in the present thesis.

As presented in [145], the 1.6 MW/ 0.4 MWh ESS past all the technical requirements (i.e., linearity, response time, and 15 minutes duration) in order to deliver the PFR service. Besides, PFR service, the ESS was evaluated with success for other services such as inertial response, power oscillation damping, and power smoothing [20]; however, at the moment none of these applications are traded.

Because asymmetrical bids are allowed in the Danish energy market and higher revenues are generated by upwards regulation, the ESS participates only on the up-regulation market. Consequently, in order to bid maximum power, the SOC of both systems is kept at approximately 90% [20]. The ESS delivers up-regulation according to the droop characteristic presented in Fig. 9.1. The re-establishing of the SOC is realized during periods of over-frequencies, following the complex procedure discussed in [145] (see Fig. 3). Moreover, in the rare case when under-frequencies persists for more than 15 minutes (e.g. ESS delivers PFR for 15 minutes continuously), the PFR service is interrupted and a 15 minutes re-charge period is granted to the ESS [145]. However, the re-charge strategy might be improved since at the moment there are no requirements imposed by the TSO regarding the re-establishing of the ESS's SOC.

As it was already mentioned, the 0.4 MW/ 0.1 MWh ESS sub-system is based on similar LFP/C battery cells as the ones investigated in this work. Thus, in order to estimate and evaluate the performance-degradation of LFP/C battery cells when they are used for providing PFR service, a one year mission profile, which has been measured on field was considered.

9.2 Procedure for Lifetime Evaluation

9.2.1 Grid frequency

Grid frequency values, which have been measured between June 2013 and May 2014, represented the base of the lifetime analysis of the LFP/C battery cells. The frequency signal, measured with one second resolution is presented in Appendix G (see Fig. G.1). Based on this frequency signal the histogram illustrated in Fig. 9.2 was derived.

As suggested by the above presented histogram, the number of occurrences when the frequency is below 49.98 Hz (i.e., ESS is delivering up-regulation) is relatively reduced (i.e., 1227 hours, which corresponds to 14% of the considered time interval). Therefore, most of the time, the ESS was idling, operation which has caused calendar ageing of the Li-ion batteries.

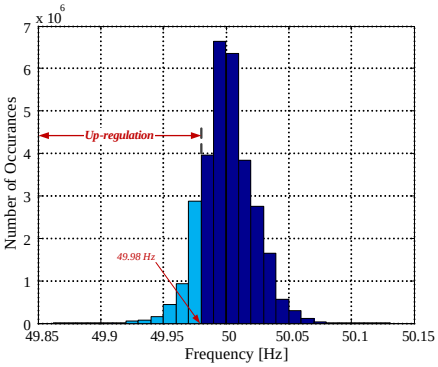

Figure 9.2: *Grid frequency values, recorded during one year, sorted according to their values.*

Fig. 9.3 shows the distribution of the under-frequencies, expressed as accumulated time, during each quarter of the considered year. As one can observe, most of the frequency deviations from the lower accepted values (i.e., 49.98 Hz), are having a reduced amplitude. Consequently, this has resulted in cycle depths with reduced amplitude for the Li-ion battery ESS.

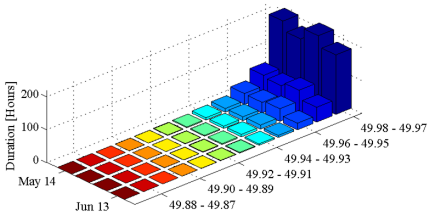

Figure 9.3: *Accumulated duration of under-frequencies, divided in frequency intervals, for a period of one year.*

9.2.2 State-of-charge profile

Based on the measured grid frequency, and according to the energy management strategy, the reference power set-point which had to be delivered (for up-regulation) or absorbed (for re-establishing SOC) by the Li-ion battery ESS was continuously generated. The power profile measured on the 0.4 MW/ 0.1 MWh LFP/C-based ESS was used as input for the developed performance-degradation model, in order to evaluate the lifetime of LFP/C battery cells when they are subjected to a PFR mission profile.

Before being applied to the performance-degradation model, the power mission profile was scaled down in order to consider the maximum allowed charging and discharging

power of an LFP/C battery cell (see Appendix A). The obtained power mission profile was feed to the proposed model and the capacity and PPC of the LFP/C battery cell were updated on a monthly basis according to the estimated degradation.

The SOC profile corresponding to the one year power profile, which was measured on field, is presented in Fig. 9.4. By applying the rainflow cycle counting algorithm to this SOC profile, following to the procedure illustrated in Fig. 8.3, the cycling mission profile to which the LFP/C battery cell is subjected was obtained and is presented in Fig. 9.4.

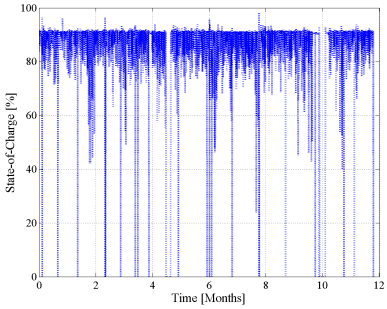

Figure 9.4: *One year SOC profile corresponding to the LFP/C-based Li-ion ESS delivering PFR (for an operating temperature T=25°C).*

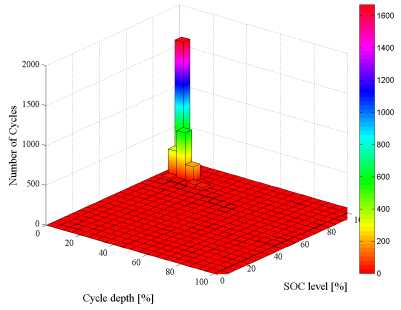

Figure 9.5: *Distribution of cycles according to their depths and average-SOC, corresponding to the SOC profile presented in 9.4.*

Since, the considered ESS is providing only up-regulation, the idling SOC of the battery cells is approximately 90%, as it was already mentioned, fact which is also visible from Fig. 9.4. Moreover, most cycles, to which the batteries were subjected, have a depth smaller than 40% (see Fig. 9.5), which is in good agreement with the distribution of the under-frequencies shown in Fig. 9.3, which have deviated only slightly from the accepted threshold frequency interval.

Furthermore, the field measured power profile was available only for a period of one year. Consequently, because the lifetime of the studied LFP/C battery cells is much longer, the same power profile was continuously applied at the input of the developed performance-degradation model until the predefined EOL criterion (i.e., 20% capacity fade) was reached.

9.3 Performance Degradation of LFP/C Battery Cells

This section presents and discusses the estimated degradation of the LFP/C battery cells performance parameters, which was obtained by applying the field measured mis-

sion profile to the developed performance-degradation model. Capacity fade and PPC decrease are discussed separately and for both cases the operating temperature of the LFP/C battery cell was considered constant during the whole lifetime and equal to 25°C.

9.3.1 Capacity fade of LFP/C battery cells

The capacity fade of the LFP/C battery cells, which has been estimated for each month, until the EOL criterion was reached is presented in Fig. 9.6; the estimated monthly capacity fade increments are presented individually for the capacity fade caused by idling operation and for the capacity fade caused by cycling operation, respectively. As expected, the capacity fade due to the idling operation is higher than the capacity fade due to cycling operation because the LFP/C-based ESS has provided up-regulation only for 14% of the total operation time (see Fig. 9.2), while the rest of the time was dedicated to the re-establishing of the SOC and to the idling.

Moreover, as one can observe from Fig. 9.6, the capacity fade increment values for both calendar and cycling dimensions are varying from month-to-month throughout one year of operation; these results are caused by the field measured power profile, which was not constant for all months and has generated thus different stress levels to the LFP/C battery cells. Nevertheless, since the same power profile was applied to the model repetitively with a resolution of one year, the obtained capacity fade increments are following a yearly pattern as well.

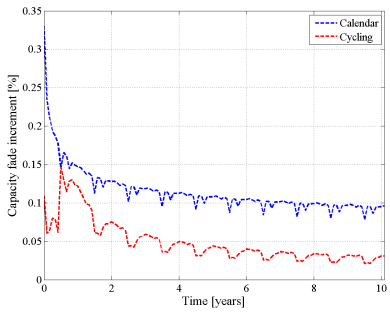

Figure 9.6: *Estimated calendar capacity fade and cycling capacity fade of the LFP/C battery cells for each month of providing PFR service.*

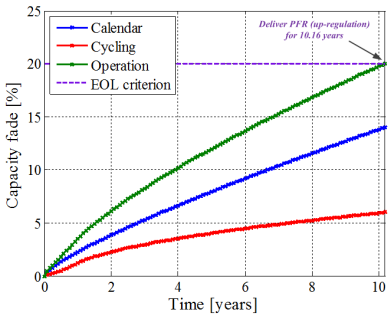

Figure 9.7: *Contribution of calendar and cycling operation to the total estimated capacity fade of the LFP/C battery cells subjected to the PFR mission profile.*

Based on the capacity fade increments, the accumulated capacity fade of the LFP/C battery cells induced by the PFR profile, was obtained and is presented in Fig. 9.7. The estimated operation capacity fade was computed by summing up the contribution of the accumulated cycling capacity fade and of the accumulated calendar capacity fade. For a

20% capacity fade EOL criterion, it was found out that the studied LFP/C battery cells would survive approximately 10 years in operation for the considered PFR profile.

As shown in Fig. 9.7, the main contribution to the overall capacity fade of the LFP/C battery cells came for the idling operation (calendar ageing); out of the 20% capacity fade, 14% were the contribution of the calendar ageing. The calendar capacity fade rate was accelerated by the idling operation at high SOC-level (i.e. 90% SOC); as it was shown in Chapter 6, the capacity of LFP/C battery cells degrades faster when they are stored at high SOC level (i.e., exponential relationship between capacity fade and storage SOC-level).

Fig. 9.8 illustrates the non-linear dependence of the capacity fade increment on the operation time. The same one-month mission profile applied to the battery performance-degradation model causes lower-and lower capacity fade (both cycling and calendar) as the ageing process evolves. This behaviour can be also observed in Fig. 9.6.

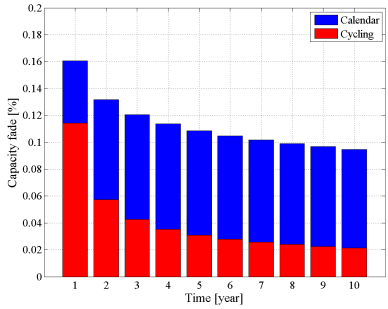

Figure 9.8: *Decrease of the capacity fade rate when the same mission profile is applied to the performance-degradation model at different ageing levels of the LFP/C battery cell (example for "Month9").*

9.3.2 PPC decrease of LFP/C battery cells

The results obatined for the PPC decrease have been investigated similarly as the ones for capacity fade.

The PPC decrease of the LFP/C battery cells, which was estimated by the developed model, for each month until the EOL was achieved, is presented in Fig. 9.9. The monthly PPC decrease increments for calendar and cycling ageing were estimated individually and are showing a ten times higher degradation of the battery cells' PPC caused by calendar ageing than by cycling ageing; these results are supported by the performance of the developed model in terms of PPC, which are showing a faster decrease of the PPC caused by the calendar ageing than by cycling ageing at quasi-similar operational conditions (see

Fig. 8.11 and Fig. 8.11, respectively).

Similar to the case of the capacity fade, month-to-month variations of the PPC decrease were observed for both cycling and calendar dimensions.

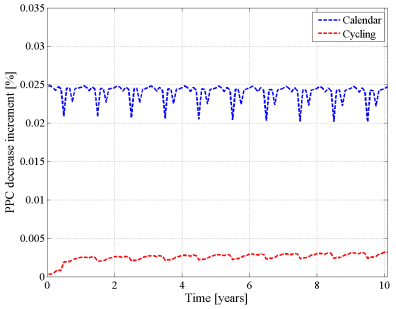

Figure 9.9: *Estimated calendar PPC decrease and cycling PPC decrease of the LFP/C battery cells for each month of providing PFR service.*

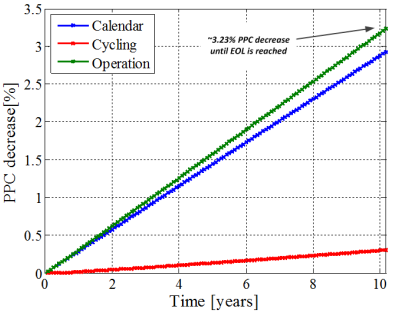

Figure 9.10: *Contribution of calendar and cycling operation to the total estimated PPC decrease of the LFP/C battery cells subjected to the PFR mission profile.*

Based on the monthly PPC decrease increments, shown in Fig. 9.9, the accumulated PPC decrease characteristics caused by both calendar and cycling operation were obtained (see Fig. 9.10). The total PPC decrease was further obtained by summing up the PPC decreases corresponding to cycling and calendar ageing.

The estimated PPC decrease of the studied LFP/C battery cells until the EOL criterion has been reached was approximately 3.25%; the main contribution, almost 3%, came from the calendar dimension. In contrast with the capacity fade, the PPC decrease depends linearly on the operation time (see also (6.15) and (7.13)) as shown in Fig. 9.10. This linear dependence of the PPC decrease on the operation time is also visible in Fig. 9.11, where the degradation obtained for the same mission profile (the same month) is not changing even though it was applied at different ageing-levels of the LFP/C battery cell.

9.4 Discussion

By comparing the results obtained for the capacity fade (see Fig. 9.7) and for the PPC decrease (see Fig. 9.10) when the field measured PFR profile was applied to the proposed performance-degradation model, it was observed that the capacity is the performance parameter, which limited the lifetime of the studied battery cells for this service.

Moreover, it has been shown that because of the characteristics of the developed performance-degradation model, the rate of the capacity fade has the tendency to slow

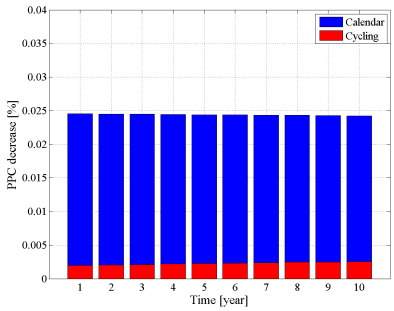

Figure 9.11: *Decrease of the PPC decrease rate when the same mission profile is applied to the performance-degradation model at different ageing levels of the LFP/C battery cell (example for "Month9").*

down while the ageing process has evolved. On the other hand, the PPC has decreased linearly in time.

The main contribution to the estimated capacity fade came from the calendar dimension. The calendar capacity fade was accelerated by the operating conditions which involved storing the LFP/C battery cell at a high SOC-level. Thus, the lifetime of the studied LFP/C battery cell might be enhanced by decreasing the idling SOC-level to values lower than 90%; however, this hypothetical decrease of the idling SOC-level would cause a decrease of the revenues obtained from the up-regulation, because lower power would need to be bid in the market. Consequently, in order to improve the present used energy management strategy, a complex optimization process has to be addressed. However, this topic was out of the scope of the present thesis.

Furthermore, it has to be stressed that the presented degradation levels (for both capacity and PPC) were obtained for the case of a single LFP/C battery cell. Therefore, they should be treated as the minimum degradation values, which could be obtained for an ESS composed of hundreds or thousand of LFP/C battery cells; this is induced by the differences between the performance and degradation behaviour between similar LFP/C battery cells, which will further reduce the lifetime of the whole ESS.

Chapter 10

Summary, Conclusions, and Future Work

10.1 Summary

Among others, the grid-integration of energy storage systems together with WPPs (as VPPs) has been identified as one of the solutions, which would enhance the wind power grid integration at even larger scales, by mitigating the issues related with the power system reliability and stability. Moreover, the inherent characteristics of the ESSs will allow the VPP to behave similar to today's CGUs, being able to comply with future more stringent grid codes and to provide various grid services such as PFR, forecast error balance etc.

Different ES technologies are available currently on the market; however, because of their characteristics, which include high efficiency, fast response, long cycle and calendar lifetime, Li-ion batteries were found to match better than other technologies the requirements of different VPP services. From, the family of Li-ion batteries, the LFP/C chemistry was selected for further investigation and for lifetime modelling.

One of the major obstacles which is preventing the utilization at a large scale of Li-ion batteries together with WPPs is their cost competitiveness. However, this issue can be minimized by an accurate estimation of the Li-ion batteries performance-degradation behaviour, which will further allow accurate lifetime prediction. Knowing the lifetime of the Li-ion battery is a key factor for precisely computing and analysing the economic feasibility of the VPP business model. Moreover, from the technical perspective, since the performance parameters of the Li-ion batteries are lifetime dependent, accurate lifetime

models allow for choosing at every moment the best operational energy management strategy and for optimally sizing the ESS.

Therefore, the main objective of this thesis was to develop accurate performance-degradation models for the selected LFP/C battery cell, which will allow to evaluate the degradation behaviour of the performance parameters (i.e., capacity and PPC) under complex operational conditions and to estimate the lifetime of the battery cell for certain applications.

In order to achieve the goal of this thesis, the following objectives were followed.

A literature survey of the services (applications) which are suitable for being provided by ESSs was carried out. For each of these applications, the requirements (i.e., size, discharge time, and lifetime) which have to be fulfilled by the ESS were summarized. Moreover, the review of the most suitable ES technology for integration into VPPs has been performed as well. Based on the requirements of the considered VPP applications and on the characteristics of the discussed ES technologies, Li-ion batteries were found to be the most suitable ES technology for integration into VPP. Different Li-ion battery chemistries are available on the market; however, a Li-ion battery based on the LFP/C chemistry was selected for investigation and for performance-degradation modelling because of their superior characteristics in terms of lifetime, safety, performance, and relative reduced-cost.

The LFP/C battery cell was subjected to an extended characterization procedure at its BOL. During the characterization test, the capacity, OCV, internal resistance, and small-signal AC impedance of the battery cell were measured at different temperatures, SOCs, and using various C-rates. The obtained results have been used to develop and parametrize an electrical impedance-based performance model, which was able to estimate with accuracy the dynamic behaviour the LFP/C battery cell. The performance model was verified using various dynamic current profiles.

The degradation of Li-ion batteries is a complex process, which is influenced by many stress factors. Furthermore, Li-ion batteries operating in VPP applications are subjected to complex mission profiles, which involve both periods when the batteries are cycled and when the batteries are on stand-by. Therefore, in order to consider all these aspects and to be able to estimate with high accuracy the performance-degradation of the studied battery cells, two test matrices have been developed. The first test matrix was used for defining the conditions (i.e., stress factors and corresponding stress levels) for the accelerated calendar ageing tests, while the second matrix was used for defining the conditions for the accelerated cycling ageing tests. In order to obtain information about the ageing behaviour of the tested LFP/C battery cells in a relative reduced time, the

ageing tests were performed in accelerated manner by considering elevated temperature levels.

The results obtained from the accelerated ageing tests have been used to parametrize the EEC-based performance-degradation model of the LFP/C battery cell. The proposed model returns information about the capacity fade, PPC decrease and parameters of the EEC. For each investigate performance parameter, separate models have been developed for the calendar and cycling ageing dimensions. The total degradation to which the battery cell was subjected was obtained by summing up the degradation values separately estimated for the two considered dimensions. The developed models were verified in terms of capacity fade, considering two different mission profiles, and the obtained estimation error was in the range of 7-11%. Consequently, the proposed methodology for lifetime estimation of the studied LFP/C battery cells was validated.

Based on the developed performance-degradation model and considering a realistic one year mission profile, measured on field (characteristic for Li-ion batteries providing PFR), it was found out that the LFP/C battery cells would reached a 20% capacity fade EOL criterion after approximately 10 years of operation.

10.2 Conclusions

The most important conclusions of the present thesis can be summarized as follows:

- Energy storage systems are able to improve the characteristics of the wind power and to allow VPPs to behave similar to today's CGUs;
- Based on various requirements (e.g. high efficiency, low cost/cycle, long calendar lifetime etc.) imposed by the VPP operation, NaS, VRB, and Li-ion batteries were found to be the most suitable ES technologies for VPP integration; however, due to the continuously increasing performance levels, which have recently materialized in a high number of ongoing demonstration projects, Li-ion batteries represent the most appealing ES technology for integration in VPP for delivering short- to medium-term services;
- Because of its characteristics, which include intrinsic safety, high performances, and long lifetime, Li-ion batteries based on the LFP/C chemistry represents promising candidates for integration with VPP and their performance and degradation behaviour was studied in this thesis;
- By performing a literature survey, it was found out that the EEC-based performance model represent a good trade-off solution, between electrochemical and

mathematical models, for modelling the performance behaviour of the Li-ion batteries;

- To parametrize the performance model of the LFP/C battery cells extensive characterization tests are mandatory. Thus, a six-steps procedure for characterizing the battery cells was proposed;
- The accuracy of the performance measurements is influenced by the length of the relaxation time to which the battery is subjected before starting the desired measurements;
- Independent on the considered C-rate, for a normal operating temperature of 25^{o}C, the Coulombic efficiency of the studied LFP/C battery cell is higher than 99.5%;
- The characteristic of the internal resistance of the LFP/C battery cell, measured during discharging by following the modified HPPC test, is relatively flat in the interval 20-90% SOC, with a slight increase in the region 60-70% SOC. Moreover, this pattern did not change when other temperatures were considered during the measurement;
- An EEC based on ZARC elements was found to fit the best the measured (by EIS technique) impedance spectra of the LFP/C battery cell; thus, this EEC configuration was used as well for modelling the performance behaviour of the studied battery cell;
- In this thesis, the developed performance model for the LFP/C battery cells, is implemented using a hybrid approach. The performance model is based on an EEC which uses two ZARC elements and was parametrized using the results obtained from the EIS measurements; however, because the charge-transfer resistance depends non-linearly on the battery current, correction terms were derived based on the performed HPPC tests;
- The developed performance model estimates with high accuracy the voltage of the LFP/C battery cell; the verification was carried out using different load profiles, and the maximum voltage estimation error has ranged between 3.6% to 4.9%;
- Accurate lifetime models for Li-ion batteries are mandatory from both economical and technical point of view; accurate lifetime models allow investment profitability calculations, optimal battery ESS sizing, energy management strategy definition etc;

- The ageing mechanisms of Li-ion battery are complex and influenced by many stress factors; furthermore, the performance parameters of Li-ion batteries are degrading during both cycling (cycling ageing) and idling (calendar ageing) operation;

- The dependence of the capacity fade on the storage time was expressed using a power law function; the capacity fade was found to depend exponentially both on the storage temperature and on the storage SOC-level. Consequently, based on these dependences, it was found out that for idling at 50% SOC and 25^{o}C, the LFP/C battery cell will be able to survive approximately 20 years until a 20% capacity fade value will be reached;

- The PPC was found to decrease linearly with increasing storage time; moreover, the PPC decreases depends exponentially on the storage temperature and following a power law on the storage SOC-level, similar as in the case of the capacity fade. Nevertheless, for similar ageing conditions, it was found out that the capacity of the battery degrades much faster the PPC;

- Among the eight parameters of the EEC, only R_s, R_1, and Q_1 were found to depend consistently on the calendar ageing conditions. For the series resistance R_s similar dependence on the storage time, SOC-level, and temperature were found as for the PPC;

- The self-discharge of the LFP/C battery cells depends strongly on the storage SOC-level and temperature; the dependence of the self-discharge on the storage time tends to follow a parabolic function;

- Independent on the cycling conditions, the capacity fade of the LFP/C battery cells is decreasing following a square-root-of-number of cycles function. Moreover, the capacity fade during cycling depends following a power function on the cycle depth and on the average SOC-level, and following an exponential function on the temperature;

- Similar to the case of the calendar ageing, the PPC during cycling decrease linearly with increasing the number of cycles. Moreover, the dependence of the PPC decrease on the cycle depth and on the temperature follows a power and an exponential function, respectively;

- Among the eight parameters of the EEC, only R_s, R_2, and Q_2 were found to depend consistently on the cycling ageing conditions. For the series resistance R_s similar dependence on the temperature, number of cycles and their depths were

found as for the PPC. Moreover, by analysing the results obtained for the calendar and cycling ageing, it was observed that only the series resistance R_s depends consistently on the ageing conditions;

- The proposed performance-degradation model describes with high accuracy the capacity fade of the tested LFP/C battery cells. The estimation error obtained from two verification tests has varied between 7.12% and 10.24%;
- By performing a lifetime evaluation of the LFP/C battery cells considering a realistic one year mission profile, characteristic for the PFR service, it was found out that the cells would withstand approximately 10 years of operation until the capacity fade will drop below 20%; in the same time, the PPC would decrease with approximately 3.25%. Consequently, it can be concluded that the lifetime of the tested LFP/C battery cells for the PFR service is rather limited by their capacity fade and not by their PPC decrease.

10.3 Future Work

The results obtained in this thesis might be improved and extended by following the directions summarized below:

- Extend the proposed and verified performance model of the LFP/C battery cell for the other temperatures (i.e., 15^{o}C, 35^{o}C, and 45^{o}C), which were considered during the extended characterization test performed at BOL;
- Continue the accelerated ageing tests (both calendar and cycling), for the conditions in which the LFP/C batteries cells have not reached the EOL criterion. Based on the obtained results, update the developed lifetime models for capacity fade, PPC decrease, and R_s increase;
- Continue the verification ageing tests until the subjected LFP/C battery cells will reach the EOL criterion;
- Improve the proposed performance-degradation model by considering the degradation behaviour of the battery cell voltage. Thus, the model would be able to estimate the dynamic behaviour of the LFP/C battery cell at different SOH levels;
- Perform the other tests from the proposed extended calendar and cycling ageing test matrices in order to analyse if there are any interactions between the stress

factors, which will cause joint effects on the degradation of the battery cells' performance parameters;

- Based on the obtained and verified performance-degradation model, perform optimization studies in order to define the optimal energy management strategy (seen from both lifetime and revenues perspectives) for delivering the PFR service with LFP/C-based ESSs;

Bibliography

[1] EWEA. Wind in power: 2013 european statistics. Technical report, European Wind Energy Association, February 2014.

[2] EWEA. Wind in power: 2009 european statistics. Technical report, European Wind Energy Association, February 2010.

[3] Directive 2009/28/ec of the european parliament and of the council of 23 april 2009 on the promotion of the use of energy from renewable sources. *Official Journal of the European Union*, June 2009.

[4] P.B. Eriksen, T. Ackermann, H. Abildgaard, P. Smith, W. Winter, and J.M. Rodriguez Garcia. System operation with high wind penetration. *Power and Energy Magazine, IEEE*, 3(6):65--74, Nov 2005.

[5] C.N. Rasmussen. Energy storage for improvement of wind power characteristics. In *PowerTech, 2011 IEEE Trondheim*, pages 1--8, June 2011.

[6] Guodong Liu and K. Tomsovic. Quantifying spinning reserve in systems with significant wind power penetration. *Power Systems, IEEE Transactions on*, 27(4):2385--2393, Nov 2012.

[7] M.A. Ortega-Vazquez and D.S. Kirschen. Estimating the spinning reserve requirements in systems with significant wind power generation penetration. *Power Systems, IEEE Transactions on*, 24(1):114--124, Feb 2009.

[8] E. Ela, B. Kirby, E. Lannoye, M. Milligan, D. Flynn, B. Zavadil, and M. O'Malley. Evolution of operating reserve determination in wind power integration studies. In *Power and Energy Society General Meeting, 2010 IEEE*, pages 1--8, July 2010.

[9] T. Ackermann, editor. *Wind Power in Power Systems*. Wiley, 2nd edition, 2012.

[10] E. Spahic, G. Balzer, B. Hellmich, and W. Munch. Wind energy storages - possibilities. In *Power Tech, 2007 IEEE Lausanne*, pages 615--620, July 2007.

[11] J. Conto. Grid challenges on high penetration levels of wind power. In *Power and Energy Society General Meeting, 2012 IEEE*, pages 1--3, July 2012.

[12] Warren Katzenstein, Emily Fertig, and Jay Apt. The variability of interconnected wind plants. *Energy Policy*, 38(8):4400 -- 4410, 2010.

[13] S.S. Soman, H. Zareipour, O. Malik, and P. Mandal. A review of wind power and wind speed forecasting methods with different time horizons. In *North American Power Symposium (NAPS), 2010*, pages 1--8, Sept 2010.

[14] D. Lew, M. Milligan, G Jordan, and R Piwko. The value of wind power forecasting. Technical Report NREL/CP-5500-50814, National Renewable Energy Laboratory, April 2011.

[15] A. Tuohy, B. Kaun, and R Entriken. Storage and demand-side options for integrating wind power. *Wiley Interdisciplinary Reviews: Energy and Environment*, 3(1):93--109, Janury/February 2014.

[16] Federal Energy Regulatory Commission. Assessment of demand response & advanced metering. Technical report, October 2013.

[17] Wind power integration technology assessment and case studies. Technical Report 1004806, EPRI, Palo Alto, CA, 2004.

[18] EPRI-DOE handbook supplement of energy storage for grid connected wind generation applications. Technical Report 1008703, EPRI, Palo Alto, CA, and the U.S. Department of Energy, Washington, DC, 2004.

[19] P. Denholm, E. Ela, B. Kirby, and M. Milligan. The role of energy storage with renewable electricity generation. Technical Report NREL/TP-6A2-47187, National Renewable Energy Laboratory, January 2010.

[20] P.C. Kjaer, R. Larke, and G.C. Tarnowski. Ancillary services provided from wind power plant augmented with energy storage. In *Power Electronics and Applications (EPE), 2013 15th European Conference on*, pages 1--7, Sept 2013.

[21] Y. Iijima, Y. Sakanaka, N. Kawakami, M. Fukuhara, K. Ogawa, M. Bando, and T. Matsuda. Development and field experiences of nas battery inverter for power stabilization of a 51 mw wind farm. In *Power Electronics Conference (IPEC), 2010 International*, pages 1837--1841, June 2010.

[22] D. Manz, R. Walling, N. Miller, B. LaRose, R. D'Aquila, and B. Daryanian. The grid of the future: Ten trends that will shape the grid over the next decade. *Power and Energy Magazine, IEEE*, 12(3):26--36, May 2014.

[23] ENTSO-E. Implementation guidline for network code - "requirements for grid connection applicable to all generators". Technical report, European Network of Transmission System Operators for Electricty, Brussels, Belgium, October 2013.

[24] M. Swierczynski, D.-I. Stroe, A.-I. Stan, R. Teodorescu, R. Laerke, and P.C. Kjaer. Field tests experience from 1.6mw/400kwh li-ion battery energy storage system providing primary frequency regulation service. In *Innovative Smart Grid Technologies Europe (ISGT EUROPE), 2013 4th IEEE/PES*, pages 1--5, Oct 2013.

[25] C. Abbey and G. Joos. Supercapacitor energy storage for wind energy applications. *Industry Applications, IEEE Transactions on*, 43(3):769--776, May 2007.

[26] M. Swierczynski, D.-I. Stroe, A.-I. Stan, and R. Teodorescu. Lifetime and economic analyses of lithium-ion batteries used for balancing the wind power forecast error: A case study for a single wind turbine. *International Journal of Energy Research, Wiley*, accepted for publication.

[27] Electric Energy Storage Technology Options: A White Paper Primer on Applications, Costs, and Benefits. Technical Report 1020676, EPRI, Palo Alto, CA, 2010.

[28] M. Swierczynski, D.I. Stroe, A.-I. Stan, R. Teodorescu, and D.U. Sauer. Selection and performance-degradation modeling of $LiMO_2/Li_4Ti_5O_{12}$ and $LiFePO_4/C$ battery cells as suitable energy storage systems for grid integration with wind power plants: An example for the primary frequency regulation service. *Sustainable Energy, IEEE Transactions on*, 5(1):90--101, Jan 2014.

[29] Grid energy storage. Technical report, U.S. Department of Energy, December 2013.

[30] O. Gross and S. Clark. Optimizing electric vehicle battery life through battery thermal management. *SAE International Journal of Engines*, 4(1):1928--1943, 2011.

[31] E. Schaltz, A. Khaligh, and P.O. Rasmussen. Influence of battery/ultracapacitor energy-storage sizing on battery lifetime in a fuel cell hybrid electric vehicle. *Vehicular Technology, IEEE Transactions on*, 58(8):3882--3891, Oct 2009.

[32] Madeleine Ecker, Jochen B. Gerschler, Jan Vogel, Stefan Käbitz, Friedrich Hust, Philipp Dechent, and Dirk Uwe Sauer. Development of a lifetime prediction model for lithium-ion batteries based on extended accelerated aging test data. *Journal of Power Sources*, 215:248 -- 257, 2012.

[33] A.-I. Stan, M. Swierczynski, D.-I. Stroe, R. Teodorescu, and S.J. Andreasen. Lithium ion battery chemistries from renewable energy storage to automotive and back-up power applications. In *Optimization of Electrical and Electronic Equipment (OPTIM), 2014 14th International Conference on*, 2014.

[34] D.-I. Stroe, M. Swierczynski, A.-I. Stan, R. Teodorescu, and S.J. Andreasen. Accelerated lifetime testing methodology for lifetime estimation of lithium-ion batteries used in augmented wind power plants. *Industry Applications, IEEE Transactions on*, PP(99):1--1, 2014.

[35] M. Swierczynski, D.-I. Stroe, R Laerke, A.-I. Stan, R. Teodorescu, P.C. Kjaer, and S.K. Kjaer. Field experience from li-ion bess delivering primary frequency regulation in the danish energy market. *ECS Transactions*, 2014 - under review.

[36] D.-I. Stroe, A.-I. Stan, R. Diosi, R. Teodorescu, and S.J. Andreasen. Short term energy storage for grid support in wind power applications. In *Optimization of Electrical and Electronic Equipment (OPTIM), 2012 13th International Conference on*, pages 1012--1021, May 2012.

[37] D.-I. Stroe, M. Swierczynski, A.-I. Stan, R. Teodorescu, and S.J. Andreasen. Performance-degradation model for $Li_4Ti_5O_{12}$-based battery cells used in wind power applications. In *7th International Renewable Energy Storage Conference and Exhibition, IRES 2012*, 2012.

[38] M. Swierczynski, D.-I. Stroe, A.-I. Stan, and R. Teodorescu. Evaluation of different operational strategies for lithium ion battery systems connected to a wind turbine for primary frequency regulation and wind power forecast accuracy improvement. In *11th International Workshop on Large-Scale Integration of Wind Power into Power Systems*, 2012.

[39] D.-I. Stroe, M. Swierczynski, A.-I. Stan, and R. Teodorescu. Accelerated lifetime testing methodology for lifetime estimation of lithium-ion batteries used in augmented wind power plants. In *Energy Conversion Congress and Exposition (ECCE), 2013 IEEE*, pages 690--698, Sept 2013.

[40] D. Stroe, M. Swierczynski, A.-I. Stan, R. Teodorescu, and S.J. Andreasen. Experimental investigation on the internal resistance of lithium iron phosphate battery cells during calendar ageing. In *Industrial Electronics Society, IECON 2013 - 39th Annual Conference of the IEEE*, pages 6734--6739, Nov 2013.

[41] M. Swierczynski, D. Stroe, A.-I. Stan, and R. Teodorescu. The lifetime of the lifepo4/c battery energy storage system when used for smoothing of the wind power plant variations. In *Industrial Electronics Society, IECON 2013 - 39th Annual Conference of the IEEE*, pages 6825--6830, Nov 2013.

[42] M. Swierczynski, D.-I. Stroe, A.-I. Stan, R. Teodorescu, R. Laerke, and P.C. Kjaer. Field tests experience from 1.6mw/400kwh li-ion battery energy storage system providing primary frequency regulation service. In *Innovative Smart Grid Technologies Europe (ISGT EUROPE), 2013 4th IEEE/PES*, pages 1--5, Oct 2013.

[43] M. Swierczynski, D.I. Stroe, A.I. Stan, and R. Teodorescu. Primary frequency regulation with li-ion battery energy storage system: A case study for denmark. In *ECCE Asia Downunder (ECCE Asia), 2013 IEEE*, pages 487--492, June 2013.

[44] M. Swierczynski, D.I. Stroe, A.I. Stan, R. Teodorescu, and H. Vikelgaard. Selection and impedance based model of a lithium ion battery technology for integration with virtual power plant. In *Power Electronics and Applications (EPE), 2013 15th European Conference on*, pages 1--10, Sept 2013.

[45] D.-I. Stroe, M. Swierczynski, A.-I. Stan, V. Knap, R. Teodorescu, and S.J. Andreasen. Diagnosis of lithium-ion batteries state-of-health based on electrochemical impedance spectroscopy technique. In *Energy Conversion Congress and Exposition (ECCE), 2014 IEEE*, 2014, in press.

[46] V. Knap, R. Sinha, M. Swierczynski, D.-I. Stroe, and S.K. Chaudhary. Grid inertial response with lithium-ion battery energy storage. In *Industrial Electronics (ISIE), 2014 IEEE International Symposium on*, 2014.

[47] DOE/EPRI 2013 Electricty Storage Handbook in Collaboration with NRECA. Technical Report SAND2013-5131, Sandia National Laboratories, July 2013.

[48] M. Swierczynski. *Lithium ion battery energy storage system for augmented wind power plants*. PhD thesis, Aalborg University, 2012.

[49] P.W. Christensen and G.C. Tarnowski. Inertia for Wind Power Plants - state of the art review - year 2011. In *10th International Workshop on Large-Scale Integration of Wind Power*, Arhus, Denmark, Oct. 25-26 2011.

[50] N.W. Miller, K. Clark, and M. Shao. Impact of frequency responsive wind plant controls on grid performance. In *9th International Workshop on Large-Scale Integration of Wind Power*, Quebec, Canada, Oct. 18-19 2010.

[51] Y.G. Rebours, D.S. Kirschen, M. Trotignon, and S. Rossignol. A survey of frequency and voltage control ancillary services mdash;part i: Technical features. *Power Systems, IEEE Transactions on*, 22(1):350--357, Feb 2007.

[52] E. Muljadi, V. Gevorgian, M. Singh, and S. Santoso. Understanding inertial and frequency response of wind power plants. In *Power Electronics and Machines in Wind Applications (PEMWA), 2012 IEEE*, pages 1--8, July 2012.

[53] G.C. Tarnowski, P.C. Kjaer, S. Dalsgaard, and A. Nyborg. Regulation and frequency response service capability of modern wind power plants. In *Power and Energy Society General Meeting, 2010 IEEE*, pages 1--8, July 2010.

[54] Technical regulation 3.2.5 for wind power plants with a power output greater than 11 kw. Technical Report 55986/10, Energinet.dk, September 2010.

[55] A. Oudalov, D. Chartouni, and C. Ohler. Optimizing a battery energy storage system for primary frequency control. *Power Systems, IEEE Transactions on*, 22(3):1259--1266, Aug 2007.

[56] M.L. Lazarewicz and T.M. Ryan. Integration of flywheel-based energy storage for frequency regulation in deregulated markets. In *Power and Energy Society General Meeting, 2010 IEEE*, pages 1--6, July 2010.

[57] Y.V. Makarov, C. Loutan, Jian Ma, and P. de Mello. Operational impacts of wind generation on california power systems. *Power Systems, IEEE Transactions on*, 24(2):1039--1050, May 2009.

[58] Gaudenz Koeppel and Magnus Korpas. Improving the network infeed accuracy of non-dispatchable generators with energy storage devices. *Electric Power Systems Research*, 78(12):2024 -- 2036, 2008. Special Issue Papers Presented at the 6th World Energy System Conference 6th World Energy System Conference.

[59] P. Pinson, G. Papaefthymiou, B. Klockl, and J. Verboomen. Dynamic sizing of energy storage for hedging wind power forecast uncertainty. In *Power Energy Society General Meeting, 2009. PES '09. IEEE*, pages 1--8, July 2009.

[60] Changling Luo, H. Banakar, B. Shen, and Boon-Teck Ooi. Strategies to smooth wind power fluctuations of wind turbine generator. *Energy Conversion, IEEE Transactions on*, 22(2):341--349, June 2007.

[61] J.P. Barton and D.G. Infield. Energy storage and its use with intermittent renewable energy. *Energy Conversion, IEEE Transactions on*, 19(2):441--448, June 2004.

[62] J. Pedersen. Progress on recent utility-scale energy storage systems for integration of solar and wind power. In *International Renewable Storage Conference and Exhibition, 2011 6th*, Berlin, Germany.

[63] EPRI-DOE handbook of Energy Storage for Transmission & Distribution Applications. Technical Report 1001834, EPRI, Palo Alto, CA, and the U.S. Department of Energy, Washington, DC, 2003.

[64] T. DeVries, J. McDowall, N. Umbricht, and G. Linhofer. Cold storage - Battery energy storage system for Golden Valley Electric Association. Technical report, ABB Review, Janury 2004.

[65] H. Ibrahim, A. Ilinca, and J. Perron. Energy storage systems - Characteristics and comparisons. *Renewable and Sustainable Energy Reviews*, 12(5):1221 -- 1250, 2008.

[66] K. Bradbury. Energy Storage Technologies Review. Technical report, Duke University, August 2010.

[67] Leading the Energy Transition - Electricity Energy . Technical report, SBC Energy Institute, September 2013.

[68] Haisheng Chen, Thang Ngoc Cong, Wei Yang, Chunqing Tan, Yongliang Li, and Yulong Ding. Progress in electrical energy storage system: A critical review. *Progress in Natural Science*, 19(3):291 -- 312, 2009.

[69] Peter J. Hall and Euan J. Bain. Energy-storage technologies and electricity generation. *Energy Policy*, 36(12):4352 -- 4355, 2008. Foresight Sustainable Energy Management and the Built Environment Project.

[70] Maxwell Technologies and Soitec join forces to demonstrate benefits of integrating energy storage with concentrated photovoltaic (CPV) technology. http://www.soitec.com/en/news/press-releases/.

[71] Electricity storage - technology brief. Technical report, IEA-ETSAP and IRENA, April 2012.

[72] Prudent Energy. http://www.pdenergy.com/case-studies.php/.

[73] C. Winter. Comparison of field results between a flow-battery susupport 340 kw PV array and an equivalent unsupported PV array. In *International Renewable Storage Conference and Exhibition, 2012 7th*, Berlin, Germany.

[74] M. Terada and H. Takabayashi. Industrial Storage Device for Low-carbon Society. *Hitachi Review*, 60(1):22 -- 27, 2011.

[75] Xtreme Power. http://www.xtremepower.com//.

[76] Xtreme Power, Experience - Kaheawa Wind Power I. http://www.xtremepower.com/advantage/experience.

[77] Jim McDowall. Integrating energy storage with wind power in weak electricity grids. *Journal of Power Sources*, 162(2):959 -- 964, 2006. Special issue including selected papers from the International Power Sources Symposium 2005 together with regular papers.

[78] Energy Development in Island Nations. http://www.edinenergy.org/bonaire.html.

[79] Sodium Sulfur Battery Energy Storage And Its Potential To Enable Further Integration of Wind (Wind-to-Battery Project). Technical report, Xcel Energy, December 2011.

[80] EOS Energy Storage. http://www.eosenergystorage.com/technology-and-products/.

[81] C. Vartanian and N. Bentley. A123 systems' advanced battery energy storage for renewable integration. In *Power Systems Conference and Exposition (PSCE), 2011 IEEE/PES*, pages 1--6, March 2011.

[82] B. Scrosati and Garche. J. Lithium batteries: Status, prospects and future. *Journal of Power Sources*, 195(9):2419 -- 2430, 2010.

[83] Linden David, editor. *Handbook of Batteries*. McGraw-Hill, 3rd edition, 2002.

[84] Bruce Dunn, Haresh Kamath, and Jean-Marie Tarascon. Electrical energy storage for the grid: A battery of choices. *Science*, 334(6058):928--935, 2011.

[85] Vehicle battery safety roadmap guidance. Technical Report NREL/SR-5400-54404, National Renewable Energy Laboratory, October 2012.

[86] A. Burke and M. Miller. Performance characteristics of lithium-ion batteries of various chemistries for plug-in hybrid vehicles. In *EVS24 International Battery, Hybrid and Fuel Cell Electric Vehicle Symposium*, Stavanger, Norway, May 13-16 2009.

[87] Batteries for electric cars - challenges, opportunities, and the outlook to 2020. Technical report, The Boston Consulting Group, 2010.

[88] K.E. Aifantis, S.A. Hackney, and R.V. Kumar. *High Energy Density Lithium Batteries*. Wiley-VCH, 2010.

[89] X. Yuan, H. Liu, and J. Zhang, editors. *Lithium-ion batteries. Advanced Materials and Technologies*. CRC Press, 2011.

[90] Altairnano - Introducing the ppower-intensive ALTI-ESS suite. http://www.altairnano.com/wp-content/uploads/2012/03/ALTI-ESS_Brochure_10.pdf.

[91] J. Geinzer. AES Laurel Mountain Overview. http://www.wvcommerce.org/App_Media/assets/doc/energy/WWG/2012/AES-LM-Overview2012.pdf, 2012.

[92] BYD Energy. http://www.bydenergy.com/epri/zeng1/chunengchanpin1/014jizhuangxiang1.html.

[93] L. Gaillac, J. Castaneda, A. Edris, D. Elizondo, C. Wilkins, C. Vartanian, and D. Mendelsohn. Tehachapi wind energy storage project: Description of operational uses, system components, and testing plans. In *Transmission and Distribution Conference and Exposition (T D), 2012 IEEE PES*, pages 1--6, May 2012.

[94] Saft Batteries. http://www.saftbatteries.com/sites/default/files/21861-2-0313_CS_Cowessess_Protected.pdf.

[95] A.K. Padhi, K.S. Nanjundaswamy, and J.P. Goodenough. Phospho-olivines as positive-electrode materials for rechargeable lithium batteries. *Journal of the Electrochemical Society*, 144(4):1188--1194, 1997.

[96] A.S. Arico, P. Bruce, B. Scrosati, J.-M. Tarascon, and W. van Schalkwijk. Nanostructured materials for advanced energy conversion and storage devices. *Nature Materials*, 4:366--377, 2005.

[97] G.-A. Nazri and G. Pistoia, editors. *Lithium Batteries. Science and Technology*. Springer, 2009.

[98] Min Chen and G.A. Rincon-Mora. Accurate electrical battery model capable of predicting runtime and i-v performance. *Energy Conversion, IEEE Transactions on*, 21(2):504--511, June 2006.

[99] D. Andre, M. Meiler, K. Steiner, H. Walz, T. Soczka-Guth, and D.U. Sauer. Characterization of high-power lithium-ion batteries by electrochemical impedance spectroscopy. ii: Modelling. *Journal of Power Sources*, 196(12):5349 -- 5356, 2011. Selected papers presented at the 12th Ulm ElectroChemical Talks (UECT):2015 Technologies on Batteries and Fuel Cells.

[100] D.W. Dees, V.S. Battaglia, and A. B langer. Electrochemical modeling of lithium polymer batteries. *Journal of Power Sources*, 110(2):310 -- 320, 2002.

[101] Alfred V. Randall, Roger D. Perkins, Xiangchun Zhang, and Gregory L. Plett. Controls oriented reduced order modeling of solid-electrolyte interphase layer growth. *Journal of Power Sources*, 209(0):282 -- 288, 2012.

[102] John Newman, Karen E. Thomas, Hooman Hafezi, and Dean R. Wheeler. Modeling of lithium-ion batteries. *Journal of Power Sources*, 119–121(0):838 -- 843, 2003. Selected papers presented at the 11th International Meeting on Lithium Batteries.

[103] M. Doyle, T. Fuller, and J. Newman. Modeling of galvanostatic charge and discahrge of the lithium/polymer/insertion cell. *Journal of the Electrochemical Society*, 140(6):1526--1533, 1993.

[104] K.A Smith, C.D. Rahn, and Chao-Yang Wang. Model-based electrochemical estimation and constraint management for pulse operation of lithium ion batteries. *Control Systems Technology, IEEE Transactions on*, 18(3):654--663, May 2010.

[105] S. Li and B. Ke. Study of battery modeling using mathematical and circuit oriented approaches. In *Power and Energy Society General Meeting, 2011 IEEE*, pages 1--8, July 2011.

[106] C.M. Shepher. Design of primary and secondary cells ii . an equation describing battery discharge. *Journal of the Electrochemical Society*, 112(7):657--664, 1965.

[107] O. Tremblay and L.-A. Dessaint. Experimental validation of a battery dynamic model for ev applications. In *Electrical Vehicle Symposium 24*, Stavanger, Norway, May 13-16 2009.

[108] D.U. Sauer and H. Wenzl. Comparison of different approaches for lifetime prediction of electrochemical systems—using lead-acid batteries as example. *Journal of Power Sources*, 176(2):534 -- 546, 2008.

[109] H. Zhang and M.-Y. Chow. Comprehensive dynamic battery modeling for phev applications. In *Power and Energy Society General Meeting, 2010 IEEE*, pages 1--6, July 2010.

[110] R. Jackey, M. Saginw, P. Sanghvi, J. Gazzari, T. Huria, and M. Ceraolo. Battery model parameter estimation using a layered technique: An example using a lithium iron phosphate cell. In *SAE World Congress*, 2013.

[111] F. Huet. A review of impedance measurements for determination of the state-of-charge or state-of-health of secondary batteries. *Journal of Power Sources*, 70(1):59 -- 69, 1998.

[112] E. Brasoukov and J.R. Macdonald, editors. *Impedance Spectroscopy. Theory, Experiment and Applications*. Wiley, 2 edition, 2005.

[113] Eckhard Karden, Stephan Buller, and Rik W. De Doncker. A frequency-domain approach to dynamical modeling of electrochemical power sources. *Electrochimica Acta*, 47(13–14):2347 -- 2356, 2002.

[114] D. Andre, M. Meiler, K. Steiner, Ch. Wimmer, T. Soczka-Guth, and D.U. Sauer. Characterization of high-power lithium-ion batteries by electrochemical impedance spectroscopy. i. experimental investigation. *Journal of Power Sources*, 196(12):5334 -- 5341, 2011.

[115] A. Jossen. Fundamentals of battery dynamics. *Journal of Power Sources*, 154(2):530 -- 538, 2006. Selected papers from the Ninth Ulm Electrochemical Days.

[116] Electrical propelled road vehicles - test specification for lithium-ion traction battery packs and systems - part 1: High-power applications, September 2011.

[117] O. Bohlen. *Impedance based battery monitoring*. PhD thesis, RWTH Aachen, 2008.

[118] Lijun Gao, Shengyi Liu, and R.A Dougal. Dynamic lithium-ion battery model for system simulation. *Components and Packaging Technologies, IEEE Transactions on*, 25(3):495--505, Sep 2002.

[119] FreedomCAR Battery Test Manual For Power-Assist Hybrid Electric Vehicles. Technical Report DOE/ID-11069, Idaho National Engineering & Environmental Laboratory, October 2003.

[120] Sauer. D.U. *Storage Systems based on Electrochemical Batteries for Grid Support Applications*, October 2013. Industrial/PhD Course at Aalborg University.

[121] S. Buller, M. Thele, R.W.AA De Doncker, and E. Karden. Impedance-based simulation models of supercapacitors and li-ion batteries for power electronic applications. *Industry Applications, IEEE Transactions on*, 41(3):742--747, May 2005.

[122] W. Waag, S. K□ bitz, and Sauer D.U. Experimental investigation of the lithium-ion battery impedance characteristic at various conditions and aging states and its influence on the application. *Applied Energy*, 102:885 -- 897, 2013.

[123] J.A. Bard, G. Inzelt, and F. Scholz, editors. *Electrochemical Dictionary*. Springer, 2nd edition, 2012.

[124] J. Vetter, P. Novak, M.R. Wagner, C. Veit, K.-C. Moller, J.O. Besenhard, M. Winter, M. Wohlfarht-Mehrens, C. Vogler, and A. Hammouche. Ageing mechanisms in lithium-ion batteries. *Journal of Power Sources*, 147:269--281, 2005.

[125] M. Broussely, Ph. Biensan, F. Bonhomme, Ph. Blanchard, S. Herreyre, K. Nechev, and R.J. Staniewicz. Main aging mechanisms in li ion batteries. *Journal of Power Sources*, 146(1-2):90 -- 96, 2005.

[126] J. Groot. *State-of-Health Estimation of Li-ion Batteries: Cycle Life Test Methods*. PhD thesis, Chalmers University of Technology, 2012.

[127] D. Aurbach, E. Zinigrad, Y. Cohen, and H. Teller. A short review of failure mechanisms of lithium metal and lithiated graphite anodes in liquid electrolyte solutions. *Solid State Ionics*, 148(3-4):405 -- 416, 2002.

[128] E. Peled. The electrochemical behavior of alkali and alkaline earth metals in nonaqueous battery systems - the solid electrolyte interphase model. *Journal of the Electrochemical Society*, 126(12):2047--2051, 1979.

[129] M. Kassem, J. Bernard, R. Revel, S. Pelissier, F. Duclaud, and C. Delacourt. Calendar aging of a graphite/lifepo4 cell. *Journal of Power Sources*, 208(0):296 -- 305, 2012.

[130] John Wang, Ping Liu, Jocelyn Hicks-Garner, Elena Sherman, Souren Soukiazian, Mark Verbrugge, Harshad Tataria, James Musser, and Peter Finamore. Cycle-life model for graphite-lifepo4 cells. *Journal of Power Sources*, 196(8):3942 -- 3948, 2011.

[131] R.B Wright, J.P Christophersen, C.G Motloch, J.R Belt, C.D Ho, V.S Battaglia, J.A Barnes, T.Q Duong, and R.A Sutula. Power fade and capacity fade resulting from cycle-life testing of advanced technology development program lithium-ion batteries. *Journal of Power Sources*, 119–121(0):865 -- 869, 2003.

[132] H. Wenzl, I. Baring-Gould, R. Kaiser, B.Y. Liaw, P. Lundsager, J. Manwell, A. Ruddell, and V. Svoboda. Life prediction of batteries for selecting the technically most suitable and cost effective battery. *Journal of Power Sources*, 144(2):373 -- 384, 2005.

[133] H. Bindner, T. Cronin, P. Lundsager, J. Manwell, U. Abdulwahid, and I. Baring-Gould. Lifetime Modelling of Lead Acid Batteries. Technical Report Ris-R-1515(EN), Riso National Laboratory, Roskilde, April 2005.

[134] J.F. Manwell, A. Rogers, G. Hayman, C.T. Avelar, J.G. McGowan, U. Abdulwahid, and K. Wu. HYBRID2- a hybrid system simulation model - theory manual. Technical Report XL-1-11126-1-1, Renewable Energy Research Laboratory, University of Massachusetts, June 2006.

[135] C. Amzallag, J.P. Gerey, J.L. Robert, and J. Bahuaud. Standardization of the rainflow counting method for fatigue analysis. *International Journal of Fatigue*, 16(4):287 -- 293, 1994.

[136] MATLAB. *version 8.1.0.604 (R2013a)*. The MathWorks, Inc., 2013.

[137] R. Yazami and Y. F. Reynier. Mechanism of self-discharge in graphite-lithium anode. *Electrochimica Acta*, 47(8):1217 -- 1223, 2002.

[138] M. Swierczynski, D.-I. Stroe, A.-I. Stan, R. Teodorescu, and S.K. Kaer. Investigation on the self-discharge of the lifepo4/c nanophosphate battery chemistry at different conditions. In *Transportation Electrification Conference and Expo (ITEC), 2014 IEEE*, 2014, in press.

[139] M. Broussely, S. Herreyre, P. Biensan, P. Kasztejna, K. Nechev, and R. Staniewicz. Aging mechanism in li ion cells and calendar life predictions. *Journal of Power Sources*, 97-98(0):13 -- 21, 2001.

[140] R. Spotnitz. Simulation of capacity fade in lithium-ion batteries. *Journal of Power Sources*, 113(1):72 -- 80, 2003.

[141] M. Matsuishi and T. Endo. Fatigue of metals subjected to varying stress. *Japan Society of Mehcanical Enfineering*, 1968.

[142] M. Swierczynski, R. Teodorescu, and Rodriguez P. Lifetime investigations of a lithium iron phosphate battery system connected to a wind turbine for forecast improvement and output power gradient reduction. In *BATTCON*, pages 20--1 -- 20--8, 2011.

[143] M. Safari, M. Morcrette, A. Teyssot, and C. Delacourt. Life prediction methods for lithium-ion batteries derived from a fatigue approach ii. capacity-loss prediction of batteries subjected to complex current profiles. *Journal of the Electrochemical Society*, 157(7):A892--A898, 2010.

[144] Energinet.dk. Ancillary services to be delivered in Denmark. Tender conditions. Technical Report Doc. 8871/11 v3, Case 10/2932, Fredericia, Denmark, 2012.

[145] P.C. Kjaer and R Laerke. Experience with primary reserve supplied from energy storage system. In *Innovative Smart Grid Technologies Europe (ISGT EUROPE), 2013 4th IEEE/PES*, 2013.

Appendix A

Parameters of the LiFePO$_4$/C battery cells under study

The parameters of the LFP/C battery cells under test are listed in the table below.

Table A.1: *Parameters of the studied LiFePO$_4$/C battery cells.*

Parameter	Value
Chemistry	naophosphate-based LiFePO$_4$/C
Shape	Cylindrical
Cell Dimensions [mm]	ϕ 26 x 65
Cell Weight [g]	76
Capacity [Ah]	2.5
Nominal Voltage [V]	3.3
Max. Voltage [V]	3.6
Min. Voltage [V]	2.0
Max. Continuous Charge Current [A]	10
Max. Continuous Discharge Current [A]	70
Operating Temperature	-30^{o}C to +60^{o}C
Storage Temperature	-50^{o}C to +60^{o}C

Appendix B

Laboratory Equipment

B.1 Description of battery test stations

This appendix presents the battery test stations, which have been used for:

- performing the full characterization test at BOL (see Chapter 3.2.1);
- carrying out all the accelerated cycling ageing tests (see Chapter 5.3);
- performing all the RPTs.

FuelCon battery test station

The FuelCon battery test station (BTS), presented in Fig. B.1, was used to perform a part of the accelerated calendar cycling. Moreover, all the RPTs were performed using this BTS.

The FuelCon BTS consists of two charging-discharging channels rated at 18 V/ 200 A. Each of these channels is placed inside a water cooled temperature chamber; the temperature of the battery cell is controlled by controlling the temperature of the cooling plate in the range 10^{o}C - 80^{o}C. Moreover, one of the channels is equipped with an EIS-analyser, which was used to perform all the EIS measurements presented in this thesis.

Maccor battery test station

The Maccor BTS, presented in Fig. B.2, was used to perform the full characterization test of the LFP/C battery cell (see Chapter 3.2.1). Furthermore, this BTS was used to perform a part of the accelerated cycling ageing tests.

The Maccor BTS consists of eight charging-discharging channels rated each at 9 V/ 50 A; these channels are placed inside four forced-air cooled temperature chambers (2 channels per chamber).

Figure B.1: *FuelCon battery test station.*

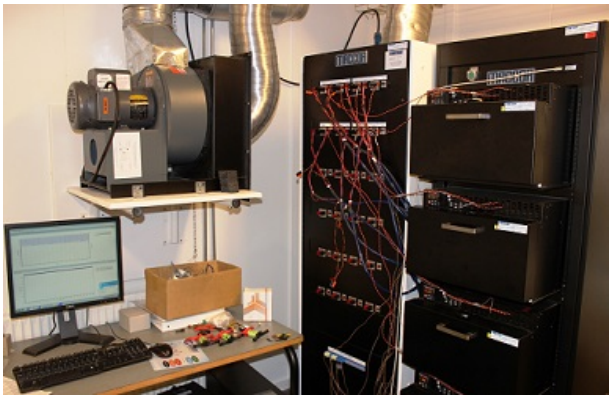

Figure B.2: *Maccor battery test station.*

B.2 Description of universal ovens

All the laboratory accelerated calendar lifetime tests (see Table 5.1) were performed using several Memmert UNP 500 universal ovens, as the one shown in Fig. B.3. These ovens are using natural convection to control the temperature in the range 30^{o}C - 250^{o}C. Fig. B.4 illustrates three LFP/C battery cells inside the oven during one of the performed accelerated lifetime tests.

Figure B.3: *Memmert UNP 500 universal oven used for accelerated calendar ageing tests.*

Figure B.4: *LFP/C battery cells placed inside one of the Memmert UNPP 500 universal ovens.*

Appendix C

Characterization test of the LFP/C battery cell

C.1 Preconditioning Test

The procedure, which was used to perform the preconditioning test is presented in Table C.1.

Fig. C.1 and Fig. C.2 present the measured voltage profiles during charging and discharging, respectively.

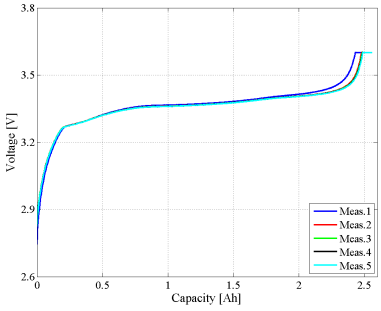

Figure C.1: *Charging voltage profiles measured during the preconditioning test*

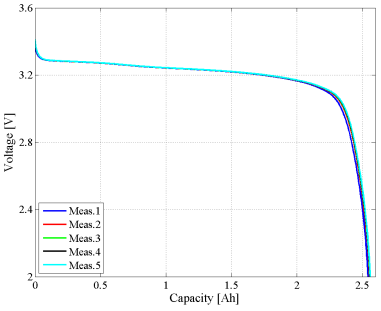

Figure C.2: *Discharging voltage profiles measured during the preconditioning test*

The values of the charging and discharging capacities measured during the preconditioning test are summarized in Table C.2.

Table C.1: *Procedure followed during the preconditioning test.*

Step	Action
1	Tempering of the LFP/C battery cell at 25 ^{o}C for one hour
2	Full charge of the battery cell using a constant current (CC) - constant voltage (CV) pattern, considering 1C-rate current (2.5 A) and maximum cell voltage; the charging process was considered finished once the current has reached a pre-defined
3	Relaxation of the battery cell at 25 ^{o}C for one hour
4	Full discharge of the battery cell, by applying 1C-rate current (2.5 A); the discharging process was considered finished once the voltage has reached the minimum voltage (i.e. 2 V)
5	Relaxation of the battery cell at 25 ^{o}C for one hour
6	Repetition of steps 2. - 5. for other four times

Table C.2: *Charged and discharged capacity values measured during the preconditioning test (part of the full characterization test for the LFP/C battery cell)*

Meas. No	Charging		Discharging	
#	Capacity [Ah]	Change in Capacity [%]	Capacity [Ah]	Change in Capacity [%]
1	2.553	0	2.543	0
2	2.554	0.041	2.554	0.463
3	2.556	0.118	2.557	0.562
4	2.557	0.166	2.559	0.605
5	2.558	0.202	2.560	0.647

C.2 Relaxation Test

The procedure, which was used to perform the preconditioning test is presented in Table C.3.

Table C.3: *Procedure followed during the relaxation test.*

Step	Action
1	Tempering of the LFP/C battery cell at 25 ^{o}C for one hour
2	Full charge of the battery cell using a constant current (CC) - constant voltage (CV) pattern, considering 1C-rate current (2.5 A) and maximum cell voltage; the charging process was considered finished once the current has reached a pre-defined cut-off value (4% of the nominal battery cell capacity)
3	Relaxation of the battery cell at 25 ^{o}C for one hour
4	Discharge of the battery cell, by applying 1C-rate current (2.5 A) until SOC = 80%
5	Relaxation of the battery cell at 25 ^{o}C for 24 hours
6	Discharge of the battery cell, by applying 1C-rate current (2.5 A) until SOC = 50%
7	Relaxation of the battery cell at 25 ^{o}C for 24 hours
8	Discharge of the battery cell, by applying 1C-rate current (2.5 A) until SOC = 20%
9	Relaxation of the battery cell at 25 ^{o}C for 24 hours
10	Discharge of the battery cell, by applying 1C-rate current, until the cut-off voltage is reached

The results obtained for the relaxation test performed at 20% and 80% SOC for both charging and discharging conditions are presented in Fig. C.3 - Fig. C.10.

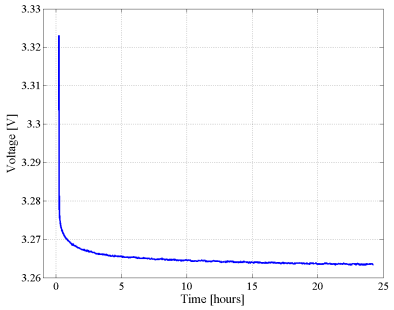

Figure C.3: *Voltage recovery during 24 hours relaxation, after charging (SOC=20%)*

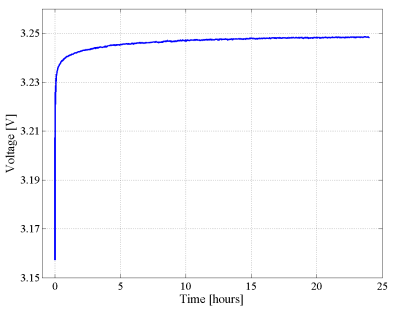

Figure C.4: *Voltage recovery during 24 hours relaxation, after discharging (SOC=20%)*

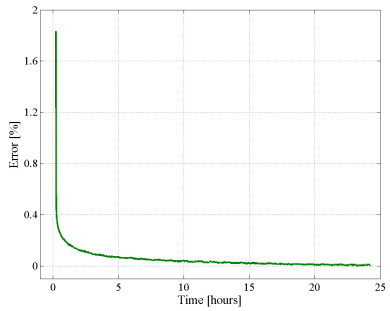

Figure C.5: *Open-circuit voltage error depending on the relaxation time (charging case, SOC=20%)*

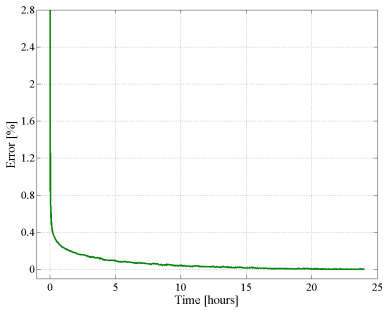

Figure C.6: *Open-circuit voltage error depending on the relaxation time (discharging case, SOC=20%)*

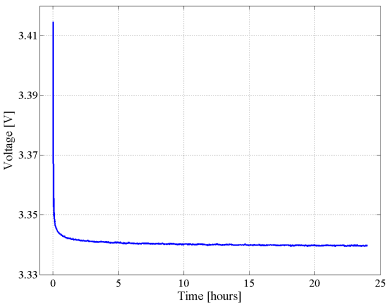

Figure C.7: *Voltage recovery during 24 hours relaxation, after charging (SOC=80%)*

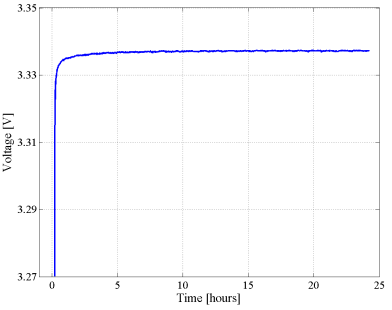

Figure C.8: *Voltage recovery during 24 hours relaxation, after discharging (SOC=80%)*

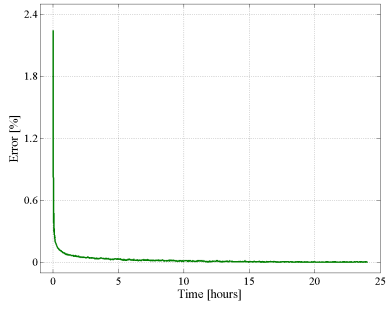

Figure C.9: *Open-circuit voltage error depending on the relaxation time (charging case, SOC=80%)*

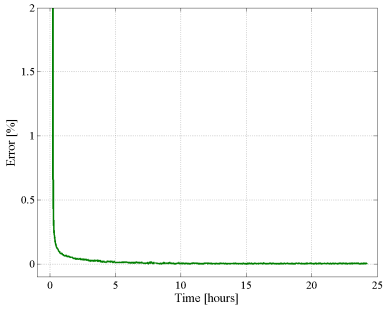

Figure C.10: *Open-circuit voltage error depending on the relaxation time (discharging case, SOC=80%)*

Table C.4 and Table C.5 are summarizing the OCV values and their corresponding errors measured after different relaxation time periods, at 20% and 80% SOC, re-

spectively. Similar to the measurements performed at 50% SOC, the error of the OCV measurements is only slightly dependent on the relaxation period.

Table C.4: *Voltage of the LFP/C battery cell measured at 20% SOC after various relaxation time periods*

Relaxation time	**Charging**		**Discharging**	
	Voltage [V]	OCV error [%]	Voltage [V]	OCV error [%]
1 second	3.323	1.83	3.157	2.80
15 minutes	3.277	0.41	3.236	0.37
1 hour	3.269	0.18	3.241	0.23
2 hours	3.267	0.12	3.243	0.17
24 hours	3.263	0	3.248	0

Table C.5: *Voltage of the LFP/C battery cell measured at 80% SOC after various relaxation time periods*

Relaxation time	**Charging**		**Discharging**	
	Voltage [V]	OCV error [%]	Voltage [V]	OCV error [%]
1 second	3.415	2.24	3.270	2.00
15 minutes	3.345	0.16	3.325	0.37
1 hour	3.342	0.07	3.335	0.07
2 hours	3.341	0.05	3.226	0.04
24 hours	3.340	0	3.337	0

C.3 Capacity Test

The procedure, which was used to perform the capacity test with different C-rates is presented in Table C.1.

Table C.6: *Procedure followed during the capacity test.*

Step	Action
1	Tempering of the LFP/C battery cell at 15 ^{o}C for one hour
2	Full charge of the battery cell using a constant current (CC) - constant voltage (CV) pattern, considering C/4-rate current and maximum cell voltage; the charging process was considered finished once the current has reached a predefined cut-off value (4% of the nominal battery cell capacity)
3	Relaxation of the battery cell at 15 ^{o}C for one hour
4	Full discharge of the battery cell, by applying C/4-rate current; the discharging process was considered finished once the voltage has reached the minimum voltage (i.e. 2 V)
5	Relaxation of the battery cell at 15 ^{o}C for one hour
6	Repetition of steps 2. - 5. for the following C-rate values: C/2, 1C, 2C, 3C, and 4C
7	Repetition of steps 2. - 6. for the following temperatures: 25^{o}C, 35^{o}C, 45^{o}C

The measured voltage profiles during the capacity test of the LFP/C battery cell are illustrated in Fig. C.11.

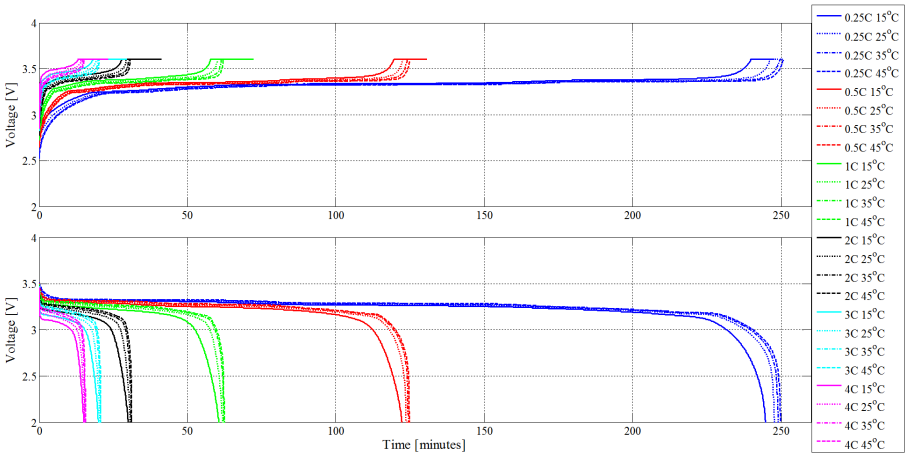

Figure C.11: *Measured voltage profiles on the LFP/C battery cell during the capacity test for charging (top) and discharging conditions (bottom).*

C.4 OCV vs SOC Test

The procedure, which was used to perform the OCV vs SOC test is summarized in Table C.7.

Table C.7: *Procedure followed during the OCV vs SOC test.*

Step	Action
1	Tempering of the LFP/C battery cell at 15 ^{o}C for one hour
2	Full discharge of the battery cell, with 1C-rate current, until the end of discharge voltage (i.e. 2 V) is reached
3	Relaxation of the battery cell at 15 ^{o}C for one hour
4	Charging of the LFP/C battery cell with 1C-rate for 5% SOC
5	Relaxation of the battery cell at 15 ^{o}C for one hour; the voltage after 1 hour is considered the OCV
6	Repetition of steps 4. - 5. until the battery cell is fully charged
7	Discharging of the LFP/C battery cell with 1C-rate for 5% SOC
8	Relaxation of the battery cell at 15 ^{o}C for one hour; the voltage after 1 hour is considered the OCV
9	Repetition of steps 7. - 8. until the battery cell is fully discharged
10	Repetition of steps 1. - 9. for the following temperatures: 25^{o}C, 35^{o}C, 45^{o}C

The OCV vs SOC characteristics measured on the LFP/C battery cell at 15 ^{o}C and 35 ^{o}C are presented in Fig. C.12 and Fig. C.13, respectively.

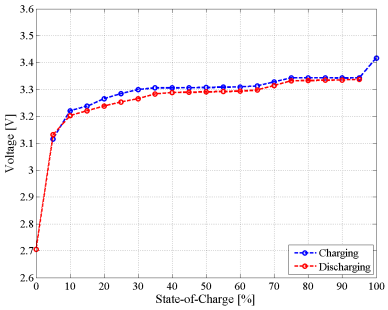

Figure C.12: *The OCV vs SOC characteristic of the LFP/C battery cell measured at 15 ^{o}C.*

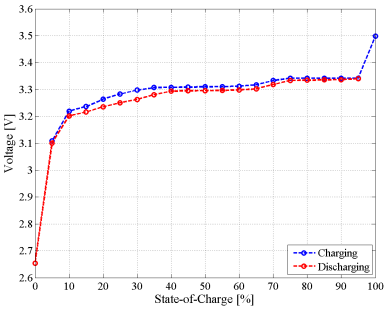

Figure C.13: *The OCV vs SOC characteristic of the LFP/C battery cell measured at 35 ^{o}C.*

The OCV vs SOC characteristics measured on the LFP/C battery cell at 45 ^{o}C is presented in Fig. C.14.

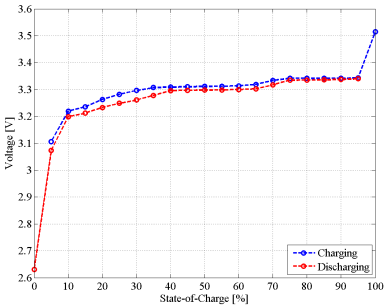

Figure C.14: *The OCV vs SOC characteristic of the LFP/C battery cell measured at 45 ^{o}C.*

C.5 HPPC Test

The procedure, which was used to perform the HPPC test is summarized in Table C.8.

Table C.8: *Procedure followed during the measurement of the internal resistance using the HPPC test.*

Step	Action
1	Tempering of the LFP/C battery cell at 15 ^{o}C for one hour
2	Full discharge of the battery cell, with 1C-rate current, until the end of discharge voltage (i.e. 2 V) is reached
3	Relaxation of the battery cell at 15 ^{o}C for one hour
4	Charging of the LFP/C battery cell with 1C-rate for 5% SOC
5	Relaxation of the battery cell at 15 ^{o}C for 15 minutes
6	Measurement of the internal resistance of the LFP/C battery based on the profile presented in Fig. 3.13
7	Repetition of steps 4. - 6. for all SOCs, considering a 5% SOC increment
8	Repetition of steps 1. - 7. for the following temperatures: 25^{o}C, 35^{o}C, 45^{o}C

The dependence of the charging internal resistance on the operating temperature, measured with 1C-rate, is presented in Fig. C.15.

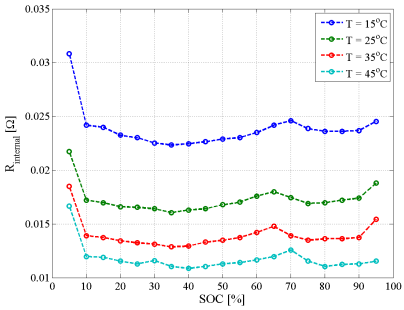

Figure C.15: *Dependence of the charging internal resistance on the operating temperature (measured for 1C).*

C.6 Pulse Power Capability calculation

Fig. C.16 and Fig. C.17 present the maximum PPC characteristics of the tested LFP/C battery cell, measured for the charging and discharging, respectively. The maximum PPC characteristics of the LFP/C battery cell are flat for almost the entire SOC interval and almost independent on the operating temperature.

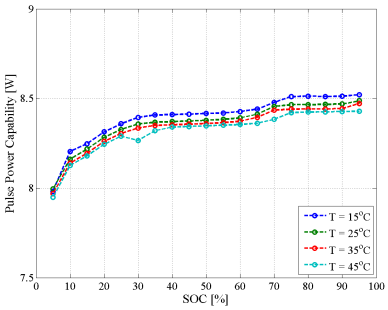

Figure C.16: *Maximum charging PPC of the LFP/C battery cell measured for the entire SOC range at various temperatures (measurements performed with nominal current, 10 A).*

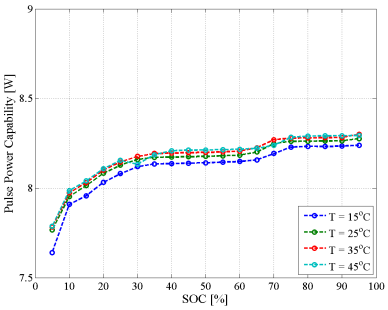

Figure C.17: *Maximum discharging PPC of the LFP/C battery cell measured for the entire SOC range at various temperatures (measurements performed with nominal current, 10 A).*

C.7 EIS Test

The procedure, which was used to perform the EIS measurements is summarized in Table C.9.

Table C.9: *Procedure followed during the EIS test.*

Step	Action
1	Tempering of the LFP/C battery cell at 15 ^{o}C for one hour
2	Full discharge of the battery cell, with 1C-rate current, until the end of discharge voltage (i.e. 2 V) is reached
3	Relaxation of the battery cell at 15 ^{o}C for one hour
4	Charging of the LFP/C battery cell with 1C-rate for 5% SOC
5	Relaxation of the battery cell at 15 ^{o}C for 15 minutes
6	Measurement of the impedance spectrum of the LFP/C battery considering the aforementioned measurement parameters
7	Repetition of steps 4. - 6. for all SOCs, considering a 5% SOC increment
8	Repetition of steps 1. - 7. for the following temperatures: 25^{o}C, 35^{o}C, 45^{o}C

In Fig. C.18, the measured impedance spectra of tested LFP/C battery cell are presented for the whole SOC interval. On the zoom view, while the SOC has been increased, a decrease of the first semi-circle of the Nyquist curve was observed.

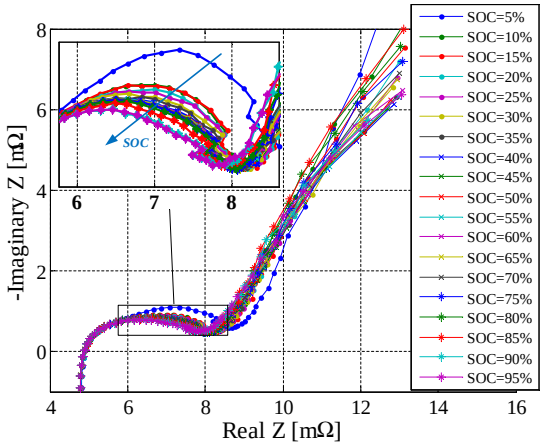

Figure C.18: *Dependence of the impedance spectra on the SOC (measured at T = 25^{o}C for whole SOC interval).*

In Fig. C.19 and Fig. C.20, there are presented the measured impedance spectra of

tested LFP/C battery at 20% SOC and 80% SOC, respectively, for different temperatures. As shown in this plots, the dependence of the Nyquist plots on the operating temperature is not changing with the SOC level.

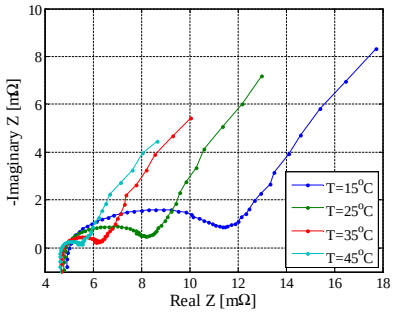

Figure C.19: *Dependence of the impedance spectra on the temperature (measured at SOC = 20%).*

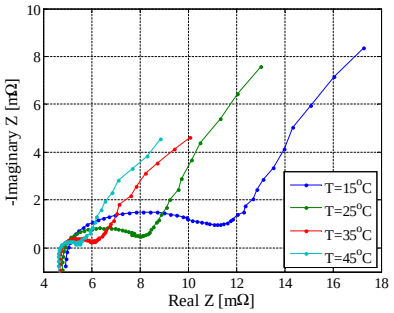

Figure C.20: *Dependence of the impedance spectra on the temperature (measured at SOC = 80%).*

Appendix D

Verification of the LFP/C battery cell performance model

D.1 Verification based on dynamic charge - discharge profile

The procedure used to validate the developed LFP/C battery cell performance model using a dynamic charge/discharge current pulses profile is summarized in Table D.1. The current profile applied to the LFP/C battery cell is presented in Fig. D.1.

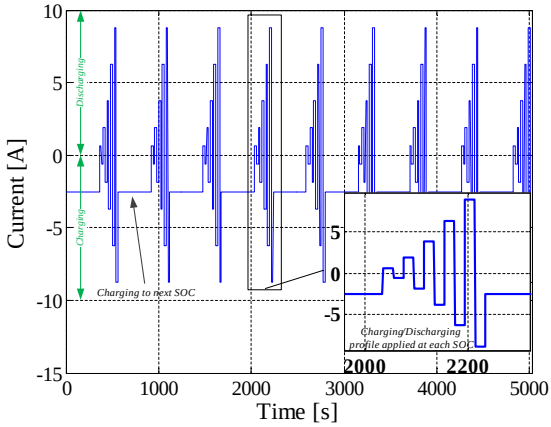

Figure D.1: *Current profile applied to the LFP/C battery cell during the verification of the performance model.*

Table D.1: *Procedure based on dynamic charging/discharging current pulses used for verification of the developed performance model.*

Step	Action
1	Charge battery with 1C until SOC=10%
2	Apply the following pulses with 20sec length:
3	0.25C discharge followed by 0.25C charge pulse (no relaxation in between)
4	0.75C discharge followed by 0.75C charge pulse (no relaxation in between)
5	1.5C discharge followed by 1.5C charge pulse (no relaxation in between)
6	2.5C discharge followed by 2.5C charge pulse (no relaxation in between)
7	3.5C discharge followed by 3.5C charge pulse (no relaxation in between)
8	Charge battery with 1C by another SOC=10% and repeat procedure 2-7 until SOC=90%
9	Fully discharge battery with 1C (15min relaxation time)

D.2 Verification based on PFR current profile

The PFR current profile, used to verify the accuracy of the developed performance model, was measured on field on a 400 kW/ 100 kWh Li-ion battery ESS. The Li-ion battery ESS is located in Lemkaer, Denmark and it is actively providing PFR service in the Danish energy market [42]. Moreover, the battery ESS is based on almost similar Li-ion cells (same manufacturer, but older generation) as the the ones for which the performance model was built.

In order to be applied to the LFP/C battery cell, which was tested in laboratory, the real current profile had to be scaled-down. Based on the ratings of the tested LFP/C battery cell, the maximum allowed continuously charging and discharging currents were set at 10 A. Thus, the obtained PFR current profile which was used to verify the developed LFP/C battery cell performance model is illustrated in Fig. D.2.

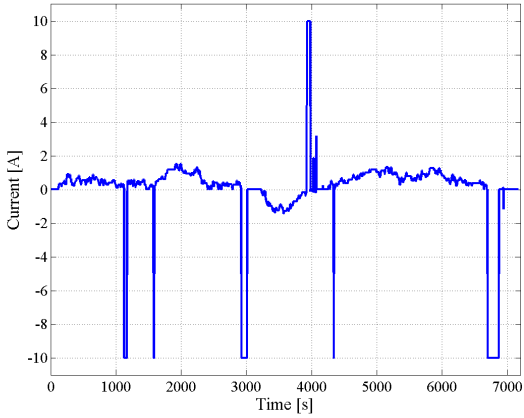

Figure D.2: *Realistic PFR current profile applied to the LFP/C battery cell during the verification of the performance model.*

The PFR profile was derived for a period of 2 hours, which was considered long enough to verify the developed model. The procedure for laboratory testing the LFP/C battery cell with the derived PFR current profile is summarized in Table D.2.

Table D.2: *Procedure based on PFR current profile for verification of the developed performance model.*

Step	Action
1	Charge battery with 1C until SOC=50%
2	Apply 15 minutes relaxation time.
3	Apply the 2 hours PFR current profile to the LFP/C battery cell.

Appendix E

Results of the Accelerated Ageing Tests

This Appendix presents various results obtained from the accelerated calendar and cycling lifetime tests, which were performed on the LFP/C battery cells.

The accelerated test conditions, and the battery cells assigned to each TC, are summarized in Table E.1.

E.1 Results from accelerated calendar ageing tests

E.1.1 Measured Capacity Fade

The measured capacity fade for all the calendar TCs, expressed both as absolute and relative values are presented in the followings.

E.1.2 Dependence of capacity fade on storage time

Different functions have been initially evaluated for fitting the capacity fade of the tested battery cells caused by the accelerated ageing tests. These functions are the following:

- **Logarithmic function:**

$$C_{fade} = a \cdot \ln(b \cdot time) \tag{E.1}$$

- **Linear function:**

$$C_{fade} = a \cdot time \tag{E.2}$$

Table E.1: *Accelerated calendar and cycling lifetime tests - testing conditions.*

Test case	LFP/C cells	Stress factors/levels			Performance check
		Temp.	Cycle depth	SOC	
Calendar 1	C.1, C.2, C.3	55^oC	---	50%	1 month
Calendar 2	C.4, C.5, C.6	47.55^oC	---	50%	
Calendar 3	C.7, C.8, C.9	40^oC	---	50%	
Calendar 4	C.10, C.11, C.12	55^oC	---	10%	
Calendar 5	C.13, C.14, C.15	55^oC	---	90%	
TC 1	3.7, 3.8, 3.9	50^oC	10%	50%	1 month
TC 2	3.4, 3.5, 3.6	50^oC	35%	50%	
TC 3	3.1, 3.2, 3.3	50^oC	60%	50%	
TC 5	3.22, 3.23, 3.24	42.5^oC	35%	50%	
TC 6	3.10, 3.11, 3.12	42.5^oC	60%	50%	
TC 9	3.13, 3.14, 3.15	35^oC	60%	50%	
TC 10	3.32, 3.35, 3.36	42.5^oC	35%	27.5%	
TC 11	3.37, 3.38, 3.39	42.5^oC	35%	72.5%	

• **Square-root-of-time:**

$$C_{fade} = a \cdot \sqrt{time} \tag{E.3}$$

• **Power Law:**

$$C_{fade} = a \cdot time^b \tag{E.4}$$

• **Power Law with fixed coefficient:**

$$C_{fade} = a \cdot time^{0.8} \tag{E.5}$$

The obtained accuracy values for fitting the measured capacity fade with the considered functions are summarized in Table E.2. The best fitting accuracies were obtained for the power law and for the power law with fixed coefficient functions; however, because the difference in the obtained accuracy values is extremely small between these two fitting functions (i.e. 0.9989 vs. 0.9978), the power law with fixed coefficient was selected since it involves only one free parameter.

The results obtained for fitting the capacity fade over time for the LFP/C battery cells stored at various conditions are presented in Fig. E.12 - E.16.

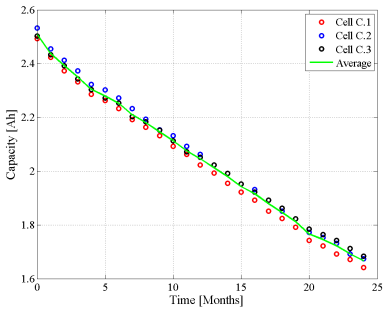

Figure E.1: *Capacity values measured on LFP/C cells subjected to Calendar 1 ageing conditions.*

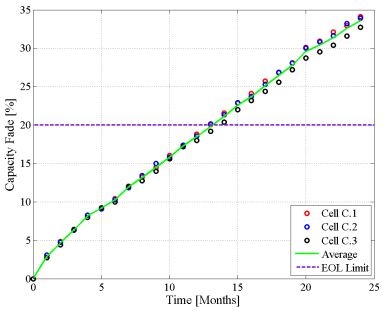

Figure E.2: *Capacity fade of LFP/C battery cells subjected to Calendar 1 ageing conditions.*

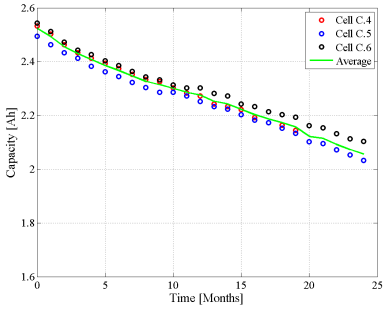

Figure E.3: *Capacity values measured on LFP/C cells subjected to Calendar 2 ageing conditions.*

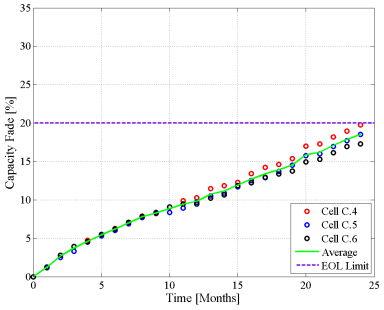

Figure E.4: *Capacity fade of LFP/C battery cells subjected to Calendar 2 ageing conditions.*

E.1.3 Measured Discharge Pulse Power Capability

The measured PPC decrease for the LFP/C battery cells tested under the calendar conditions summarized in E.1 are presented both as absolute and relative values in Fig. E.17 - Fig. E.46.

Measured PPC and PPC decrease at 20% SOC

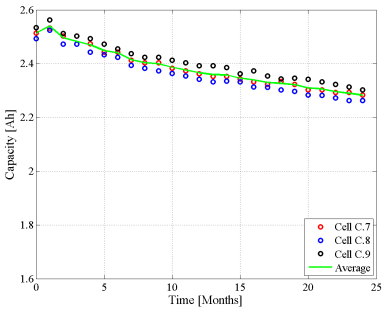

Figure E.5: *Capacity values measured on LFP/C cells subjected to Calendar 3 ageing conditions.*

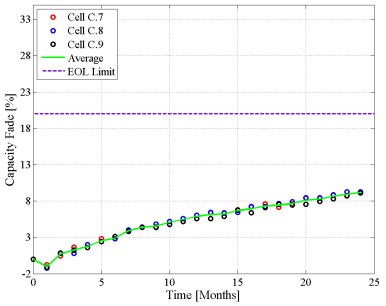

Figure E.6: *Capacity fade of LFP/C battery cells subjected to Calendar 3 ageing conditions.*

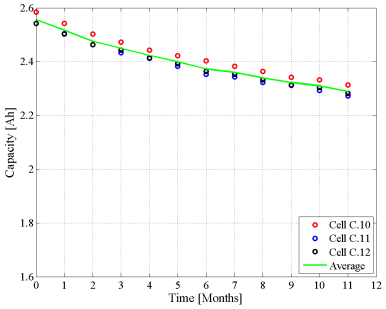

Figure E.7: *Capacity values measured on LFP/C cells subjected to Calendar 4 ageing conditions.*

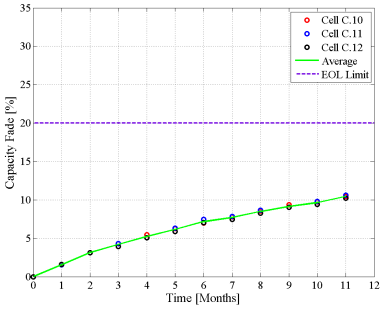

Figure E.8: *Capacity fade of LFP/C battery cells subjected to Calendar 4 ageing conditions.*

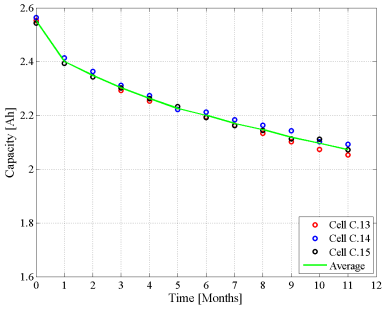

Figure E.9: *Capacity values measured on LFP/C cells subjected to Calendar 5 ageing conditions.*

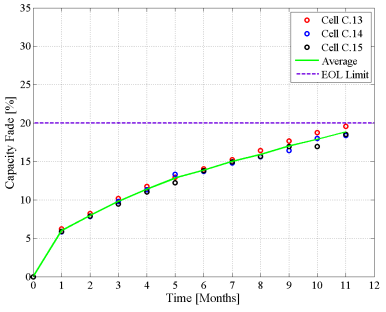

Figure E.10: *Capacity fade of LFP/C battery cells subjected to Calendar 5 ageing conditions.*

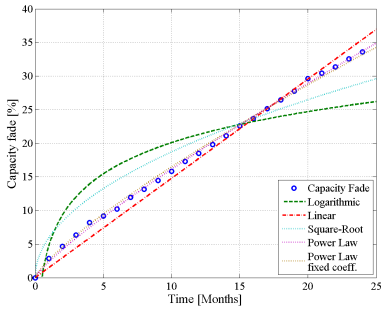

Figure E.11: *Comparison of results obtained from fitting the capacity fade of LFP/C battery cells with different functions (capacity fade results obtained from Calendar 1 test used for curve fitting selection).*

Table E.2: *Accuracy obtained for fitting the capacity fade with various functions.*

Fitting Function	No. of Parameters	R^2
Logarithmic	2	0.7463
Linear	1	0.9852
Square-Root	1	0.9061
Power Law	2	0.9989
Power Law with fixed coeff.	1	0.9978

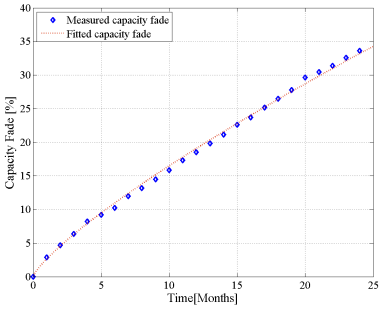

Figure E.12: *Measured and fitted capacity fade of the LFP/C cells subjected to Calendar 1 ageing conditions.*

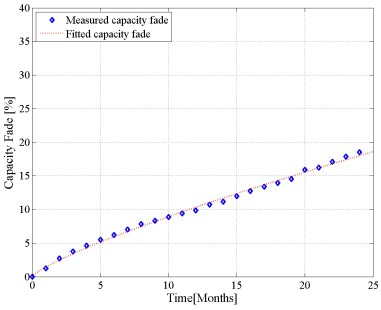

Figure E.13: *Measured and fitted capacity fade of the LFP/C cells subjected to Calendar 2 ageing conditions..*

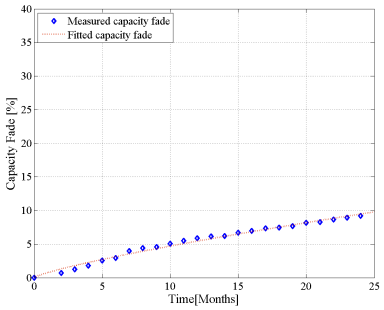

Figure E.14: *Measured and fitted capacity fade of the LFP/C cells subjected to Calendar 3 ageing conditions.*

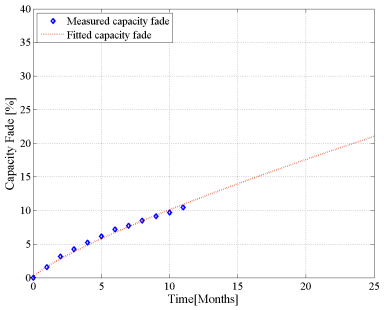

Figure E.15: *Measured and fitted capacity fade of the LFP/C cells subjected to Calendar 4 ageing conditions.*

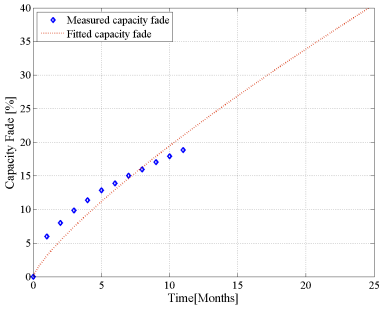

Figure E.16: *Measured and fitted capacity fade of the LFP/C cells subjected to Calendar 5 ageing conditions.*

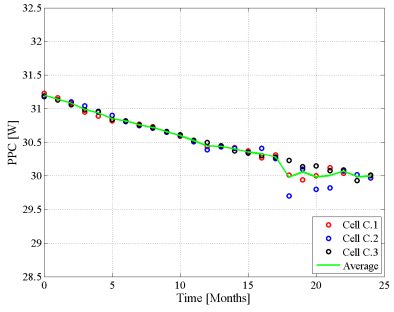

Figure E.17: *Discharge PPC values measured on LFP/C cells subjected to Calendar 1 ageing conditions (RPT: SOC=20%, I_{dc}=10A).*

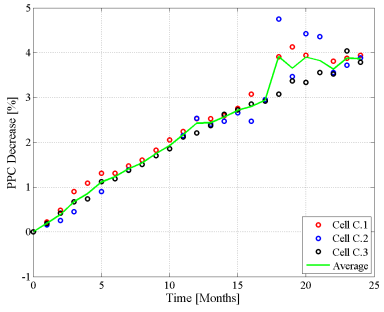

Figure E.18: *Discharge PPC decrease of LFP/C battery cells subjected to Calendar 1 ageing conditions (RPT: SOC=20%, I_{dc}=10A).*

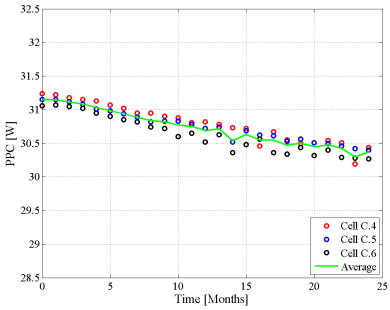

Figure E.19: *Discharge PPC values measured on LFP/C cells subjected to Calendar 2 ageing conditions (RPT: SOC=20%, I_{dc}=10A).*

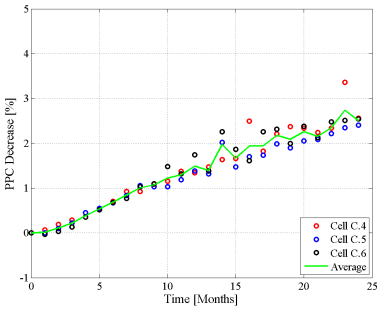

Figure E.20: *Discharge PPC decrease of LFP/C battery cells subjected to Calendar 2 ageing conditions (RPT: SOC=20%, I_{dc}=10A).*

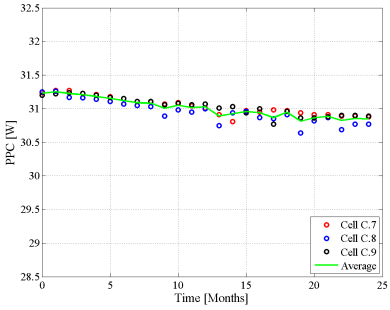

Figure E.21: *Discharge PPC values measured on LFP/C cells subjected to Calendar 3 ageing conditions (RPT: SOC=20%, I_{dc}=10A).*

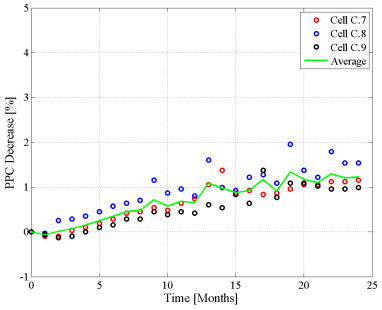

Figure E.22: *Discharge PPC decrease of LFP/C battery cells subjected to Calendar 3 ageing conditions (RPT: SOC=20%, I_{dc}=10A).*

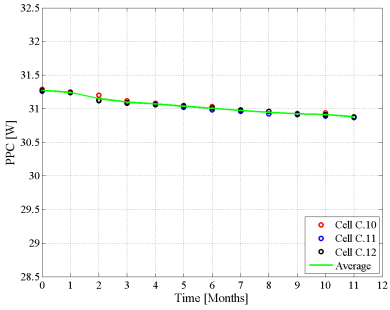

Figure E.23: *Discharge PPC values measured on LFP/C cells subjected to Calendar 4 ageing conditions (RPT: SOC=20%, I_{dc}=10A).*

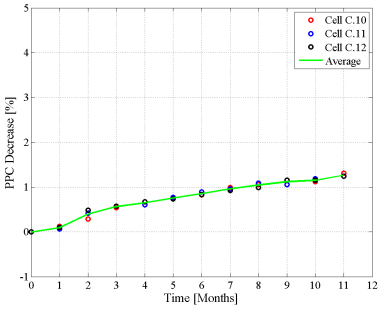

Figure E.24: *Discharge PPC decrease of LFP/C battery cells subjected to Calendar 4 ageing conditions (RPT: SOC=20%, I_{dc}=10A).*

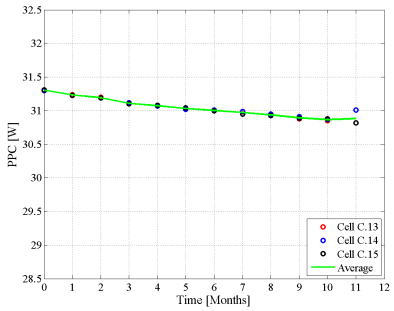

Figure E.25: *Discharge PPC values measured on LFP/C cells subjected to Calendar 5 ageing conditions (RPT: SOC=20%, I_{dc}=10A).*

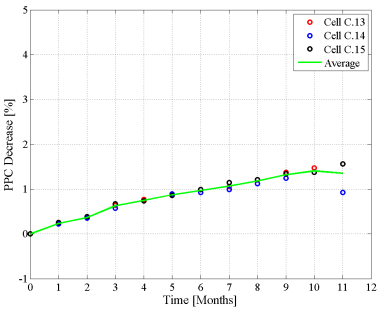

Figure E.26: *Discharge PPC decrease of LFP/C battery cells subjected to Calendar 5 ageing conditions (RPT: SOC=20%, I_{dc}=10A).*

Measured PPC and PPC decrease at 50% SOC

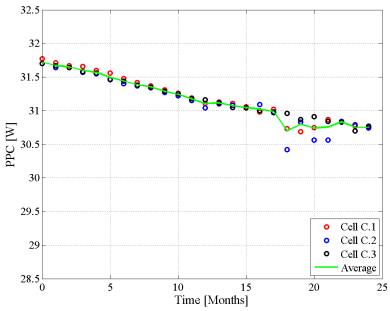

Figure E.27: *Discharge PPC values measured on LFP/C cells subjected to Calendar 1 ageing conditions (RPT: SOC=50%, I_{dc}=10A).*

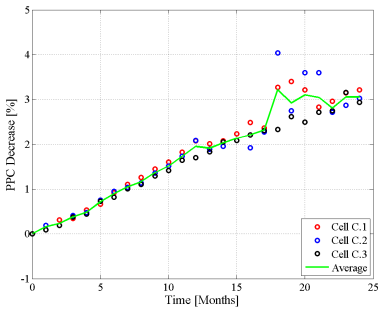

Figure E.28: *Discharge PPC decrease of LFP/C battery cells subjected to Calendar 1 ageing conditions (RPT: SOC=50%, I_{dc}=10A).*

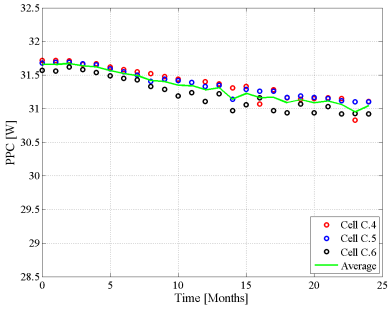

Figure E.29: *Discharge PPC values measured on LFP/C cells subjected to Calendar 2 ageing conditions (RPT: SOC=50%, I_{dc}=10A).*

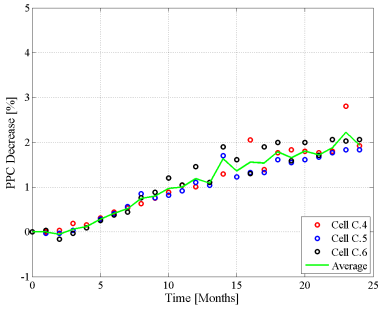

Figure E.30: *Discharge PPC decrease of LFP/C battery cells subjected to Calendar 2 ageing conditions (RPT: SOC=50%, I_{dc}=10A).*

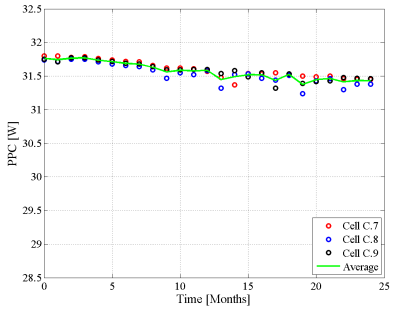

Figure E.31: *Discharge PPC values measured on LFP/C cells subjected to Calendar 3 ageing conditions (RPT: SOC=50%, I_{dc}=10A).*

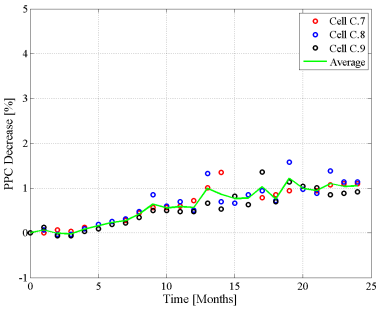

Figure E.32: *Discharge PPC decrease of LFP/C battery cells subjected to Calendar 3 ageing conditions (RPT: SOC=50%, I_{dc}=10A).*

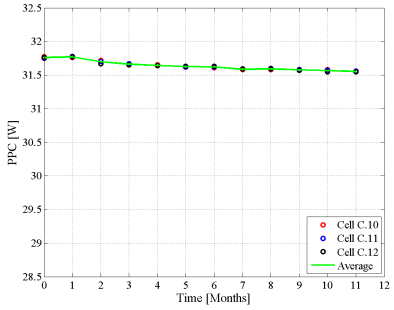

Figure E.33: *Discharge PPC values measured on LFP/C cells subjected to Calendar 4 ageing conditions (RPT: SOC=50%, I_{dc}=10A).*

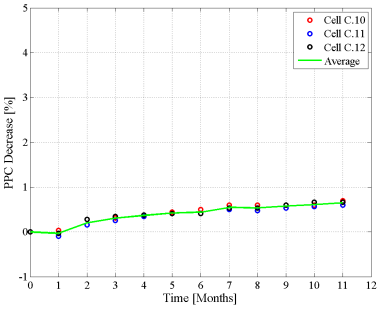

Figure E.34: *Discharge PPC decrease of LFP/C battery cells subjected to Calendar 4 ageing conditions (RPT: SOC=50%, I_{dc}=10A).*

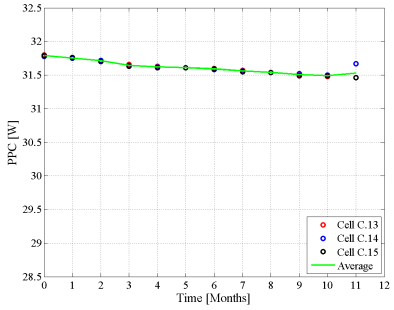

Figure E.35: *Discharge PPC values measured on LFP/C cells subjected to Calendar 5 ageing conditions (RPT: SOC=50%, I_{dc}=10A).*

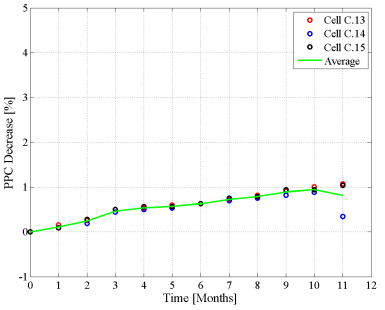

Figure E.36: *Discharge PPC decrease of LFP/C battery cells subjected to Calendar 5 ageing conditions (RPT: SOC=50%, I_{dc}=10A).*

Measured PPC and PPC decrease at 80% SOC

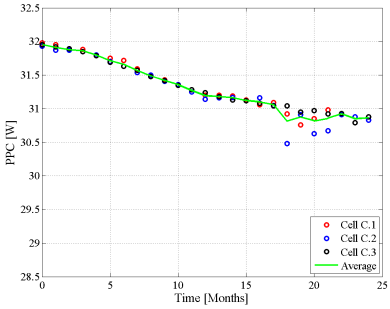

Figure E.37: *Discharge PPC values measured on LFP/C cells subjected to Calendar 1 ageing conditions (RPT: SOC=80%, I_{dc}=10A).*

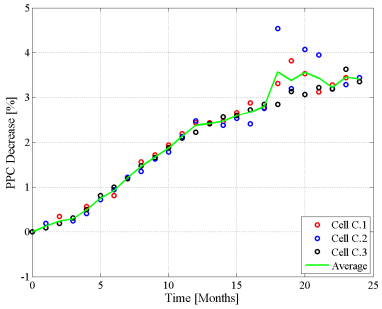

Figure E.38: *Discharge PPC decrease of LFP/C battery cells subjected to Calendar 1 ageing conditions (RPT: SOC=80%, I_{dc}=10A).*

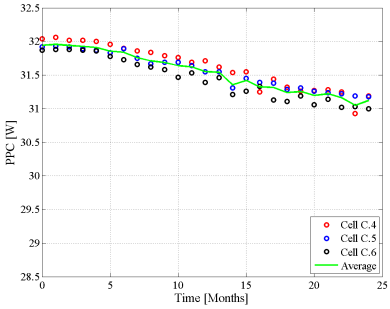

Figure E.39: *Discharge PPC values measured on LFP/C cells subjected to Calendar 2 ageing conditions (RPT: SOC=80%, I_{dc}=10A).*

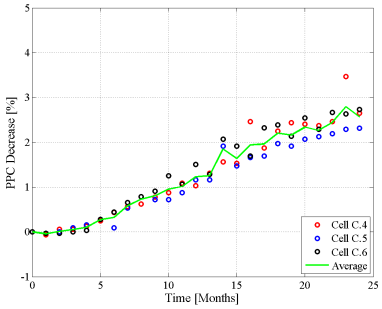

Figure E.40: *Discharge PPC decrease of LFP/C battery cells subjected to Calendar 2 ageing conditions (RPT: SOC=80%, I_{dc}=10A).*

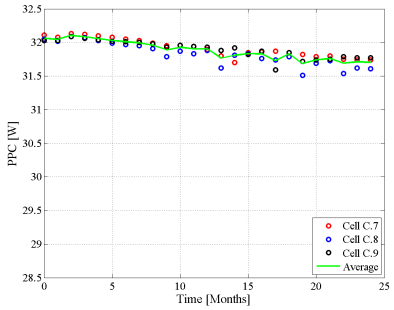

Figure E.41: *Discharge PPC values measured on LFP/C cells subjected to Calendar 3 ageing conditions (RPT: SOC=80%, I_{dc}=10A).*

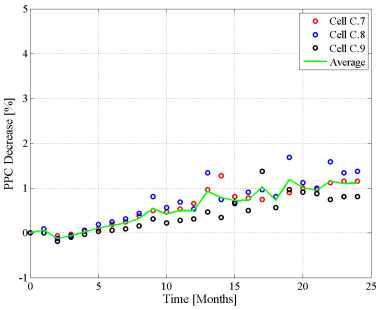

Figure E.42: *Discharge PPC decrease of LFP/C battery cells subjected to Calendar 3 ageing conditions (RPT: SOC=80%, I_{dc}=10A).*

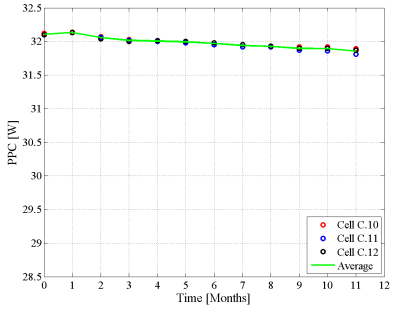

Figure E.43: *Discharge PPC values measured on LFP/C cells subjected to Calendar 4 ageing conditions (RPT: SOC=80%, I_{dc}=10A).*

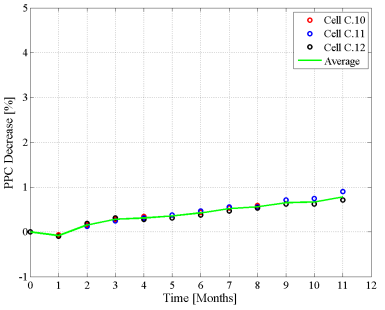

Figure E.44: *Discharge PPC decrease of LFP/C battery cells subjected to Calendar 4 ageing conditions (RPT: SOC=80%, I_{dc}=10A).*

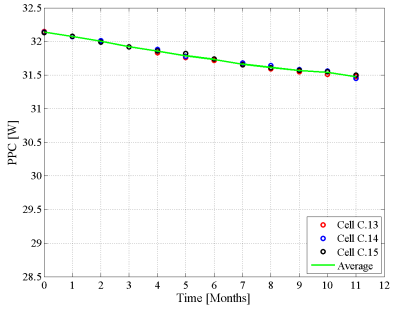

Figure E.45: *Discharge PPC values measured on LFP/C cells subjected to Calendar 5 ageing conditions (RPT: SOC=80%, I_{dc}=10A).*

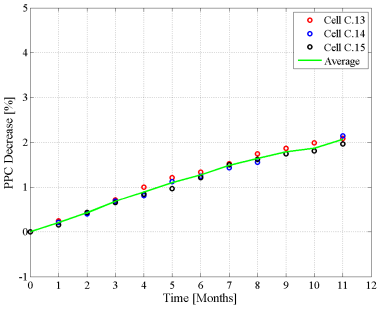

Figure E.46: *Discharge PPC decrease of LFP/C battery cells subjected to Calendar 5 ageing conditions (RPT: SOC=80%, I_{dc}=10A).*

E.1.4 Dependence of PPC decrease on storage time

The results obtained for fitting the PPC decrease over time of the LFP/C battery cells stored at various conditions are presented in Fig. E.47 - E.51.

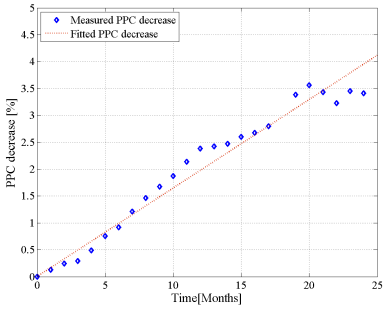

Figure E.47: *Measured and fitted PPC decrease of the LFP/C cells subjected to Calendar 1 ageing conditions.*

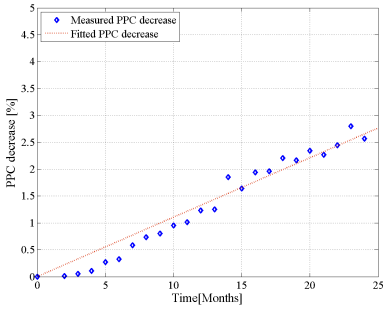

Figure E.48: *Measured and fitted PPC decrease of the LFP/C cells subjected to Calendar 2 ageing conditions.*

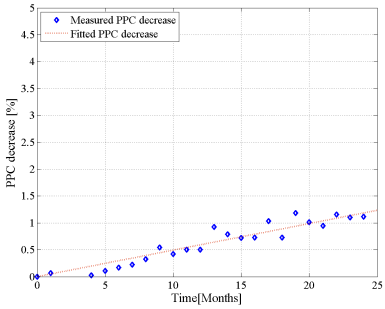

Figure E.49: *Measured and fitted PPC decrease of the LFP/C cells subjected to Calendar 3 ageing conditions.*

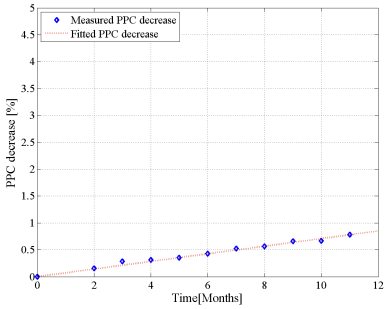

Figure E.50: *Measured and fitted PPC decrease of the LFP/C cells subjected to Calendar 4 ageing conditions.*

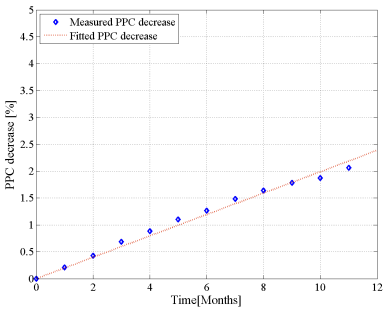

Figure E.51: *Measured and fitted PPC decrease of the LFP/C cells subjected to Calendar 5 ageing conditions.*

E.1.5 Measured EIS spectra

This section summarizes the results obtained from EIS measurements (performed at 20%, 50%, and 80% SOC) on the LFP/C battery cells, which were aged based on *Calendar 2 - Calendar 5* conditions.

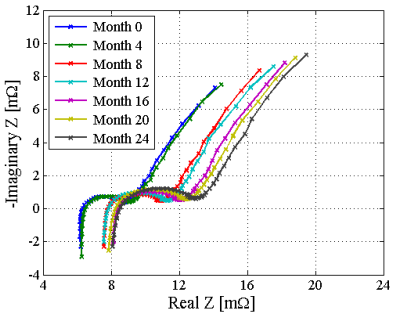

Figure E.52: *Dependence of LFP/C battery cells' EIS spectra on the storage time (calendar ageing conditions: T=47.5°C, SOC=50%, RPT conditions: T=25°C, SOC=20%).*

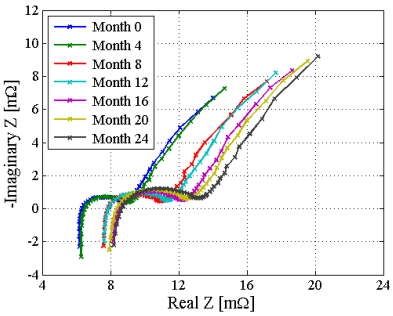

Figure E.53: *Dependence of LFP/C battery cells' EIS spectra on the storage time (calendar ageing conditions: T=47.5°C, SOC=50%, RPT conditions: T=25°C, SOC=50%).*

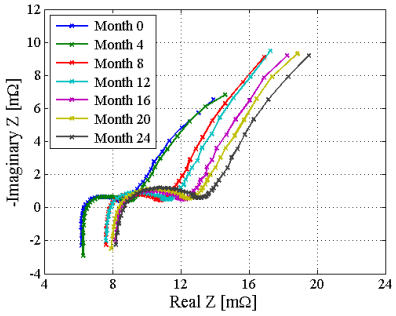

Figure E.54: *Dependence of LFP/C battery cells' EIS spectra on the storage time (calendar ageing conditions: T=47.5°C, SOC=50%, RPT conditions: T=25°C, SOC=80%).*

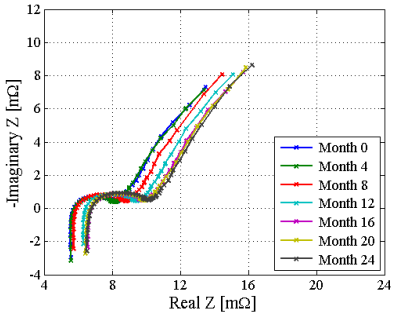

Figure E.55: *Dependence of LFP/C battery cells' EIS spectra on the storage time (calendar ageing conditions: T=40°C, SOC=50%, RPT conditions: T=25°C, SOC=20%).*

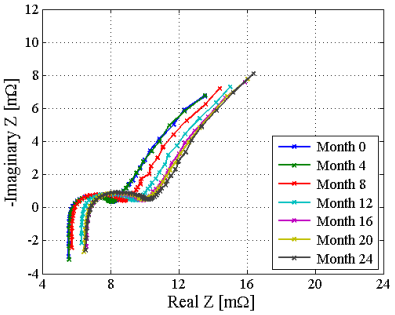

Figure E.56: *Dependence of LFP/C battery cells' EIS spectra on the storage time (calendar ageing conditions: T=40°C, SOC=50%, RPT conditions: T=25°C, SOC=50%).*

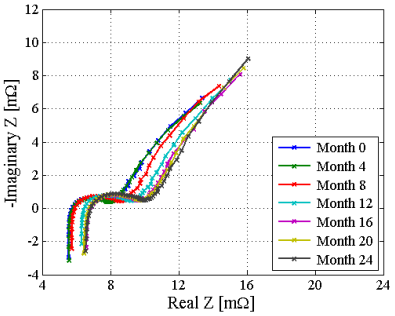

Figure E.57: *Dependence of LFP/C battery cells' EIS spectra on the storage time (calendar ageing conditions: T=40°C, SOC=50%, RPT conditions: T=25°C, SOC=80%).*

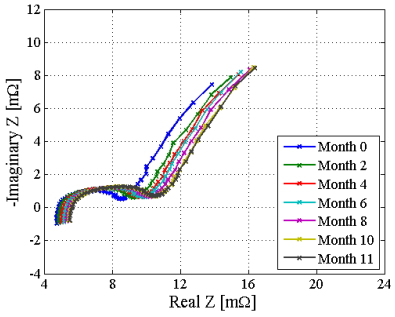

Figure E.58: *Dependence of LFP/C battery cells' EIS spectra on the storage time (calendar ageing conditions: T=55°C, SOC=10%, RPT conditions: T=25°C, SOC=20%).*

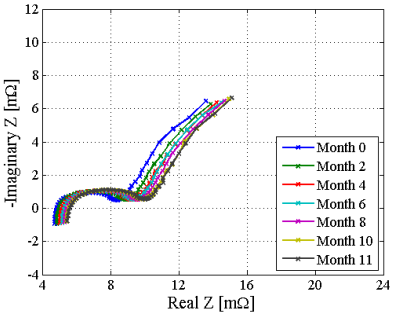

Figure E.59: *Dependence of LFP/C battery cells' EIS spectra on the storage time (calendar ageing conditions: T=55°C, SOC=10%, RPT conditions: T=25°C, SOC=50%).*

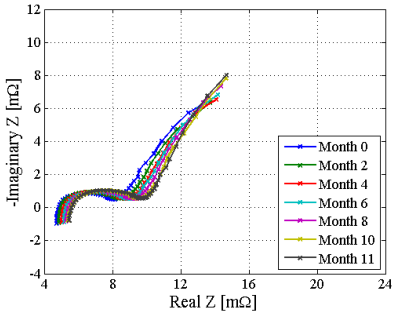

Figure E.60: *Dependence of LFP/C battery cells' EIS spectra on the storage time (calendar ageing conditions: T=55°C, SOC=10%, RPT conditions: T=25°C, SOC=80%).*

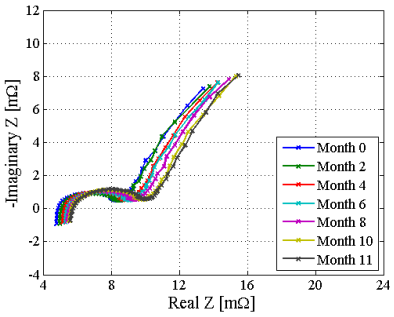

Figure E.61: *Dependence of LFP/C battery cells' EIS spectra on the storage time (calendar ageing conditions: T=55°C, SOC=90%, RPT conditions: T=25°C, SOC=20%).*

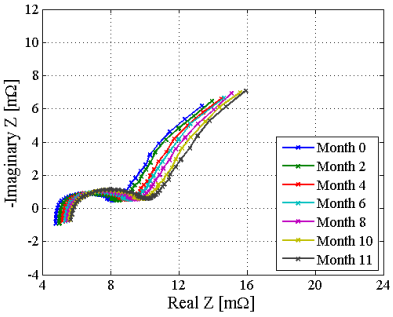

Figure E.62: *Dependence of LFP/C battery cells' EIS spectra on the storage time (calendar ageing conditions: T=55°C, SOC=90%, RPT conditions: T=25°C, SOC=50%).*

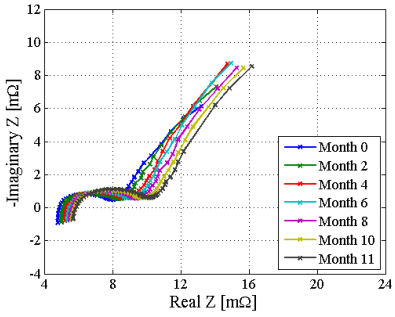

Figure E.63: *Dependence of LFP/C battery cells' EIS spectra on the storage time (calendar ageing conditions: T=55°C, SOC=90%, RPT conditions: T=25°C, SOC=80%).*

E.1.6 Time evolution of EEC parameters and their dependence on storage temperature and SOC-level

This section summarizes the time evolution of the EEC parameters (i.e., R_s, R_1, Q_1) obtained from curve fitting the measured impedance spectra (see Fig. 6.17 - Fig. 6.19 and Fig. E.52 - E.63) of the LFP/C battery cells.

Dependence of resistance R_s on storage time, temperature, and SOC-level

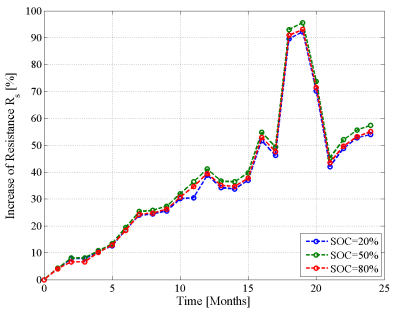

Figure E.64: *Increase of series resistance R_s during calendar ageing (ageing conditions: T=55°C, SOC=50%, RPT conditions: T=25°C, different SOCs).*

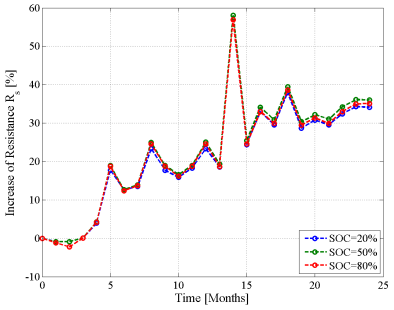

Figure E.65: *Increase of series resistance R_s during calendar ageing (ageing conditions: T=47.5°C, SOC=50%, RPT conditions: T=25°C, different SOCs).*

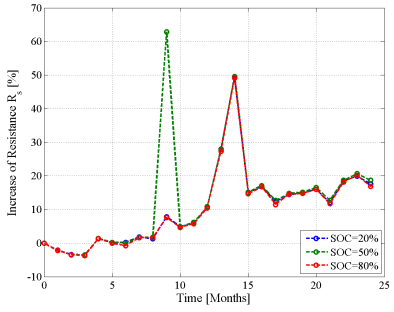

Figure E.66: *Increase of series resistance R_s during calendar ageing (ageing conditions: T=40°C, SOC=50%, RPT conditions: T=25°C,different SOCs).*

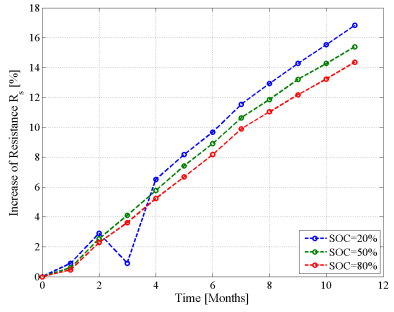

Figure E.67: *Increase of series resistance R_s during calendar ageing (ageing conditions: T=55°C, SOC=10%, RPT conditions: T=25°C, different SOCs).*

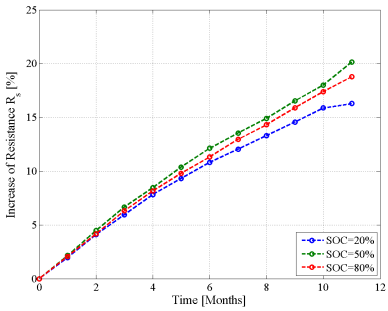

Figure E.68: *Increase of series resistance R_s during calendar ageing (ageing conditions: T=55ºC, SOC=90%, RPT conditions: T=25ºC, different SOCs).*

Dependence of resistance R_1 on storage time, temperature, and SOC-level

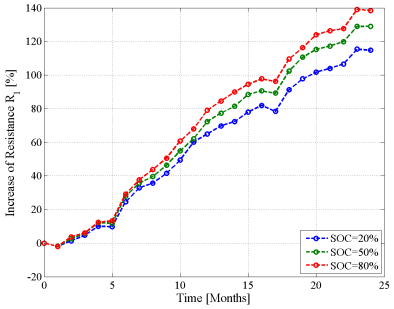

Figure E.69: *Increase of resistance R_1 during calendar ageing (ageing conditions: T=55°C, SOC=50%, RPT conditions: T=25°C, different SOCs).*

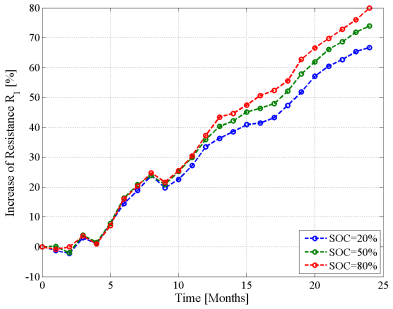

Figure E.70: *Increase of resistance R_1 during calendar ageing (ageing conditions: T=47.5°C, SOC=50%, RPT conditions: T=25°C, different SOCs).*

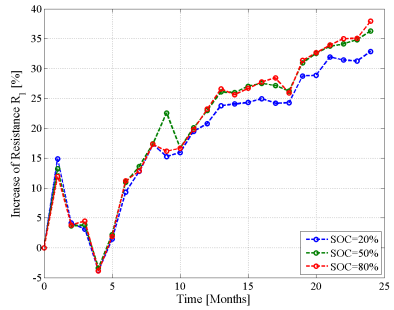

Figure E.71: *Increase of resistance R_1 during calendar ageing (ageing conditions: T=40°C, SOC=50%, RPT conditions: T=25°C,different SOCs).*

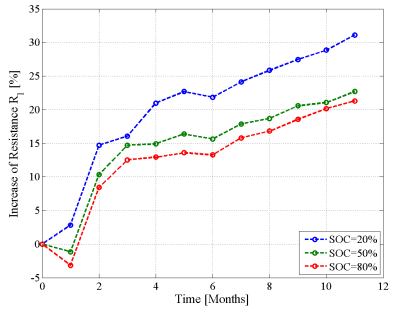

Figure E.72: *Increase of resistance R_1 during calendar ageing (ageing conditions: T=55°C, SOC=10%, RPT conditions: T=25°C, different SOCs).*

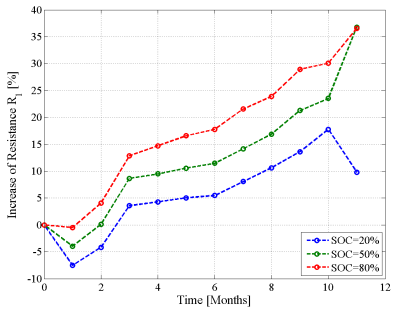

Figure E.73: *Increase of resistance* R_1 *during calendar ageing (ageing conditions: T=55ºC, SOC=90%, RPT conditions: T=25ºC, different SOCs).*

Dependence of generalized capacitance Q_1 on storage time, temperature, and SOC-level

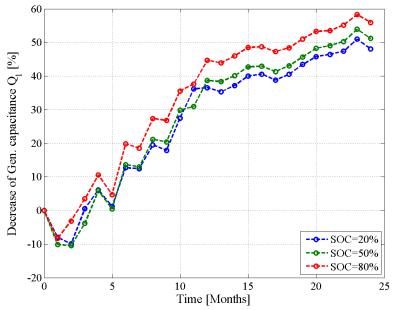

Figure E.74: *Decrease of gen. capacitance Q_1 during calendar ageing (ageing conditions: T=55°C, SOC=50%, RPT conditions: T=25°C, different SOCs).*

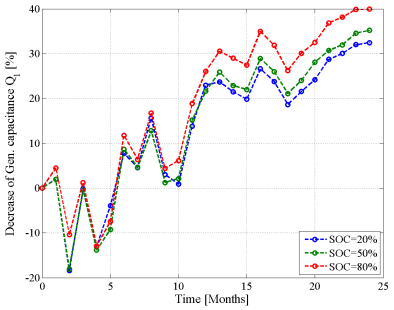

Figure E.75: *Decrease of gen. capacitance Q_1 during calendar ageing (ageing conditions: T=47.5°C, SOC=50%, RPT conditions: T=25°C, different SOCs).*

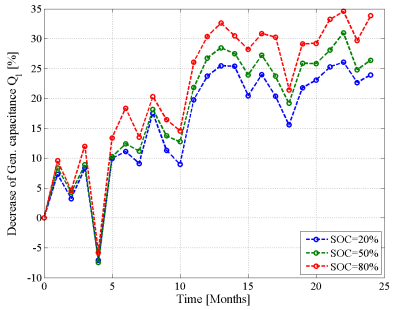

Figure E.76: *Decrease of gen. capacitance Q_1 during calendar ageing (ageing conditions: T=40°C, SOC=50%, RPT conditions: T=25°C, different SOCs).*

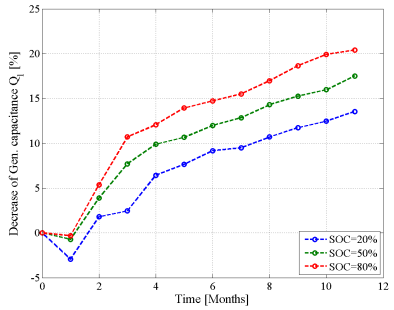

Figure E.77: *Decrease of gen. capacitance Q_1 during calendar ageing (ageing conditions: T=55°C, SOC=10%, RPT conditions: T=25°C, different SOCs).*

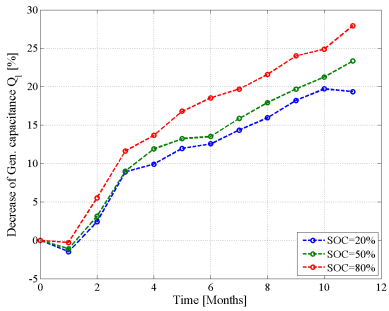

Figure E.78: *Decrease of gen. capacitance Q_1 during calendar ageing (ageing conditions: T=55°C, SOC=90%, RPT conditions: T=25°C, different SOCs).*

E.1.7 Dependence of EEC parameters' time evolution on storage temperature and SOC-level

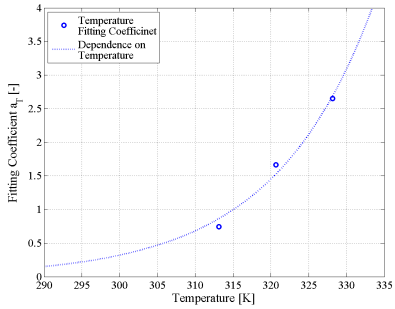

Figure E.79: *Exponential relationship between the curve fitting coefficients (see Table 6.4) and the storage temperature.*

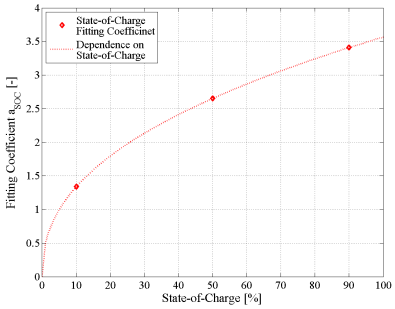

Figure E.80: *Power-law relationship between the curve fitting coefficients (see Table 6.4) and the storage SOC-level.*

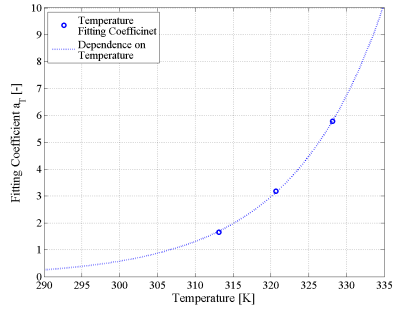

Figure E.81: *Exponential relationship between the curve fitting coefficients (see Table 6.5) and the storage temperature.*

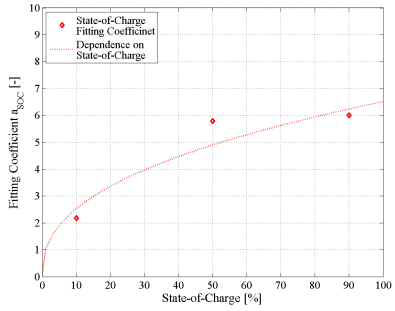

Figure E.82: *Power-law relationship between the curve fitting coefficients (see Table 6.5) and the storage SOC-level.*

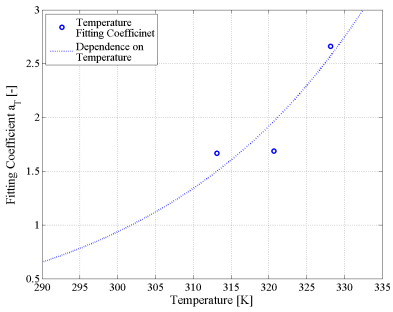

Figure E.83: *Exponential relationship between the curve fitting coefficients (see Table 6.6) and the storage temperature.*

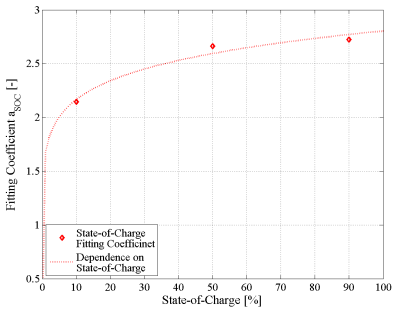

Figure E.84: *Power-law relationship between the curve fitting coefficients (see Table 6.6) and the storage SOC-level.*

E.2 Results of the Accelerated Ageing Tests

E.2.1 Measured Capacity Fade

The measured capacity fade for all performed cycling TCs (see Table 5.2), expressed both as absolute values and relative values (related to the capacity values measured at cells' BOL) are presented in Fig. E.85 - Fig. E.100.

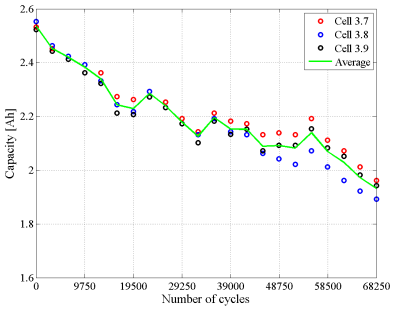

Figure E.85: *Capacity values measured on LFP/C cells subjected to TC1 ageing conditions.*

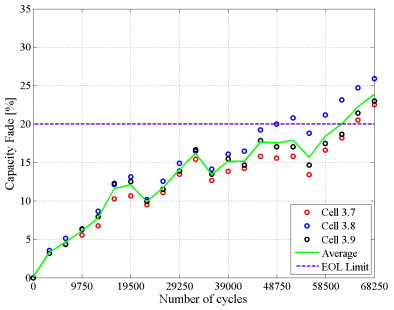

Figure E.86: *Capacity fade of LFP/C battery cells subjected to Calendar TC1 ageing conditions.*

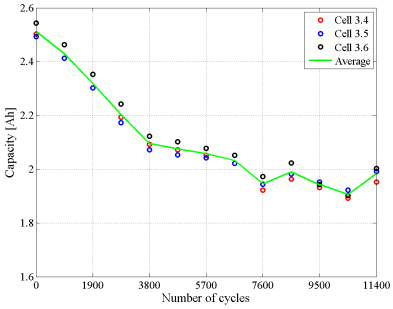

Figure E.87: *Capacity values measured on LFP/C cells subjected to TC2 ageing conditions.*

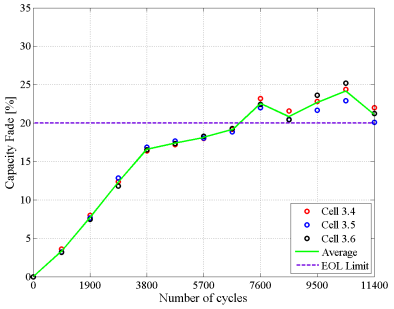

Figure E.88: *Capacity fade of LFP/C battery cells subjected to Calendar TC2 ageing conditions.*

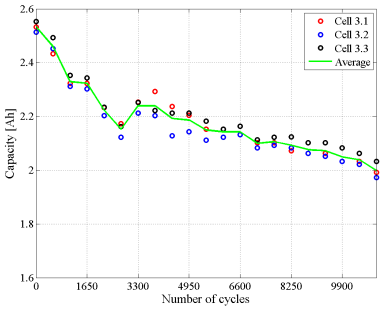

Figure E.89: *Capacity values measured on LFP/C cells subjected to TC3 ageing conditions.*

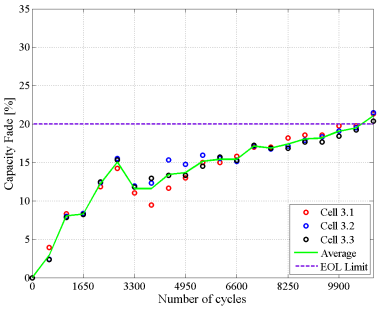

Figure E.90: *Capacity fade of LFP/C battery cells subjected to Calendar TC3 ageing conditions.*

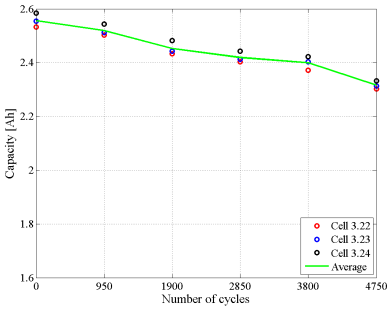

Figure E.91: *Capacity values measured on LFP/C cells subjected to TC5 ageing conditions.*

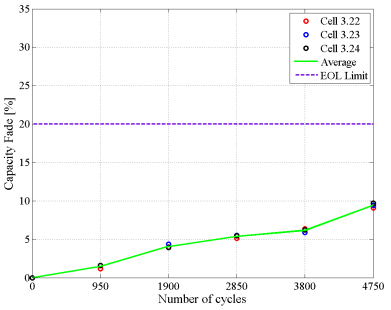

Figure E.92: *Capacity fade of LFP/C battery cells subjected to Calendar TC5 ageing conditions.*

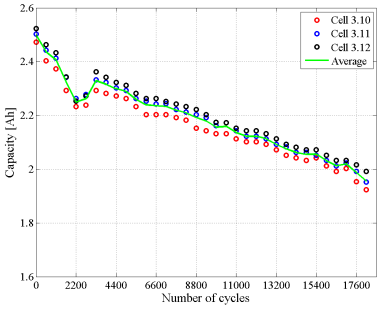

Figure E.93: *Capacity values measured on LFP/C cells subjected to TC6 ageing conditions.*

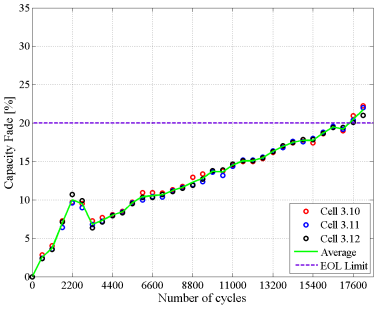

Figure E.94: *Capacity fade of LFP/C battery cells subjected to Calendar TC6 ageing conditions.*

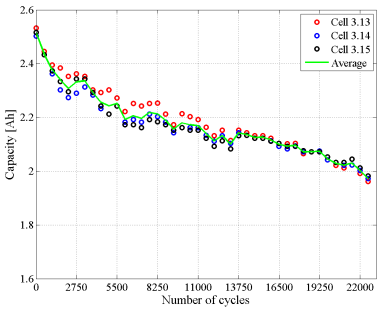

Figure E.95: *Capacity values measured on LFP/C cells subjected to TC9 ageing conditions.*

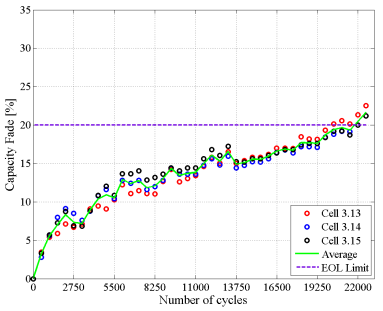

Figure E.96: *Capacity fade of LFP/C battery cells subjected to Calendar TC9 ageing conditions.*

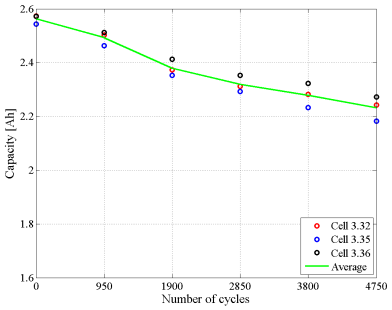

Figure E.97: *Capacity values measured on LFP/C cells subjected to TC10 ageing conditions.*

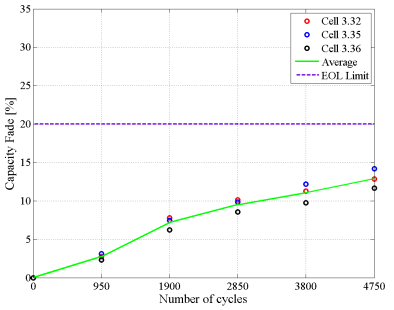

Figure E.98: *Capacity fade of LFP/C battery cells subjected to Calendar TC10 ageing conditions.*

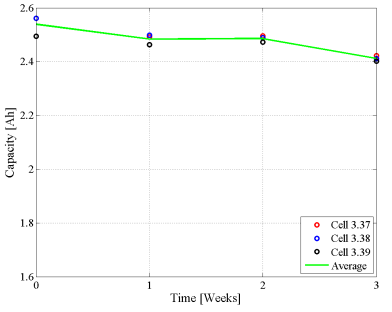

Figure E.99: *Capacity values measured on LFP/C cells subjected to TC11 ageing conditions.*

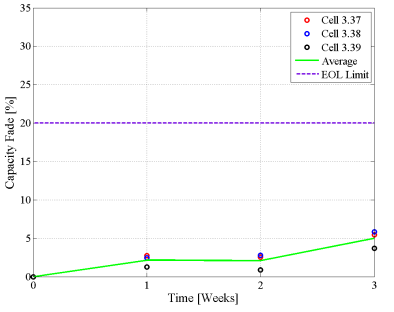

Figure E.100: *Capacity fade of LFP/C battery cells subjected to Calendar TC11 ageing conditions.*

E.2.2 Dependence of capacity fade on the number of cycles

The suitability of different functions for fitting the capacity fade of the tested battery cells caused by the accelerated cycling ageing conditions has been evaluated. These functions are the following:

- **Logarithmic function:**

$$C_{fade} = a \cdot \ln(b \cdot nc) \tag{E.6}$$

- **Linear function:**

$$C_{fade} = a \cdot nc \tag{E.7}$$

- **Square-root-of-time function:**

$$C_{fade} = a \cdot \sqrt{nc} \tag{E.8}$$

- **Power Law function:**

$$C_{fade} = a \cdot nc^{b} \tag{E.9}$$

- **Power Law + Linear function:**

$$C_{fade} = a \cdot nc^{b} + c \tag{E.10}$$

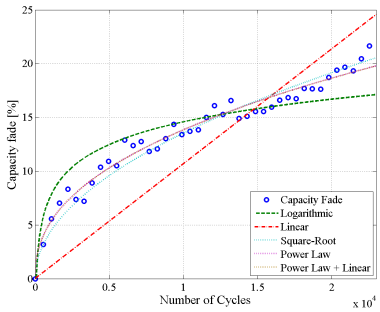

Figure E.101: *Comparison of results obtained from fitting the capacity fade of LFP/C battery cells with different functions (capacity fade results obtained from TC9 test used for curve fitting selection).*

The obtained accuracy values for fitting the measured capacity fade with the functions (E.6) - (E.10) are summarized in Table E.3. The best fitting accuracy was obtained for a function, which combines the attributes of a power law and of a first degree polynomial function. however, the disadvantage of this function represents the increased

Table E.3: *Accuracy obtained for fitting the capacity fade measured on TC9 cells with various functions.*

Fitting Function	No. of Parameters	R^2
Logarithmic	2	0.8040
Linear	1	0.4582
Square-Root	1	0.9464
Power Law	2	0.0.9626
Power Law + Linear	3	0.9703

number of free parameters (i.e., three) which are used. Thus, since it involves only one free parameter and it has also physic-chemical meaning, a square-root function was selected for fitting the "time" (number of cycles) dependence of the measured capacity fade characteristics for cycling aged LFP/C battery cells.

E.2.3 Measured Discharge Pulse Power Capability

The measured PPC decrease for the LFP/C battery cells tested under the cycling conditions summarized in E.1 are presented both as absolute and relative values in Fig. **??** - Fig. E.117.

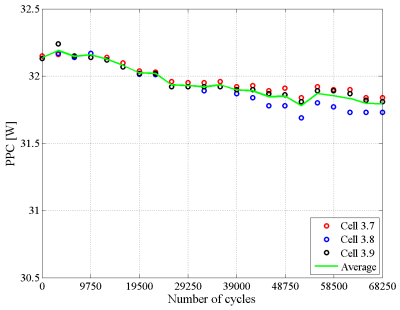

Figure E.102: *Capacity values measured on LFP/C cells subjected to TC1 ageing conditions.*

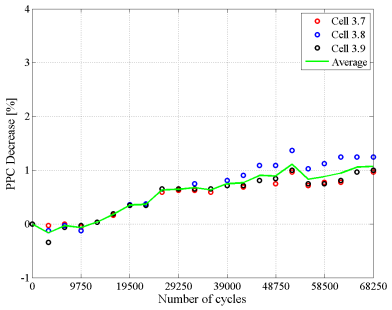

Figure E.103: *Capacity fade of LFP/C battery cells subjected to TC1 ageing conditions.*

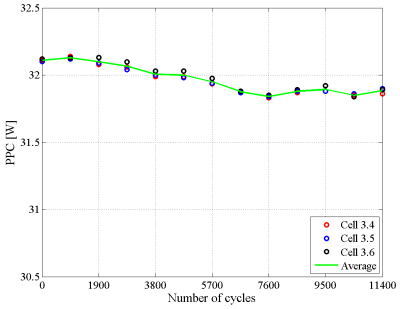

Figure E.104: *Capacity values measured on LFP/C cells subjected to TC2 ageing conditions.*

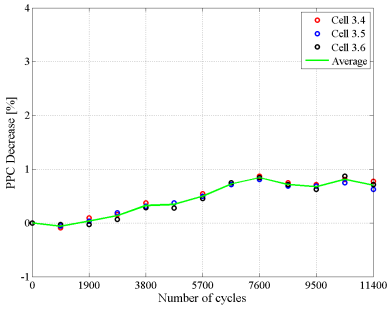

Figure E.105: *Capacity fade of LFP/C battery cells subjected to TC2 ageing conditions.*

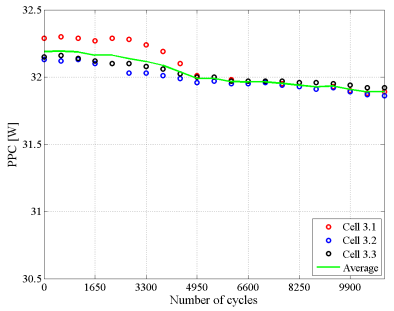

Figure E.106: *Capacity values measured on LFP/C cells subjected to TC3 ageing conditions.*

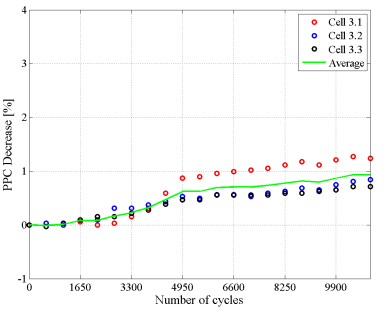

Figure E.107: *Capacity fade of LFP/C battery cells subjected to TC3 ageing conditions.*

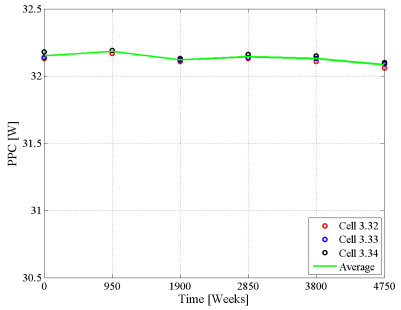

Figure E.108: *Capacity values measured on LFP/C cells subjected to TC5 ageing conditions.*

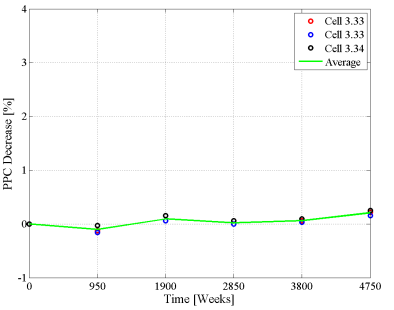

Figure E.109: *Capacity fade of LFP/C battery cells subjected to TC5 ageing conditions.*

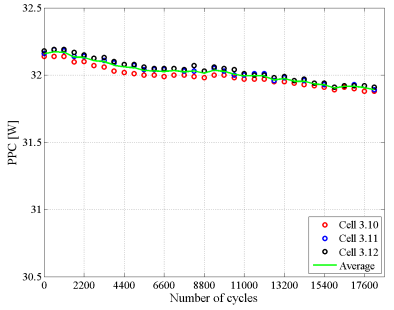

Figure E.110: *Capacity values measured on LFP/C cells subjected to TC6 ageing conditions.*

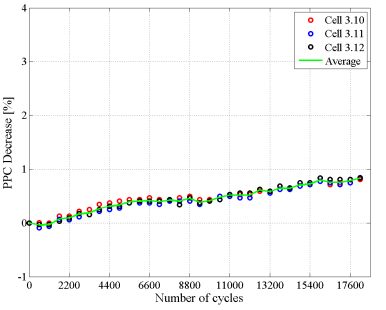

Figure E.111: *Capacity fade of LFP/C battery cells subjected to TC6 ageing conditions.*

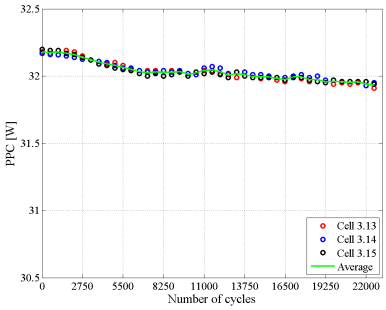

Figure E.112: *Capacity values measured on LFP/C cells subjected to TC9 ageing conditions.*

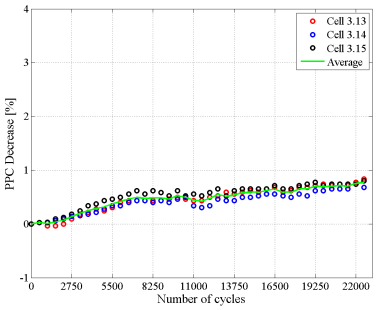

Figure E.113: *Capacity fade of LFP/C battery cells subjected to TC9 ageing conditions.*

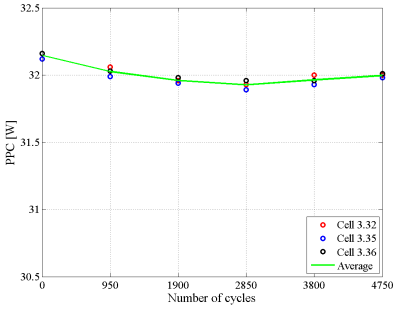

Figure E.114: *Capacity values measured on LFP/C cells subjected to TC10 ageing conditions.*

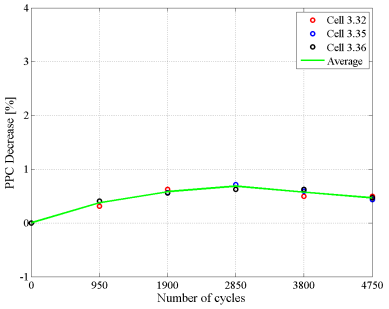

Figure E.115: *Capacity fade of LFP/C battery cells subjected to TC10 ageing conditions.*

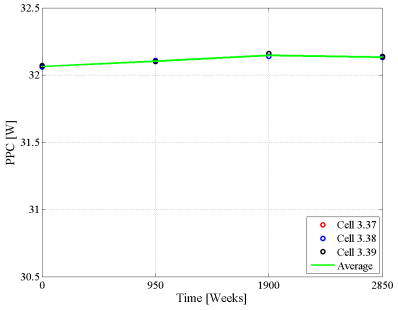

Figure E.116: *Capacity values measured on LFP/C cells subjected to TC11 ageing conditions.*

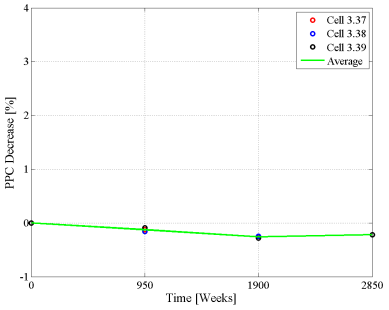

Figure E.117: *Capacity fade of LFP/C battery cells subjected to TC11 ageing conditions.*

E.2.4 Dependence of PPC decrease on the number of cycles

The results obtained for fitting the PPC decrease over time of the LFP/C battery cells stored at various conditions are presented in Fig. E.118 - Fig. E.125.

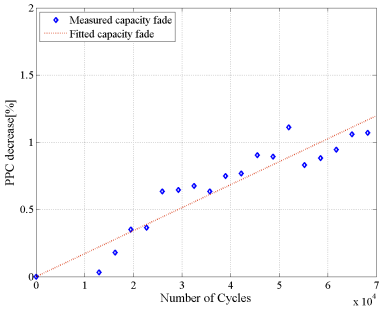

Figure E.118: *Measured and fitted PPC decrease of the LFP/C cells subjected to TC1 ageing conditions.*

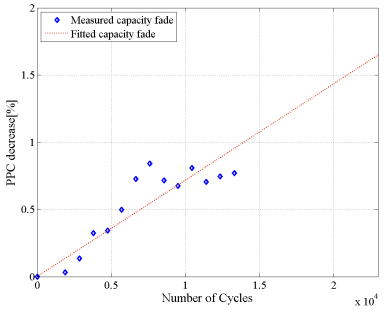

Figure E.119: *Measured and fitted PPC decrease of the LFP/C cells subjected to TC2 ageing conditions..*

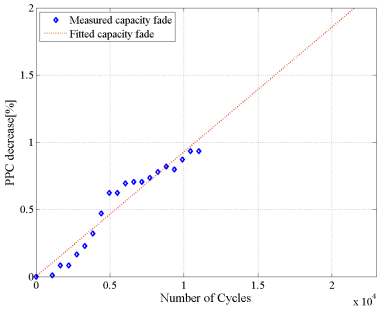

Figure E.120: *Measured and fitted PPC decrease of the LFP/C cells subjected to TC3 ageing conditions.*

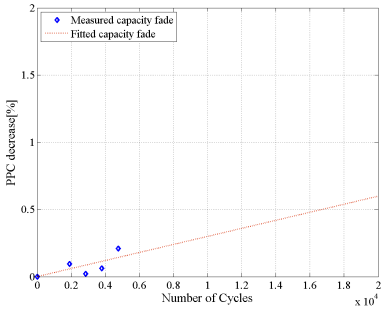

Figure E.121: *Measured and fitted PPC decrease of the LFP/C cells subjected to TC5 ageing conditions..*

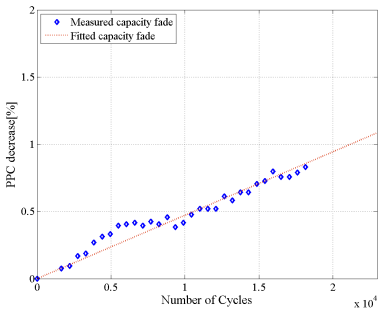

Figure E.122: *Measured and fitted PPC decrease of the LFP/C cells subjected to TC6 ageing conditions.*

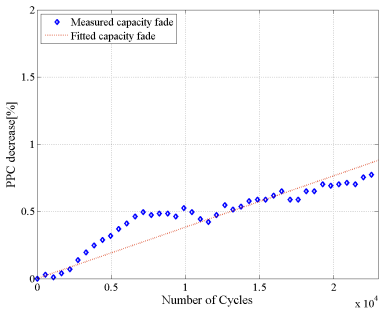

Figure E.123: *Measured and fitted PPC decrease of the LFP/C cells subjected to TC9 ageing conditions..*

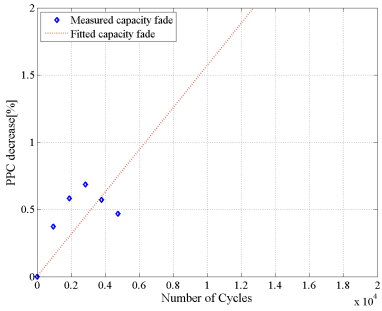

Figure E.124: *Measured and fitted PPC decrease of the LFP/C cells subjected to TC10 ageing conditions.*

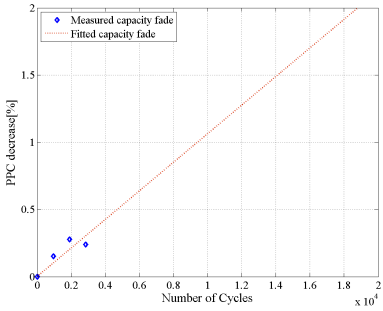

Figure E.125: *Measured and fitted PPC decrease of the LFP/C cells subjected to TC11 ageing conditions..*

E.2.5 Measured EIS spectra

This section summarizes the results obtained from EIS measurements (performed at 80% SOC) on the LFP/C battery cells, which were aged based on *TC1 - TC11* cycling conditions.

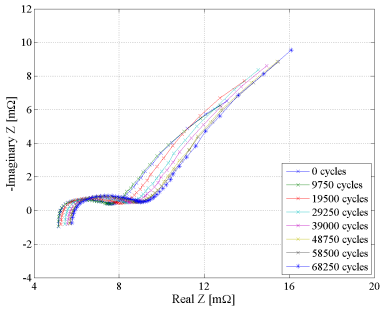

Figure E.126: *Dependence of LFP/C battery cells' EIS spectra on the number of cycles (cycling ageing conditions: T=50° C, cycle depth = 10% average SOC=50%, RPT conditions: T=25° C, SOC=80%).*

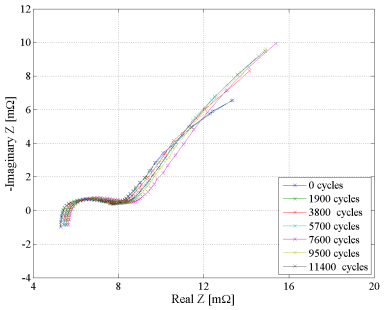

Figure E.127: *Dependence of LFP/C battery cells' EIS spectra on the number of cycles (cycling ageing conditions: T=50° C, cycle depth = 35% average SOC=50%, RPT conditions: T=25° C, SOC=80%).*

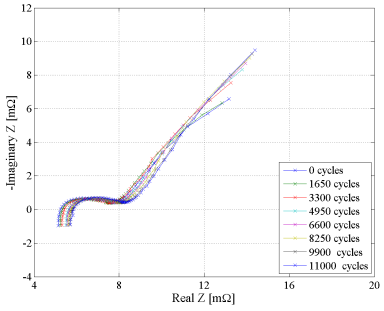

Figure E.128: *Dependence of LFP/C battery cells' EIS spectra on the number of cycles (cycling ageing conditions: T=55° C, cycle depth = 60% average SOC=50%, RPT conditions: T=25° C, SOC=80%).*

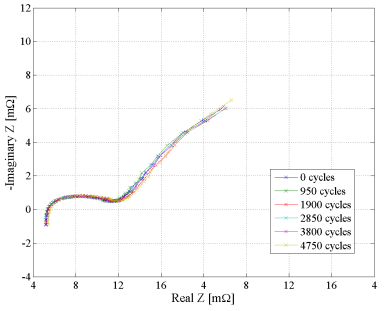

Figure E.129: *Dependence of LFP/C battery cells' EIS spectra on the number of cycles (cycling ageing conditions: T=42.5° C, cycle depth = 35% average SOC=50%, RPT conditions: T=25° C, SOC=80%).*

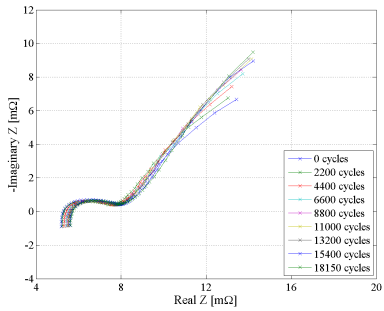

Figure E.130: *Dependence of LFP/C battery cells' EIS spectra on the number of cycles (cycling ageing conditions: T=42.5°C, cycle depth = 60% average SOC=50%, RPT conditions: T=25°C, SOC=80%).*

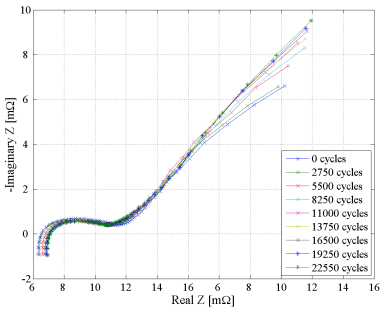

Figure E.131: *Dependence of LFP/C battery cells' EIS spectra on the number of cycles (cycling ageing conditions: T=35°C, cycle depth = 60% average SOC=50%, RPT conditions: T=25°C, SOC=80%).*

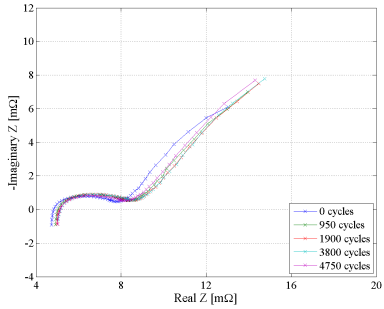

Figure E.132: *Dependence of LFP/C battery cells' EIS spectra on the number of cycles (cycling ageing conditions: T=42.5°C, cycle depth = 35% average SOC=27.5%, RPT conditions: T=25°C, SOC=80%).*

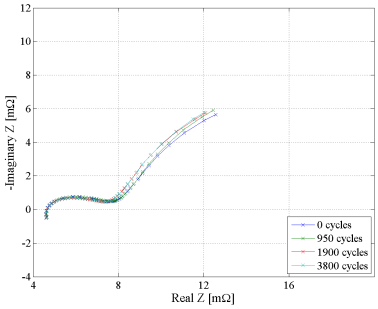

Figure E.133: *Dependence of LFP/C battery cells' EIS spectra on the number of cycles (cycling ageing conditions: T=42.5°C, cycle depth = 35% average SOC=72.5%, RPT conditions: T=25°C, SOC=80%).*

E.2.6 Time evolution of EEC parameters and their dependence on cycle depth, temperature, and average SOC-level

This section summarizes the ageing evolution of the EEC parameters (i.e., R_s, R_2, Q_2) obtained from curve fitting the measured impedance spectra of the LFP/C battery cells.

Dependence of series resistance R_s on cycling conditions

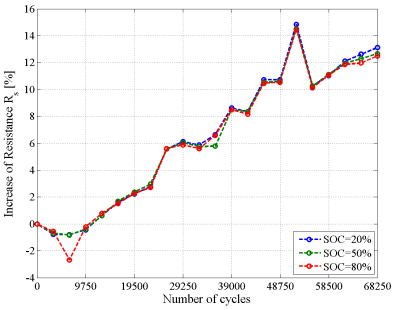

Figure E.134: *Increase of series resistance R_s during accelerated calendar ageing TC1.*

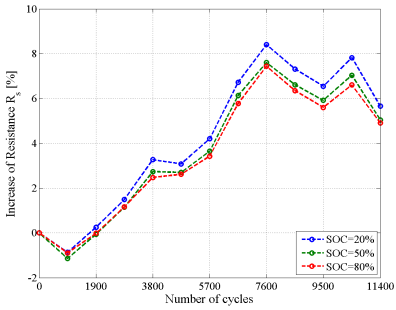

Figure E.135: *Increase of series resistance R_s during accelerated calendar ageing TC2.*

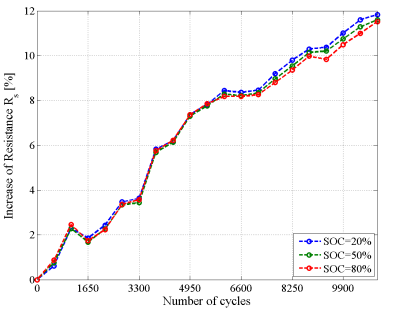

Figure E.136: *Increase of series resistance R_s during accelerated calendar ageing TC3.*

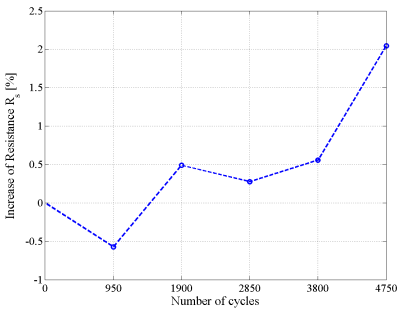

Figure E.137: *Increase of series resistance R_s during accelerated calendar ageing TC5.*

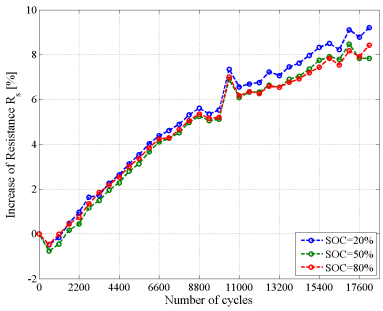

Figure E.138: *Increase of series resistance R_s during accelerated calendar ageing TC6.*

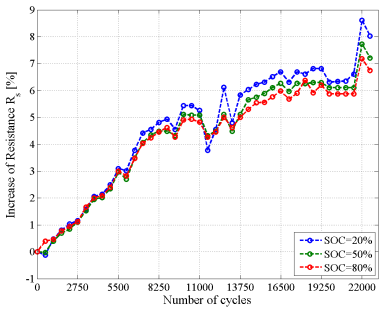

Figure E.139: *Increase of series resistance R_s during accelerated calendar ageing TC9.*

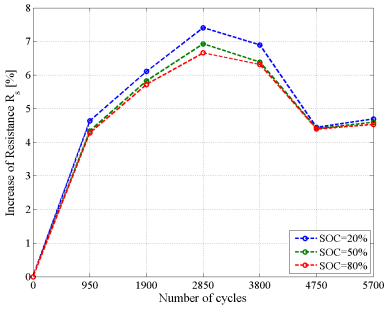

Figure E.140: *Increase of series resistance R_s during accelerated calendar ageing TC10.*

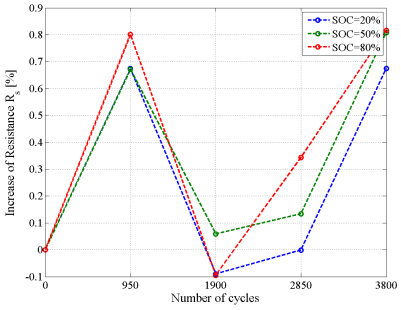

Figure E.141: *Increase of series resistance R_s during accelerated calendar ageing TC11.*

Dependence of resistance R_2 on cycling conditions

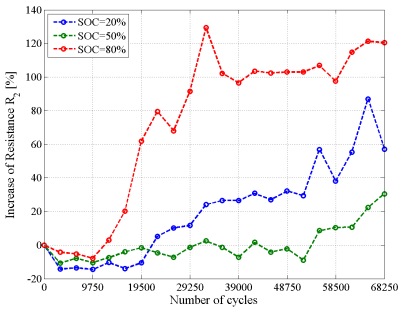

Figure E.142: *Increase of resistance R_2 during accelerated calendar ageing TC1.*

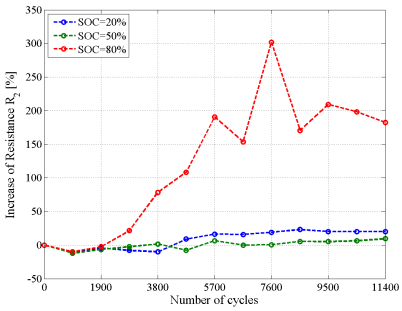

Figure E.143: *Increase of resistance R_2 during accelerated calendar ageing TC2.*

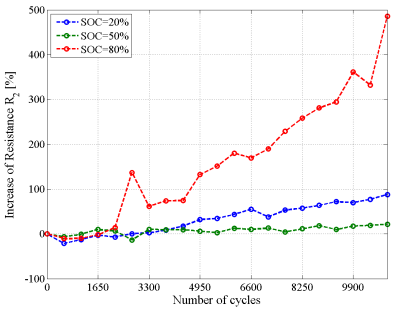

Figure E.144: *Increase of resistance R_2 during accelerated calendar ageing TC3.*

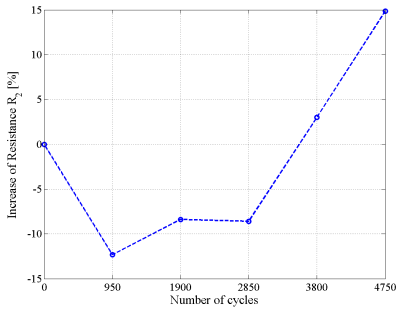

Figure E.145: *Increase of resistance R_2 during accelerated calendar ageing TC5.*

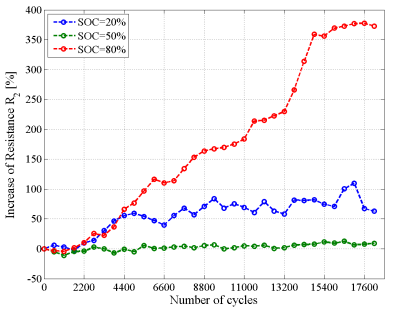

Figure E.146: *Increase of resistance R_2 during accelerated calendar ageing TC6.*

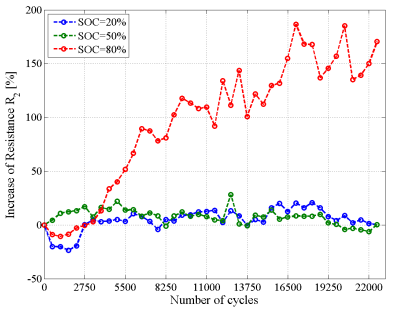

Figure E.147: *Increase of resistance R_2 during accelerated calendar ageing TC9.*

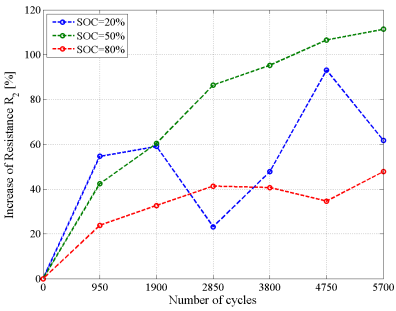

Figure E.148: *Increase of resistance* R_2 *during accelerated calendar ageing TC10.*

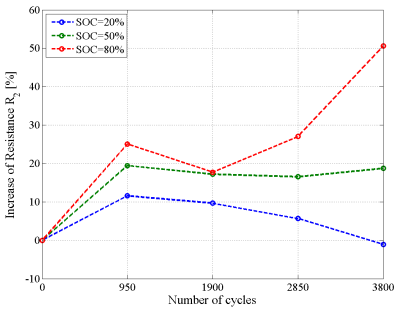

Figure E.149: *Increase of resistance* R_2 *during accelerated calendar ageing TC11.*

Dependence of generalized capacitance Q_2 on cycling conditions

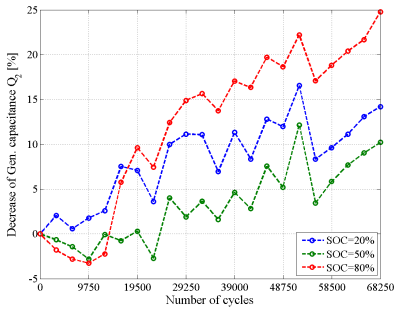

Figure E.150: *Decrease of generalized capacitance Q_2 during accelerated calendar ageing TC1.*

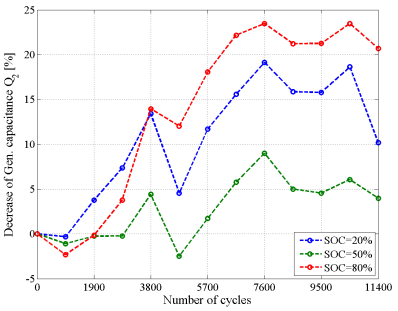

Figure E.151: *Decrease of generalized capacitance Q_2 during accelerated calendar ageing TC2.*

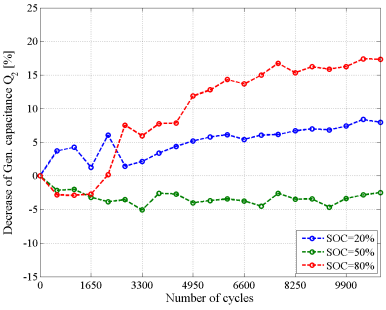

Figure E.152: *Decrease of generalized capacitance Q_2 during accelerated calendar ageing TC3.*

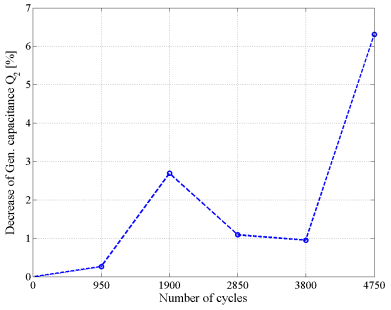

Figure E.153: *Decrease of generalized capacitance R_2 during accelerated calendar ageing TC5.*

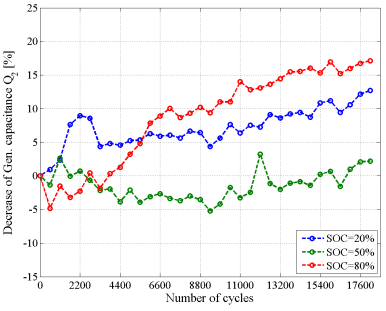

Figure E.154: *Decrease of generalized capacitance Q_2 during accelerated calendar ageing TC6.*

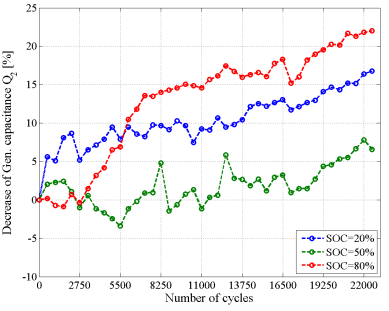

Figure E.155: *Decrease of generalized capacitance Q_2 during accelerated calendar ageing TC9.*

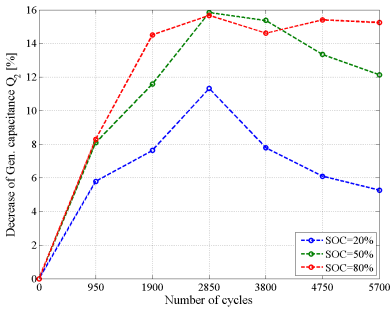

Figure E.156: *Decrease of generalized capacitance Q_2 during accelerated calendar ageing TC10.*

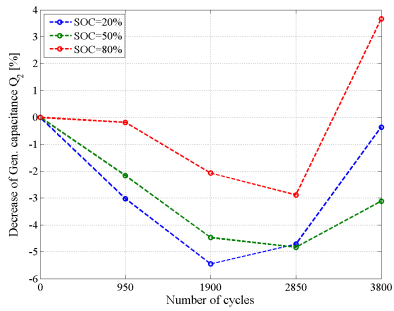

Figure E.157: *Decrease of generalized capacitance Q_2 during accelerated calendar ageing TC11.*

E.2.7 Dependence of EEC parameters' on cycle depth and cycling temperature

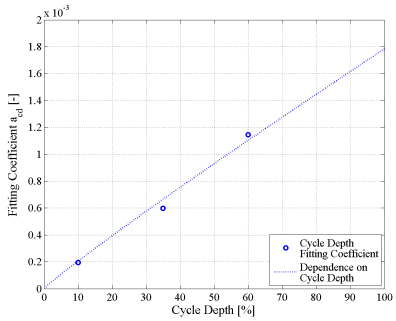

Figure E.158: *Exponential relationship between the curve fitting coefficients (see Table 7.3) and the cycle depth.*

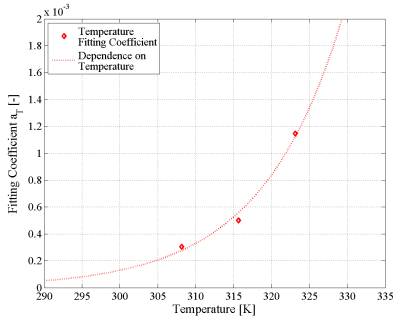

Figure E.159: *Power-law relationship between the curve fitting coefficients (see Table 7.3) and the cycling temperature.*

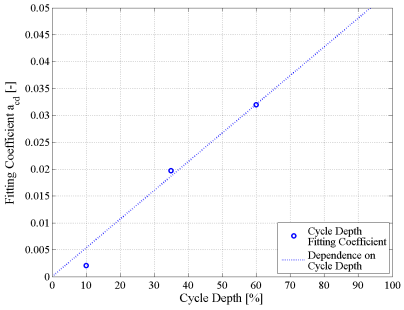

Figure E.160: *Exponential relationship between the curve fitting coefficients (see Table 7.4) and the cycle depth.*

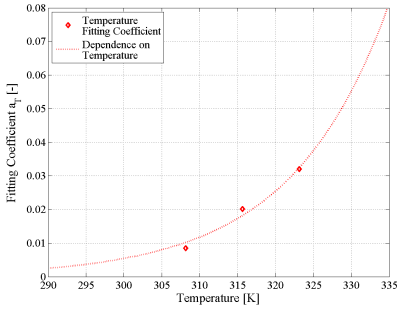

Figure E.161: *Power-law relationship between the curve fitting coefficients (see Table 7.4) and the cycling temperature.*

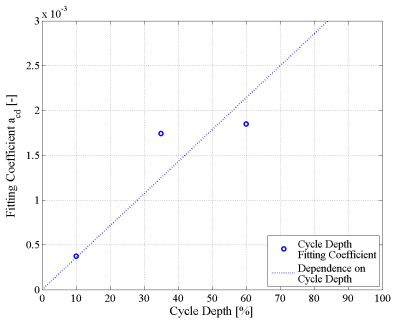

Figure E.162: *Exponential relationship between the curve fitting coefficients (see Table 7.5) and the cycle depth.*

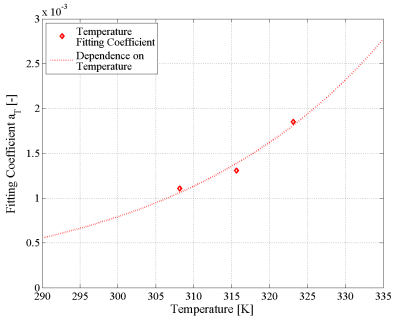

Figure E.163: *Power-law relationship between the curve fitting coefficients (see Table 7.5) and the cycling temperature.*

Appendix F

Results of the Verification Tests

F.1 Verification with symmetrical charging/discharging SOC profile

The capacity and the corresponding capacity fade measured on the LFP/C battery cells which were subjected to the first verification TC (see Table 8.1) are presented in Fig. F.1 and Fig. F.2, respectively.

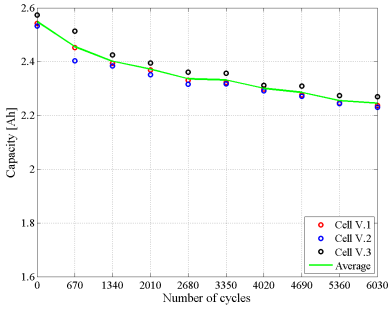

Figure F.1: *Capacity values measured on LFP/C cells subjected to verification TC with a symmetrical charging-discharging SOC profile.*

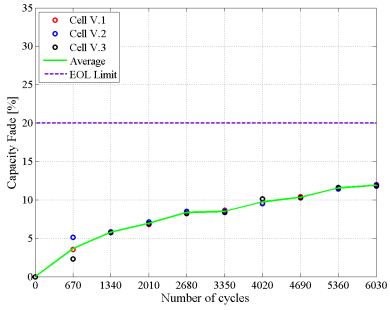

Figure F.2: *Capacity fade of LFP/C battery cells subjected to verification TC with a symmetrical charging-discharging SOC profile.*

F.2 Verification with profile characteristic for PFR service

The capacity and the corresponding capacity fade measured on the LFP/C battery cells which were subjected to the second verification TC (PFR profile) are presented in Fig. F.3 and Fig. F.4, respectively.

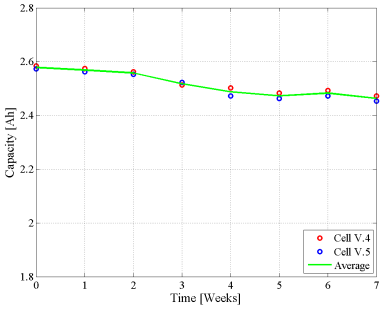

Figure F.3: *Capacity values measured on LFP/C cells subjected to verification TC with profile characteristic to PFR service.*

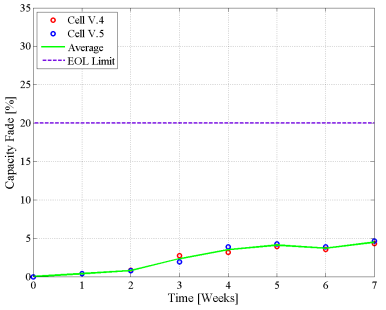

Figure F.4: *Capacity values measured on LFP/C cells subjected to verification TC with profile characteristic to PFR service.*

Appendix G

LFP/C battery cells lifetime evaluation

The grid frequency signal measured during one year, which is the base for the lifetime evaluation performed in Chapter 9 is presented in the figure below.

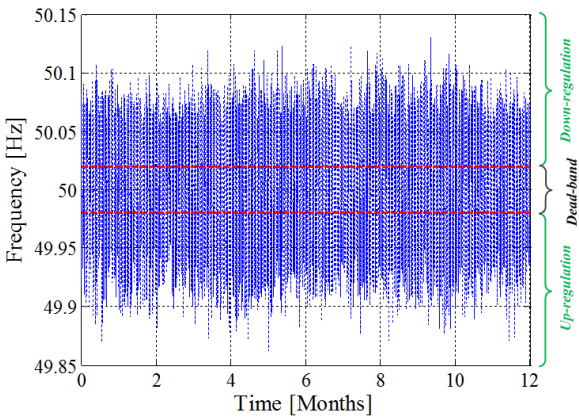

Figure G.1: *Frequency signal measured between June 2013 and May 2014.*

In Table G.1, the grid frequency values presented in Fig. G.1, are analysed for each month of the considered one year period. For each month the minimum and maximu frequency values have been found, and the number of occurrences for both under-frequencies ($f < 49.98$Hz) and over-frequencies ($f > 50.02$Hz) were calculated. The utilization factor of the ESS was obtained by calculating the ration between the total

number of frequencies values available for one month and the total number of under-frequencies values during that month.

Table G.1: *Grid frequency statistical data for the considered one year.*

Year	Month	f_{max} [Hz]	f_{min} [Hz]	No. of Occurrences $f < 49.98$	No. of Occurrences $f > 50.02$	Utilization Factor [%]
2013	June	50.107	49.869	274 400	543 486	10.74
	July	50.098	49.890	342 200	363 615	12.78
	August	50.107	49.882	318 400	374 068	11.81
	September	50.119	49.873	412 554	449 886	16.11
	October	50.119	49.862	438 202	473 867	16.36
	November	50.123	49.882	403 643	439 782	15.57
	December	50.107	49.887	332 782	416 393	14.70
2014	January	50.123	49.877	351 302	370 443	14.27
	February	50.112	49.871	364 453	398 830	15.23
	March	50.131	49.877	441 431	491 861	16.48
	April	50.107	49.889	377 485	440 036	14.57
	May	50.104	48.871	361 236	417 739	13.51